Dissertation

submitted to the

Combined Faculties of the Natural Sciences and for Mathematics

of the Ruperto-Carola University of Heidelberg, Germany

for the degree of

Doctor of Natural Sciences

presented by

Dipl.-Phys. Stefan Noll

born in Gelnhausen, Germany

Oral examination: 18th of December 2002

The FORS Deep Field Spectroscopic Survey

Referees:

Prof. Dr. Immo Appenzeller
Prof. Dr. Klaus Meisenheimer

Zusammenfassung

Die Bestimmung der Eigenschaften von Galaxienpopulationen bei verschiedenen Rotverschiebungen ergibt wichtige Einschränkungen für die aktuellen Modelle zur Entstehung und Entwicklung von Galaxien. Um diesen Evolutionsprozess systematisch untersuchen zu können, wurden 265 Galaxienspektren mit hohen S/N bei Rotverschiebungen bis zu 5.0 gewonnen. Die Galaxien wurden aus dem photometrischen Rotverschiebungskatalog des FORS Deep Fields (FDF) ausgewählt. Für eine optimale Reduktion der Spektren von sehr schwachen Objekten wurden Programmpakete entwickelt. Rotverschiebungen und grobe spektrale Typen wurde mit Hilfe einer Bibliothek empirischer SEDs bestimmt, die aus gemittelten FDF-Spektren mit sehr hohem S/N abgeleitet wurden. Die Charakteristiken der beobachteten Galaxienspektren werden präsentiert und die Verteilung der Rotverschiebungen und spektralen Typen diskutiert. Erste Analysen des exzellenten Datensatzes wurden mit Hilfe von gemittelten Spektren für Galaxien-Ensembles verschiedener Rotverschiebung und Messungen von Linienstärken in den individuellen Galaxienspektren durchgeführt. Die Resultate zeigen bei höheren Rotverschiebungen eine größere Steigung des UV-Kontinuums, eine Verstärkung des Lyα-Waldes, einen Anstieg der Häufigkeit und Stärke der Lyα-Emission und eine Verringerung der C IV-Absorption. Die Entwicklung von C IV wird mit der Veränderung der mittleren Metallizität erklärt.

Abstract

The determination of the properties of galaxy populations at different redshifts provide important constraints on current models of galaxy formation and evolution. In order to investigate this evolutionary process systematically, we obtained high S/N spectra for 265 galaxies at redshifts up to 5.0 with the FORS instruments at the VLT telescopes. The galaxies were selected from the photometric redshift catalogue of the FORS Deep Field (FDF). To achieve an optimal reduction of the spectra of these very faint objects special reduction packages were developed. Redshifts and rough spectral types were determined using a library of empirical SEDs derived from FDF mean spectra with very high S/N. The characteristics of the observed galaxy spectra are presented and the distribution of redshifts and spectral types are discussed. A first analysis of the excellent data set was carried out using mean spectra of redshift-selected galaxy subsamples and line strength measurements in individual galaxy spectra. The results show a steeper UV continuum, an increase of the Lyα forest, an increase of the frequency and strength of Lyα emission and a decrease of the C IV absorption towards higher redshifts. The C IV evolution is explained by a change of the average metallicity.

Contents

Chapter 1

Introduction

The topic of the present thesis is the spectroscopic programme of the FORS Deep Field project. The emphasis of this work will be the sample selection, the observations and especially the data reduction. Furthermore, the determination of basic parameters of galaxy spectra including a derivation of redshifts and spectral types are explained. In the last part of the thesis an overview of the properties of the spectroscopic sample of the FORS Deep Field is given. In this context I present some applications of the data in order to demonstrate the quality of the spectra and their further use.

Before describing the data the astrophysical significance of this type of study is outlined. First, I briefly present current ideas on the evolution of galaxies. To lead up to the FORS Deep Field project (Section 1.4) I further discuss deep field projects in general. After that I explain the spectroscopic approaches suited to investigate galaxies in the young universe (Section 1.3). Finally, I represent the scientific objectives of the FORS Deep Field spectroscopic survey which forms the basis of my work.

1.1 Formation and evolution of galaxies

Today, the research on the evolution of galaxies represents one of the most attractive and challenging fields in modern astronomy. The basis of all present research activities in the field was laid down by two revolutionary discoveries by Edwin Hubble. First, it was the fundamental proof that galaxies are distant star systems (1924, discovery of stars in the outer parts of the Andromeda galaxy). Secondly, it was the quantitative confirmation that (distant) galaxies generally depart from each other and that the velocity v of this process is related to the mutual distance r (1929). For velocities well below the velocity of light c this relation (Hubble's law) can simply be written

$$v = H_0\, r\,, \qquad v \ll c \tag{1.1}$$

where H_0 is the Hubble constant. Typical modern values range from 65 to $75\,\mathrm{km\,s^{-1}\,Mpc^{-1}}$ (e.g. Freedman et al. 2002). Hubble measured the galaxy velocities via Doppler effect. This effect describes the stretching of electromagnetic waves, if the radiation source and the observer increase their distance relative to

each other. As a consequence wavelengths will be shifted towards lower energies. Therefore they become 'redder'. This can be expressed by

$$\lambda = \lambda_0 \, (z + 1). \tag{1.2}$$

λ_0 is the rest wavelength and z is called 'redshift'.

The discovery of Hubble's law led to the development of cosmological theories (based on Einstein's work) requiring the evolution of the universe starting with a singularity called 'Big Bang' (models of Friedmann and Lemaître). The determination of the free parameters of these models was and still is a challenging task. Nevertheless, investigations of the structure of the cosmic microwave background radiation (Bennett et al. 1996, de Bernardis et al. 2000), the large-scale structure of the galaxy distribution (Colless et al. 2001) and distant supernovae as 'standard candles' (Riess et al. 1998) led to a convergent parameter set (e.g. Durrer & Novosyadlyj 2001, Efstathiou et al. 2002). Partly the observations required alterations of the theories. Examples are the introduction of the inflation scenario taking place in a very early epoch of the universe or the invention of a non-zero cosmological constant which causes an acceleration of the expansion counteracting the deceleration due to gravity. In fact, the present observations indicate an accelerated expanding, flat universe.

Concerning the extreme differences between the state of the universe during the Big Bang and nowadays, the matter in the universe experienced an enormous evolution, although the most spectacular changes are assumed to have happened in the first few 10^5 a (until the decoupling of radiation and matter). However, only after that time ($z \approx 1000$) galaxy formation could commence.

The current idea on galaxy evolution assumes that overdensities in the primordial (cold dark) matter distribution grew up to significant gravitational potentials which served as a basis for the formation of galaxies and galaxy clusters and as well as the overall large-scale structure. The formation of galaxies started with the condensation of gas (consisting of hydrogen and helium only) and thereafter the birth of a first generation of stars (properties still uncertain) beginning the element synthesis by nuclear fusion processes in their interior. Moreover, extremely deep gravitational wells were formed known as black holes. They serve as the energy source of quasars (transformation of the gravitational energy of infalling matter) which are observed up to very high redshifts ($6 < z < 7$, Fan et al. 2001).

The following processes at high redshift are assumed as due to the hierarchical evolution of galaxies. This means, that the formation of today's galaxies started with small gas-rich proto-galaxies. These irregular clumps merged causing bursts of star formation (starbursts). That is, this early phase is characterised by a high star formation rate and the enrichment of the interstellar and intergalactic medium with metals, because of a high supernova rate. Then, the galaxies grew bigger and finally reached the present-day sizes and masses. Moreover, the morphology of the galaxies altered from very irregular objects to more regular objects (spiral and elliptical galaxies) with progressing dynamical relaxation. Merging processes transform large portions of gas into stars. Furthermore, they cause heating of gas to high temperatures and its 'concentration' in the intergalactic medium. This leads to the successive reduction of

cold gas necessary for the formation of stars. Especially in case of a so-called major merger, the collision of two spiral galaxies with a similar size, the merging event is such violent that almost all gas is transformed. The result of such an event is a completely relaxed elliptical galaxy scarcely containing cold gas. The frequency of such events depends on the local galaxy density. This can be investigated in dense galaxy clusters where the fraction of ellipticals is strikingly high. In summary, the outlined bottom-top evolutionary model is supported by various observations and numerical simulations (e.g. Naab et al. 1999), although there are still numerous open questions concerning the details of such a scenario.

Reviewing the present-day models concerning the evolution of galaxies a consistent concept emerges explaining how today's galaxies are formed. Nevertheless, the details of the crucial processes partially remain highly uncertain particularly the early evolution phases of the stellar populations. However, one can expect that within the next years the knowledge will significantly increase, particularly since telescopes of the 10 m class have just become available.

In the following I will turn to the practical aspects of the research into the evolution of galaxies.

1.2 The role of deep fields

The evolution of galaxies can be investigated most directly by surveying galaxies at the early phases of the universe, that is, at high redshifts ($z > 2$). Since the apparent surface brightness of galaxies dims with redshift as $(z+1)^{-4}$ (aside from object specific corrections), observations of high-redshift galaxies are very challenging. Thus, recent developments in astronomical instrumentation were necessary in order to reach very faint magnitudes by imaging and even spectroscopy. Hence the invention of the CCD detectors led to the first promising 'deep' observations due to their high efficiency (see Tyson 1988). But the crucial jumps ahead were attained by the use of the Hubble Space Telescope (HST) and telescopes of the 10 m-class since the mid-nineties. Now, 'Deep fields' have become one of the scientifically most promising topics in astronomy. By now, there is a high diversity of deep field projects. The various projects differ in field area, depth, covered wavelength ranges, the filter set, resolution, photometric accuracy and the preferred objects which are observed. Examples are:

Hubble Deep Field North: The HDF-N (Williams et al. 1996, review by Ferguson et al. 2000) is certainly the most prominent deep field. It was obtained using the Hubble Space Telescope (HST, mirror diameter = 2.4 m). As the observations were not influenced by atmospheric disturbances, which decrease the resolution and increase the background noise, the HDF-N represents (apart from the HDF-S) the deepest ($\gtrsim 29^{\mathrm{m}}$) and sharpest image (FWHM[1] $= 0.15''$) of the universe, so far (especially in the near infrared where the night sky emission is particularly high; compare Fig. 4.6). However, the covered sky region is quite small (only amounting to 5.6 arcmin^2). Therefore, the field statistics are affected by the local

[1] **F**ull **W**idth **H**alf **M**aximum

large-scale structure (Kajisawa & Yamada 2001) and too small object numbers ($N \sim 3000$). In fact, the HDF-N is surrounded by so-called 'flanking fields', but these fields are distinctly less deep. The follow-up spectroscopy of field objects was mainly carried out using the 10 m Keck telescopes on Mauna Kea. This is essential, because long exposure times are needed for the spectroscopy of faint objects. Finally, I still want to mention that the HDF-N was extensively observed in almost all wavelength domains.

Hubble Deep Field South: The HDF-S (Williams et al. 2000, Ferguson et al. 2000) represents the southern counterpart of the HDF-N. Consequently, the field has similar properties as the HDF-N.

William Herschel Deep Field: The WHDF (Metcalfe et al. 2001 and references therein) was observed at the 4.2 m William Herschel Telescope (WHT) on La Palma. The covered field (area: $7' \times 7'$) is larger and somewhat less deep (one magnitude and more) than the HDFs. The greatest drawback of the field represents the lack of sub-arcsecond resolution.

Calar Alto Deep Imaging Survey: The photometric observations of CADIS (Meisenheimer et al. 1997) are mainly carried out at the 2.2 m telescope of the Calar Alto Observatory. CADIS comprises several fields covering the large total area of $0.3\,\mathrm{deg}^2$. As a consequence, the fields are less deep as other optical deep fields. Besides, the broad band photometry observations are carried out using a special set of narrow band filters optimised for the detection of emission lines (especially Lyα) within small redshift bins.

Chandra Deep Field North: The CDF-N (Brandt et al. 2001) is an example for a non-optical deep field. The data were obtained by the Chandra X-Ray Observatory. For the purpose of comparison with deep optical data the field (covering an area of about $450\,\mathrm{arcmin}^2$) includes the HDF-N.

Chandra Deep Field South: The CDF-S (Giacconi et al. 2002) forms the southern counterpart of the CDF-N. In contrary to CDF-N, optical observations (mainly using the VLT, see Section 3.1) were performed as complement to the x-ray measurements.

The descriptions above show the great variety of deep field projects. Each project has strengths and weaknesses. Nevertheless, the Hubble Deep Fields have indisputably got a great impact on the current imaginations on the evolution of galaxies. Therefore, a new deep field project (especially in the optical) has to compete with the HDFs.

1.3 Deep spectroscopic surveys

Before I come to the discussion of the objectives and characteristics of the spectroscopic programme of the FORS Deep Field (Section 1.5), I briefly discuss

the different spectroscopic methods including their limits applied to investigate the properties of galaxies particularly at high redshifts.

With regard to the scientific outline of deep field projects (Section 1.2 and 1.4) spectroscopic observations constitute an ambitious and essential element of such projects. Spectroscopy allows to study the physical properties of galaxies in great detail using spectral line analysis techniques. Therefore, it is important to conduct spectroscopic follow-up studies of photometric deep fields. Although one has to keep in mind that only a small fraction of the photometric sample will be accessible by spectroscopy with sufficient resolution.

The Hubble Deep Fields are the basis of a series of spectroscopic studies. Most of the follow-up observations were carried out at the Keck telescopes. The desired targets were selected either by a two-colour selection method or by photometric redshifts mostly derived by the use of spectral templates. The two-colour selection method benefits from high colour indices of adjacent filters caused by the Lyman limit and Lyman forest breaks. Using this approach Steidel et al. (1996a, 1996b) succeeded in the discovery of a population of the so-called 'Lyman-break galaxies' at $z > 3$. Lowenthal et al. (1997) could extend this sample significantly. Further progress was reached by the application of photometric redshifts to the sample selection. With this technique galaxies at $z > 5$ could be identified (Spinrad et al. 1998, Weymann et al. 1998). According to Ferguson et al. (2000) the objects with spectroscopic redshifts in the HDF-N amounts to about 150 (adding the less deep flanking fields the number increases to about 700).

High redshift galaxies are faint. Thus, it is difficult to obtain spectra of sufficient high quality for detailed spectroscopic studies, even when taking advantage of 10 m-class telescopes. Hence, most of the spectroscopic projects have been restricted to the determination of high-quality redshifts or to the investigation of strong lines like Lyα or C IV$\lambda\lambda$ 1548, 1551. Redshift surveys of the large-scale structure (Colless et al. 2001) are good examples for the limited usage of such spectra. Solutions to the dilemma are, in principle, either the investigation of mean spectra (averaging of a subsample of galaxies, Lowenthal et al. 1997, Steidel et al. 2001) or studies of lensed galaxies (Pettini et al. 2000, 2002, Mehlert et al. 2001, Hu et al. 2002). Both possibilities increase the available signal-to-noise ratio (S/N). Indeed, the former approach is limited to statements about properties of the whole averaged population. Individual specialities are not accessible. The latter variant benefits from the amplification of light by gravitational lensing. Of course, only a very small fraction of galaxies is sufficiently amplified in order to conduct detailed spectroscopy. One may increase the chance to find higher numbers of amplified galaxies in a small field by observing rich galaxy clusters within a high gravitational potential ('gravitational telescope'). Nevertheless, a systematic study of field galaxies at high redshift is not possible with this method.

Furthermore, the investigation of Damped Lyα systems (DLAs) and similar absorption systems in spectra of bright distant quasars ($\rightarrow$ 'Lyman forest' short-wards of Lyα) opens the door to high redshifts as well. Such studies are successful in deriving the physical properties of the absorbers casually located on the line of sight towards the quasar. The absorbers rather tend to be located

in the outskirts of galaxies as in the luminous star-forming regions we see on the deep field images, so that the gained results may not be transfered easily. In addition, knowledge on the spatial distribution of the absorbers is essentially restricted to one dimension (given by the redshift).

The discussion above indicates the difficulties which are involved with an extensive spectroscopic investigation of high-redshift galaxies. Mostly the objects are simply too faint for a detailed spectroscopic study, so that extensive analyses are restricted to rare bright objects mainly amplified by lensing. Therefore, the great challenge to deep spectroscopic surveys is the acquisition of a statistically significant sample of high quality spectra of high-redshift galaxies.

1.4 The FORS Deep Field

In this section I briefly describe the project which is the basis for this thesis, namely the 'FORS Deep Field' (FDF, see Appenzeller et al. 2000, Heidt et al. 2002).

In view of the great success of the Hubble Deep Field project (see Section 1.2) and the construction of the Very Large Telescope (VLT) at Paranal (see Section 3.1), it was an obvious thing to initiate a ground-based deep field project using the power of this new generation of large optical telescopes. The construction of the important FORS[2] instruments (see Section 3.1) put the consortium of German astronomical institutes (comprising the Heidelberg State Observatory and the University Observatories Göttingen and Munich) in a position to carry out such an ambitious project using a great deal of the guaranteed time allocated in return.

Although deep ground-based observations suffer from the strong sky background and the seeing-reduced resolution (compare Section 3.3), there are couple of reasons which make a FORS Deep Field competitive with the Hubble Deep Fields:

(1) The large mirror diameter of the VLT telescopes (8.2 m in contrast to 2.4 m in case of Hubble) make it possible to obtain deep images in a relatively short time.

(2) Compared to the area of both Hubble Deep Fields together, the about four times larger field of view of FORS ($\sim 46\,\mathrm{arcmin}^2$) allows us to observe a significantly higher number of objects which results in better statistics to gain a more representative sample for the whole sky.

(3) The excellent observing conditions at Paranal and the superior optical quality of FORS allows under optimal conditions to reach the same angular resolution as single HST WFPC[3] images, although in practice for the FDF the effective resolution ($\geq 0.5''$) was inferior to the HDFs (see Heidt et al. 2002), since the large demand of observing time for deep fields makes it impossible to carry out such observations only during times of optimal seeing.

[2] **FO**cal **R**educer and low dispersion **S**pectrograph
[3] **W**ide-**F**ield **P**lanetary **C**amera

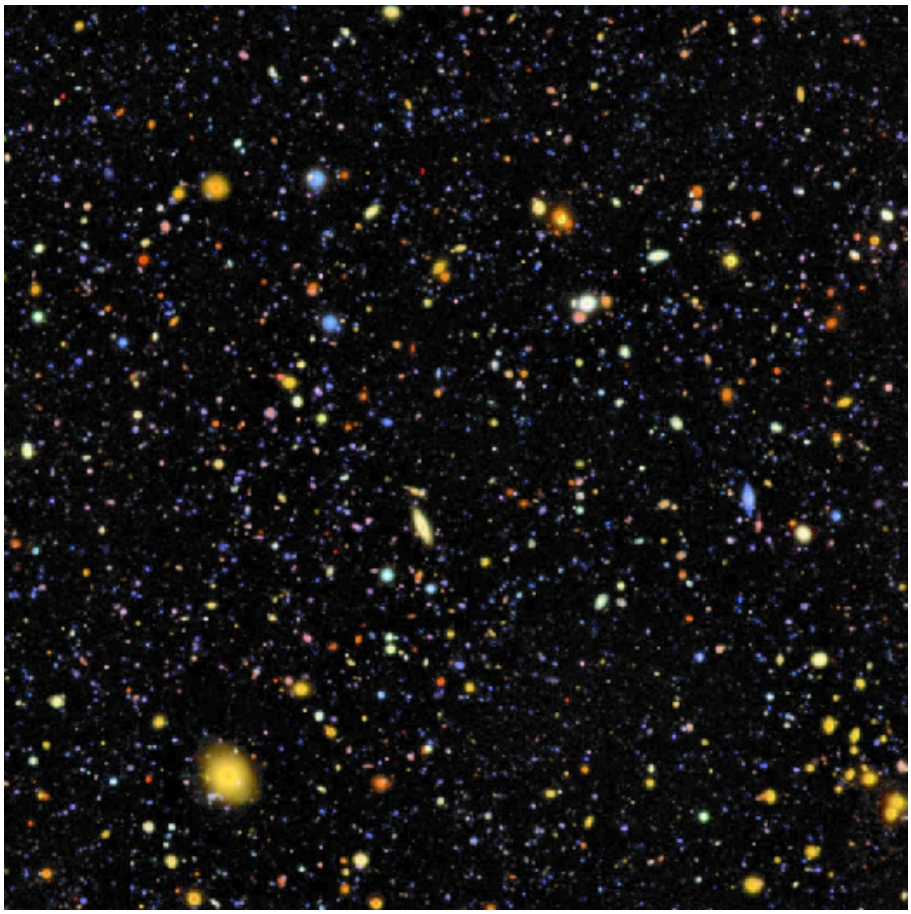

Figure 1.1: BRI colour composite image of the FORS Deep Field (B = blue, R = green, I = red). The quasar Q 0130–260 is the bright, turquoise coloured object close to centre of the field. Orientation: north is up and east is left.

(4) The flexibility of FORS (see Section 3.1) allows photometric observations to be carried out with numerous broad and narrow band filters. Furthermore, follow-up spectroscopy can be done with the same instrument.

The choice of a suitable FORS Deep Field required an thorough selection (see Heidt et al. 2002). It was important to avoid strong contaminations by stars and interstellar matter located in our own galaxy. Furthermore, galaxy clusters may affect galaxy number counts. Thus, we attempted to avoid foreground clusters to obtain a representative cosmological probe. Finally, we decided to include a previously known high-redshift quasar to allow the investigation of the line-of-sight distribution of intergalactic matter.

It turned out that a field located close to the south Galactic pole with the central coordinates $\alpha_{2000} = 1^{\rm h}06^{\rm m}03\overset{\rm s}{.}6$ and $\delta_{2000} = -25^\circ 45' 46''$ met the selection criteria best, although on the final frames a small cluster in the southwestern corner of the field was discovered (see Fig. 1.1). The field contains no stars brighter than $18^{\rm m}$ and the Galactic extinction amounts to only $E_{\rm B-V} = 0\overset{\rm m}{.}018$. The quasar in the field is Q 0130–260 at a redshift of 3.36 (Warren et al. 1991).

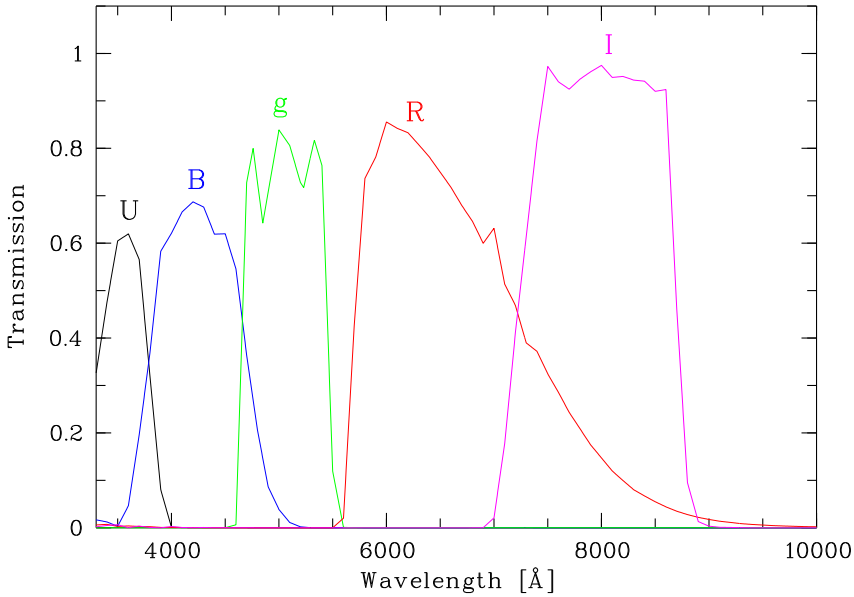

Figure 1.2: Transmission curves of the broad band filters Bessel U, Bessel B, Gunn g, Bessel R and Bessel I (compare FORS Manual). The use of Gunn g instead of Bessel V avoids the strong night sky line [O I]λ 5577.

After the determination of the field location, the photometric observations were carried out. Images of the FDF were obtained in the broad band filters U, B, g, R, I, J and K_s and some narrow band filters covering a huge wavelength range (see Heidt et al. 2002). The main observations in the 'optical' (filters U – I, see Fig. 1.2) were carried out with FORS 1 during a couple of runs in the years 1999 and 2000 (compare Table A.1). The infrared observations in J and K_s (outside range of FORS) were performed with SOFI[4] at the ESO NTT[5] (La Silla, Chile) in October 1999.

An overview of the photometric observations and the properties of the resulting sum frames can be found in Heidt et al. 2002. Here, I restrict myself to some properties of the co-added B (Fig. 1.3) and I frames:

Band	Exposure time [h]	Frames	FWHM ["]	50 % completeness limit [mag]
B	6.3	44	0.60	27.69
I	6.9	83	0.53	26.37

The source detection was carried out in both frames resulted in 8753 (at the level of 5 σ) significant objects.

The initial goals could not entirely be achieved, since a significant portion of the observing time suffered from untypically poor observing conditions. This was mainly caused by the La Niña phenomenon during this period (see Sarazin & Navarrete 1999, Sarazin 2000). Nevertheless, the FORS Deep Field represents

[4] **S**on **OF** **I**SAAC
[5] **N**ew **T**echnology **T**elescope

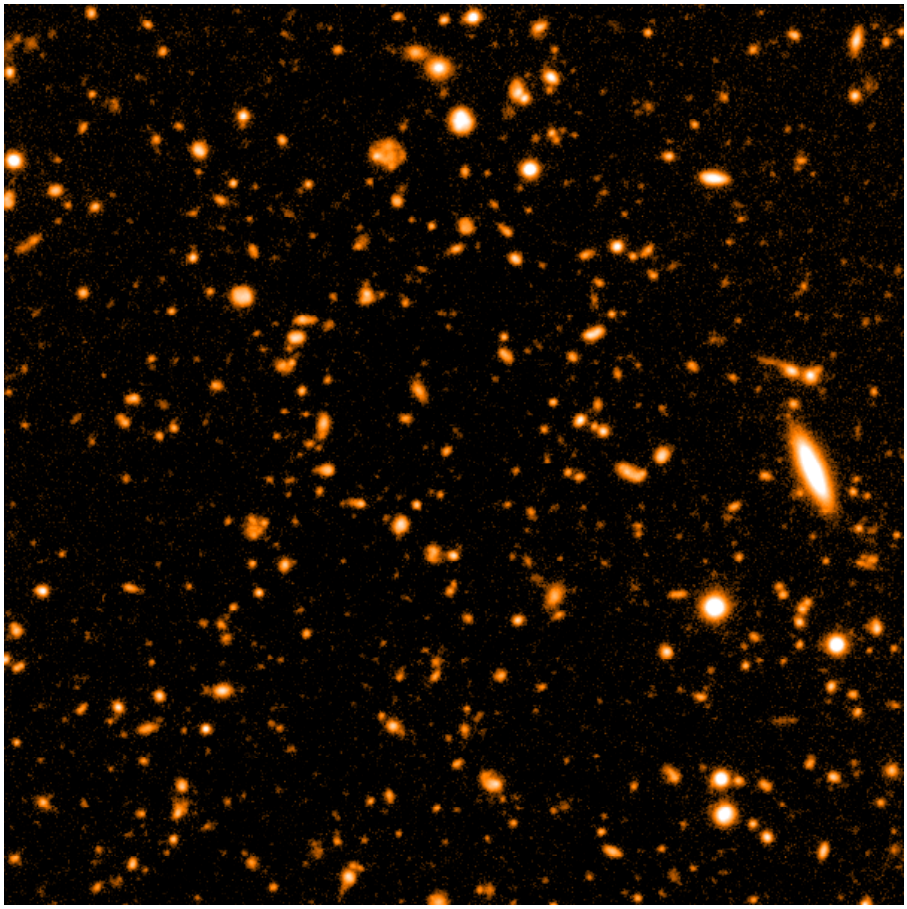

Figure 1.3: Small section ($2' \times 2'$) of the FORS Deep Field in B ($N(\text{objects}) \lesssim 10^3$). Orientation as in Fig. 1.1.

one of the deepest views of the (early) universe, so far. The high number of (faint) objects ($\lesssim 10^4$), mostly at high redshifts, forms an excellent basis for the investigation of the evolution of galaxies. Especially in the context of this work the success of follow-up spectroscopy of high-redshift galaxy candidates depends on the accuracy of photometric redshifts based on high quality imaging data (see Chapter 2).

1.5 Objectives of the FDF spectroscopic survey

Our knowledge about the early phases of the cosmic evolution is especially incomplete regarding the luminous matter like stars and gas (compare Section 1.1). There are many open questions concerning the composition of the stellar populations, the star formation history, the production of heavy elements and their enrichment in the interstellar medium, the amount of dust, gas dynamics and so on. Such problems cannot be tackled without involving the power of detailed spectroscopic studies, since in most cases the intensities and shapes of spectral lines provide essential informations. Thus, spectroscopic

investigations which concentrate on the evolution of the physical properties of galaxies on cosmic age are of high interest.

In this context, the FORS Deep Field spectroscopic survey was initiated in order to study the change of galaxy properties due to cosmic evolution systematically. This means that the FDF spectroscopic sample should allow comparative investigations of galaxies at different redshifts. This requires a statistically significant, sufficiently deep, representative spectroscopic sample which has to cover a wide redshift range. Particularly the presence of a large sample of high S/N spectra of high-redshift galaxies is important. In this thesis I will show that the sample of the FDF spectroscopic survey (benefitting from the power of the VLT and FORS) meets these basic requirements. For this, I will focus the discussion of the scientific implications from the present data set on the possible changes of the average properties of high-redshift galaxies between $z = 2$ and 4. That is, spectral properties as the UV continuum slope, the strength of Lyα emission and C IV absorption are subjected to a first (preliminary) analysis in order to reveal possible evolutionary effects like the change of the average metallicity.

Chapter 2

The spectroscopic sample

In this chapter I focus on the discussion of the selection of the FORS Deep Field spectroscopic sample. In order to reach the scientific objectives represented in Section 1.5 there are some basic requirements to the project. I discuss these demands with regard to the selection of the spectroscopic sample in Section 2.1. Then I turn to the FDF photometric catalogue which forms an important basis for the definition of suitable selection criteria. Finally, the composition of an optimum spectroscopic sample is subject to Section 2.3.

2.1 Basic requirements for the spectroscopic programme

In this section I discuss the requirements for the FDF spectroscopic survey stated in Section 1.5 with regard to the definition of suitable selection criteria.

The objective to improve our knowledge about the question how galaxies have evolved by the investigation of high-redshift galaxy spectra puts a couple of constraints on a suitable spectroscopic programme. These requirements are as follows:

- **Sufficiently large subsamples for each redshift domain**
  First, it is important to obtain sufficiently large subsamples of galaxies (selected by redshift and/or spectral type) to minimise the effects of statistical fluctuations. The higher the number of subsamples is, the more detailed the galaxy evolution can be investigated. A significant subsample of very high-redshift galaxies ($z \geq 3$) is especially interesting, because the comparison of galaxies in the local ($z \approx 0$) and the young universe (high z) should reveal the main evolutionary effects.

- **Avoidance of selection biases**
  The sample selection should not be affected by biases in order to attain representative results. That is, the applied selection procedure should be equally sensitive to all types of objects as far as possible. However, selection biases may appear for the unavoidable brightness limits which restrict the observations to absolutely rather bright objects particularly in case

of high redshift galaxies. For that reason, limiting magnitudes as faint as possible are desirable.

- **High signal-to-noise ratios**
  Many applications of the spectra will only succeed if the signal-to-noise ratio is high. Hence, regarding high-redshift galaxies (mostly $I > 23^{\mathrm{m}}$) long exposure times may be necessary, if one wants to know more about an object as the redshift and a rough spectral type. Anyway, a sufficient S/N is the most important precondition for the feasibility of spectroscopic analyses at all.

- **Large wavelength range**
  It is of advantage if the spectrum covers a broad wavelength range, because this allows the investigation of a higher number of spectral lines. Furthermore, the determination of spectral types is simplified, since the effect of interstellar extinction, which causes a reddening of spectra, can be determined in a better way. In case of low S/N spectra large wavelength ranges may become important with respect to the derivation of redshift.

- **Sufficiently high resolution**
  Finally, analyses like the investigation of line profiles and weak lines requires a sufficient high spectral resolution. Here, high redshift galaxies profit from the stretching of the spectrum corresponding to the factor $(z + 1)$. In general, an increase of spectral resolution also leads to an increase of the necessary exposure time, if the S/N per resolution element is kept constant.

The listed requirements can only be fulfilled if the investigated sample is large enough and the integrated exposure time of individual objects are sufficient. Thus, a project with the above requirements needs a large amount of exposure time at telescopes of the 8–10 m-class. This basic condition could be met by the FORS Deep Field project, since as a guaranteed time project it received a relatively large amount of observing time (~ 100 h of exposure time so far) at the VLT. And without doubt, the combination of FORS and VLT belongs to the best existing in optical astronomy so far.

However, since there are contrary demands and the total exposure time was not unlimited priorities had to be set up dependent on the preferential scientific aims. Since the high-redshift domain ($z > 2$) provide the most valuable informations about the evolution of galaxies, the selection criteria were optimised in this direction. Owing to the faintness of high-redshift galaxies observations require long exposure times (~ 10 h) in order to reach reasonable S/N for spectroscopic studies. Therefore, one has to restrict the number of targets which leads to a limitation of the redshift range which can be covered by statistically significant subsamples. For that reason, the preferential redshift domain was limited to $2 < z < 5$. Another limitation is caused by the contrast of the demand of a high spectral resolution to the demand of a high S/N and a large wavelength range, respectively. Owing to the preference given to faint high-redshift galaxies, S/N and wavelength range (important to the redshift identification in weak spectra

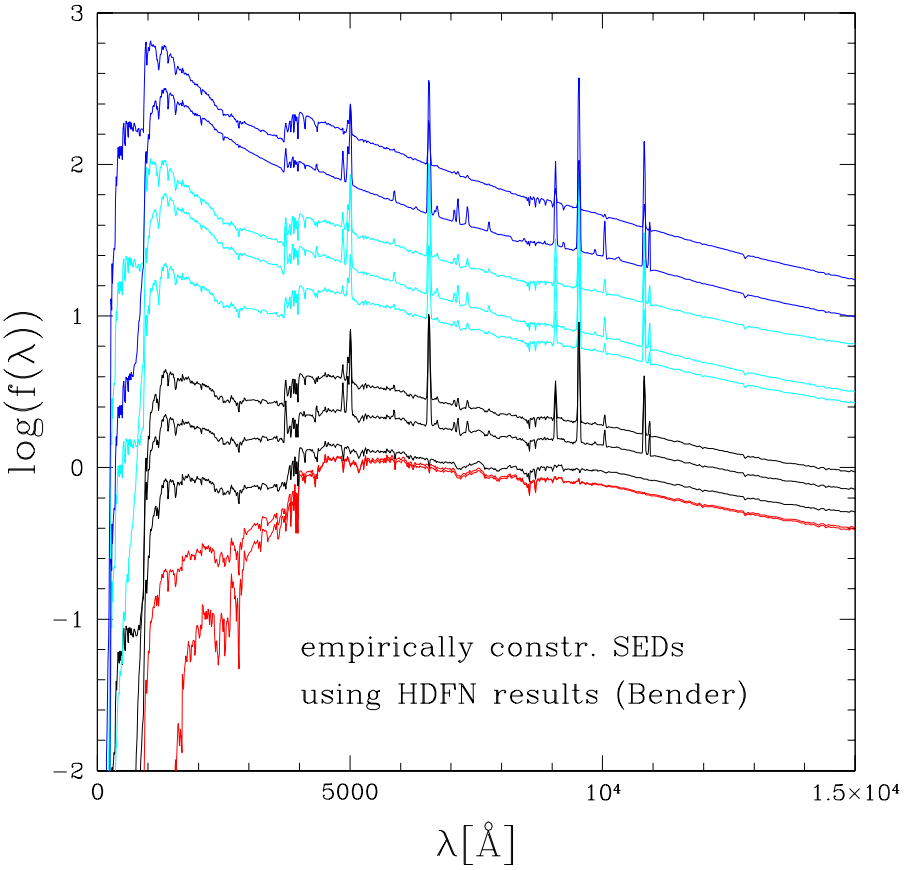

Figure 2.1: Selection of semi-empirical spectral energy distributions applied for the derivation of photometric redshifts (see text). The SEDs are plotted as logarithm of the flux (in arbitrary units) over the rest-frame wavelength in Å. The blue coloured curves represent galaxies with high star formation rate (→ starburst galaxies). The red coloured curves are related to passively evolving early-type galaxies (→ elliptical galaxies).

and the comparability of objects at different redshifts) were given a higher priority than the resolution. Therefore, the observations were carried out in a low resolution mode (see Section 3.2).

The final selection criteria resulting from the above considerations are discussed in Section 2.3.

2.2 Photometric redshifts and types

The photometry of the FORS Deep Field (Heidt et al. 2002, see Chapter 1) forms an excellent basis for the spectroscopic sample selection. In fact, the photometric data can be used to obtain rough redshifts and spectral types by fitting spectral templates to the filter fluxes (see Bender et al. 2001 and Gabasch et al. 2002). The procedure needs a very accurate photometry in as many filters as possible for a large wavelength range. This is guaranteed by the deep photomet-

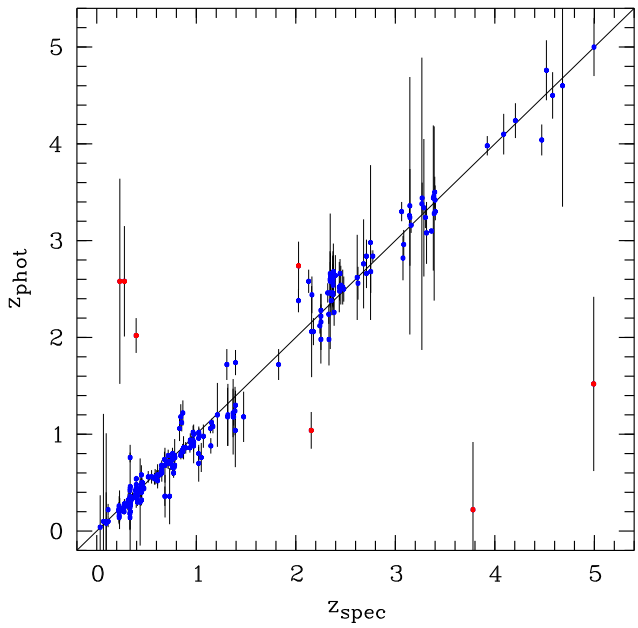

Figure 2.2: Comparison of the photometric and spectroscopic redshifts for the FDF galaxies with certain z_{spec}. The errors of the photometric redshifts as given by the redshift code are indicated by black bars. Objects with $|z_{\mathrm{phot}} - z_{\mathrm{spec}}| > 0.5$ are marked by red dots.

ric images of the FDF in the filter bands U, B, g, R, I, J and K. Moreover, the set of spectral templates applied has to be chosen carefully in order to minimise false identifications (which results in wrong redshifts). It turned out that a set of 15 independent semi-empirical spectral energy distributions (SEDs) represents the most suitable combination (see Fig. 2.1). The templates are constructed by the adaption of simple stellar population models of Maraston et al. (1998) to representative broad-band SEDs produced by photometric data of galaxies in the Hubble Deep Field North (Williams et al. 1996) with known spectroscopic redshifts.

Principally, the photometric redshift technique can identify all types of objects for which templates are available. Therefore, correct redshift derivations are not restricted to special classes of objects. This lowers the probability of misidentifications and avoids selection biases concerning special types of objects. Thus, the technique constitutes the ideal method to obtain reliable object informations for a successful selection of spectroscopic targets which is essential in order to waste no valuable observing time by exposures of wrong candidates.

Nevertheless, the photometric redshift technique reaches its limits regarding objects with unusual SEDs. In fact, the number of templates cannot be increased too much, since this would increase the probability of misidentifications due to unsuitable templates for all kinds of objects. Thus, it is inevitable that a small fraction of objects with rather 'exotic' spectra (like quasars or highly reddened objects) may be under- or even overrepresented in the spectroscopic sample

compared to the frequency in the photometric sample. For instance, the latter scenario may occur for candidates at very high redshift ($z > 5$). Here, the sample can be contaminated by very low mass stars (spectral type M and L, see Martín et al. 1998 and 1999) which also show very red SEDs. However, point-like sources like stars (a small minority in the FDF) and quasars can be discovered by their intensity profile which should match the corresponding point-spread function. Using this additional information, the number of unrecognised unusual objects should be very small.

The reliability of the photometric redshifts $z_{\rm phot}$ can be checked by comparison with spectroscopic redshifts $z_{\rm spec}$. This is shown in Fig. 2.2. The diagram indicates an excellent agreement of $z_{\rm phot}$ with $z_{\rm spec}$ for the galaxies in the FORS Deep Field. Fig. 2.2 indicates a typical uncertainty of the photometric redshifts of $\Delta z_{\rm phot} \sim 0.1$. The number of outliers (red dots) is very small ($< 3\,\%$), although objects with unusual spectra (quasars, galaxies with strong Lyα emission) were not excluded. Consequently, photometric redshifts constitute a very effective tool for the selection of suitable candidates for the spectroscopic survey.

2.3 Selection criteria for the spectroscopic programme

An optimal use of a limited amount of observing time requires a careful selection of suitable targets. The targets should be chosen such that the requirements specified in section 2.1 are fulfilled as far as possible.

Brightness limits

The detailed investigation of evolution effects requires a sufficiently large sample of candidates for every redshift domain. In order to get a complete sample, one should attempt to observe all objects which are brighter than a limiting apparent magnitude. As the characteristic apparent magnitudes vary with redshift, the brightness limits have to be redshift dependent to obtain subsamples of comparable volume for every redshift domain. The brightness limits are mainly determined by the amount of available observing time, which restricts the number of objects, as well as by the practicable individual exposure times and consequently the achievable signal-to-noise ratios. It is advisable to use I band magnitudes for the specification of the brightness limits, because the I fluxes depend less on the specific properties and states of the stellar populations and of the interstellar reddening in the observed galaxies than the flux in bluer filters.

Fig. 2.3 shows the I magnitudes of the selected objects versus the photometric redshift (Section 2.2). Since the object selection was carried out using I magnitudes, the diagram illustrates well the redshift dependent selection limits. So, for photometric redshifts between 2.0 and 4.0 the selected spectroscopic sample seems to be almost complete ($> 90\,\%$) down to an I magnitude of about $23\overset{\rm m}{.}9$. In contrast, between $z_{\rm phot} = 1.0$ and 1.5 a 'completeness' of $\sim 50\,\%$ only could be attained for objects brighter than $23\overset{\rm m}{.}0$. The 'completeness' values have to be handled with care, since the quality of the values sensitively depends on the accuracy of the photometric redshifts. The accuracy derived from Fig. 2.2

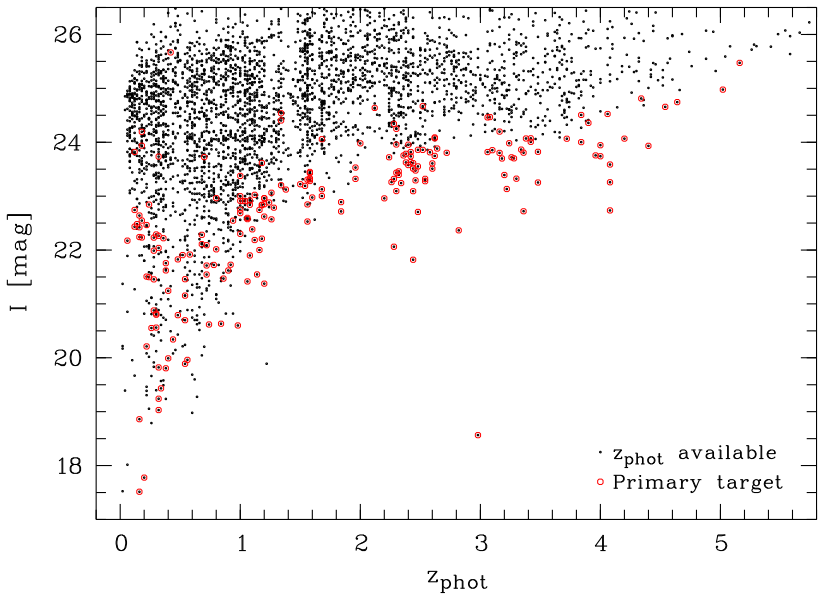

Figure 2.3: Photometric redshifts and I magnitudes of primary targets of the FDF spectroscopic survey (red circles). For comparison the complete photometric redshift catalogue (applied to the object selection) was plotted as well (small black circles).

indicates that this issue may only be a minor problem. However, particularly the number of high-redshift candidates is easily affected by incorrectly classified objects at supposedly low redshifts, because the number of objects brighter than a given magnitude decreases rapidly with increasing redshift.

Choice of exposure time

The achievement of sufficient signal-to-noise ratios (S/N $\gtrsim$ 10) requires exposure times of about 10 h (or even more) for galaxies at redshifts higher than 1.5, whereas for brighter objects (mostly at low redshifts) exposure times of 2 h or less are enough. These time values are valid for low resolution spectroscopy (i.e. grism 150 I of FORS, see Section 3.2) at a large telescope (such as the VLT, see Section 3.1). For higher resolutions and smaller telescopes the required integration time increases dramatically.

Limits to multi-object spectroscopy

In order to observe as many objects as possible, spectra were obtained using the technique of multi-object spectroscopy (MOS). In case of FORS, a minimum of 19 objects can be observed simultaneously (see Chapter 3). This allows to obtain large spectroscopic samples in a relatively short time. However, the choice of targets which can be observed is limited, even if the positioning and orientation of the slitlets is quite flexible. The strongest limitations are given by the dispersion direction. Since a shift of a slitlet along this direction also causes a shift of the spectrum on the CCD (see Chapter 3), spectral informa-

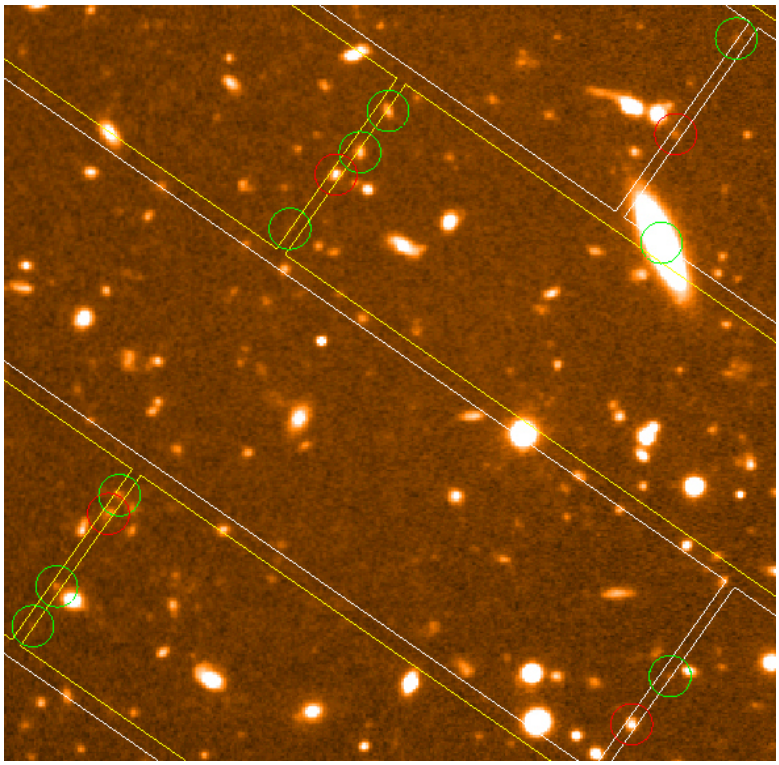

Figure 2.4: Section of a virtual MOS mask superposed on a combined R + I band image of the FORS Deep Field. The slitlets are adjusted to the primary targets (red circles). Secondary targets additionally covered by the slitlets are indicated by green circles. The virtual mask was prepared using the FIMS tool provided by ESO.

tion can be lost in case of an excessive deviation of a slitlet from the central position. This leads to a significant reduction of the useful field area. Moreover, it is not possible to get spectra of several objects located in the same row in dispersion direction. As the reduction procedure (see Chapter 4) needs several arcseconds of sky for each spectrum, this problem also concerns objects with small projected distances in the spatial direction. Regarding this limitations the mask preparation may cause selection biases which particularly concern objects located in the margin of the field and in close groups of interesting objects. Thus, it is very important to use a number of variant masks differing by their central coordinates, orientation, slitlet positions and inclinations (if possible). In this way it is possible to obtain a spectroscopic sample with a fairly homogeneous distribution of field positions. Optimally the distribution of exposure time should be independent of the location of the objects.

Secondary targets

The lengths of the slitlets are often much larger than the extension of the objects. Especially in case of the MOS unit (see Chapter 3) the fixed slitlet lengths reach more than 20″. Thus, it may happen that additional objects are located on the slitlets which had not been selected beforehand. Hence, up

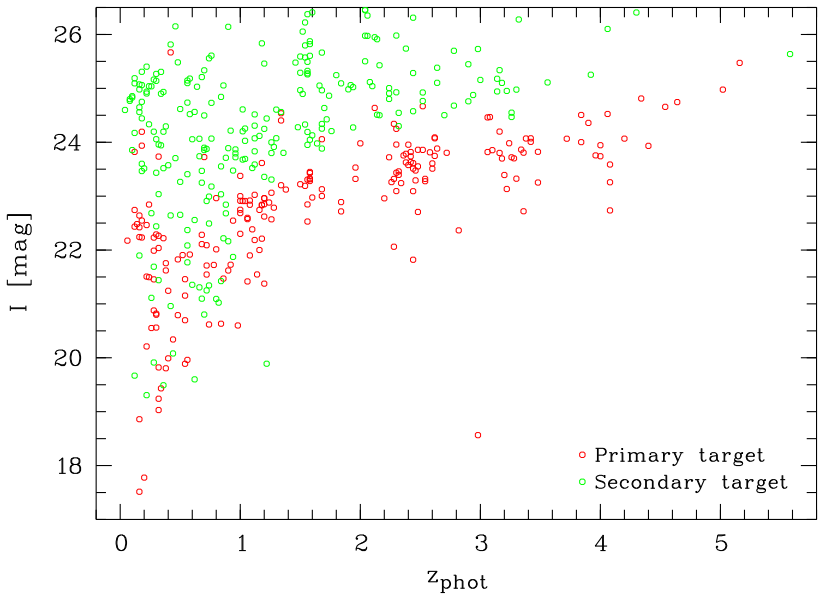

Figure 2.5: Photometric redshifts and I magnitudes of primary (red circles) and secondary targets (green circles) of the FDF spectroscopic survey in comparison.

to three or four secondary objects can be found adjacent the primary target. This effect leads to further kind of object selection which has a serendipitous character.

Fig. 2.4 shows a part of a virtual MOS mask created using the FIMS[1] tool provided by ESO (see FIMS Manual). The mask is superimposed on the selection image (R + I band image of the FORS Deep Field). In the slitlets depicted more objects than the originally selected (red circles) are found. The presentation indicates that the majority of the secondary objects are either very weak or only covered by part (in case of extended objects). For that reason, high quality spectra for the secondary objects are expected to be an exception, particularly since these objects are usually located on only a single mask with typical integration times between 2 and 4 h (see Chapter 3). Nevertheless, the serendipitous selection can be very useful in discovering objects such as faint Lyα emission galaxies and for statistical investigations in random samples.

The distribution of apparent brightnesses, redshifts and spectral types among the secondary objects should represent the respective distribution of the photometric sample. For that reason, one may expect a high frequency of faint low redshift galaxy candidates. Indeed, this is indicated by Fig. 2.5 which shows the I magnitudes of the observed secondary objects (in comparison with the primary objects) over the photometric redshift. However, one cannot expect to see such a distribution in the whole spectroscopic sample, because the secondary objects are often too weak to obtain a reasonable spectroscopic redshift (see Chapter 5.6). Thus, the selection of the primary targets should be decisive for the composition of the spectroscopic sample.

[1] **F**ORS **I**nstrumental **M**ask **S**imulator

Chapter 3

Observations

In this chapter I describe the observations of the spectroscopic programme of the FORS Deep Field project which were all performed using the FORS instruments at the VLT. Therefore, a brief introduction to the VLT and FORS in general is given in the first section. Then, I describe the instrumental set-ups applied to the spectroscopic observations. Moreover, I present an overview of all observing runs concerning the spectroscopic programme.

3.1 The instrumentation

The VLT

At Paranal mountain in the Atacama desert in Chile, one of the driest locations on earth, the European Southern Observatory (ESO) has built the largest optical observatory, so far. First light was in July 1998. The so-called Very Large Telescope (VLT) is basically an array of four telescopes with a mirror diameter of 8.2 m each (Fig. 3.1; see VLT White Book, ESO web page).

The four telescopes called Antu, Kueyen, Melipal and Yepun are mounted azimuthally which resulted in mechanical advantages and allowed very compact domes. However, this installation requires a very precise and simultaneous tracking of the telescope in three axes (azimuth, altitude and field orientation). This accounts for an 'observation hole' in the vicinity of the zenith due to a singularity of the rotation velocity of the telescope (compare Section 3.3).

The monolithic primary mirror of each telescope was made out of zerodur and was kept very thin with a thickness of 175 mm only. Therefore, each mirror has to be kept in form by permanent control and active shape adaption by means of 150 axial force actuators. The time scale of this so-called active optics system is about 1 – 30 s. Alternations of the mirror shape to be compensated are caused by motions of the telescope (variation of the influence of gravity on the telescope statics), wind and temperature effects.

Up to now, the telescopes were mostly used as separate devices. For each telescope one to two instruments (optimised for different wavelength regions and observing modes) are available.

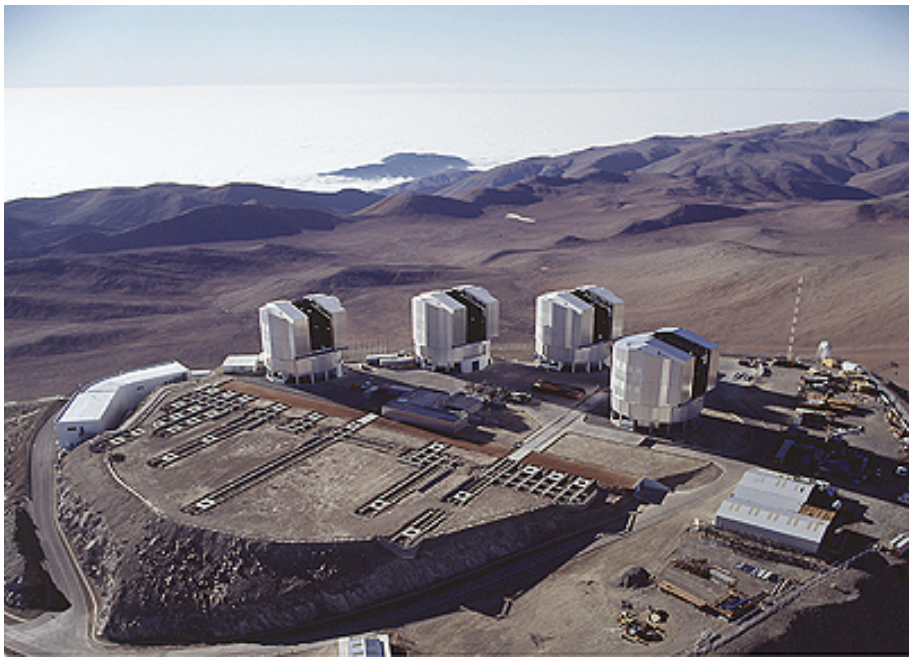

Figure 3.1: Image of the ESO VLT at Paranal. The mountain is located in the Chilean Atacama desert close to the Pacific coast. The VLT mainly consists of four 8.2 m-telescopes called (from the left to the right) Antu (UT 1), Kueyen (UT 2), Melipal (UT 3) and Yepun (UT 4). In the foreground is space for movable auxiliary telescopes which will be used for interferometric observations. The control room for all telescopes is situated in the white building on the left-hand side. (origin: ESO web page).

FORS

The FORS instruments (Fig. 3.2) represent the workhorses at the VLT. Both instruments were built by a consortium of the German observatories of Heidelberg, Göttingen and Munich (see Appenzeller & Rupprecht 1992, Szeifert et al. 1998). They form the basis for a great deal of the scientific results achieved by observations at the Paranal in the past years. FORS 1 & 2 are universal instruments optimised for the optical wavelength domain (wavelength range: 3300 – 10000 Å) which is indicated by the efficiency curves of the CCD[1] detectors (see Fig. 3.4).

The FORS instruments offer various observing modes (see FORS Manual). Besides imaging with a large filter set, different kinds of spectroscopic observations are possible. The spectroscopic modes provide long-slit spectroscopy (LSS), medium dispersion Echelle spectroscopy (ECH) and multi-object spectroscopy with movable slitlets (MOS) or laser-cut masks (MXU[2]). The modes ECH and MXU are available at FORS 2 only. This also concerns high time resolution observations. In contrast, FORS 1 has optics for polarimetric measurements. Thus, imaging polarimetry as well as multi-object spectro-polarimetry are possible. The high number of available observing modes make the instru-

[1] **c**harge-**c**oupled **d**evice
[2] **M**ask e**X**change **U**nit

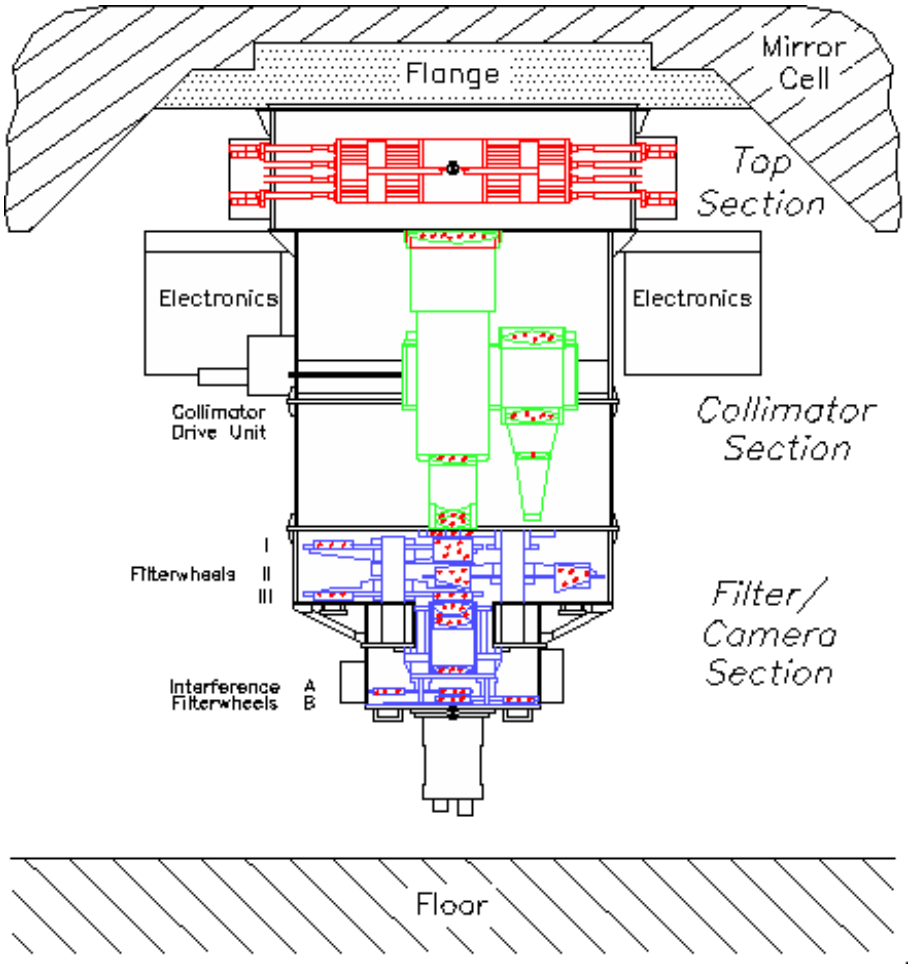

Figure 3.2: Schematic view of the FORS instruments (origin: Appenzeller & Rupprecht 1992).

ments very flexible, so that FORS is well suited for numerous kinds of applications.

The atmospheric dispersion due to the wavelength dependent refraction of light in air represents a important disturbing effect, especially for spectroscopy, resulting in significant flux losses. At low altitudes the effect reaches the order of arcseconds. Consequently, atmospheric dispersion correction is necessary. For the FORS instruments this is managed by the Longitudinal Atmospheric Dispersion Corrector (LADC). The LADC solves the problem by two thin prisms with variable distances (see Avila et al. 1997).

3.2 The observational set-up

Since the FORS Deep Field project represents a guaranteed time programme (see Section 1.4), it has been possible to create a large spectroscopic sample, which is very homogenous regarding the instrumental set-up. This simplifies the data reduction (Chapter 4), since all reduction steps can be done in the same

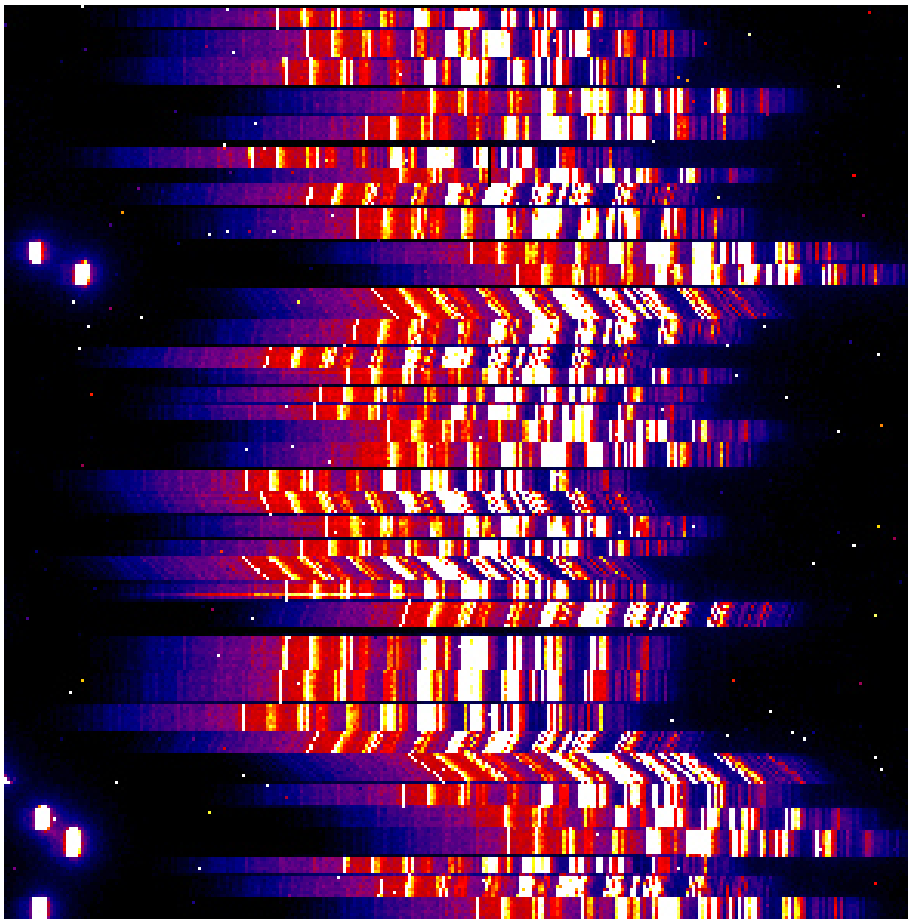

Figure 3.3: Multi-object spectrum (ID 094) of a MXU mask using grism 150 I without order separation filter. The basic mask had 37 slitlets with a slit width of 1″ and variable length. Parts of the slitlets were inclined, which is indicated by the oblique night sky emission lines. The blue wavelength range is located on the left-hand side of the frame. The spectra are dominated by night sky emission. The object spectra are in most cases only faintly visible. Spectra of zeroth order are visible in some cases close to the left margin of the image. The small dots correspond to cosmics.

manner. Furthermore, a homogeneous sample is helpful for the comparison of results extracted from different spectra, because possible systematic errors tend to cancel out. Therefore, it is advantageous to use a fixed spectroscopic set-up optimised for the scientific objectives.

Observing mode

The acquisition of a large spectroscopic sample requires the simultaneous observation of a large number of objects. Therefore, FORS provides two modes of multi-object spectroscopy (compare Section 3.1), the MOS and the MXU mode. A MOS mask consists of a fixed number of 19 slitlets each of them is formed by two blades mounted on opposite carriers. This technique allows a free positioning of the slitlets in dispersion direction and also a free choice of the slit width.

The MXU masks are individually manufactured using a laser-cut method. Thus, the MXU mode provides more freedom than the MOS mode. Hence, it is possible to create a higher number of slitlets (up to 80). Furthermore, the slitlets can be inclined relative to the dispersion direction. Even circular and curved slitlets are possible (see FORS Manual), but these options were not applied in order to avoid unnecessary complications of the data reduction. Although MXU is the more effective mode, most observations were carried out using the MOS mode (see Section 3.3), since MXU became available at FORS 2 only in 2001. Fig. 3.3 represents an example of a MXU spectrum with 37 slitlets, part of which are inclined.

The CCD

The wavelength dependent efficiency of the CCD detector basically limits the spectral range for spectroscopic analyses. Fig. 3.4 shows the quantum efficiency of the two FORS CCDs as a function of the wavelength. The quantum efficiency denotes the fraction of photons hitting the CCD and generating free electrons which can be collected and counted. According to the diagram, the maximum quantum efficiencies achieved in the R band (see Fig. 1.2) are above the 80 % level, higher for FORS 2. In the near UV and near IR wavelength regime the sensitivity decreases rapidly.

The grism

The goal to investigate the physical properties of galaxies at different cosmic epochs (see Section 1.5) requires the observation of objects with very different redshifts and spectral types. Thus, a suited standard set-up has to cover a spectral range as large as possible in order to match the important spectral regions for all kinds of spectra. Moreover, a great deal of the objects is very faint and was previously unobserved which is especially true in case of the high-redshift candidates. Thus, one also depends on the presence of extensive spectral informations for a correct identification.

This requirement is met best by the low resolution grism 150 I (Fig. 3.5). A 'grism' is a combination of grating and prism, which is particularly effective and provides an almost linear dispersion relation (see Section 4.2). The 150 I covers the whole wavelength range available by the CCD (3300 – 10000 Å, Fig. 3.4) with a relative high efficiency. The maximum efficiency of the grism is reached at around 5000 Å. There, the transmission amounts to about 80 %. In the near UV and the near IR (where the CCD is less efficient) the sensitivity drops below 40 %.

The maximum wavelength range is only available if one does not use an order separation filter (OSF). The OSF prevents a superposition of the first and second order spectra, but cuts the blue part of the spectrum. In case of grism 150 I this affects wavelengths higher than 6500 Å. However, except for very blue objects like O stars, which are not present in the FDF (compare Section 4.4), the second order only contributes by a small amount of the order of a few percent. The effect is often negligible in the face of the achievable signal-to-noise ratios

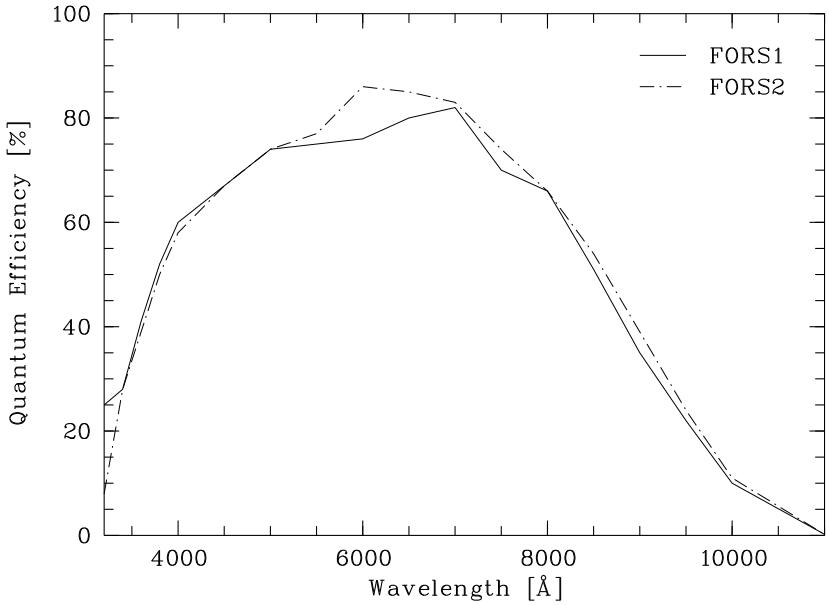

Figure 3.4: Quantum efficiencies of the two FORS CCDs (state of commissioning phase). The solid line denotes the FORS 1 CCD, the dash-dotted line the FORS 2 CCD (substituted in April 2002, see FORS Manual).

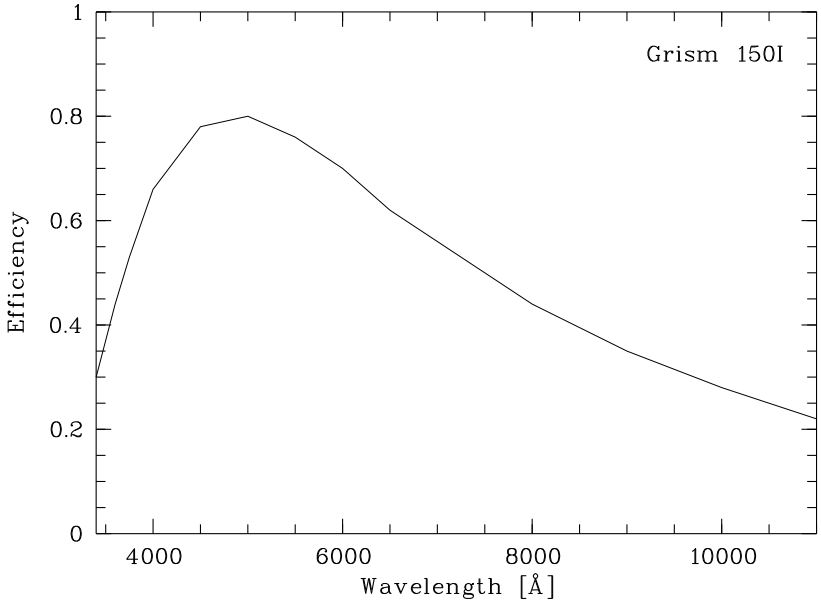

Figure 3.5: Efficiency curve of the FORS grism 150 I (compare FORS manual).

in the wavelength range concerned. Therefore, the loss of the blue part of the spectrum would have been more serious than the contribution of the second order for the present programme. Hence, no order separation filter was used.

Slit width

For the choice of the slit width one has to balance between two opposite conditions. On the one hand, the spectral resolution is inversely related to the slit width. This implies the use of small slit widths. This is supported by the fact that grism 150 I represents the FORS grism with the lowest resolution (see FORS Manual). On the other hand, one has to avoid significant flux losses caused by too small slit widths (compare Section 4.4). The amount of the losses depends on the angular size of the objects and the seeing which is a measure of the reduction of the angular resolution by atmospheric turbulence. For typical seeing conditions of $< 1''$ (FWHM of a point-like object) and small objects with extensions of the order of several $0.1''$ a slit width of $1''$ represents good a compromise to get as much as possible of the flux *and* a reasonable spectral resolution simultaneously. The assumption of small object sizes is reasonable for most of the spectroscopic candidates, since a deep field lacks large foreground galaxies and is expected to be dominated by such compact objects. Hence $1''$ was chosen as standard slit width. Measurements of the width of calibration lines result in an almost constant spectral resolution element of $\lesssim 23$ Å (FWHM) for the combination of grism 150 I and a slit width of $1''$.

Exposure time

As already mentioned high-redshift galaxy candidates typically have an apparent brightnesses of $I > 23^{\mathrm{m}}$. On the other hand, signal-to-noise ratios of 10 and more are needed for quantitative spectroscopic studies. Thus, in case of the grism 150 I total integration times of about 10 h are necessary to achieve the desired quality. This long exposure time has to be realized by combining a number of shorter exposures. First, different mask configurations with integration times of 2 to 4 h were created. Each object can therefore be found in a couple of different masks. This strategy allows a very flexible observing time allocation. Furthermore, systematic problems caused by CCD defects and object locations in the margin of slitlets (see Chapter 4) are reduced. Then, each mask set-up was usually divided in couple of single exposures with an integration time of 30, 40 or 48 min (see Appendix A). The values are small enough for a flexible observation schedule. Furthermore, systematic effects increasing with time such as cosmics (see Section 4.3) remain acceptable. On the other hand, the integration times are long enough to attain sufficient signal-to-noise ratios.

In summary, the objectives of the spectroscopic programme are achieved best using the multi-object spectroscopy units of the FORS instruments with a slit width of $1''$ and the low resolution grism 150 I without order separation filter. The individual integration times ranged between 30 and 48 min.

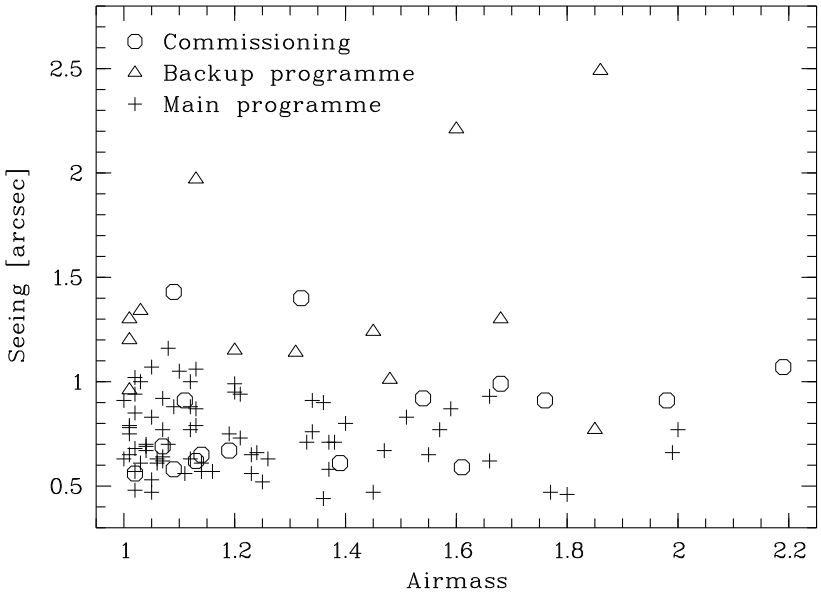

Figure 3.6: Effective airmass and average seeing (seeing monitor) during the observations of the spectroscopic programme. The character of the observing run is indicated by different symbols: circle = commissioning phase, triangle = backup programme and cross = main programme.

3.3 Observational details

The spectroscopic data of the FORS Deep Field were obtained during the commissioning phases of the FORS instruments and several campaigns using the guaranteed time allocated for the development of these instruments (compare Section 1.4). Table A.1 in Appendix A provides a compilation of information on the observations. Fig. 3.6 shows the distribution of airmass and seeing values relevant to the observations. The effective airmass values were computed according to equation (4.3). The seeing values are those measured by the seeing monitor and may significantly deviate from the seeing at the telescope (up to $0.3''$) in case of particular climatic conditions (e.g. very low wind velocities, see Appendix A). But in most cases the deviations did not exceed the $0.1''$ level.

The spectroscopic observations started during the first commissioning phase for FORS 1 in September 1998. Further commissioning observations were carried out in December 1998 (second commissioning of FORS 1), November 1999 and January / February 2000 (commissioning phases of FORS 2). These observations were essentially carried out for testing the instrument. Therefore, the scientific output was not at optimum. Especially some of the calibration exposures (see Chapter 4) are of low quality. In a few cases they are even absent. The observing conditions of the commissioning runs were quit variable (circles in Fig. 3.6). Since the observations (especially regarding FORS 1) took place in a early phase of the FORS Deep Field project when the photometric survey was not completed and high quality photometric redshifts were not yet available, the spectroscopy was mainly focused on brighter objects in the field ($I < 23^{\mathrm{m}}$, $z < 1$).

In 1999 several observing runs were carried out mainly dedicated to photometric observations of the FORS Deep Field (see Section 1.4). Since the weather conditions were in part too poor for imaging, spectra were also obtained. Of course, the weather conditions were not ideal for these backup observations as well. The seeing varied between 1 and 2.5″ (triangles in Fig. 3.6). However, in order to get useful spectra it was necessary to restrict the observations to brighter objects ($I < 23^{\mathrm{m}}$), similar to the commissioning observations. A further backup exposure (ID 091) was taken in October 2001 also including brighter objects only.

The spectroscopic main project was dedicated essentially to study high-redshift galaxies and was performed in a couple of distinct runs (visitor mode as well as service mode) since September 2000 (see Table A.1). All observations (19 set-ups) have been prepared using photometric redshifts as described in Chapter 2. Thus, it was possible to focus the observations on faint high-redshift galaxy candidates. The weather conditions during these runs were good, in part even excellent (crosses in Fig. 3.6). In almost all cases the sky was photometric and the relevant seeing below 1″. The mean seeing of the main programme amounts to 0.74″ which is better than the mean value for Paranal ($\sim 0.8''$, see ESO web page). Since almost no time losses occurred, a large number (73 exposures) of high quality spectra with a total integration time of 42.6 h have been obtained. Taking into account the number of slit positions per mask (19 in case of MOS, 37 in case of both MXU masks) the total number of slitlets for the main programme amounts to 1585. Including commissioning and backup observations the above values increase to 27 set-ups, 102 exposures, a total integration time of 56.3 h and 2087 slit positions.

Chapter 4

Data reduction

A careful reduction procedure is very important, because the success of all further analysis depends on the quality of this basic data processing. Unfortunately, the reduction of a large data sample is very time-consuming. Hence, data reduction has constituted the main part of this work and it is appropriate to give wide space to the detailed description of the individual reduction steps.

All the data processing was carried out using MIDAS[1] routines. Especially the MIDAS context MOS[2] was used for the basic reduction. In this connection, I benefitted from the basic work of W. Fürtig, S. Möhler, W. Seifert, O. Stahl, E. Sutorius and T. Szeifert (former and present members of the Landesternwarte, Heidelberg, Germany) on the optimisation of the reduction procedures for FORS multi-object spectra. This was the precondition for the development of a suitable reduction approach for the spectra of faint FDF objects represented in this thesis.

The data reduction method applied roughly consists of the following steps:

(1) Bias subtraction (see Section 4.1)

(2) Flat-field correction (see Section 4.1)

(3) Relative wavelength calibration applying calibration lamp spectra (see Section 4.2)

(4) Sky subtraction (see Section 4.3)

(5) Extraction of the one-dimensional spectra and rejection of cosmics using the Horne algorithm (see Section 4.3)

(6) Absolute wavelength calibration using the night sky line [O I]λ 5577 (see Section 4.2)

(7) Relative flux calibration correcting for atmospheric extinction by means of an extinction law and for instrumental flux losses using standard stars (see Section 4.4)

[1] **M**unich **I**mage **D**ata **A**nalysis **S**ystem
[2] **M**ulti-**O**bject **S**pectroscopy

(8) Absolute flux calibration correcting slit losses using photometric data (see Section 4.4)

(9) Computation of S/N optimised co-added spectra and simultaneous rejection of defective data points (see Section 4.5)

(10) Refined absolute flux calibration (see Section 4.4)

(11) Interstellar extinction correction (see Section 4.7)

(12) Correction for atmospheric A and B bands (see Section 4.7)

In the following, these reduction steps will be discussed in detail.

4.1 Bias subtraction and flat-field correction

Bias subtraction

All raw frames were bias corrected using bias images (obtained by closed shutter exposures) provided by ESO. First, a normalised bias frame was created which then was multiplied by the mean value calculated from the unexposed left margin (prescan) and right margin (overscan) of the corresponding frame. Finally the calculated bias was subtracted. This method has the advantage of taking into account possible changes of the absolute bias value and the exposure time dependent amount of the dark current (a few electrons per pixel and hour, see FORS manual).

Flat-field correction

In order to correct pixel-to-pixel sensitivity variations a so-called flat-field correction was applied to the raw spectra. 'Flat-fields' are obtained by 'observing' light sources providing a spatial and spectral intensity distribution as homogeneous as possible. In the spectroscopic mode of FORS internal screen flats are obtained during daytime with the telescope pointing to zenith (see FORS Manual). The exposures are taken using the same instrumental set-up as in the case of the scientific frames. Thus, individual flat-fields are necessary for each mask set-up.

Flat-fielding aims at correcting the small-scale sensitivity variations only. Hence, the flat-fields were smoothed to obtain the low-frequency fluctuations. In case of the present data a 50 pixel median filter was selected. Then, the large-scale fluctuations were removed dividing the original by the median filtered image. This resulted in an normalised flat-field which could be used to remove the small-scale variations in the raw spectrum by division.

There is a general problem concerning the MOS flat-fields at the edges of the slitlets (see Fig. 4.1). This is caused by contaminating light coming through gaps between the blade carriers. As this light is not dispersed the pixels involved can be saturated. In such cases the flat-field correction fails. This problem affected particularly the flat-fields obtained during the commissioning runs of FORS 1 since the production of flat-fields was not yet optimised. Hence the reduction

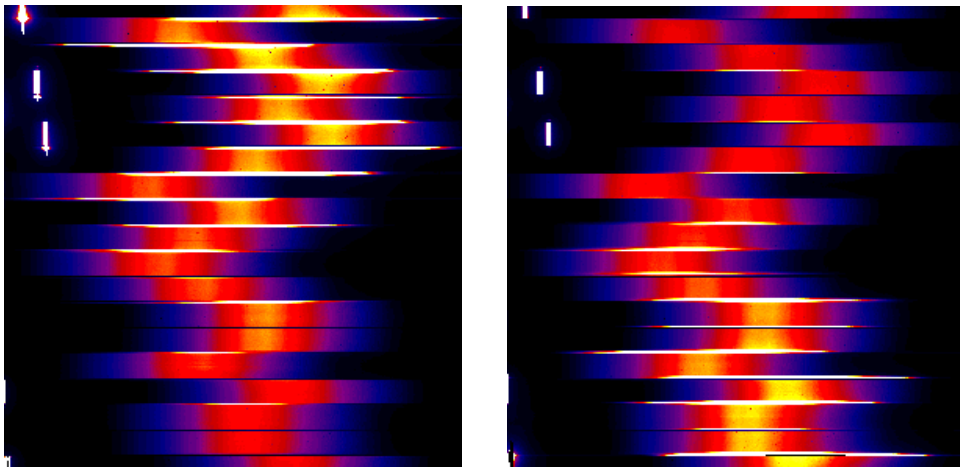

(a) Upper lamps on. **(b)** Lower lamps on.

Figure 4.1: The two kinds of flat-fields provided for MOS exposures (19 slitlets). The frames differ in lamp positions an therewith in their field illumination. The production of two types of flat-fields is necessary, because contaminating undispersed light (white horizontal stripes) coming through gaps between the blade carriers causes over-exposures. Thus, the masks have to be illuminated indirectly which can be realized by two complementary lamp configurations. The over-exposed bars in the left part of the frames constitute 0th order spectra (scarcely dispersed images of the slitlets).

of a couple of spectra positioned at the margin of slitlets was very difficult. Consequently the process was modified in producing two complementary kinds of flat-fields, each optimised for another part of the frame (see Fig. 4.1). The usage of two distinct calibration frames avoids subsequent reduction problems to a great extent.

In case of the MXU spectra contaminating light does not play a role (Fig. 4.2). However, the flat-fields provided are not satisfactory for other reasons. The accuracy of the slitlets produced by laser-cutting is significantly lower than in case of the blades of the MOS unit. The MXU slits are characterised by sporadic width contractions concerning one to three pixels in slit direction. The photometric effect is typically of the order of 2 to 3 % but can reach up to 5 %. Variations of the slit width cause striking intensity fluctuations in the scientific as well as in the calibration frames (Fig. 4.2). Thus, the positioning of the masks in the mask exchange unit (MXU) must be very accurate, because calibration frames are taken independent of the object spectra during daytime. In fact, the reduction of the MXU data showed that this requirement is not met in all cases. As illustrated in Fig. 4.3(a) the presented sky-subtracted spectrum still shows bright stripes. This certainly affects the extraction of object spectra. The unsatisfactory result can be explained by a shift of the flat-field by one pixel in slit direction. Reducing the concerned frames using a back-shifted flat-field significantly improved the result (Fig. 4.3(b)). However, a simple shift is not a perfect solution, because, e.g., the correction of CCD defects can decrease.

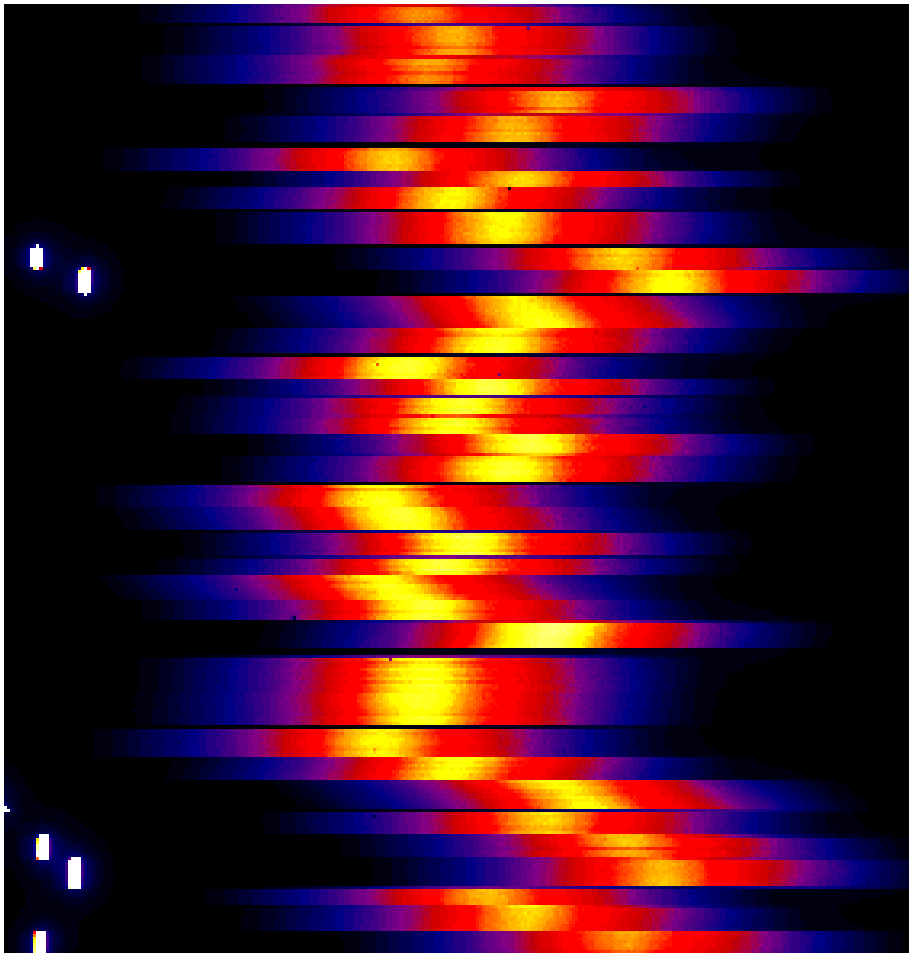

Figure 4.2: Flat-field exposure of a MXU mask with 37 slitlets. The image is not affected by undispersed light as in case of the MOS mode (see Fig. 4.1). On the other hand, the flat-field is interspersed with horizontal stripes (intensity decrease) caused by variations of the slit width.

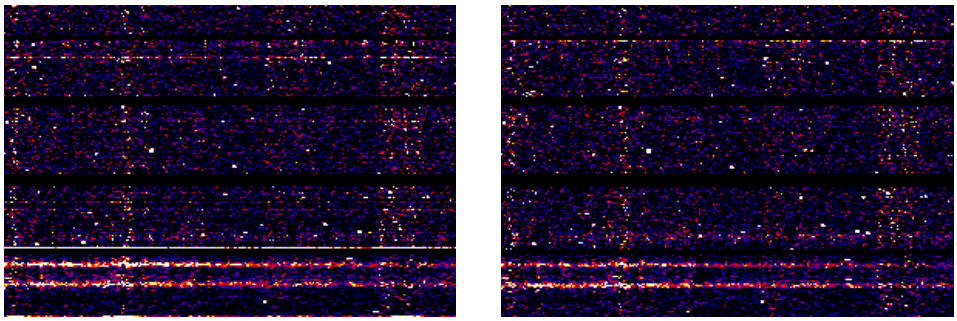

(a) Flat-field shift not compensated.

(b) Flat-field shifted back by one pixel up.

Figure 4.3: The effect of shifted flat-fields on the MXU data reduction. In (a): the imperfect correspondence of the flat-field and the scientific frame leads to stripes in the flat-fielded and the sky-subtracted MXU spectrum 094 (see Appendix A). In (b): the results are improved significantly by shifting the flat-field by one pixel upwards, that is by compensating the initial shift. The two strong traces in the lower part of the images represent real spectra.

Furthermore shifts by fractions of pixels require a rebinning of the data which can smear out cosmics (see Section 4.3) and reduces the S/N. Thus, only full pixel shifts of flat-fields were performed. A shifted flat-field was only used in case of a significant improvement of the resulting spectrum's quality.

4.2 Wavelength calibration

In order to convert pixels into wavelength units, it is necessary to derive a dispersion relation. As described in the last chapter we used the grism 150 I for almost all observations. This low resolution grism provides a wavelength range from the UV (3300 Å) to the near IR (10000 Å). Thus, many reference lines are needed to cover the large wavelength range.

Usually, ESO offers suitable reference spectra, which are obtained during daytime. These spectra are produced by means of gas discharge lamps of the chemical elements He, Ar, Hg/Cd and Ne, respectively (see FORS manual). Using a combination of at least the first three lamps, a good coverage of the available wavelength range is guaranteed by dozens of strong emission lines (see Fig. 4.4).

Only in the UV part of the reference spectrum conspicuous emission lines are missing. This may affect the accuracy of the wavelength calibration, since it was necessary to extrapolate the dispersion relation towards the UV. Nevertheless, as the relation is almost linear and the wavelength region concerned is small ($\lambda < 4000$ Å), possible deviations should be well below the size of a spectral resolution element ($\lesssim 23$ Å).

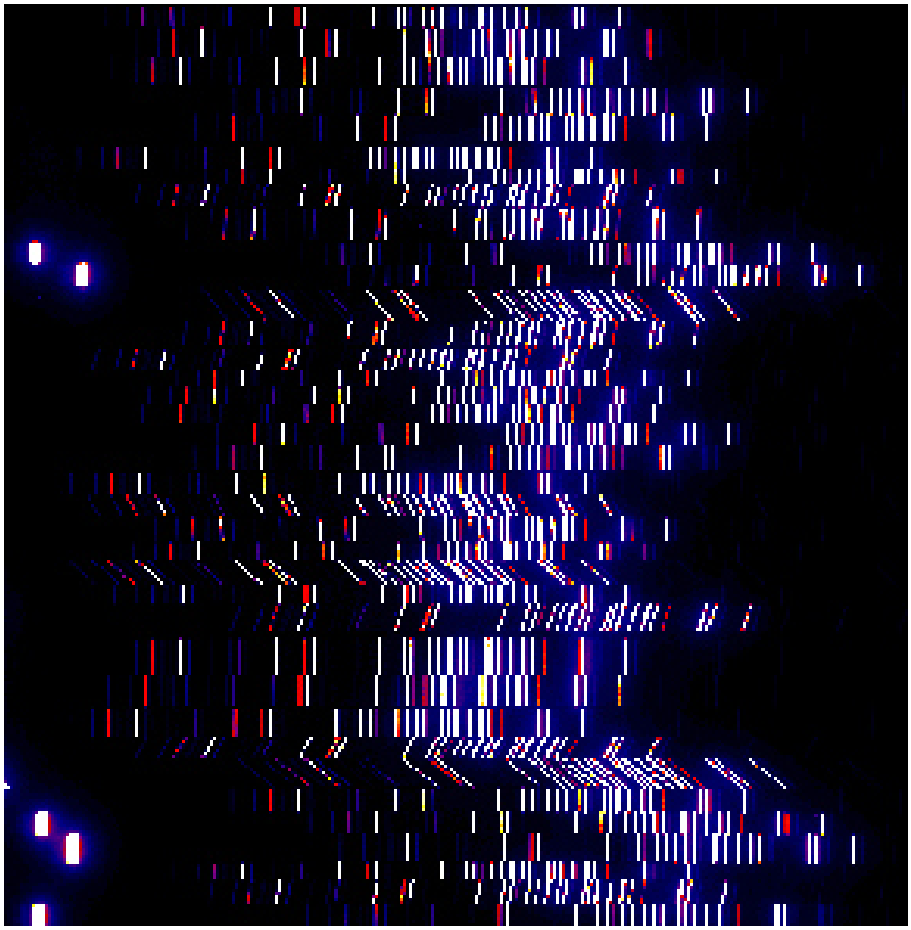

Figure 4.4: Wavelength calibration frame of a MXU mask with 37 slitlets. The whole wavelength range with exception of the UV is covered by numerous emission lines of He, Hg, Cd and Ar generated by gas discharge lamps.

The dispersion relation

The wavelength calibration procedure was carried out in the following way:

(1) Searching for emission lines in the calibration spectrum.

(2) Derivation of accurate positions by fitting Gaussians to the line profile.

(3) Calculation of a rough dispersion relation using the grism parameters.

(4) Identification of the lines using a reference wavelength table.

(5) Computation of the final dispersion relation by fitting a polynomial of fourth order in λ direction and of second order in y direction to the positions of the identified lines.

(6) Rebinning of the spectra according to the derived relation.

Originally the pixel scale in case of grism 150 I is about 5.5 Å/pixel. By the rebinning this was slightly modified to 5 Å/pixel, because even binning makes

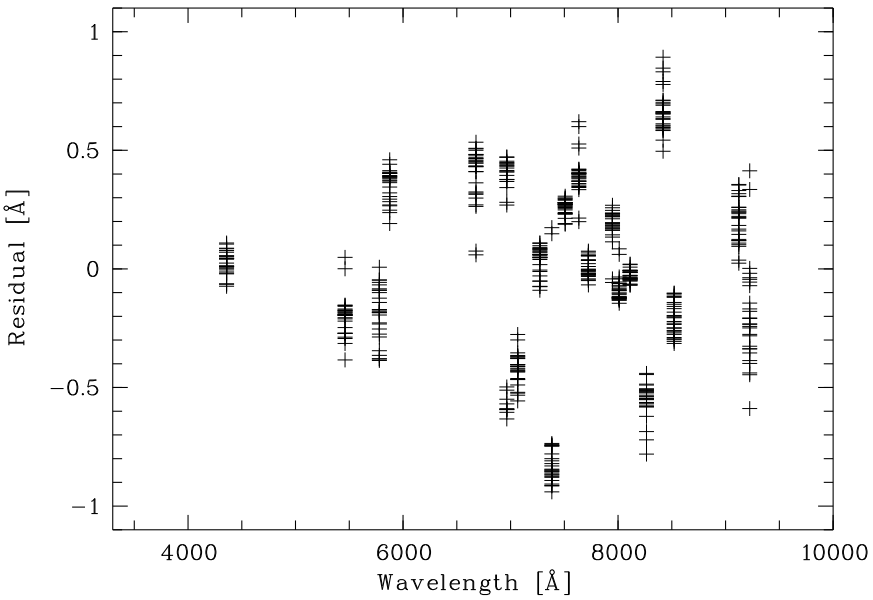

Figure 4.5: Residuals of the wavelength calibration of a typical MOS slitlet depending on the rest wavelength of the calibration lines. The results of several rows of the slitlet spectrum are indicated. The residuals were computed from the differences between the dispersion relation (a fourth order polynomial fit) and the measured calibration line positions (derived from the centreing via Gaussians). The mean error amounts to about 0.4 Å. The wavelength calibration is more uncertain in case of wavelengths below 4000 Å, since there are not any useful calibration lines.

data handling easier. The small change hardly alters the kind of sampling, since in both cases the data is clearly oversampled (4 – 5 pixels corresponding to one resolution element).

For strongly inclined MXU slitlets ($> 20° - 30°$) the two-dimensional fit of the dispersion may fail. Thus, prior to the wavelength calibration critical slitlets were 'straightened'. That is, the concerned frame rows are shifted and rebinned, so that the row spectra are aligned perpendicular to the dispersion direction. The necessary information about the slit position and the rotation angle can be taken from the frame descriptors. In order to avoid the additional rebinning and likely new uncertainties caused by the aligning method (see below) the procedure was applied to really critical slitlets only. Using the corrected spectra the wavelength calibration routine worked well in all cases.

Relative accuracy of the wavelength calibration

As one can see in Fig. 4.5 typical errors of the relative wavelength calibration are around 0.5 Å ($\sim 1/10$ pixel). This is the best accuracy one can attain by line centreing via Gaussians and dispersion relation fitting using low order polynomials. As stated above this value may be exceeded in the UV part of the spectrum, because there suitable reference lines are rare. In case of the slitlet shown in Fig. 4.5, the dispersion relation below 5000 Å depends on only one cal-

ibration line. This indicates a gradually decrease of accuracy of the wavelength calibration towards the UV.

Absolute accuracy of the wavelength calibration

The accuracy given above is only valid regarding the relative errors, that is the deviations of the line-to-line distances from the theoretical values. In contrast, the exclusive use of wavelength calibration frame limits the accuracy of the absolute wavelength values to the order of magnitude of a few pixels. These relatively large errors are caused by the fact that the wavelength calibration frames are obtained during the day at a telescope position different from that of the object spectra. The issue is similar to that described in Section 4.1 concerning the shifting of the MXU flat-fields. A shift in dispersion direction of the calibration frame in reference to the scientific frame causes a wavelength independent shift of the calibration. In case of tilted slitlets deviations perpendicular to the dispersion direction are responsible for an additional error in the wavelength determination by projection. Since this effect depends on the tangent of the slitlet slope, higher inclination angles cause larger errors in the wavelength calibration. Moreover, spectra of straightened slitlets may be affected in a different manner: The real reference point for the 'rotation' of the slitlet will deviate from the theoretical one, if a frame is shifted. This also causes an absolute error in the wavelength calibration.

The calculation of the deviations and finally the correction of wavelength errors are in principle possible using night sky lines in the object spectra.

Regarding the spectra obtained by FORS (see Fig. 3.3) the impact of night sky lines is remarkable (Fig. 4.6). These lines are mainly produced by the absorption of solar UV radiation by air molecules in the upper atmosphere (altitudes of about 100 km and more, see Ghosh 2002 and references therein). Strength and shape of such lines are highly variable with time. The characteristics of the variations can be very complex. The intensity depends on daytime, season, geographic latitude, solar activity and further causes. In the red and infrared part the sky spectra are dominated by OH lines. These spectral lines are generated by vibration and rotation transitions of the ground state in OH radicals. At the low resolution of grism 150 I these lines generally merge to form bands. The resulting blends are only interrupted by small windows. These almost line free windows are very important for the investigation of spectra of faint objects in the near infrared.

The variability of line shapes and the frequent occurrence of sky lines in blends limit the use of such lines for wavelength calibration. Therefore, the gas lamp spectra are important, at least, for the relative wavelength calibration. However, as the sky lines are obtained at the same time as the object spectra, the frame shift problem is not present for these lines. In principle, this allows a very accurate determination of wavelengths. Nevertheless, only one sky line meets the requirements of a strong, isolated line. In fact, this is [O I]λ 5577 normally the most powerful line in the sky spectrum. Deriving the location of the line centre by fitting Gaussians is very useful to link the calibration spectra to the object spectra. In this way one can reduce wavelength calibration errors

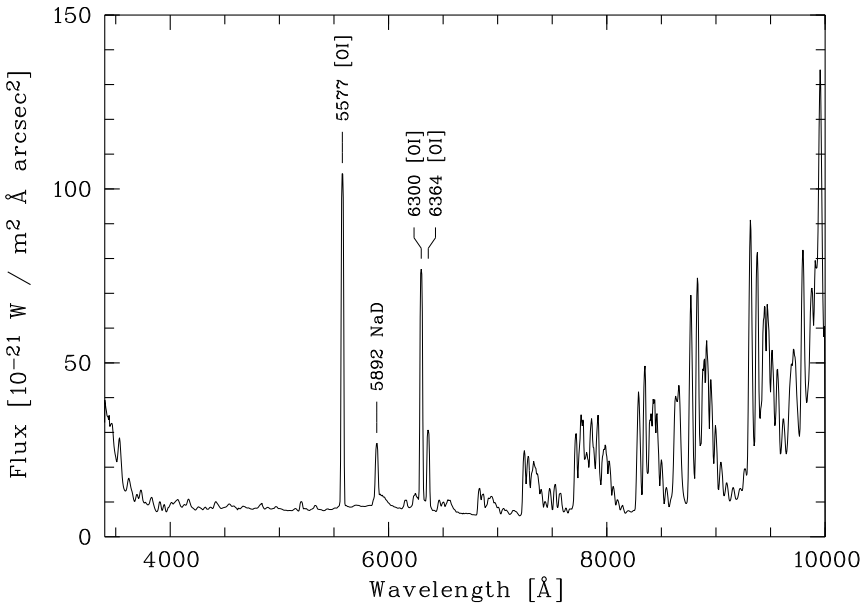

Figure 4.6: Mean night sky spectrum composed of the exposures of the spectroscopic main programme (frames 029 – 102, see Appendix A). The spectrum is flux calibrated and shows the sky brightness per Å and arcsec^2. The most prominent lines in the optical are marked. The red and infrared part of the spectrum is dominated by bands of OH lines. The sky spectrum is highly variable. Especially the [O I]$\lambda\lambda$ 6300, 6364 show strong variations with equivalent widths ranging from 10 Å to 700 Å in case of [O I]λ 6300.

to less than 1 Å.

In Fig. 4.7 one can see for MXU frame 092 the deviations of the [O I]λ 5577 positions from the positions expected by the wavelength calibration as a function of the tangent of the slitlet inclination angle. The non-inclined slitlets show a remarkable shift of about 4 Å. Furthermore, the inclined slitlets indicate the expected more complex behaviour. For strongly tilted, 'back-rotated' slitlets one gets an almost linear dependency. Another kind of deviation is presented in Fig. 4.8: For MXU frame 098 one finds a connection between the wavelength shift and the y position of the slitlets. This pattern can be explained by a rotation of the mask. For a central rotation point the shifts convert into a rotation angle of about 2′. In general, successively obtained frames obtained show similar effects, whereas frames for which the MXU masks were independently mounted the shift patterns can differ considerably. This indicates that the installation of MXU masks is critical. One dust grain may already cause conspicuous deviations.

Fig. 4.9 shows the distribution of the average shifts for all masks. It is conspicuous that MOS frames have got deviations of up to several Å as well. This effect needs another explanation. Fig. 4.10 presents the wavelength shifts measured by [O I]λ 5577 as a function of the sky positions where the telescope is pointing to for MOS observations. The figure shows that the telescope positioning has an influence on the wavelength calibration. Obviously the deviations are larger at high zenith distance. Furthermore, the sign of the shifts seems to depend on

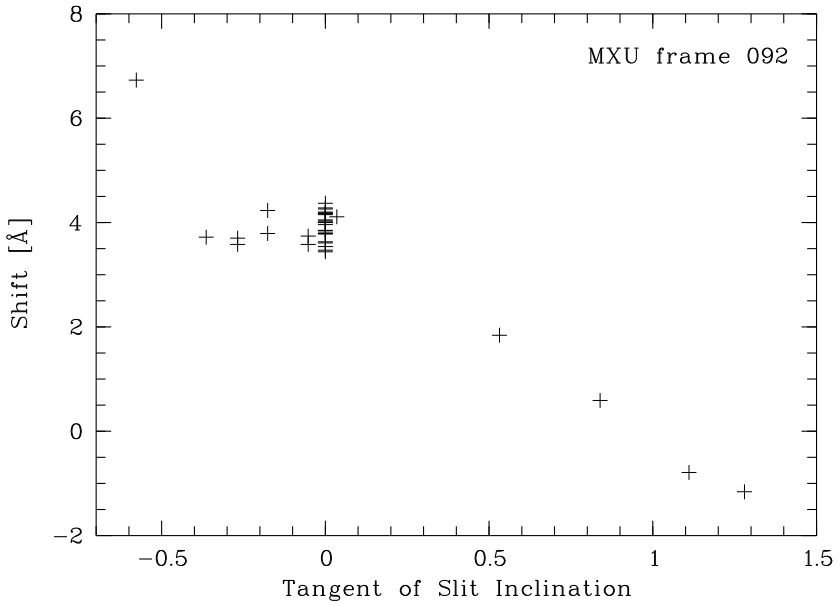

Figure 4.7: Shift of [O I]λ 5577 as a function of the tangent of the slit inclination angle for the slitlets of MXU frame 092.

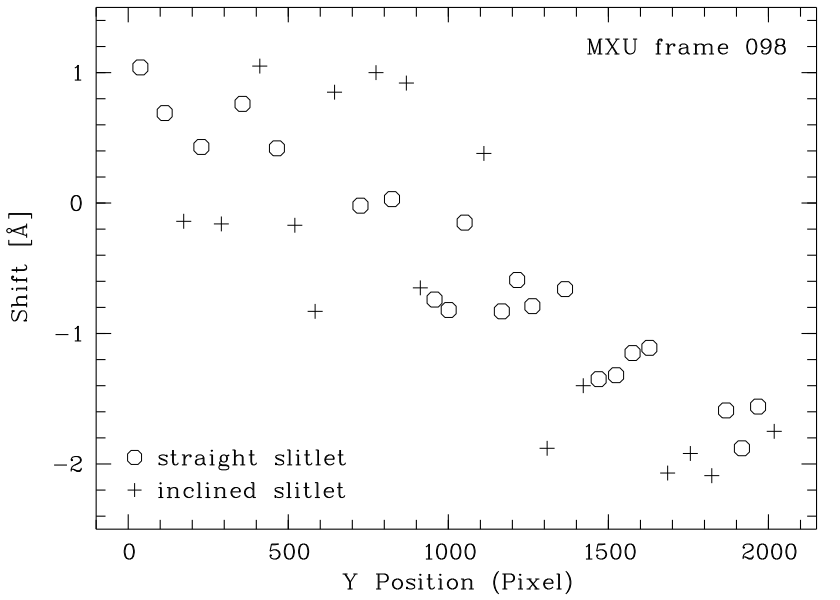

Figure 4.8: Shift of [O I]λ 5577 as a function of the y position of the slitlet for MXU frame 098. Straight slitlets are denoted by circles and inclined slitlets are marked by crosses.

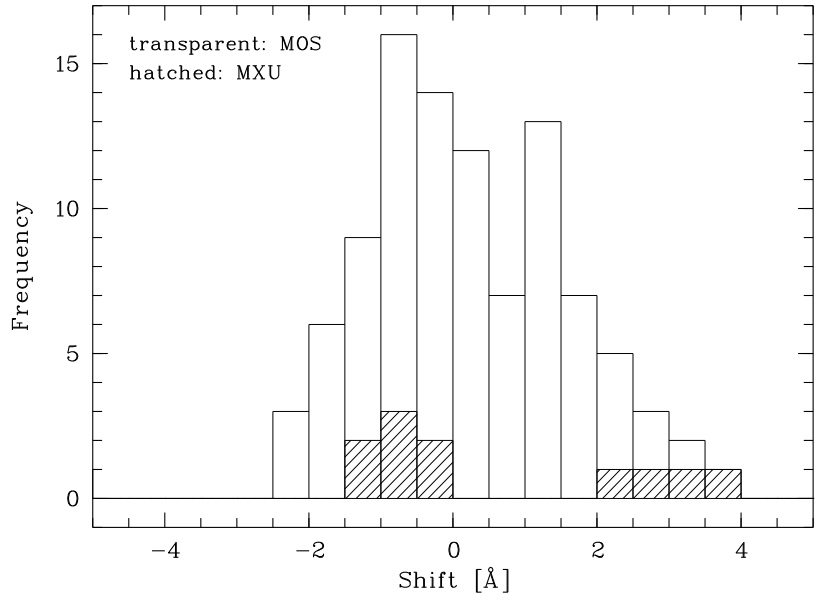

Figure 4.9: Distribution of the average shifts of [O I]λ 5577 for all exposures (MOS and MXU). The MXU spectra are marked by hatched bars.

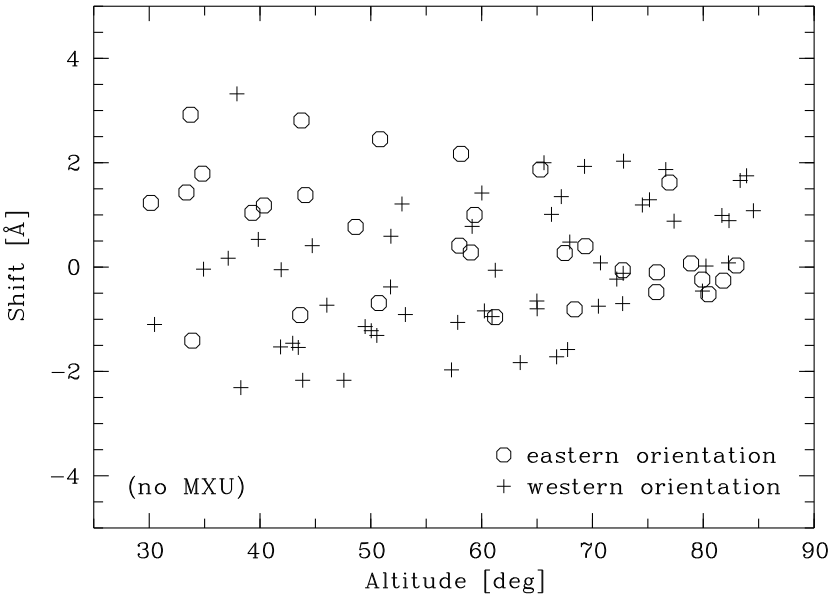

Figure 4.10: Average shift of [O I]λ 5577 dependent on the altitude of the telescope for all MOS frames. Furthermore the azimuthal orientation of the telescope is indicated either by circles (east, field ascending) or crosses (west, field descending).

the azimuth of the observed field. Taking into account that the calibration spectra are made in zenith position, this leads to the conclusion that gravitational bending effects shifting the mask relative to the detector are mainly responsible for the described features. Regarding the remaining scatter of the shifts further influences like thermal effects are imaginable.

The correction of the wavelength shifts was carried out using the values derived from the [O I]λ 5577 measurements. For MOS, global values for the whole mask were used. In case of MXU, the individual values of the slitlets were used because of the slitlet inclination effects. The error of the corrected wavelength calibration is about 0.5 to 1 Å. This is higher than the relative error (Fig. 4.5) because of the added error of the [O I]λ 5577 measurements.

The realization of the absolute wavelength calibration requires a shifting and therefore further rebinning of the spectra. This causes a smoothing of the spectra. Especially in case of pixels in the vicinity of strong defects like cosmics (see Section 4.3) this can lead to a contamination of principally well-behaved data points. In order to avoid this, the rebinning procedure was carried out after the extraction of the one-dimensional spectra. Therefore, all aspects concerning the rebinning are discussed in the end of Section 4.3.

Summarising, daytime calibrations clearly cause problems with regard to the absolute wavelength calibration. However, the problem is solvable using the [O I]λ 5577 night sky line for correction. Moreover, very importantly, daytime calibrations do not consume valuable observing time. Thus, using daytime calibrations is certainly preferable despite of the higher reduction efforts.

4.3 Sky subtraction and extraction of the one-dimensional spectra

In this section the aspects of the data reduction are discussed which concern:

- **The sky subtraction:**
  This is the most critical part of the reduction procedure for weak object spectra. It contains the definition of object and sky positions and the sky fit itself.

- **The extraction of the one-dimensional spectra:**
  This procedure was carried out applying the S/N optimised algorithm of Horne (1986). The approach also includes an elimination of cosmic ray hits.

- **The noise level of the spectra:**
  The Horne algorithm provides an error function indicating the statistical noise level. The discussion comprises a description of the basic properties, the dependence of the noise level on systematic errors and the modification of the errors by rebinning of spectra (as is necessary in the case of the absolute wavelength calibration, see Section 4.2).

In the following, the individual reduction steps are described in detail.

Object and sky definition

Before subtracting the sky it is necessary to define on the two-dimensional frames which CCD rows are supposed to include object spectra. This information can be derived from a combination of the FIMS mask file (see Section 2.3) and a deep image of the field. For very faint objects, hardly discernible in the sky dominated spectra, it is the best and sometimes only way to estimate the location of objects in the slitlets. In practice, a deep combined R + I image of the FDF was used allowing the detection of almost all objects accessible to spectroscopy. Red filter images are advantageous in order to get very red high-redshift galaxies.

However, there are uncertainties caused by telescope positioning errors, the seeing, light losses at the slitlet and wavelength dependent sizes of the objects. Thus, an accurate definition of the object limits requires the determination of the object light distributions along the slitlets in the spectra. For this purpose, the spectra were added up along the dispersion direction. This improves the signal-to-noise ratio and averages wavelength dependent size variations. Thereafter, the object limits were derived in an interactive graphical way taking into account the object positions estimated above. The procedure also defines the limits of the pure sky. In most cases object and sky domains were separated by three pixels. On the edges of the slitlets one has to be especially careful in setting object and sky boundaries, because these regions are subject to systematic flat-field errors (see Section 4.1).

Sky subtraction

Once the boundaries have been defined, the sky intensity along the slitlets in the object domains can be approximated by interpolating (respectively extrapolating) the intensity in the sky domains. Therefore, polynomial fits of second or third order as well as median fits using 7 to 15 pixels and a linear interpolation in the object domains were applied. In order to obtain the optimum fit, in each case the sky subtraction results (see Fig. 4.11) of both methods were analysed with regard to the strength of residuals of prominent sky lines and the quality of the continuum definition which is determined, e.g., by the absence of negative mean intensities. Residua of the sky subtraction are unavoidable and a consequence of small shape variations of the steep flanks of strong sky lines (see Fig. 4.6). Thus, the strongest deviations occur in the wings of lines (compare Fig. 4.13). Reducing these residuals is one of the major challenges of the sky subtraction, and hence a great deal of the time spent on data reduction was used to a careful adjustment of the parameters concerning the object and sky definition and the sky fit.

Extraction of the one-dimensional spectra

The next step of the data reduction is the extraction of one-dimensional object spectra from two-dimensional MOS spectra. In order to maximise the signal-to-noise ratio for the resulting spectra the optimal extraction algorithm of Horne (1986) was applied.

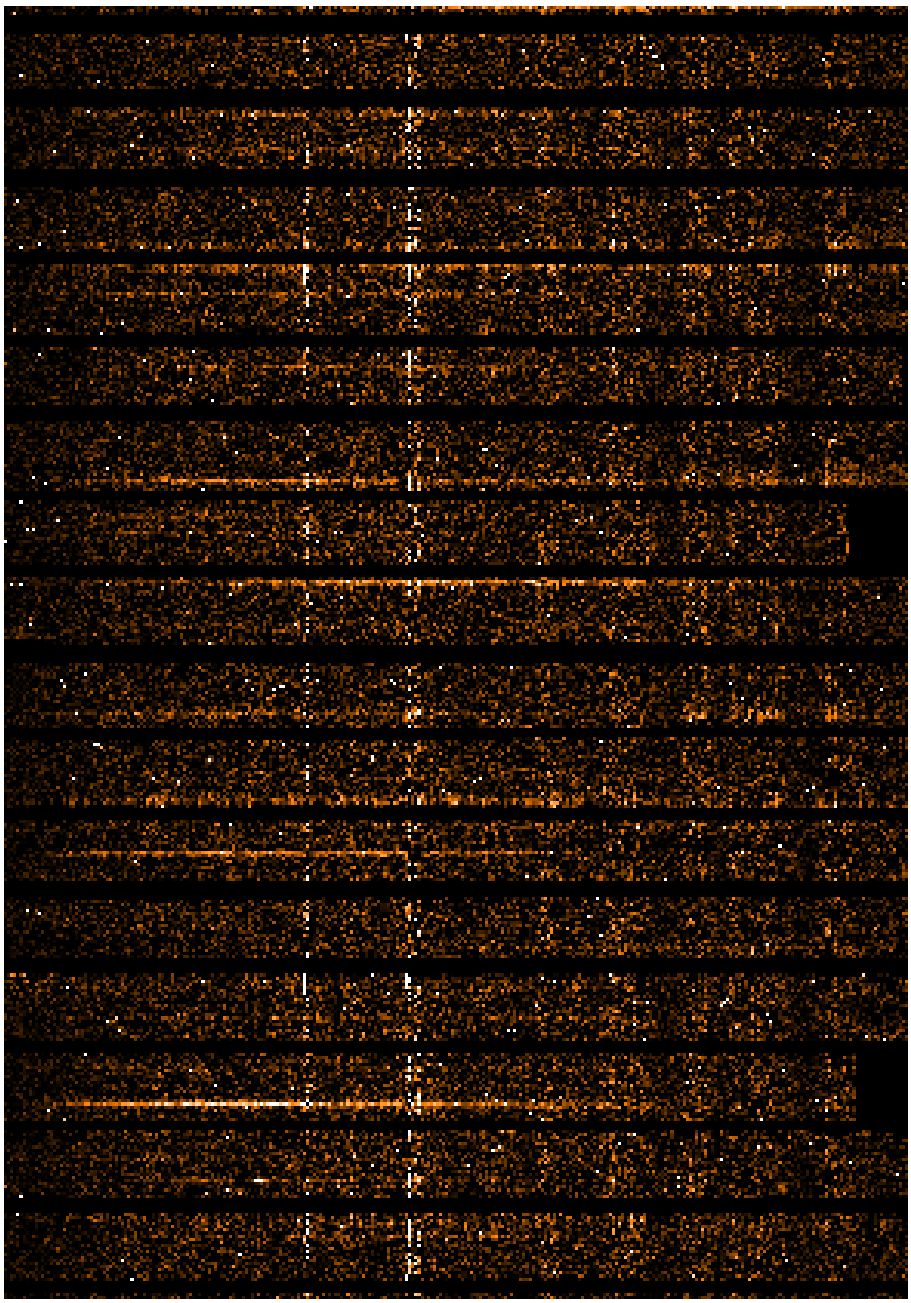

Figure 4.11: Wavelength calibrated and sky-subtracted MOS spectrum (frame 085). The presented wavelength region ranges from 3400 Å (left margin) to 10000 Å (right margin). The horizontal stripes represent residuals of strong night sky lines. The frame still includes cosmics (white dots).

The efficiency of this algorithm is based on a summation over the variance-weighted pixels while preserving the photometric accuracy. This increases the contribution of pixels containing a high fraction of the object emission while pixels which mainly contain noise contribute only little to the final spectrum. This leads to a maximum of the S/N in the resulting spectrum. To estimate the weights of the individual pixels it is necessary to determine a rough intensity profile of the corresponding object in slit direction as a function of wavelength. Therefore, in order to allow a clear separation of statistical fluctuations and profile variations, the estimate of a reliable intensity profile requires that the profile shape varies as a smooth function of wavelength (given by a high order polynomial). This condition limits the efficiency of this approach to the investigation of spatially resolved objects showing a significant wavelength dependent variation of their appearance. Consequently, the Horne algorithm provides optimum results in the case of faint, marginally resolved objects like high-redshift galaxies. This approach is, therefore, well suited to the application to the spectroscopic sample of the FDF.

Elimination of cosmics

The Horne algorithm also offers the possibility to eliminate pixels which are affected by so called cosmics produced by cosmic ray particles and natural radioactivity. This is achieved by a σ-clipping procedure which rejects pixels exceeding a maximum admitted deviation from the expected intensity distribution. Despite of cosmic ray hits, negative artifacts like CCD defects can also be rejected by this routine. It turned out that in most cases a $5\,\sigma$ threshold provides satisfying results. Only in a few cases defects were so extended that the programme failed to reject them. In these cases the elimination could be achieved either by the application of a median filter (see Section 4.4) or during the calculation of the co-added spectra (see Section 4.5).

The error function

The Horne algorithm estimates the statistical variance of the data values which is used to derive the weight for the individual pixels applied during the optimal extraction of the one-dimensional spectra. Thus, as a by-product of the extraction procedure, the algorithm provides for each final spectrum $f(\lambda)$ an error function $\Delta f(\lambda)$ indicating the photon noise level.

In case of faint objects, the appearance of the error function is mainly given by the shape of the sky spectrum (Fig. 4.12). Especially in the red part of the function, the amount of noise strongly depends on the presence and strength of night sky lines. This behaviour is caused by the proportionality of the noise to the square root of the spectral intensity ($\rightarrow$ Poisson error) which is dominated by the sky. Furthermore, the wavelength dependent efficiency of the instrumental configuration essentially given by the efficiency of the CCD (Fig. 3.4) and the grism (Fig. 3.5) has also a great impact on the shape of the error function.

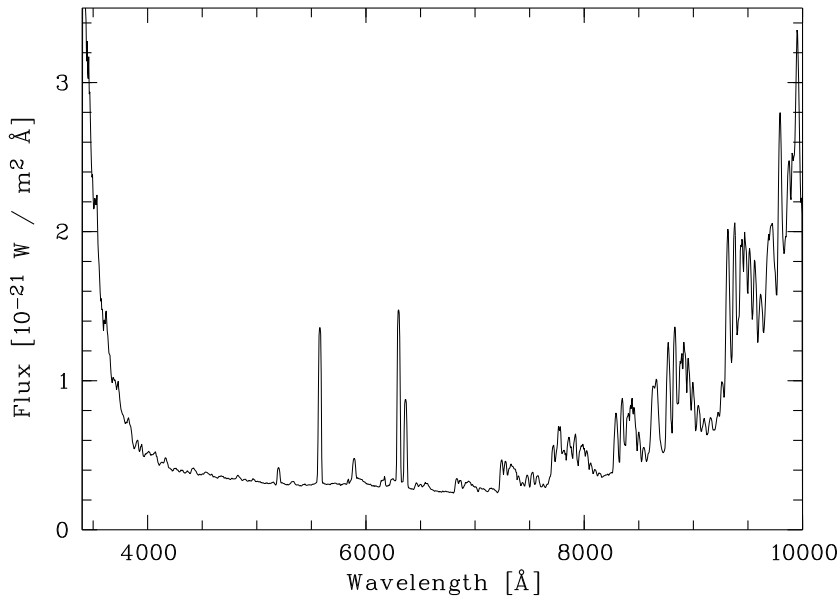

Figure 4.12: Example of a flux calibrated error function indicating the statistical noise level. It can be calculated by the Horne algorithm. In case of faint objects the fine structure of the error function is essentially given by the night sky spectrum. In contrast, the large scale shape is mainly determined by the response curve and the atmospheric extinction.

Estimate of the real noise level

The error function $\Delta f(\lambda)$ only provides lower limits for the real noise level, since, e.g., the intense residuals produced by an insufficient sky subtraction may increase the error significantly. The strength of this effect can be estimated by calculating the wavelength dependent standard deviation $\sigma(\lambda)$ of the fluctuations $f_{\sigma,i}(\lambda)$ in a series of n spectra i. $f_{\sigma,i}(\lambda) = f_i(\lambda) - f_{\mathrm{r},i}(\lambda)$, that is $f_{\sigma,i}(\lambda)$ represents the difference between the observed and the original noise-free spectrum. In principle, $\sigma(\lambda)$ provides the full information on the amount of the involved statistical errors. In practice, it is very difficult to estimate this quantity, since the entire separation between fluctuations $f_{\sigma,i}(\lambda)$ and object information $f_{\mathrm{r},i}(\lambda)$ in a single spectrum is hardly possible. Thus, it is necessary to calculate $\sigma(\lambda)$ for a high number of spectra n in order to minimise the uncertainties produced by residual contributions of the object spectra. In the present case $n > 1000$ spectra were used. $f_{\sigma,i}(\lambda)$ was approximated by the subtraction of the continuum (calculated by the application of a 100 pixels median filter) and the masking of strong spectral lines. In this way a reliable $\sigma(\lambda)$ representing the average fluctuations in the applied spectra could be calculated.

In Fig. 4.13 it is shown the resulting ratio of $\sigma(\lambda)$ and the error function $\Delta f(\lambda)$. As expected, the additional fluctuations caused by the residua of strong sky lines like [O I]λ 5577 and [O I]λ 6300 are the most conspicuous. The shape of the features resembles double peak profiles, since the residuals are strongest at the positions of the flanks of the sky lines. The shown strength of the residuals

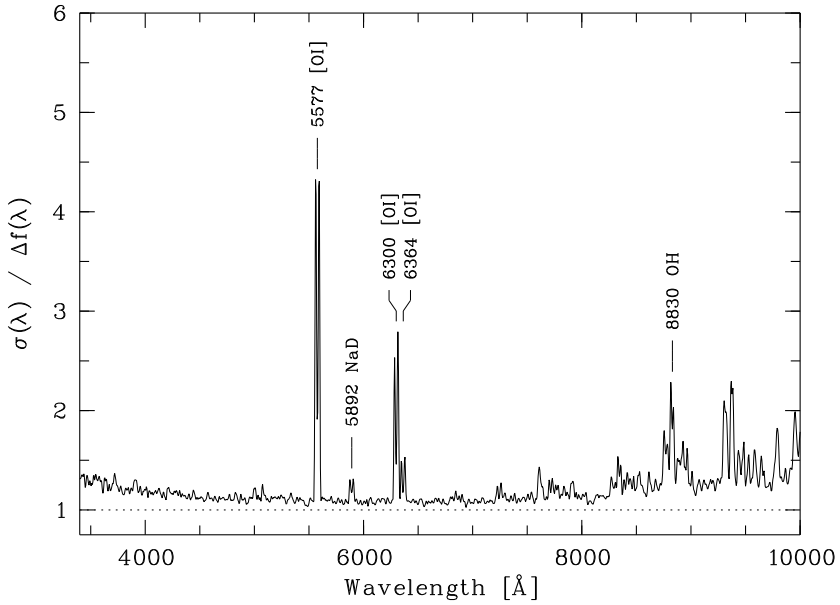

Figure 4.13: Ratio of the spectrum-to-spectrum variations (measured by the standard deviation $\sigma(\lambda)$) and the statistical noise level (error function $\Delta f(\lambda)$) for the spectra with $0.2 \times 10^{-21}\,\mathrm{W/m^2\AA} \leq f(\lambda) < 2.0 \times 10^{-21}\,\mathrm{W/m^2\AA}$. In order to avoid significant contributions of object features and spectral defects to σ, the continuum of the spectra was subtracted, strong spectral lines were masked and strong cosmics and CCD defects were removed using a median filter. However, a low underground caused by such features could not be avoided ($\sigma(\lambda)/\Delta f(\lambda) > 1$). Nevertheless, the curve is dominated by double-peak residua of strong night sky lines, like [O I]$\lambda\,5577$ or [O I]$\lambda\,6300$. The most prominent lines are labelled.

relative to the noise level is not the same for all objects, but it tends to be stronger for brighter ones. This means that even in case of low noise levels residuals of strong sky lines may cause considerable errors.

A further source of errors is caused by the uncertainties of the zero-flux line. This will be discussed in Section 4.4.

Effects of rebinning on noise level

As already discussed in Section 4.2 the absolute wavelength calibration exploiting [O I]$\lambda\,5577$ requires a following rebinning of the shifted spectra. Since the spectra usually have to be shifted by fractions of full pixels, a recalculation of the pixel intensities by interpolation is necessary. This causes a slight smoothing of the data which affects the error function as well as the signal-to-noise ratio per pixel. One can avoid the pixel interpolation by rebinning the spectra using a sufficiently smaller wavelength step size, but this causes a large increase of data. This is not desirable in view of the inconveniences connected with increased computing times. Furthermore, the original data is already oversampled (resolution element $\approx 4-5$ pixels). Thus, modest smoothing will hardly deteriorate the resolution. For that reason, the bin size was not changed. Nevertheless,

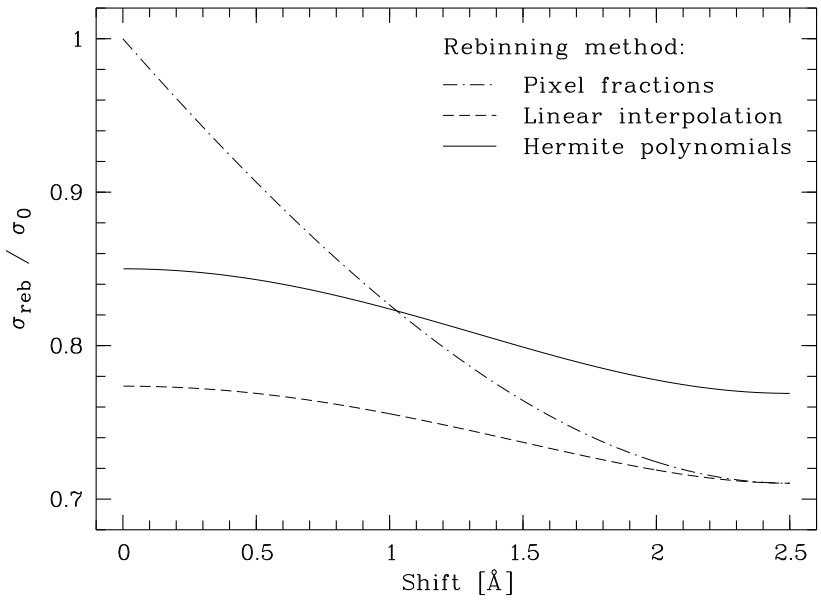

Figure 4.14: Decrease of standard deviation σ of a pure noise spectrum due to shifting and rebinning. $\sigma_{\rm reb}/\sigma_0$ is plotted as a function of the shift in Å (1 pixel = 5 Å) for three distinct rebinning algorithms. The pixel re-calculations were made by (1) use of pixel fractions (dash-dotted curve), (2) linear interpolation and consequent addition of polygons (dotted curve) and (3) interpolation with Hermite polynomials and integration with Gaussian formula (solid curve).

the rebinning varies the error function computed by the Horne algorithm. In order to optimise the result of the rebinning and to minimise effects on the error function, the pixels were interpolated using Hermite polynomials. Moreover, the Gaussian formula was applied to calculate the new pixel fluxes by integration. Compared to other approaches like linear interpolation or simply taking pixel fractions the described method provides the best conversation of the spectral information. This can be demonstrated by rebinning pure noise spectra and calculating the standard deviation of the resulting spectra as a function of the pixel shift (see Fig. 4.14). The diagram indicates that contrary to the pixel fraction approach the accuracy is only slightly dependent on the amount of the wavelength shift. Furthermore, the spectra will be smoothed distinctly less than in case of the linear interpolation method. Thus, the approach applied (based on the interpolation with Hermite polynomials) reproduces the shape of spectral features most successfully.

The rebinning affects the error function $\Delta f(\lambda)$ in a complicated way, since the fluxes of adjacent pixels are not independent from each other. Preceding reduction steps as the relative wavelength calibration and the 'straightening' of tilted slitlets (see Section 4.2) have already caused a linking of neighboured pixels by rebinning. Hence, the change of the error function from $\Delta f_0(\lambda)$ to $\Delta f_{\rm r}(\lambda)$ by the rebinning procedure can only be derived by means of the computation of the spectral variance. This raises the already mentioned difficulties to separate fluctuations caused by noise $f_\sigma(\lambda)$ from variations of the undisturbed

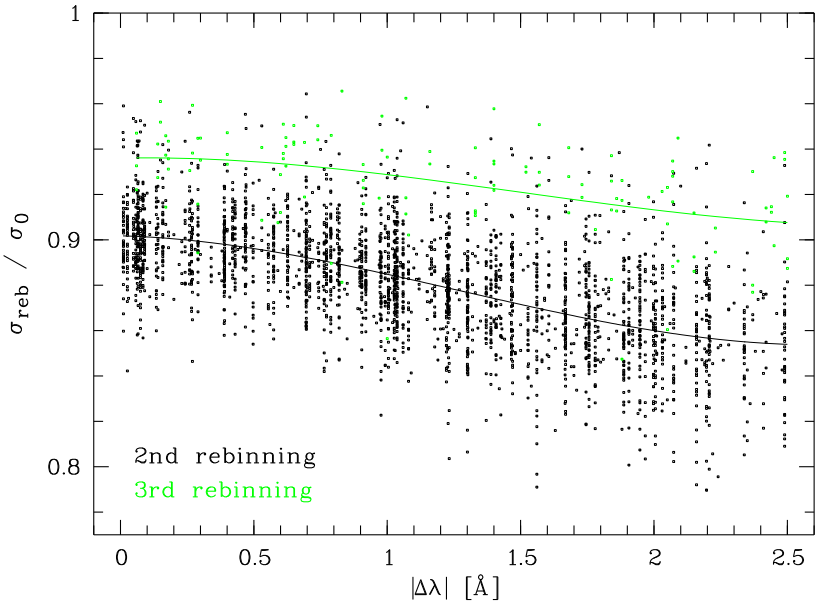

Figure 4.15: Decrease of standard deviation σ of the spectral data due to shifting and rebinning. $\sigma_{\mathrm{reb}}/\sigma_0$ is plotted as a function of the absolute value of the shift in Å (1 pixel = 5 Å). The green dots mark data values of spectra which were extracted from 'straightened' slitlets (see Section 4.2). For that reason, these spectra were rebinned once more than the large majority of the other spectra which were previously rebinned only in case of the basic wavelength calibration. The additional rebinning causes a smaller decrease of σ, since the spectra were already smoothed stronger. Probably the scattering of the values is mainly caused by uncertainties concerning the derivation of σ. Thus, the decrease of noise (depending on the wavelength) was derived by fitting a third order polynomial to the $\sigma_{\mathrm{reb}}/\sigma_0$ belonging to the two times (black) and the three times rebinned spectra (green), respectively. The resulting factors can be used to correct the error function.

spectral energy distribution $f_{\mathrm{r}}(\lambda)$. On the assumption that the difference of the error fluxes of adjacent pixels is small compared to the absolute error values the rebinned original error function $\Delta f_{0,\mathrm{reb}}(\lambda)$ roughly reproduces the wavelength dependency of $\Delta f_{\mathrm{r}}(\lambda)$. Consequently, it is possible to limit the calculation of the spectral fluctuations on the derivation of global values of the standard deviation before and after the rebinning σ_0 and σ_{reb} in a fixed wavelength range. Therefore $\Delta f_{\mathrm{reb}}(\lambda)$ can be approximated by

$$\Delta f_{\mathrm{reb}}(\lambda) \approx \Delta f_{0,\mathrm{reb}}(\lambda)\,\frac{\sigma_{\mathrm{reb}}}{\sigma_0}\,. \tag{4.1}$$

The calculation of reasonable σ values requires the subtraction of the object continua from the spectra. Thus, in each case the continuum was fitted using a rough median filter. As a further approximation the reliability of σ can be increased by a statistically instead of a individual treatment. In this way spectra indicating $\sigma_0 \gg \Delta f_0(\lambda)$ owing to strong spectral features can be ignored. This allows a limitation of the σ derivation to spectra which are dominated by statistical fluctuations. In practice, for such spectra the ratio of the standard

deviation of the spectral fluctuations after and before the rebinning $\sigma_{\rm reb}/\sigma_0$ was plotted over the applied wavelength shift (see Fig. 4.15). Thereafter, a shift depending error correction factor was derived by fitting a third order polynomial to the data. Spectra extracted from 'straightened' slitlets were treated separately, because these spectra were rebinned once more. Fig. 4.15 indicates that the rebinning-caused smoothing results for quarter-pixel shifts in an noise reduction of about 12 % (two times rebinned) and 7 % (three times rebinned), respectively.

The above discussion shows that the error calculation is somewhat tricky, since the fluxes of adjacent pixels are correlated and the absolute errors are not determined by pure photon noise. However, an accurate error treatment is worthwhile, because this allows a reliable calculation of the signal-to-noise ratio which constitutes a valuable input to following data analysis steps.

4.4 Flux calibration

Next, I turn to a detailed discussion of the flux calibration with regard to the correction of atmospheric and instrumental flux losses. In detail, this contains:

- Atmospheric extinction correction
- Correction of the instrumental efficiency (especially of CCD and grism) using spectrophotometric standard stars
- Slit loss correction using photometry
- Summary of the flux calibration errors
- Amount of the deviations of the zero-flux level
- Accuracy of the total flux calibration in relation to the photometry

Furthermore, the calculation of defect-cleaned spectra will be described. These spectra were used for the derivation of reliable mean spectral fluxes needed for the slit loss correction.

Atmospheric extinction correction

In the earth atmosphere a reduction of the flux of astronomical objects is caused by photon scattering at atmospheric molecules (Rayleigh scattering) and at aerosols (Mie scattering). The Rayleigh scattering mainly reduces the flux in the blue ($\propto 1/\lambda^4$). A correction of the atmospheric extinction can be carried out using the standard extinction curve provided by ESO (Tüg 1977, see Fig. 4.16). On the assumption, that the observed intensity I decreases exponentially with regard to the optical thickness of the atmosphere which depends on the zenith distance z, the intensity I_0 outside the atmosphere can be calculated by

$$I_{\lambda,0} = I_\lambda \, e^{\tau_\lambda \sec z} = I_\lambda \, 10^{\,0.4\, A_\lambda \sec z}. \tag{4.2}$$

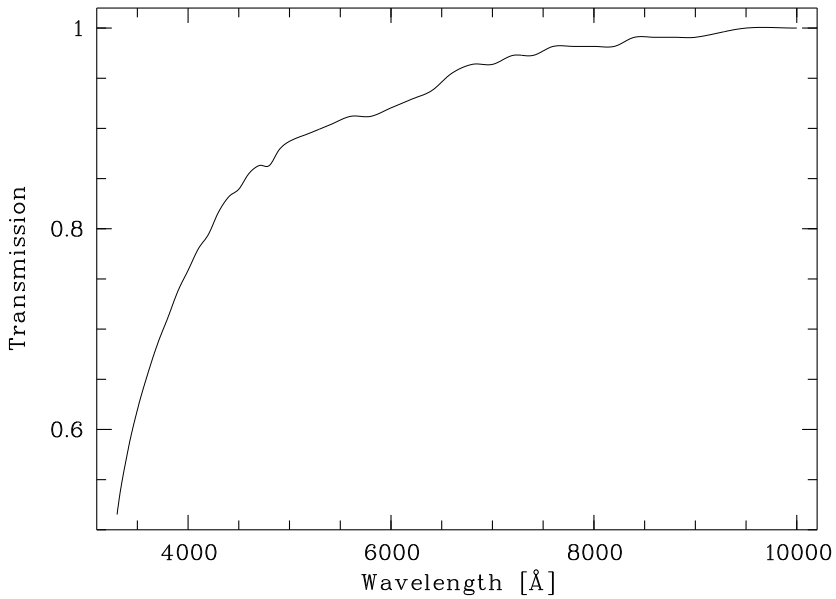

Figure 4.16: Atmospheric extinction law for La Silla (Tüg 1977, related to airmass $AM = 1.0$). The diagram shows the fraction of the transmitted flux as a function of the wavelength.

The index λ indicates the wavelength dependency of the extinction. A_λ (in magnitudes) $\approx 1.08\,\tau_\lambda$ is given by the extinction curve. Finally, $AM = \sec z = 1\,/\cos z$ is the so-called airmass (see Section 3.3). In case of higher zenith distances the airmass varies significantly during the exposure. For instance, in case of the FORS Deep Field the airmass increases from $AM = 1.5$ ($z \approx 48°$) to $AM = 1.75$ ($z \approx 55°$) within a typical exposure time of about 30 min. During this time the standard extinction rises from 34 % to 38 % of the original flux at 4000 Å. Therefore, it is necessary to determine an effective airmass in order to get a realistic flux correction. A suitable approach is given by

$$AM = \frac{1}{6}\big(AM(t_\mathrm{s}) + 4AM(t_\mathrm{m}) + AM(t_\mathrm{e})\big) \tag{4.3}$$

(Stetson 1988) where t_s, t_m and t_e denote the times of the start, the middle and the end of the exposure, respectively.

The extinction correction works well as long as the observing conditions are photometric. This is the case for the vast majority of the obtained spectra. Nevertheless, there exists an uncertainty concerning the commissioning and backup observations, because the weather conditions were partly poor and spectrophotometric standard star observations (see below) were scarcely made. Thus, in cases for which a comparison to spectra of the same object obtained at better conditions was not possible, an incorrect flux calibration in the blue part, where the extinction is stronger, cannot be excluded.

Correction for the instrumental efficiency

In principle, all optical components of the instrumental set-up reflect and/or absorb different amounts of light. However, the most critical optical components are CCD detectors, light dispersion elements (grisms) and photometric filters. The efficiency curves of the FORS CCDs and the grism 150 I were already discussed in Section 3.2. Photometric filters were not applied to the spectroscopic standard set-up. The CCD and grism used reach their highest efficiencies ($\gtrapprox 80\,\%$ each) in the red and green wavelength range, respectively (see Fig. 3.4 and 3.5). The loss of efficiency in the UV and IR is more pronounced for the CCD detector than for the grism.

Although ESO provides curves like those depicted in Fig. 3.5 and 3.4 the combined efficiency of the set-up as a whole cannot be calculated easily, since there are time dependent effects like contamination of the CCD (see FORS manual) or dirty telescope mirrors. In order to estimate the amount of these effects direct measurements of the instrumental efficiency, the so-called 'response curve' are essential. Thus, during the observations of the main programme two spectra of spectrophotometric standard stars (Oke 1990, Hamuy et al. 1992 and 1994) were usually obtained each night. In order to avoid slit flux losses the spectra were obtained using widely opened slits ($5''$). During the commissioning and backup observations such spectra were taken less frequently (one or two exposures per run).

The standard star spectra were reduced in the same manner as described in the previous sections. The flux calculation was carried out taking into account the atmospheric extinction (see above), the mirror area, the exposure time and the factor for the conversion of ADUs[3] into flux units (here: $10^{-21}\,\mathrm{W/m^2\AA}$). Then, the response curve could be derived by the division of the flux-calibrated observed spectrum by the corresponding standard star spectrum from literature. In order to remove residual star specific features finally the resulting response curve was smoothed by spline interpolation.

The results for standard star spectra obtained during the same run are very similar. This means that the time scale of the variability of the instrumental efficiency is clearly longer than a few days. Hence, it was possible to derive an optimal and representative response curve by means of standard stars being observed during the run. This is important for the red part of the curve ($\lambda > 6500\,\mathrm{\AA}$), since for the grism 150 I without order separation filter one has a contribution of the second order spectrum to the total flux. Although the intensity of the superimposed spectrum only amounts to a few percent of the intensity of the first order, it cannot be neglected for a significant fraction of the standard stars like O stars which show very blue spectral energy distributions. For these stars the relative contribution of the second order may reach 20 % or even more. Thus, preferentially redder stars were observed. Nevertheless, blue stars are suitable to estimate the response curve in the UV domain. The final response curve was composed of spectra of different wavelength domains. The resulting accuracy is best in the wavelength range between 4500 and 6500 Å. There the internal errors of the response curve are probably smaller than $\pm 5\,\%$.

[3] **a**nalogue-to-**d**igital **u**nits

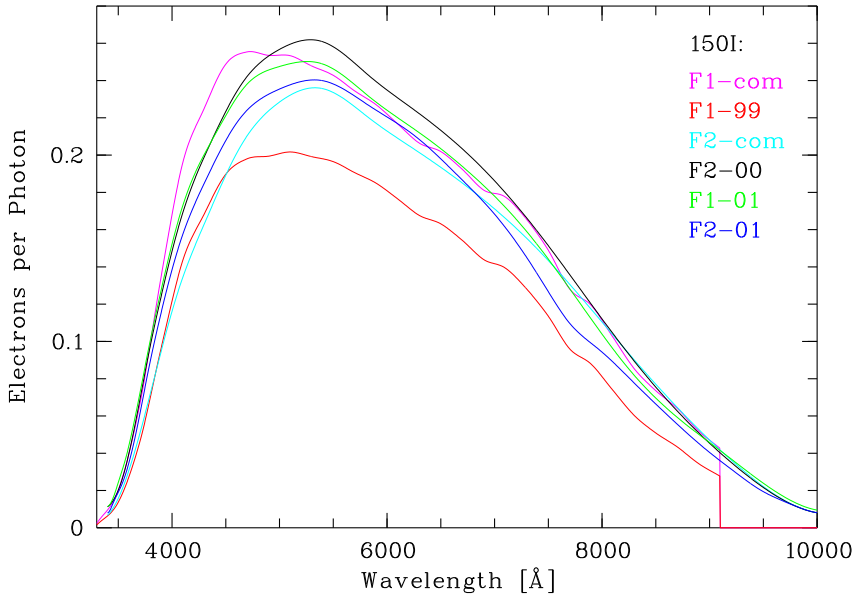

Figure 4.17: Response curves of the different observing runs in CCD electrons per incoming photon for the grism 150 I. A presentation in electrons per energy unit can be calculated using $E_{\mathrm{phot}} = h\,c/\lambda$ where h is Planck's constant, c the velocity of light and λ the wavelength. The labels of the observing runs consist of an abbreviation for the instrument (FORS 1 or FORS 2) and the two last digits of the year or 'com' indicating the commissioning phase. The diagram demonstrates the presence of striking variations of the response curve. Especially during the year 1999 the instrumental efficiency of UT 1/FORS 1 was quite low.

In the second order-contaminated R band the errors can reach up to ±10 %. In the UV and IR, where the efficiency of the set-up is very low, the relative errors can be significantly higher.

Fig. 4.17 shows a compilation of the response curves of the different observing runs. The diagram shows striking differences between the individual curves for FORS 1 as well as FORS 2. The differences reach up to 30 % in the visual part. As already mentioned the main reasons for this are a contamination of the CCD of FORS 1 and variations of the quality of the primary mirror reflectivity.

Defect-cleaned spectra

In preparation for the discussion of the correction of the slit losses in the next subsection, now I treat the calculation of defect-liberated spectra used to derive accurate mean fluxes.

Part of the individual one-dimensional spectra show conspicuous defects. In a few cases these are strong cosmics or CCD defects which were not detected by the Horne algorithm programme because of their extent (see Section 4.3). Furthermore, prominent sky lines can leave striking residuals. Defects of such an order of magnitude are able to change the local spectroscopic mean fluxes significantly. Therefore, these defects were removed from the affected spectra.

This was done in three steps:

(1) **Rejection of strong extended defects:**
First, a median filter with a radius of 10 pixels was used. The rejection threshold for the central pixel relative to the median value was 2.5×10^{-21} W/m^{2}Å in case of $\langle f(\lambda_{\rm optical})\rangle \leq 2 \times 10^{-21}$ W/m^{2}Å. At higher object fluxes the fixed threshold was substituted by a relative threshold proportional to the continuum flux in order to avoid the removal of real emission lines.

(2) **Rejection of narrow but intense defects:**
The filter is similar to (1) but with a pixel radius of 3 and a low flux threshold of 0.8×10^{-21} W/m^{2}Å.

(3) **Manual rejection of residuals (optional):**
The spectra were checked up by eye and the remaining residuals were manually rejected.

The defect-cleaned spectra were mainly used for the calculation of mean fluxes. For further applications these spectra were not preferred, since the substitution of pixels by the median of the adjacent pixels modify the information about the wavelength range concerned. This involves a certain danger of misinterpreting apparently but spuriously well-behaved spectral energy distributions to be realistic. Furthermore, for the pixels concerned it is almost impossible to specify a reasonable flux error. Thus, the data reduction follows the philosophy of Horne (1986) that bad data should be rejected, not repaired (see Section 4.3 and 4.5).

Slit loss correction

After the correction of atmospheric extinction and instrumental efficiency the resulting object spectra are still affected by the limited width of the slitlets, which was $1''$ for all runs. This causes flux losses, since especially bright, low-redshift galaxies have sizes clearly exceeding $1''$. Usually it was attempted to centre the objects on the slitlet in such a way that losses would be as small as possible. However, especially in the case of the not very flexible MOS masks this was a difficult task. Moreover, the limited positioning accuracy of the masks is of the order of half a pixel ($\approx 0.1''$) and may cause further losses. Possibly more important, but also more difficult to estimate, are uncertainties due to the conversion of object positions in the image used to the mask preparation into positions at the sky. These uncertainties can be caused by astrometrical errors of the sum image of the FDF used as well as inaccuracies of the position conversion procedure (see FORS manual). Partially, this could lead to positioning uncertainties of the order of one pixel or even more. Finally, the seeing, which was typically between $0.5''$ and $1.1''$ (FWHM, see Section 3.3), enlarges the object images, so that even very small objects may have significant flux losses. Hence the measured fluxes of all objects are by some amount reduced by slit losses. This flux loss can even be wavelength dependent if an object has clearly separated regions of different colour. For instance, if a slitlet has been

centred on the bulge of a large spiral galaxy, the obtained spectrum would appear redder than in reality, since the blue star forming regions in the outer areas of the galaxy would be underrepresented in the integrated spectrum. On the other hand, the inverse situation would be possible, if the slit has been centred on a bright blue star forming region in the outskirts of a galaxy showing a red bulge. Moreover, extended secondary objects (see Section 2.3), of which only an outer part of the galaxy could be obtained, might appear bluer or redder. But the fraction of these galaxies is rather low ($< 10\,\%$ of the whole sample, see Table C.1), because preferentially small-sized high-redshift candidates were observed.

Since photometry does not suffer from the limitations caused by the slitlets, the slit losses were estimated and corrected by means of the excellent photometric data available for the FDF (see Section 1.4). On the assumption that the flux losses are not wavelength dependent, the spectroscopic fluxes were adjusted by a simple multiplication by a correction factor which was calculated by fitting the spectroscopic data to the photometric filter fluxes. For this, the defect-cleaned spectroscopic fluxes (see above) were converted to filter fluxes applying the filter efficiency curves provided by ESO (see Fig. 1.2). Usually the g and R filter values were used, in part supplemented or substituted by the B or I values, dependent on the spectral energy distribution. For instance, in case of very-high-redshift candidates only the R and I filter fluxes were used. On the basis of the relatively high uncertainties concerning the spectroscopic as well as the photometric UV fluxes the U filter was not used in any case. For a small fraction of the FDF galaxies fluxes are not available for all filters (see Table C.1). Furthermore, there exist a few spectra of objects which are not included in the photometric catalogue. Consequently, the approach described could not be applied in such cases.

The correction factors $f_{\mathrm{spec}}/f_{\mathrm{phot}}$ resulting from this procedure are represented in Fig. 4.18. The diagram indicates that for primary targets (see Section 2.3) these factors mainly range between 0.3 and 0.8, with a mean value of 0.51. The variations of $f_{\mathrm{spec}}/f_{\mathrm{phot}}$ are caused mainly by apparent object sizes. The impact of seeing is indicated in Fig 4.19 which shows the dependency of the flux losses averaged for individual masks (in order to reduce the influence of object specific effects) on the mean seeing during the exposures. The increase of the flux losses is especially striking for seeing values exceeding the slit width of $1''$. The relatively large scatter of the data points indicates the presence of additional effects which cause flux losses (see discussion above).

For spectra having a flux smaller than $0.1 \times 10^{-21}\,\mathrm{W/m^2\AA}$ the described flux correction approach is not sufficient because of the high impact of systematic flux errors at this low level (see below). In this case the spectra could not be corrected by the corresponding photometric filter fluxes. Nevertheless, a rough correction was possible if the position of an object on the slitlet was similar for all relevant exposures. Then, the slit loss differences are expected to be caused mainly by the atmospheric conditions. As already mentioned above (Fig. 4.19), the influence of the seeing can be estimated by averaged flux losses calculated for each MOS image. Hence, a rough flux correction was possible using the averaged values. This method could also be applied to objects without any

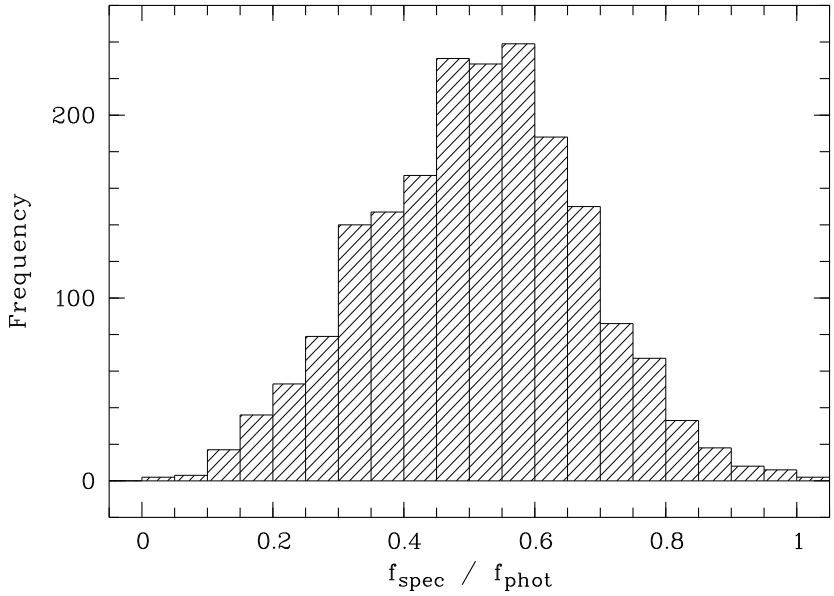

Figure 4.18: Distribution of $f_{\rm spec}/f_{\rm phot}$ (ratio of the spectroscopic to the photometric flux) for spectra of primary targets (see Section 2.3). $1 - f_{\rm spec}/f_{\rm phot}$ indicates the amount of the flux loss caused by the limited width of the slitlets ($1''$).

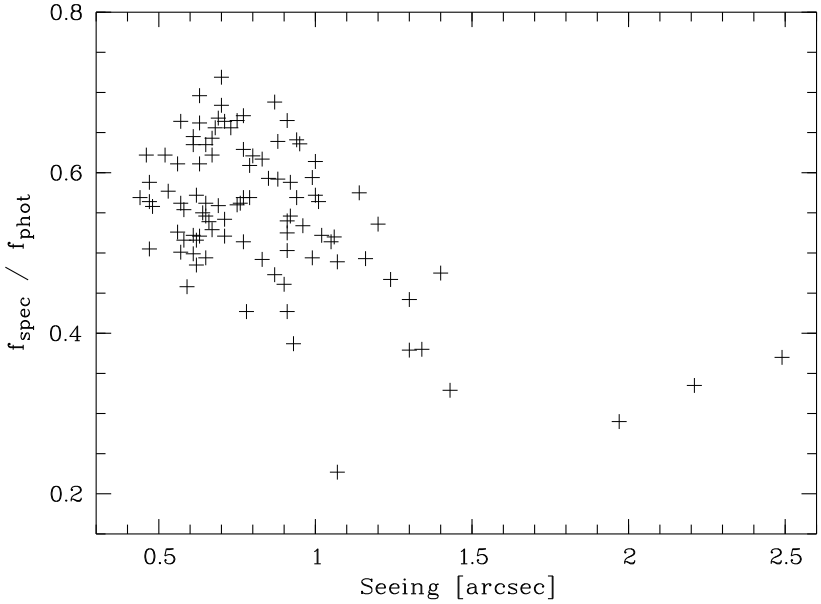

Figure 4.19: Average $f_{\rm spec}/f_{\rm phot}$ (compare Fig. 4.18) including all spectra of objects suitably positioned on the slitlets of a mask versus seeing during the exposure.

photometry.

An improvement of the total flux calibration can be achieved, if the slit loss correction is repeated after the calculation of the co-added spectra (see Section 4.5), since statistical as well as systematic flux errors of co-added spectra are lower than in case of single spectra. Consequently, flux corrections of a higher accuracy could be carried out especially in case of faint objects.

Flux calibration errors

The derivation of accurate total fluxes by slit loss correction can be affected by three types of errors:

(1) **Statistical flux fluctuations:**
In case of very low fluxes close to zero statistical fluctuations (although averaged over hundredth of Ångströms) could cause flux uncertainties which would prevent the derivation of reasonable slit loss correction factors. Nevertheless, for the primary target spectra the flux level uncertainties caused by these statistical fluctuations are negligible.

(2) **Relative systematic flux errors:**
Systematic errors like uncertainties due to the atmospheric extinction correction or the instrumental response curve are significantly higher than statistical errors averaged over full filter bands. Since these errors scale with the object flux, the relative error for bright and faint objects is of the same order. Hence, although they have considerable impact on the accuracy of the flux adjustment, they should not cause a general failure of the flux correction approach itself.

(3) **Absolute systematic flux errors:**
In respect of the slit loss correction, errors which are independent of the brightness of the spectrum are most serious, because such errors can dominate the flux level of faint objects. The main source of such errors is the imperfect sky subtraction (see Section 4.3) which causes uncertainties in the determination of the zero-flux level.

Deviations of the zero-flux level

The amount of the sky subtraction errors can be estimated by the calculation of the variance of the flux level in a sample of low-photometric-flux spectra. To avoid an influence of the photon noise on the result the spectra have to be averaged over large wavelength ranges. Therefore, the variance values were obtained for the different photometric filter bands. The measurements indicate that in the flux calibrated spectra the wavelength regions comprising the R and the g filter are hardly affected by zero-flux line uncertainties (0.03 and $0.035 \times 10^{-21}\,\mathrm{W/m^2\AA}$). Slightly higher amounts are attained within the I and B filter domains (0.045 and $0.05 \times 10^{-21}\,\mathrm{W/m^2\AA}$). A conspicuously large value was measured for the U filter domain ($\sim 0.275 \times 10^{-21}\,\mathrm{W/m^2\AA}$) and can be explained by the low instrumental sensitivity in the UV. For that reason, even usually small defects, like those caused by imperfect flat-fields, may have a large

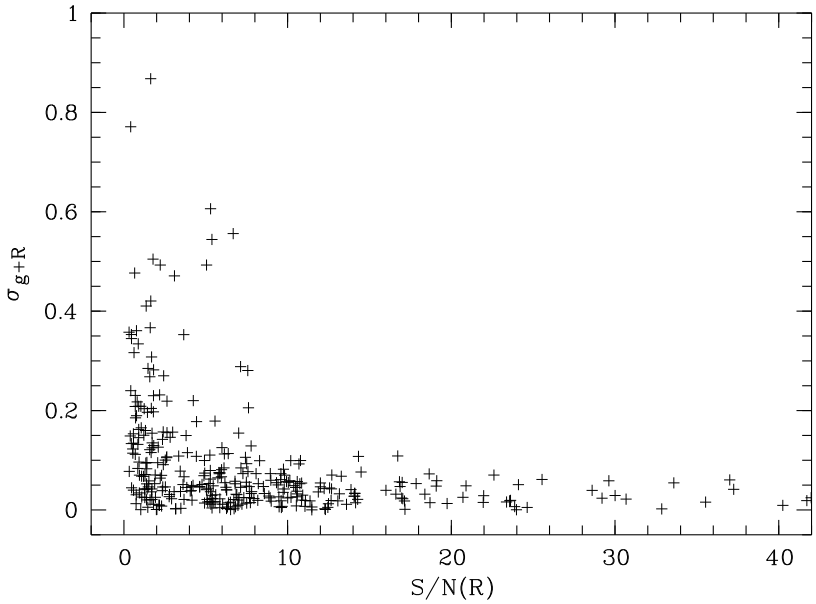

Figure 4.20: σ according to (4.4) for the combination of g and R filter as a function of the S/N in R. The diagram shows the results for the co-added spectra (see Section 4.5).

impact on the position of the UV zero-flux level. As a consequence, for some spectra located close to the slitlet margin the UV sky fit was not satisfactory.

Accuracy of the total flux calibration

In the final part of this section I check the accuracy of the final spectroscopic fluxes f_{spec} by means of a comparison with the photometric results. The deviations of the adjusted spectroscopic flux from the photometric flux f_{phot} can be expressed by

$$\sigma = \frac{\sqrt{\langle f^2 \rangle}}{\langle f \rangle} = \frac{\left(\frac{1}{n} \sum_{i=1}^{n} (f_{\mathrm{spec},i} - f_{\mathrm{phot},i})^2 \right)^{1/2}}{\frac{1}{n} \sum_{i=1}^{n} f_{\mathrm{phot},i}}. \tag{4.4}$$

Here $f_{\mathrm{spec},i}$ and $f_{\mathrm{phot},i}$ denote the flux in the photometric filter band i. n is the number of used filters i. Usually the fluxes were corrected using the g and R filters (see above). For this filter combination σ is shown in Fig. 4.20 as a function of the signal-to-noise ratio in R (see Section 4.6). The diagram clearly indicates an increase of the scatter at lower S/N. The mean σ of spectra with $S/N\,(\mathrm{R}) \geq 5$ amounts to 0.05. However, this low values are only valid for the well-behaved g and R filters. Higher values are expected for B and I and especially U, because in that cases systematic flux errors are more important (see discussion above). For comparison, Fig. 4.21 shows the corresponding diagram for the filters B and I. Here, the mean σ yields 0.14.

The previous section has shown that the flux calibration is affected by a couple of systematic effects, so that an accurate calibration is complicated especially in the UV and IR domains. However, for the faint primary targets, for

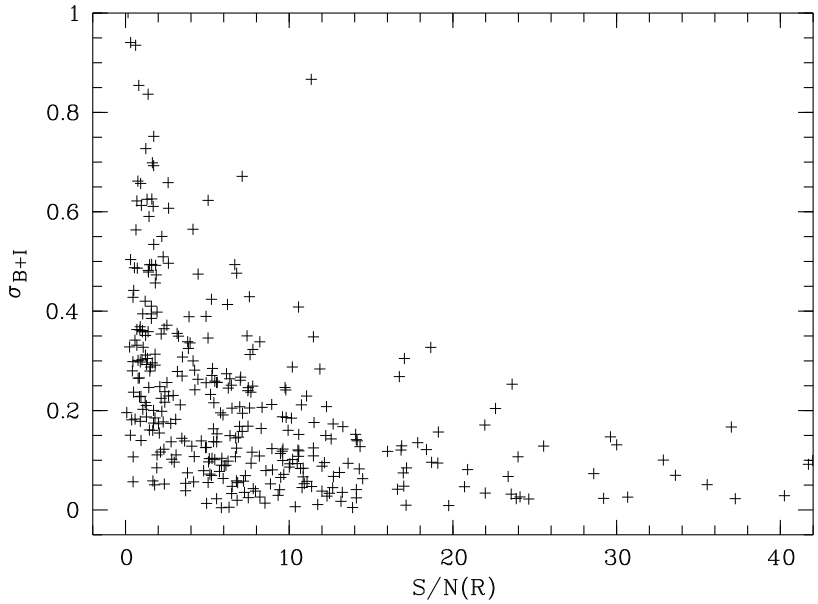

Figure 4.21: σ according to (4.4) for the combination of B and I filter as a function of the S/N in R. The diagram shows the results for the co-added spectra (see Section 4.5).

which a high number of single spectra are available (obtained during optimal conditions, see Chapter 3), the flux calibration results in convincing spectral energy distributions (at least in the optical).

4.5 Co-added spectra

To achieve the desired signal-to-noise ratios for faint high-redshift galaxy candidates, it is necessary to obtain a series of single spectra (usually 8 - 20) with typical exposure times between 30 and 48 min (see Section 3.3). To obtain a co-added spectrum, a signal-to-noise optimised averaging routine was applied. The details of this routine will be described in the following section which contains:

(1) Calculation of average spectra using wavelength dependent weights

(2) Calculation of average spectra using global weights

(3) Weight optimising

(4) σ-clipping of defective data

(5) Summary of the calculation of co-added spectra

In practice, the calculation of the co-added spectra was carried out starting with the σ-clipping procedure devoted to the rejection of defective data. In this section the σ-clipping is not described first, since the understanding of the procedure needs information on the averaging process. The co-added spectra were calculated using optimal global weights. Hence the combined formalism of

(2) and (3) was applied. I begin this section with a brief discussion on averaging using wavelength dependent weights (general case) in order to motivate the use of global weights treated thereafter.

Average spectra using wavelength dependent weights

Let assume a set of n flux calibrated spectra $f_i(\lambda)$ (see Section 4.4) of an object. The noise of $f_i(\lambda)$ is supposed to be represented sufficiently well by the error function $\Delta f_i(\lambda)$ (see Section 4.3). Then, the signal-to-noise weighted mean spectrum $f(\lambda)$ is calculable by

$$f(\lambda) = \frac{\sum_{i=1}^{n} \big(w_i(\lambda)\big)^2 f_i(\lambda)}{\sum_{i=1}^{n} \big(w_i(\lambda)\big)^2}, \tag{4.5}$$

where the weights

$$w_i(\lambda) = \frac{f_0(\lambda)}{\Delta f_i(\lambda)} \tag{4.6}$$

correspond to the wavelength dependent signal-to-noise ratio (S/N) and $f_0(\lambda)$ represents the noise-free object spectrum – which is, of course, not available. Then, the error of the mean spectrum $\Delta f(\lambda)$ would be

$$\Delta f(\lambda) = \left(\frac{\sum_{i=1}^{n} \big(w_i(\lambda)\ \Delta f_i(\lambda)\big)^2}{n\ \sum_{i=1}^{n} \big(w_i(\lambda)\big)^2} \right)^{1/2}. \tag{4.7}$$

Applying (4.6) this can be transformed to

$$\Delta f(\lambda) = \frac{f_0(\lambda)}{\big(\sum_{i=1}^{n} \big(w_i(\lambda)\big)^2\big)^{1/2}}. \tag{4.8}$$

The crucial drawback to the realization of this approach is the fact that the real spectrum $f_0(\lambda)$ is unknown. In case of $f_0(\lambda) \gg \Delta f_i(\lambda)$ the approximation $f_0(\lambda) \approx f_i(\lambda)$ can be used, but for noisy spectra this approximation does not hold any longer. Consequently, this general approach is unsuitable for much of the spectroscopic data.

Average spectra using global weights

The noise problem does not concern spectra averaged over large wavelength ranges according to

$$\langle f_i(\lambda) \rangle = \frac{1}{\lambda_2 - \lambda_1} \int_{\lambda_1}^{\lambda_2} f_i(\lambda)\, \mathrm{d}\lambda. \tag{4.9}$$

In this case

$$\langle f_0(\lambda) \rangle \approx \langle f_i(\lambda) \rangle \tag{4.10}$$

even with regard to noisy spectra. The application of average object fluxes $\langle f_i(\lambda) \rangle$ and average error functions

$$\langle \Delta f_i(\lambda) \rangle = \frac{1}{\lambda_2 - \lambda_1} \int_{\lambda_1}^{\lambda_2} \Delta f_i(\lambda)\, \mathrm{d}\lambda \tag{4.11}$$

leads to global S/N weights

$$\langle w_i(\lambda)\rangle = \frac{\langle f_i(\lambda)\rangle}{\langle \Delta f_i(\lambda)\rangle} \tag{4.12}$$

for the wavelength domain ranging from λ_1 to λ_2. Consequently, (4.5) and (4.7) have to be rewritten. Now, the mean spectrum $f(\lambda)$ is calculated by

$$f(\lambda) = \frac{\sum_{i=1}^{n} \left(\langle w_i(\lambda)\rangle\right)^2 f_i(\lambda)}{\sum_{i=1}^{n} \left(\langle w_i(\lambda)\rangle\right)^2}. \tag{4.13}$$

Furthermore, the corresponding error $\Delta f(\lambda)$ is given by

$$\Delta f(\lambda) = \left(\frac{\sum_{i=1}^{n} \left(\langle w_i(\lambda)\rangle \ \Delta f_i(\lambda)\right)^2}{n \ \sum_{i=1}^{n} \left(\langle w_i(\lambda)\rangle\right)^2} \right)^{1/2}. \tag{4.14}$$

The application of global weights cannot consider differences of $w_i(\lambda)$ between different single spectra $f_i(\lambda)$ as caused by variations of the sky spectrum (see Fig. 4.6). However, on the other hand, the most variable parts of the sky spectrum are the strong sky lines where the error function $\Delta f_i(\lambda)$ does not represent a suitable estimate of the real noise in the object spectra because of the strong residuals (see Fig. 4.13). Thus, the detailed consideration of $w_i(\lambda)$ would probably not lead to better weights in the critical parts of the spectrum. Therefore, the application of robust global weights should represent the optimal averaging approach regardless of the important insensitivity of $\langle w_i(\lambda)\rangle$ to statistical noise.

Weight optimising

According to (4.12) the weights are computed from the average signal-to-noise ratio. This works as long as the flux level of the spectra concerned is not strongly affected by systematic errors like uncertainties of the zero-flux level (see Section 4.4). Thus, in case of low spectral quality it will not be possible to derive reliable accuracy estimates. Thus, one may get better mean spectra using similar weights for the single spectra. For that reason, the weighting factors were calculated by

$$\langle w_i(\lambda)\rangle = \frac{\langle f_i(\lambda)\rangle}{\langle \Delta f_i(\lambda)\rangle} + w_0 = w_{\mathrm{S/N},i} + w_0 \tag{4.15}$$

where w_0 is a minimum weight (negative $\langle f_i(\lambda)\rangle$ are set to 0), which provides a smooth transition from the S/N weighted averaging of high quality spectra to the nearly equally weighted averaging of spectra showing a very low flux only. The crucial flux uncertainties concerning the subtraction of the sky are of the order of 0.03 – $0.05 \times 10^{-21}\,\mathrm{W/m^2\AA}$ in the optical (see Section 4.4). As the corresponding variations of the error level are distinctly smaller, this converts in uncertainties of $w_{\mathrm{S/N}}$ of about 0.2. Therefore, $w_0 = 0.5$ seems to be suitable to hold the fluctuations of the weighting factors on a low level. Fig. 4.22 shows a comparison of the dependence of $\Delta(w^2)/(w^2)$ on the S/N for $w_0 = 0$ and $w_0 = 0.5$. From this diagram one can take, for instance, that at

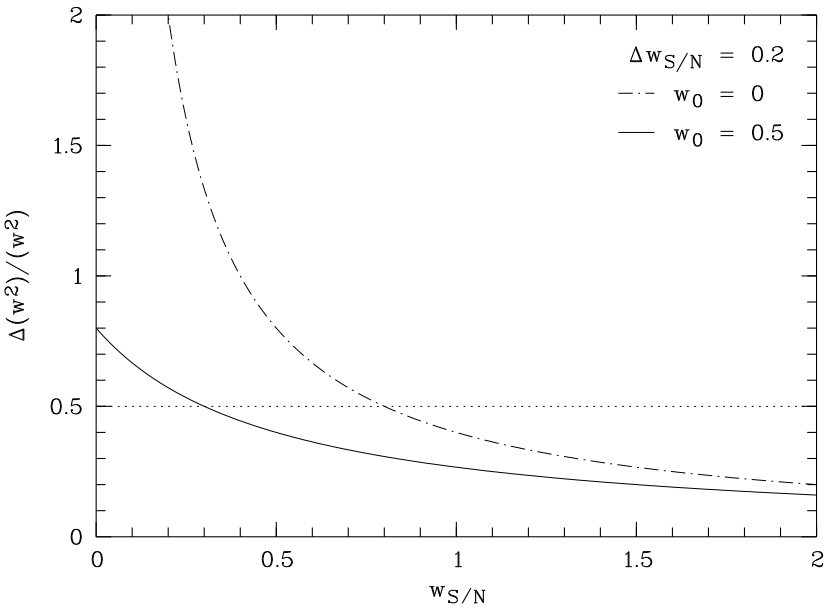

Figure 4.22: Relative errors of squared weighting factors as a function of $w_{\mathrm{S/N}} = f/\Delta f$ on the assumption of $\Delta w_{\mathrm{S/N}} = 0.2$. The dash-dotted line indicates the errors for $w = w_{\mathrm{S/N}}$. The solid line shows the case for $w = w_{\mathrm{S/N}} + w_0$ with $w_0 = 0.5$. The critical error level of 50 % is highlighted by a dotted line.

$w_{\mathrm{S/N}} = 0.8$ ($w_0 = 0$) and at $w_{\mathrm{S/N}} = 0.3$ ($w_0 = 0.5$) the relative error reaches 50 %, respectively. In contrast to the situation for $w_0 = 0$ the error remains below 100 % in any case for $w_0 = 0.5$. In principle, the errors could be lowered further choosing $w_0 > 0.5$, but this would change the weighting factors for the high S/N spectra, so that the signal-to-noise ratio of the mean spectra would no more achieve the optimum value. Hence, the introduction of $w_0 = 0.5$ turned out to be a good compromise to avoid unreasonable weighting factors for noisy spectra, but to profit from the quality of S/N weighted mean spectra for high quality data.

The average signal-to-noise ratios $\langle f_i(\lambda)\rangle/\langle \Delta f_i(\lambda)\rangle$ necessary to the derivation of $\langle w_i(\lambda)\rangle$ were calculated using the defect-cleaned spectra described in Section 4.4 in order to avoid the influence of strong defects on the average flux values. The S/N were usually derived in the optical wavelength range, since there systematic flux errors have the lowest impact (see Fig. 4.13). Mostly the wavelength range between 4200 and 7200 Å was chosen. In some cases concerning particularly blue or red faint objects the wavelength range was varied in order to maximise the available S/N. Considering faint objects essentially characterised by a single emission line (see Section 6.2), the derivation of the signal-to-noise ratio even had to be limited to line enclosing small wavelength intervals in order to attain reasonable weighting factors. Generally, the resulting ratios are consistent with that expected on the corresponding observing parameters like airmass, seeing or sky brightness.

σ-clipping of defective data

The calculation of mean spectra represents a good opportunity to get rid of strong spectral artifacts like CCD defects or unremoved cosmic ray hits without modifying the individual spectra (see Section 4.4). This was managed applying a σ-clipping method to the uncleaned single spectra which was additionally carried out *before* the averaging routine described above. For this, a reference spectrum necessary for the determination of the derivations has to be calculated first of all. It is important that the reference spectrum is nearly free of contributions from defective data, as otherwise the approach would fail. Furthermore, the reference spectrum has to resemble the S/N optimised mean spectrum calculated as described above. Therefore, a 'S/N weighted' median $\overline{f}(\lambda)$ was calculated for each set of spectra. The procedure was carried out as follows:

- Sorting of the flux values of the single spectra for each wavelength λ in increasing order according to

$$f_i(\lambda) \leq f_{i+1}(\lambda).$$

- Calculation of the weights $\langle w_i(\lambda) \rangle$ using (4.15).

- Calculation of the normalised square sum

$$x_k(\lambda) = \frac{\sum_{i=1}^{k \leq n} \left(\langle w_i(\lambda) \rangle \right)^2}{\sum_{i=1}^{n} \left(\langle w_i(\lambda) \rangle \right)^2} \tag{4.16}$$

  for each λ and for different numbers of added weights k.

- Derivation of the median flux value $\overline{f}(\lambda)$ by the condition

$$\overline{f}(\lambda) = f_k(\lambda) \quad \text{if} \quad x_{k-1}(\lambda) < 0.5 \leq x_k(\lambda) \tag{4.17}$$

  for each λ.

As next step of the procedure the sigma-clipping was carried out. This procedure excludes data points from the subsequent averaging routine for which

$$|f_i(\lambda) - \overline{f}(\lambda)| > f_{\text{thresh}}(\lambda).$$

This condition prevents that defective data values affect the calculation of mean spectra. The error function $\Delta f_i(\lambda)$ forms a well suitable basis for the derivation of the threshold $f_{\text{thresh}}(\lambda)$, since the dependency of the fluctuation intensity on the noise level is taken into account in this way. In practice, the threshold was set to $6\,\Delta f_i(\lambda)$. This limit guarantees that no noise peaks are rejected. Moreover, unavoidable small systematic flux errors (see Section 4.4) cannot cause the undesired exclusion of principally useful data. Consequently, the rejection of data points is restricted to conspicuous defects as desired.

Summary of the calculation of co-added spectra

The calculation of the co-added spectra was carried out as follows:

(1) Computation of the median spectrum $\overline{f}(\lambda)$

(2) σ-clipping of defective data points using $\overline{f}(\lambda)$

(3) Calculation of modified global weights according to (4.15) applying defect cleaned spectra (see Section 4.4)

(4) Application of the σ-clipping results for the computation of S/N weighted mean spectra and error functions using (4.13) and (4.14), respectively

In summary, the S/N weighted averaging combined with the σ-clipping of defective data represents a well suitable method to obtain co-added spectra of high quality. For the great deal of the scientifically interesting objects the S/N is rather sufficient and the approach worked very well (see Chapter 5.1). It reaches its limits in case of strong wavelength dependent systematic errors like residuals of prominent night sky lines. Especially the strength of the residua of the line [O I]λ 5577 scarcely depends on the S/N. Moreover, the method is less optimised in case of very low quality spectra for which the derivation of reliable signal-to-noise ratios is rather insufficient. In order to at least avoid unreasonable weights for these single spectra the algorithm provides weighting factors nearly independent of the apparent S/N. The limitations stated mainly concern data of which the scientific value are rather small, because of the too low object flux compared to the amount of the statistical and systematic errors.

4.6 Smoothing

In this chapter I determine the spectral resolution of the obtained data and describe the smoothing of the spectra to this resolution.

The pixel scale for the grism 150 I amounts to 5 Å in the rebinned, wavelength calibrated frames. On the other hand, the spectral resolution element as estimated from the wavelength calibration frames results in a FWHM $\lesssim$ 23 Å ($4 - 5$ pixels) which changes only little across the whole frame. Consequently the spectra are oversampled by a factor $\gtrsim 2$, since the minimum sampling is 2 pixels per resolution element. Hence the calculated S/N per pixel is clearly below that which can be expected by the spectral resolution. Thus, it is adequate to smooth the reduced spectra to the spectral resolution element of 23 Å in order to achieve a physically appropriate value for the S/N.

The easiest way to smooth a spectrum is the application of a boxcar filter. The filter substitutes pixel fluxes by the mean of all pixels within a fixed radius around the respective pixel of which the flux is recalculated. However, this method has the disadvantage that a boxcar looks very different compared to a typical instrumental profile. Thus, the shape of spectral lines can be significantly changed by this filter which prevents an optimum smoothing of the data. Hence a Gaussian filter was used which resembles the profile of the observed spectral lines much better. This filter is slightly more complicated than a simple boxcar.

The pixel values within a given radius are averaged using different weights derived with the Gaussian function

$$f(x) = \frac{1}{\sigma\sqrt{2\pi}}\, e^{-\frac{1}{2}\left(\frac{x-\mu}{\sigma}\right)^2} \tag{4.18}$$

where μ being the mean and σ being the width of the distribution. However, since $\mu \neq 0$ and a limiting filter radius would cause asymmetric filters, only σ represents a further free parameter.

The successful application of the Gaussian filter requires the determination of the optimum parameters. That is, one should achieve the best compromise between two contrary aims, namely the attainment of a high signal-to-noise ratio and the preservation of a high spectral resolution, respectively. As the number of pixels significantly belonging to one resolution element is only four to five, the filter radius should be $x_{\rm rad} \leq 2$ ($N_{\rm pix} \leq 5$) and $\sigma_{\rm G}$ should be of the same order. The suitability of a filter can be tested by its influences on (a) the shape of line profiles and (b) the spectral fluctuations: (a) Changes of the profiles can be measured by fitting Gaussians and deriving line centres, maximum intensity values and line widths (FWHM). (b) For the spectral fluctuations the ratio of the standard deviations after and before the smoothing $\sigma_{\rm smo}/\sigma_0$ represents a good indicator. This resembles the procedure used for the rebinning corrections in Section 4.3 (see Fig. 4.15). In order to get a graphic measure of the smoothing effect and hence the amount of the reduction of the spectral fluctuations one can define (based on the Poisson error) the effective number of pixels $N_{\rm eff}$ involved in the smoothing process by

$$\frac{\sigma_{\rm smo}}{\sigma_0} = \frac{1}{\sqrt{N_{\rm eff}}}. \tag{4.19}$$

This suggests that optimum smoothing should result in a $N_{\rm eff}$ somewhat smaller than the FWHM of unresolved lines, that is, $N_{\rm eff} \sim 4$.

Tests have indicated that a *double* application of the simple filter characterised by $x_{\rm rad} = 1$ and $\sigma_{\rm G} = 1$ complies best with the requirement of balancing the competing demands on high signal-to-noise ratio (increased by smoothing) and on high spectral resolution (decreased by smoothing). The effect of the filter on a single pixel is indicated in Fig. 4.23 (solid line).

The final $\sigma_{\rm smo}/\sigma_0$ can be obtained by

$$\frac{\sigma_{\rm smo}}{\sigma_0} = \prod_{i=1}^{n} \frac{\sigma_{{\rm smo},i}}{\sigma_{{\rm smo},i-1}} \tag{4.20}$$

where $\sigma_{\rm smo,0} = \sigma_0$ and $\sigma_{{\rm smo},n} = \sigma_{\rm smo}$.

Fig. 4.24 shows the resulting noise reduction $\sigma_{\rm smo}/\sigma_{\rm smo,0}$ by the application of the smoothing filter described above dependent on $\langle\sigma_{\rm reb,fit}/\sigma_{\rm reb,0}\rangle$ which indicates the effective noise reduction by rebinning as described in Section 4.3 for the co-added spectra. This representation was chosen, since the effect of a smoothing process on the reduction of spectral fluctuations depends on the extent of preceeding smoothing operations. Using Fig. 4.24 the correction factors for the error function (see Section 4.3) can be derived by linear fitting. The

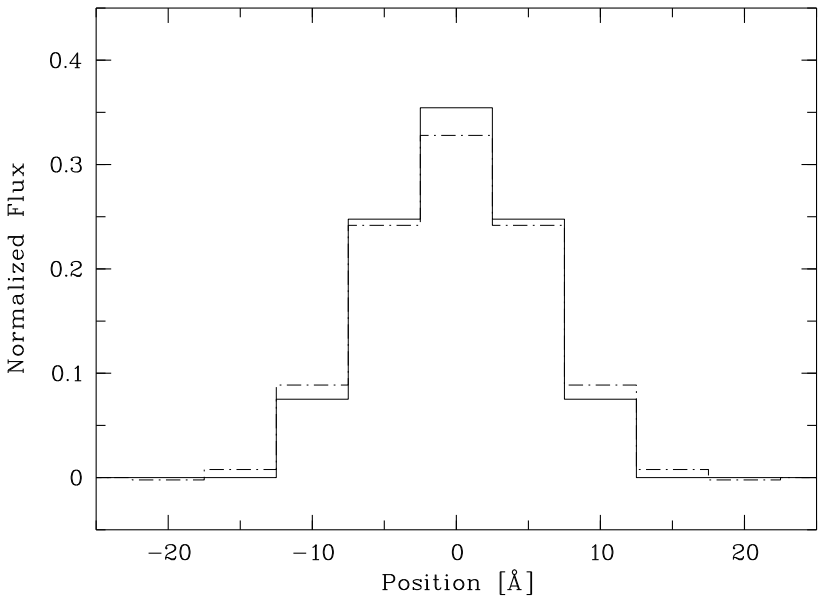

Figure 4.23: Result of the smoothing procedure on a synthetic spectrum showing only one pixel with a non-zero flux (position = 0 Å, pixel width = 5 Å, initial intensity = 1.0). The solid line indicates the result for a Gaussian filter with $\sigma = 5$ Å (1 pixel) and a maximum number of involved pixels of 3 (pixel radius = 1). The filter was done twice which increases the effective pixel radius up to 2. Finally, the dash-dotted line shows the result for the case that smoothing effects generated by data rebinning are taken into account as well. Since the relative and the absolute wavelength calibration requires a rebinning of the data (see Section 4.2 and 4.3), the rebinning was simulated by: first, a quarter pixel shift to the left; subsequently a rebinning using Hermite polynomials (see Section 4.3); then, a quarter pixel shift to the right; and at the end, a repetition of the rebinning procedure. This approach ensures that no residual asymmetry will remain. The resulting histogram indicates that smoothing caused by rebinning is responsible for a small part of the whole effect only.

average noise reduction by smoothing amounts to $\sigma_{\rm smo}/\sigma_{\rm smo,0} = 0.69 \pm 0.04$ in case of the two times rebinned spectra.

According to equation (4.20) the total noise reduction by all rebinning (2× wavelength calibration) and smoothing operations (see above) amounts to

$$0.81 \times 0.88 \times (0.69 \pm 0.04) = 0.49 \pm 0.03.$$

The first value is taken from Fig. 4.14 and estimates the average noise reduction by the first rebinning. The second value comes from Fig. 4.15 and describes the average lowering of the spectral fluctuations by the second rebinning (absolute wavelength calibration). Following equation (4.19) the result above can be transformed in an equivalent number of pixels involved in smoothing. For the described series of operations $N_{\rm eff} = 4.1 \pm 0.3$. This value is precisely located within the optimum range which confirms the suitability of the used smoothing filter ($x_{\rm rad} = 1$, $\sigma_{\rm G} = 1$, double use). Finally, the joint effect of all operations on a single pixel is shown in Fig. 4.23 (dash-dotted line).

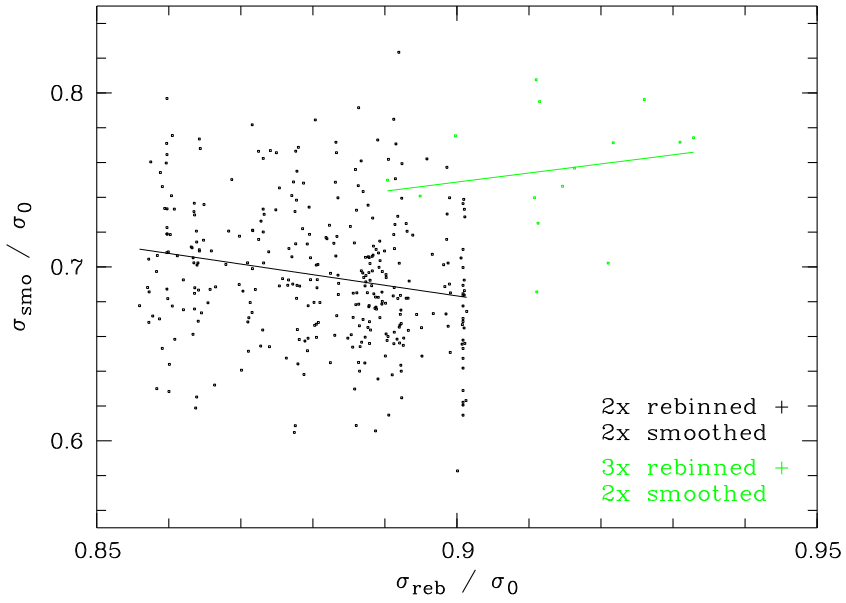

Figure 4.24: Noise reduction $\sigma_{\rm smo}/\sigma_{\rm smo,0}$ by the double application ($n = 2$) of a smoothing filter with $x_{\rm rad} = 1$ and $\sigma_{\rm G} = 1$ dependent on $\langle\sigma_{\rm reb,fit}/\sigma_{\rm reb,0}\rangle$ which represents for each object the weighted average (see Section 4.5) of the relevant fit values of the single spectra derived from Fig. 4.15 for the noise reduction by rebinning (see Section 4.3). The different colours distinguish between mainly two times (black) and mainly three times rebinned spectra (green). Assuming that the large scatter in the data values is mainly caused by the uncertainties concerning the $\sigma_{\rm smo}$ derivation, representative noise reduction values can be determined by a simple linear fit. The values obtained in this way can be used for the correction of the error function (compare Section 4.3). The mean $\sigma_{\rm smo}/\sigma_{\rm smo,0}$ are 0.69 for the 'black' and 0.76 for the 'green' group of spectra. The corresponding scatter of the data values amounts to 0.04 and 0.03, respectively.

4.7 Additional corrections

Before I turn to analyses of the reduced spectra it remains to correct the spectra for Galactic extinction. Furthermore, I discuss a rough correction of the atmospheric A and B bands.

Galactic extinction correction

The plain of the Galactic disk contains interstellar dust. which absorbs optical and UV radiation and re-emits the energy in the infrared. Thus, the transparency of the Galaxy for radiation of shorter wavelengths is reduced. The distribution of the interstellar dust is very inhomogeneous. This causes a direction dependent Galactic extinction (scattering and absorption) which can be determined by the measurement of the dust emission in the infrared (see Schlegel et al. 1998).

The FORS Deep Field is located close the south Galactic pole which is characterised by a low extinction (compare Section 1.4). According to Schlegel et

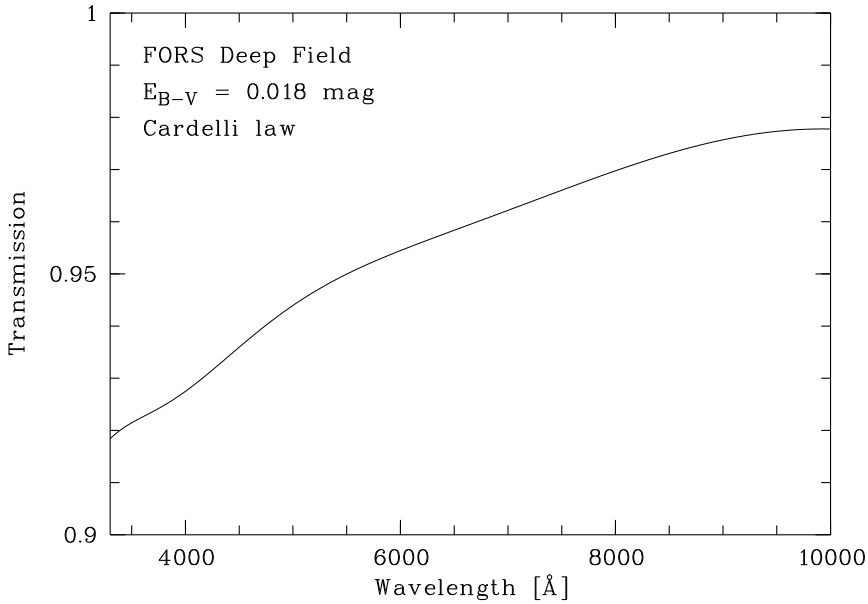

Figure 4.25: Wavelength dependent flux reduction by Galactic extinction in direction towards the FORS Deep Field ($E_{\mathrm{B-V}} = 0\overset{\mathrm{m}}{.}018$). The diagram shows the transmission versus the wavelength. A Cardelli (et al. 1989) law was used for the calculation of the extinction.

al. (1998) the extinction-induced colour excess $E_{\mathrm{B-V}}$ amounts to $0\overset{\mathrm{m}}{.}018$ in direction towards the FDF. Using

$$A_\lambda = R_{\mathrm{V}}\, E_{\lambda-\mathrm{V}} \tag{4.21}$$

with $\lambda = \mathrm{B}$ and the approximation $R_{\mathrm{V}} \approx 3.1$ for the optical wavelength range (see Cardelli et al. 1989) this results in a low total Galactic extinction of $A_{\mathrm{V}} \approx 0\overset{\mathrm{m}}{.}056$ in the visual (V band). Applying

$$\frac{I_\lambda}{I_{\lambda,0}} = 10^{\,-0.4\,A_\lambda} \tag{4.22}$$

(compare equation 4.2) A_{V} transforms in an intensity reduction of about 5 %.

For the other optical wavelength ranges equations (4.21) and (4.22) indicate an exponential increase of the extinction towards the UV. To calculate the precise shape of the extinction law the empirical formula for A_λ/A_{V} from Cardelli et al. 1989 was used to correct the FDF spectra. The corresponding wavelength dependent flux reduction is indicated by Fig. 4.25. The amount of the Galactic extinction correction was often smaller than the uncertainties of the flux calibration (see Section 4.4). Nevertheless, the application of this correction avoids systematic flux errors particularly in the blue and UV part of the spectra.

Correction of the atmospheric A and B bands

The vibration rotation band of the O_2 molecule (A band) and of the OH radical (B band) partly become optical thick to radiation from astrophysical objects.

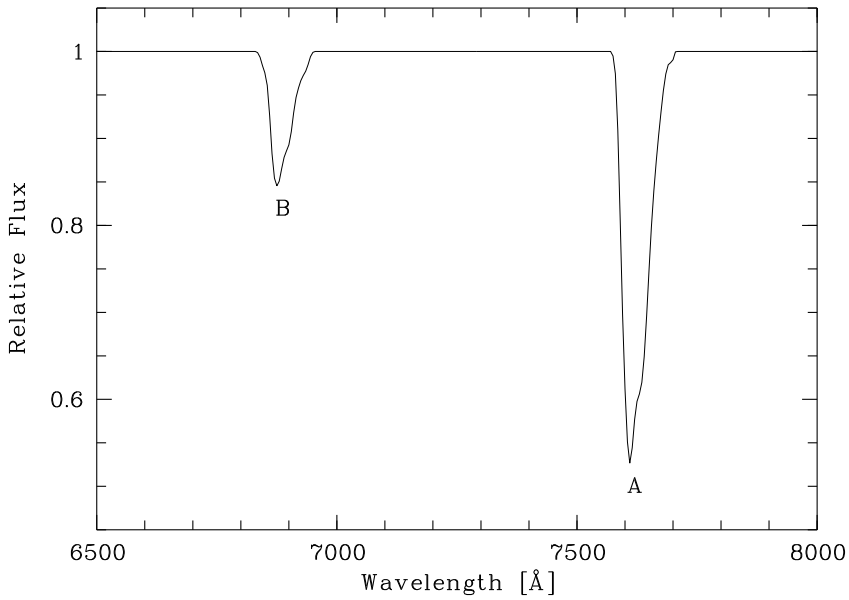

Figure 4.26: Mean profiles of the A and B band. The profiles were computed from good S/N spectra of the whole spectroscopic sample.

This causes strong absorption features in the wavelength regions mainly ranging from 6830 to 6950 Å (B band) and from 7570 to 7710 Å (A band). The features cannot be removed by sky subtraction (see Section 4.3), because the absolute strength of the bands is proportional to the level of the continuum being different comparing object and sky spectra. This will lead to a systematic flux error in the wavelength regions concerned unless one corrects the fluxes for this effect. For this correction the profile of the bands were determined by averaging a large number of distinct spectra (normalised on the continuum close to the bands), so that the only remaining spectral features will be the A and B band (Fig. 4.26). Consequently the bands could be removed dividing the spectra by the resulting band model. With this correction the variability of the A and B band were neglected, but it turned out that this approach is absolutely sufficient in view of the signal-to-noise ratios and spectral resolutions of the obtained spectra. The error functions were corrected in the same manner as the object spectra which leads to an absolute error increase up to about two in case of the A band. Relative error raising by fluctuations of the band profile were not taken into account, since this is a rather small effect.

Chapter 5

Derivation of redshifts and spectral types

This chapter deals with a basic characterisation of the final object spectra (for the reduction procedure see Chapter 4). I start with a brief discussion on the quality of the spectra, since minimum requirements on spectral quality are indispensable for the realization of various spectral analyses. After that, I focus on the basic characterisation of galaxy spectra by redshift and a rough spectral type. The derivation of these parameters was realized by the application of an iterative self-consistent procedure. This procedure is as follows:

(1) First redshift approximation from visual line identification (Section 5.2).

(2) Derivation of spectral types by fitting characteristic spectral energy distributions (Section 5.3).

(3) Averaging of the spectra for each spectral class to construct empirical templates (Section 5.4).

(4) Derivation of improved redshifts and types by cross-correlation with the template spectra (Section 5.5).

(5) Iteration of steps (3) and (4), if needed.

The results of this method are presented in Section 5.6. The chapter closes with a discussion of the uncertainties concerning the redshift determination (Section 5.7).

5.1 Description of the spectra

In general, the 539 obtained co-added spectra (Appendix D) are characterised by the following properties:

- All spectra start at 3300 Å and end at 10000 Å. The step size amounts to 5 Å.

- The wavelength region covered ($f(\lambda) \neq 0$) ideally ranges from 3400 to 10000 Å for the main programme and from 3300 to 9100 Å for the commissioning and backup observations (see Section 3.3). The values are caused by the limitations of the response curves used for the flux corrections (see Section 4.4). The spectral limits are upper limits, since in a few percent of the cases the available wavelength range is reduced by a cut-off of the spectrum due to a position close to the edge of the CCD. In part those effects are cancelled out by averaging spectra located on different masks.

- The use of grism 150I with $1''$ slit width (see Section 3.2) and the total effect of all smoothing operations (see Section 4.6) leads to a characteristic FWHM of unresolved lines around 23 Å.

- Almost all spectra show absolute fluxes adjusted to the photometric filter fluxes (see Section 4.4). Just a small number of very low quality spectra could not be calibrated in this way.

- The spectra are often affected by residua of strong night sky emission lines (compare Section 4.2).

- For each spectrum exists a corresponding error function indicating the statistical noise level (see Section 4.3).

Typical examples of spectra are represented in the next section.

Characteristic signal-to-noise ratios

The quality of a spectrum is determined by the amount of statistical as well as systematic errors relative to the object flux. Disregarding strong systematic errors (see below), just the ratio of the object flux to the flux error, that is the signal-to-noise ratio (S/N), gives a suitable indicator for the quality of a spectrum. A high reliability of the ratio requires an accurate determination of the present errors.

The statistical errors are well represented by the error function (Section 4.3) as long as wavelength regions around strong night sky lines and marginal regions (UV and IR) are avoided. In the near IR spectra are particularly affected by residuals of strong night sky lines coming from an insufficient sky subtraction (Section 4.3). In the near UV the instrumental set-up used (Section 3.2) is inadequate in that way that small errors like flat-field errors (Section 4.1) can cause large uncertainties. In case that these systematic errors are of statistical character, they can be taken into account as additional noise, as shown in Fig. 4.13. However, effective spectral fluctuations are only reliable for larger samples of spectra. For single spectra a separation of object inherent spectral variations and noise/systematic errors is almost not possible. Therefore, in practice one should restrict quantitative error treatments on wavelength regions with small systematic errors only.

Considering the wavelength bands covered by the photometric filters shown in Fig. 1.2, especially the optical B, g and R filter bands are suited to derive

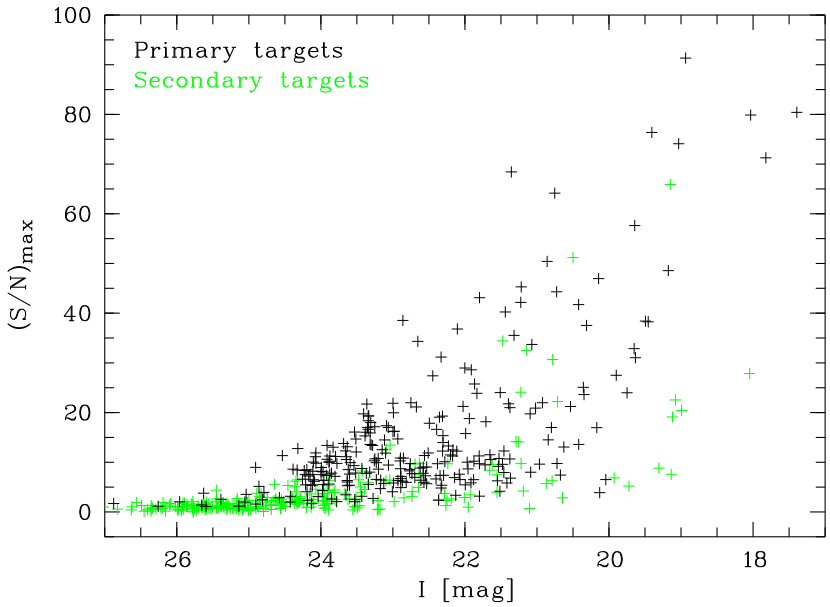

Figure 5.1: Representative signal-to-noise ratios per resolution element (maxima of the filter band values of B, g, R and I) of the FDF spectra as a function of the I magnitude. The distribution is shown for primary (black) as well as secondary targets (green).

reliable signal-to-noise ratios. A great advantage of this filter combination is the avoidance of the prominent [O I]λ 5577 line which may cause strong residuals. For the determination of a characteristic value the S/N (per resolution element) can be measured in different wavelength ranges (like filter bands). Then the maximum S/N of the considered bands can be taken as reference value. In this way the derived S/N depends less on the respective spectral energy distribution. Of course, the S/N could be taken in very narrow wavelength ranges, so that the maximum ratio could be determined by a strong emission line, but this would be a very special value with no respect to the situation of the more representative continuum. Hence, the use of a few wavelength ranges defined by photometric broad band filters (B, g, R and in case of extremely red objects also I) seems to be the most suitable constellation for the derivation of representative signal-to-noise ratios. Fig. 5.1 shows the so derived $(S/N)_{max}$ (plotted versus the I magnitude) for the spectroscopic sample of the FORS Deep Field (see also Appendix D). An average S/N of about 20 was achieved for the primary targets (black crosses, see Section 2.3). At the faint end of the apparent brightness distribution, there are a high number of spectra with very low S/N (1 and less). These are essentially spectra of secondary objects (green crosses). Regarding the low quality such spectra were not used for detailed analyses (except of significant emission lines). Thus, 133 spectra (25 % of the whole sample) were excluded from further investigations.

The spectral quality parameter Q_s

The derivation of reliable signal-to-noise ratios works only if the object spectrum does not show strong systematic errors. In this case the spectrum can distinctly deviate from the true spectral energy distribution. Hence, the spectral continuum can become useless for all further analyses. Such extreme cases may occur for spectra where a careful sky subtraction was not possible (see Section 4.3). Examples are spectra in the borderline region of slitlets (extreme brightness gradients) or spectra which had to be reduced with defective flat-fields (commissioning phase). In order to mark such affected spectra the parameter Q_s indicating the quality of a spectrum was introduced (see Appendix C). The scale comprises four classes with the following meaning:

$Q_s = 3$: The spectrum does not show extended defects. Only sporadic residuals of strong sky lines are possible.

$Q_s = 2$: The spectrum is partly affected by (strong) extended defects, that is, there are limited wavelength ranges with distinctly reduced quality. In most cases this concerns either the blue/UV continuum or the IR continuum in the range of the OH bands. The optical continuum essentially remains unaffected.

$Q_s = 1$: There are strong defects affecting a great deal of the spectrum. The true shape of the continuum is highly uncertain.

$Q_s = 0$: The spectrum has got a very low S/N ($\lesssim 1$) and hence no classification was carried out.

In general, systematic errors do not exceed an acceptable level at least in the optical wavelength range (see Appendix C). Only a small fraction of spectra indicates major distortions. The FDF spectroscopic sample contains just 8 spectra with $Q_s = 1$ (2 % of the classified spectra). The number of spectra with $Q_s = 2$ amounts to 95 (23 %). Strong distorted spectra ($Q_s = 1$) are found among objects whose co-added spectra were obtained by the use of only one mask set-up (7 of 8 spectra). The strong spectral defects are mainly caused by an insufficient sky subtraction (see Section 4.3). This may arise from a marginal position of the object in the slitlet. This problem chiefly concerns secondary targets whose locations in the slitlets are randomly distributed (5 of 8 spectra). Finally, calibration data of low quality, as obtained during the FORS 1 commissioning phase (see Appendix A), may also affect the sky subtraction (2 of 8 spectra).

5.2 Visual line identification

As I described in Section 1.1 the cosmic expansion causes an extension of radiation in wavelength emitted by distant objects (1.2). This 'redshift' complicates the identification of spectral lines and features. At low S/N the observable wavelength region possibly could not provide prominent spectral features of significant strength to allow the differentiation between different combinations of redshift and spectral type (see Section 5.3). Here, a reliable derivation of redshifts is only practicable using sophisticated approaches exploiting all available spectral information (Section 5.5). Therefore, it is important to obtain spec-

tra covering a wavelength range as large as possible in order to maximise the usable spectral features. This was realized using the low resolution grism 150 I (see Section 3.2).

However, for high S/N spectra, where various lines can easily be noticed, a visual check of the spectrum principally suffices to determine the correct redshift. This offers the possibility to obtain an extensive sample of galaxy spectra with known redshift. As a consequence, the spectra can be used to create templates (Section 5.4) for an automatic redshift derivation (Section 5.5).

In this section I focus the discussion on the direct line identification and the line-based redshift measurement.

Line centre measurements

Although the resolution of the spectra is about 23 Å, line centre positions can be measured quite accurately, if the signal-to-noise ratio is sufficiently high and the line profile is fairly symmetric. Under these conditions accuracies of a few percent of the FWHM ($\lesssim 1$ Å) can be achieved limited by the uncertainties of the wavelength calibration only (see Section 4.2 and 4.3). The measurements of the line centres can be accomplished by fitting Gaussians (4.18) to the line profiles. This approach requires relatively symmetric profiles. However, since most lines are unresolved (blurring of line structures), the method is generally suitable.

Line blends

The main problem regarding low resolution spectra is the superposition of adjacent spectral lines showing a mutual distance in the order of a significant portion of the line width and similar intensities. The centres of lines involved in such a blend cannot exclusively be measured empirically. In principle, it is possible to resolve blends fitting multiple Gaussians, but this requires the determination of several free parameters which needs a high S/N. Thus, one has to estimate the line strength and profiles either by theoretical computations or by the use of values (measured in high resolution spectra) typical of the spectral type. However, the necessary assumptions have high uncertainties. Moreover, it is questionable to link the determination of redshifts to assumptions on physical conditions existing in the object whose derivation should actually be the duty of further analyses. Consequently, it is best to avoid the use of affected lines for the redshift derivation, if possible.

There is one important blend whose application is indispensable, namely the forbidden [O II]$\lambda\lambda$ 3726, 3729 doublet lines ($^2\mathrm{D}_{3/2}, ^2\mathrm{D}_{5/2} \rightarrow {}^4\mathrm{S}_{3/2}$) of the single ionised oxygen. [O II]$\lambda\lambda$ 3726, 3729 belong to the strongest emission lines emerging from ionised gas nebulae (H II regions). The strength of the doublet and the fact that the lines can be detected within a large redshift interval ranging from 0 to almost 1.5 are the main reasons why [O II] is such valuable for the determination of redshifts. Furthermore, the relatively small separation of the two components of 2.8 Å and their relationship to the same multiplet effect, that this blend can comparatively be managed in a comfortable way.

The lower energy levels $^2D_{3/2}$ and $^2D_{5/2}$ of oxygen are populated by collisions with thermal electrons. At low electron densities ($N_e \sim 10^1 - 10^2\,cm^{-3}$) there is a significant chance that the excited ion falls back to its ground level by a forbidden radiative transition (breaking the selection rules for electric dipole radiation) and not by a further collision. At increasing electron densities the de-excitation results more and more from collisions whereby the strength of [O II]λ3729 drops, because of a lower critical electron density ($N_e \approx 3\times10^3\,cm^{-3}$ in contrast to $N_e \approx 1.6\times10^4\,cm^{-3}$ for [O II]λ3726, see Osterbrock 1989). Therefore, the intensity ratio $I(\lambda3729)/I(\lambda3726)$ can vary between 1.5 ($N_e \to 0$) and 0.3 ($N_e \to \infty$). This causes positions of the common line centre between 3726.6 and 3727.7 Å for a spectral resolution of 23 Å. The effect is relatively small but it cannot be neglected if redshift accuracies of a few 10^{-4} are desired (see Section 5.7). For that reason, $I(\lambda3729)/I(\lambda3726)$ was derived for average electron densities of galaxies typical for [O II] measurements. Following Raimann et al. (2000) N_e should be of the order of a few $10^2\,cm^{-3}$ or less. This leads to representative intensity ratios of 1.1 – 1.2 (see Osterbrock 1989). These values imply a common centre of the [O II] doublet at 3727.5 Å. This wavelength is a reasonable value, although deviations of several 10^{-1} Å are possible.

The discussion on the [O II] doublet indicates how complicated it can be to derive a reasonable centre of a line blend. Thus, for the redshift derivation only blends were used either showing a small separation of the components (e.g. C III]$\lambda\lambda$1907, 1909 or having a component clearly stronger than the other lines (e.g. blend of Hα, [N II]λ6548 and [N II]λ6583). The criteria are redshift dependent, since the distance of two spectral features is proportional to $(z+1)$. Hence, at high redshift components can be resolved which would be inseparable at low redshifts. On the other hand, it is possible that a narrow pair of lines (totally unresolved at low redshifts) can become complex at higher redshifts. An overview of prominent line blends is represented in Appendix B.

Spectral lines in the optical

For a certain redshift identification and accurate derivation as many suitable lines as possible are needed. This condition is realized best in case of intensely star-forming galaxies at low redshift (see Fig. 5.2). Here, one profits by the possible presence of several strong nebular emission lines, like the forbidden [O II]$\lambda\lambda$3726, 3729 and [O III]$\lambda\lambda$4959, 5007 and the hydrogen recombination lines Hα, Hβ and probably Hγ. Taking all these lines into account it is possible to obtain redshifts of high accuracy based on line centre measurements only.

Regarding galaxies with (almost) no star formation (elliptical galaxies) the situation is worse (see Fig. 5.3). Regarding this spectral type, emission lines are (almost) completely absent. The present features are mainly absorption lines emerging from stellar photospheres. The use of absorption lines has the drawback that the attainable signal-to-noise ratios are naturally lower than in case of strong emission lines. Furthermore, a part of the strongest features are unfortunate line blends (Mg-band, G-band and E-band). Hence, the redshift derivation has to be restricted to a small number of lines, mainly calcium H and K (connected to the so called '4000 Å break') and Balmer lines, if strong

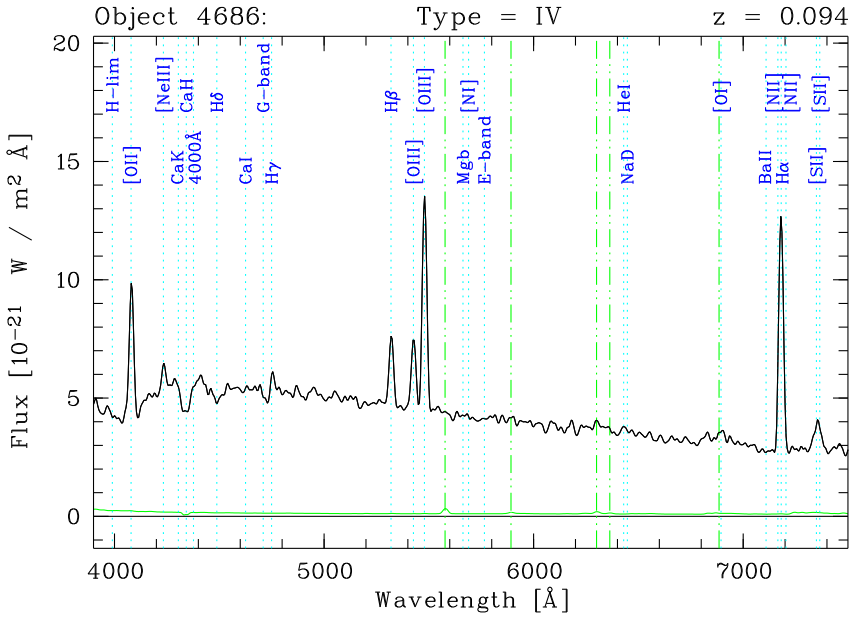

Figure 5.2: Spectrum of a typical low-redshift starburst galaxy which is dominated by emission lines like [O II]$\lambda\lambda$ 3726, 3729, [O III]$\lambda\lambda$ 4959, 5007, Hβ and Hα. The spectral lines are marked by cyan dotted lines and blue labels. The green dash-dotted lines indicate the positions of removed night sky lines. In increasing order these are [O I]λ 5577, Na I D, [O I]$\lambda\lambda$ 6300, 6364), B band and A band. The diagram also shows the error function (green solid line) which indicates the noise level. At the top of the digram identification number, spectral type and redshift of the displayed spectrum are shown (see Appendix C). Further informations to the representation can be found in Appendix D.

enough (see Fig. 5.3). Of course, this may reduce the precision of line centre measurements. Thus, it is sometimes indispensable to use model spectra or empirical templates to achieve sufficiently accurate redshifts (see Section 5.4).

Spectral lines in the rest-frame UV

At high redshifts UV lines are shifted into the optical wavelength range (Fig. 5.4). The UV is marked by numerous lines which mainly occur in absorption. In part these lines can be very strong. Especially Lyα (the most powerful line at all) shows such striking features (in emission as well as absorption, see Section 7.2) that redshift identifications are also possible regarding low S/N spectra. However, the high density of prominent lines implies a high frequency of blends as well. Actually the great majority of strong UV lines is significantly blended, although the line separation increases proportional to $(z+1)$. Blends can consist of related lines of the same ion, like Si IV$\lambda\lambda$ 1394, 1403 and C IV$\lambda\lambda$ 1548, 1551, or lines of different ions accidentally superimposed, like O Iλ 1302 and Si IIλ 1304 (both lines are composed of further components). More examples are shown in Fig. 5.4 and Table B.1. The high frequency of blends significantly reduces the number of usable lines for the redshift derivation (*not* the redshift identifica-

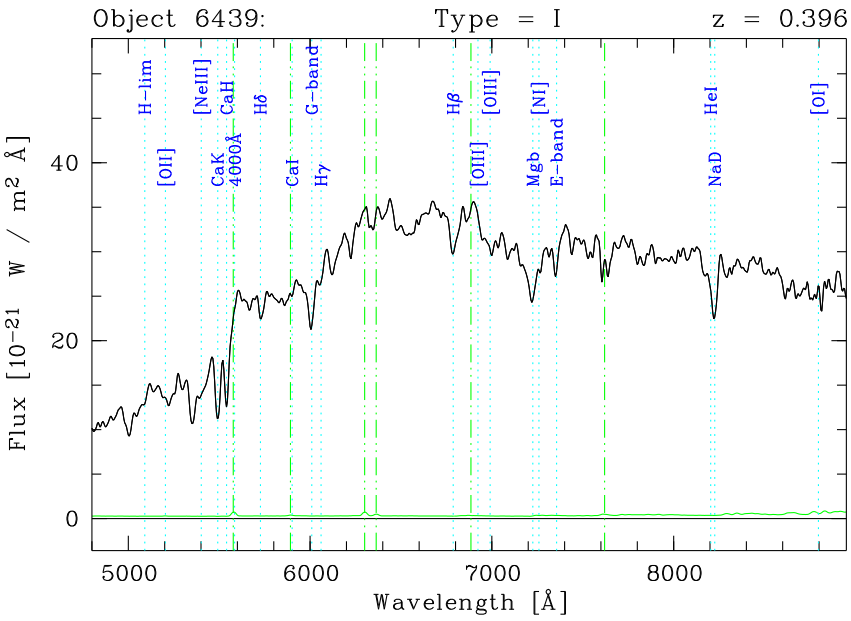

Figure 5.3: Spectrum of a typical low-redshift elliptical galaxy which is dominated by absorption lines like Ca II H & K (connected to the 4000 Å break), G band, Mg I band and Na I D. Representation details are described in Appendix D.

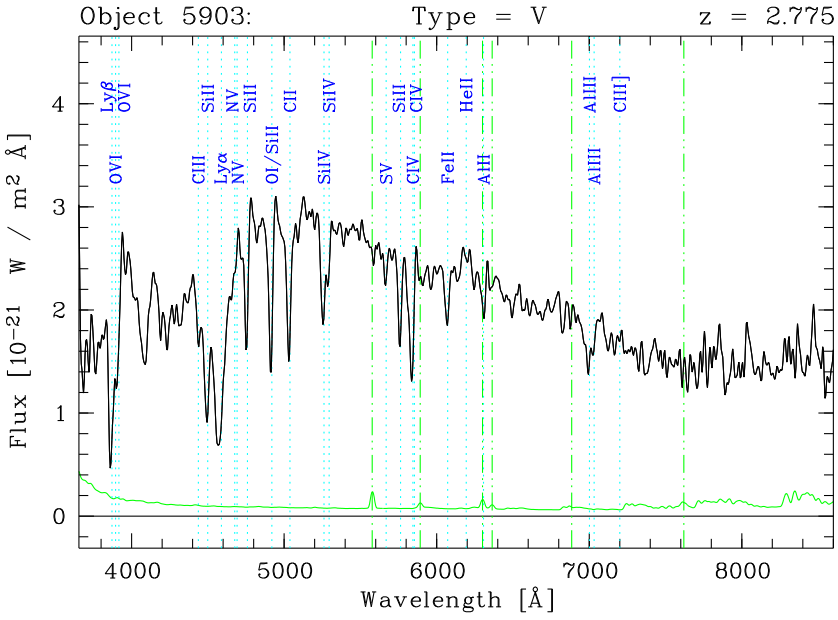

Figure 5.4: Spectrum of a typical high-redshift starburst galaxy (Lyman-break galaxy) which is dominated by numerous (blue-shifted) absorption lines like Lyα, Si IV$\lambda\lambda$ 1394, 1403, C IV$\lambda\lambda$ 1548, 1551. Lyα represents the most conspicuous feature at all and indicates in some spectra of high-redshift galaxies a significant emission component. Representation details are described in Appendix D.

tion).

The situation is getting more complicated by the tendency that UV absorption lines appear blue shifted up to several 100 km/s (compare Legrand et al. 1997, Kunth et al. 1998, Pettini et al. 2000). In part this profile is overlapped by an unshifted emission component which causes a so-called P Cygni profile (e.g. N V$\lambda\lambda$ 1239, 1242 or Mg II$\lambda\lambda$ 2796, 2803, see also Table B.1). The occurrence of such profiles can mainly be explained by outflows. In case of interstellar absorption lines (e.g. lines of [Si II], [O I] and [C II]) large-scale outflows can be caused by starbursts, that is a massive burst of star formation affecting a great deal of the galaxy. Regarding this scenario, the outflows are powered by strong winds of hot stars and a high rate of supernovae. Now, it is unlikely that every outflow points in the direction of the observer. Relative symmetrical outflow characteristics should rather be the case. The effective blue shift of spectral lines can be realized by the limitation that only material in front of the continuum sources, that is the stars, can contribute to the absorption.

A further source of blue shifted absorption components are radiation forced hot star winds which can reach velocities of 1000 km and more. Here, the preference of negative radial velocities is given by the limitation that the absorption of photospheric radiation can only occur in front of the star. This restriction is not valid regarding emission by circumstellar matter ($\rightarrow$ dense wind). This leads to a rather unshifted emission component which forms a P Cygni profile together with the blue shifted absorption. Examples of 'wind lines' are Si IV$\lambda\lambda$ 1394, 1403, C IV$\lambda\lambda$ 1548, 1551 (see Section 7.3) and Mg II$\lambda\lambda$ 2796, 2803.

In view of the frequent occurrence of blue shifted absorption components, the question arises how accurate redshifts can be derived using UV lines? In principle, the best way is to use spectral lines which are relatively unaffected by the effects described above. This mainly concerns emission lines, like He IIλ 1641 or C III]$\lambda\lambda$ 1907, 1909, and lines which are mainly originate in stellar photospheres, like C IIIλ 1176 or S Vλ 1502. A great disadvantage of these lines (particularly of the photospheric lines) is their weakness, so that often measurements in spectra of lower S/N cannot be carried out. Under these circumstances, the centres of all usable lines (see above) can be measured. Then, the average values of the one to three 'reddest' lines can be taken as relevant redshift assuming that the result is realistic. In practice, this was done in order to derive first estimates of the redshifts of high-redshift galaxies accepting uncertainties in redshift up to several 10^{-3}.

Line shifts

In order to illustrate typical shifts of various lines in relation to the rest wavelength, the redshift measurements via line centreing of each line can be compared with the final redshifts derived by spectral templates (see following Sections). If the shifts are calculated using the data of all analysed spectra (galaxies with known redshifts) representative line shifts can be obtained. Table 5.1 shows the result of such an investigation. The high blue shifts of the interstellar absorption lines in the UV, like the [C II], [Si II] and [Fe II] lines, are most conspicuous. This confirms the assumption that these lines are not suited for the

Table 5.1: Average deviations of line centres from rest wavelengths estimated by the comparison of redshifts determined by line centreing with the final redshifts derived by use of spectral templates. Altogether 258 galaxy spectra with certain redshift were used for the average calculations. The values are shown for 23 spectral lines suitable for the line centreing approach. The prominent Si IV$\lambda\lambda$ 1394, 1403, C IV$\lambda\lambda$ 1548, 1551 and Mg II$\lambda\lambda$ 2796, 2803 were not taken into account, because their very complex line profiles do not allow the derivation of reasonable line centres. In case of the also very complex Lyα profile possible emission components were considered only. The columns have the following meaning: λ = rest wavelength in Å, Line/Ion = line name or label of the ion (see Appendix B), n = frequency of measurement in % (258 $\Leftrightarrow$ 100%), $\Delta\lambda$ = average line shift and error in Å (rest-frame), σ_λ = uncertainty of a single line shift measurement in Å (rest-frame), Δz = average redshift deviation and error in 10^{-4} and σ_z = uncertainty of a single measurement of the redshift deviation. The shown values of each line are linked by the relations $\Delta z/(z+1) = \Delta\lambda/\lambda$, $\sigma_z/(z+1) = \sigma_\lambda/\lambda$, $\mathrm{ERR}(\Delta\lambda) = \sigma_\lambda/\sqrt{N}$, $\mathrm{ERR}(\Delta z) = \sigma_z/\sqrt{N}$ and $n = 100N/258$. Finally, spectral lines indicating deviations of $3\,\sigma$ significance and more are marked by blue colour in case of negative shifts and by red colour in case of positive shifts.

λ [Å]	Line/Ion	n [%]	$\Delta\lambda$ [Å]	σ_λ [Å]	$\Delta z/(z+1)$ [10^{-4}]	$\sigma_z/(z+1)$ [10^{-4}]
1025.7	Lyβ	9	-1.2 ± 0.3	1.2	-11.2 ± 2.5	12.0
1215.7	Lyα	17	0.9 ± 0.2	1.1	7.7 ± 1.4	9.3
1260.9	Si II	25	-1.3 ± 0.2	1.3	-10.5 ± 1.2	10.0
1303.3	O I/Si II	26	-1.6 ± 0.1	1.1	-12.3 ± 1.1	8.8
1334.7	C II	26	-1.1 ± 0.2	1.3	-8.2 ± 1.2	9.6
1501.8	S V	8	-0.6 ± 0.3	1.2	-4.2 ± 1.8	8.2
1526.7	Si II	23	-0.3 ± 0.1	1.1	-2.0 ± 0.9	6.9
1608.5	Fe II	26	-0.9 ± 0.2	1.7	-5.4 ± 1.3	10.9
1640.7	He II	16	-0.1 ± 0.3	1.8	-0.9 ± 1.7	10.9
1670.8	Al II	23	-0.1 ± 0.2	1.3	-0.6 ± 1.0	8.1
1907.5	C III]	19	-0.4 ± 0.2	1.5	-1.9 ± 1.2	8.1
2326.0	C II]	15	-0.5 ± 0.3	1.8	-2.1 ± 1.2	7.7
2344.2	Fe II	21	-1.1 ± 0.3	2.1	-4.6 ± 1.2	8.8
3727.5	[O II]	56	0.2 ± 0.1	1.0	0.6 ± 0.2	2.8
3868.8	[Ne III]	27	-0.4 ± 0.3	2.1	-1.1 ± 0.7	5.6
3933.7	Ca K	33	0.2 ± 0.3	2.9	0.5 ± 0.8	7.3
3968.5	Ca H	38	0.4 ± 0.3	2.9	1.1 ± 0.7	7.2
4101.7	Hδ	21	0.2 ± 0.4	2.9	0.5 ± 1.0	7.1
4340.5	Hγ	11	0.3 ± 0.4	2.4	0.7 ± 1.0	5.4
4861.3	Hβ	28	-0.3 ± 0.4	3.1	-0.5 ± 0.7	6.3
4958.9	[O III]	15	0.2 ± 0.2	1.5	0.4 ± 0.5	3.0
5006.9	[O III]	21	0.4 ± 0.3	2.1	0.7 ± 0.6	4.2
6562.8	Hα	14	-0.5 ± 0.3	1.8	-0.7 ± 0.5	2.8

derivation of redshifts. Nevertheless, not all UV lines are shifted in the same manner. For instance, in the reference system (defined by the final redshifts) the shift of Al IIλ1671 is almost zero. The blue shift of [Si II]λ1527 is quite low as well. Therefore, these lines are the main columns of the redshift determination of high-redshift galaxies together with the emission lines (He II and C III]). On the other hand, there is only one line with a significant shift towards the red, namely the emission component of Lyα (compare Section 7.2). This shift can be explained by absorption components on the blue side of the line (P Cygni profile) which results in an apparent shift of the emission towards longer wavelengths. The redshift derivation via Lyα can become essentially for Lyα emission galaxies with a hardly detectable continuum. The derived redshifts cannot be very accurate, since the composition of Lyα and the consequent line shift remain uncertain. At higher wavelengths (optical rest-frame) the redshift deviations (if present at all) are quite low (since $\Delta z \propto 1/\lambda$), so that an accurate redshift derivation using several (emission) lines is a simple task, as already stated above.

Redshift derivation of low resolution spectra by line fitting suffers from line blending. Especially in the UV an accurate redshift determination is complicated by the frequent occurrence of blue shifted absorption lines or P Cygni profiles. Nevertheless, redshift measurements on the small number of suitable lines can provide a good first estimate. Hence, the resulting redshifts can be used to create spectral templates (see Section 5.4) for an improved redshift determination (see Section 5.5). The great advantage of such an approach is that the uncertainties of single measurements are reduced by the averaging of various spectra for the template construction. Consequently, the redshift derivation by line fitting represents an suitable first step to the determination of redshifts as precise as possible.

5.3 Definition of spectral types

In this section I describe the definition of a suitable spectral classification system for the FDF spectroscopic sample. I show that in case of a sample covering a large redshift range the classic Hubble system and representative spectra of local galaxies ($z \approx 0$) are not useful to classify the FDF galaxies. As suitable solution I discuss the application of empirical spectral types based on the shape of the spectral continua. This classification scheme can be obtained in a self-consistent way by adapting the system to the FDF spectroscopic sample itself. The section is completed by a discussion of spectra which are not covered by this system of five basic types.

Hubble types

Since the discovery of galaxies as distant star systems (Hubble 1924) various efforts were made to classify galaxies. However, the most prominent system represents the morphological classification scheme of Hubble himself. It is the so-called 'tuning fork' diagram which was extended and refined by de Vaucouleurs (1959) and Sandage (1961, 'Hubble Atlas of Galaxies'). Although in

the beginning the evolutionary connections between the individual types were misinterpreted ('early-type' and 'late-type' galaxies), today Hubble's system constitutes the standard classification scheme for galaxies. Roughly the system has the following categories:

Ellipticals (E): Spheroidal shape (tri-axial or rotational symmetric), no significant gas and dust content.

Lenticulars (S0, SB0): Dominant central spheroidal ('bulge'), base of a disk including gas and dust.

Spirals (Sa – Sd): Central bulge, flat disk with spiral arms consisting of gas, dust and young stars; from Sa to Sd: increase of the importance of the disk compared to the bulge and of the opening angle of the spiral arms.

Barred spirals (SBa – SBd): Similar as spirals, but showing a bar-shaped pattern (density wave) in the inner parts of the galaxy.

Irregular galaxies (S{B}m, I{B}m or Irr I): galaxies with a very weak disk or bulge, cloudy appearance, high gas and dust content.

Peculiar galaxies (Irr II): Untypical morphology not matching the classification scheme, frequently high gas and dust content (→ merging galaxies, starbursts).

Tendentiously the portion of gas, dust and young stellar populations increases from ellipticals ('early type') via spirals to irregular galaxies ('late type'). This suggests an increase of the star formation rate towards irregular galaxies.

The appearance of a galaxy spectrum mainly depends on the composition of the stellar populations, the amount of gas and dust and consequently the star formation activity and history. Thus, a suitable definition of spectral types classifying galaxies has to consider these parameters. In principle, the Hubble sequence can be used as pattern for the allocation of spectral types, since the classification scheme roughly depends on the star formation activity (Kennicutt 1998). Then, reference templates of the so defined spectral types can be derived by averaging various integrated galaxy spectra of each Hubble type. The basic spectra can be obtained by observing nearby galaxies with large apertures (see Kennicutt 1992 and Kinney et al. 1996).

However, the Hubble sequence is mainly a morphological classification scheme optimised for present-day galaxies. Thus, it is questionable whether galaxies at higher redshifts can reasonably be classified using Hubble types. Hence, it is evident that the galaxy population in the early universe (see Section 1.1) has looked very different from the galaxy population in the local universe. Consequently, a spectrum may resemble a certain spectral type, but the morphology of the galaxy may feature significant differences regarding the corresponding Hubble type. Furthermore, it is possible to obtain spectra which does not match any Hubble type template. In part this could taken into account by Kinney et al. (1996) implementing a series of spectra of nearby starburst galaxies. Then, just violent star formation should be occurred in the early universe much more frequently as today (see Section 1.1). A further problem is caused by the fact that

the classification of high-redshift galaxies spectra requires templates covering the rest-frame UV. Using nearby galaxy spectra this demands UV observations outside the atmosphere. Thus, up-to-date the number of UV galaxy spectra with sufficient high S/N is quite small (see Kinney et al. 1993).

Empirical spectral types

The discussion above has shown that the use of nearby galaxy spectra for the spectral classification of galaxies at higher redshift has some drawbacks. Therefore, spectra of high-redshift galaxies can directly be used for the definition of a suitable set of spectral types. In principle, such spectra can be taken from literature (see Section 1.3), but this would result in a very inhomogeneous sample of spectra which were obtained with various instrumental set-ups and object selection techniques. Therefore, it is questionable whether the so derived spectral templates could adequately represent the FDF spectroscopic sample. This suggests to use the present sample itself to define spectral types and derive reference templates. This provides the following advantages:

- The very homogeneous sample (same observational set-up for all spectra, see Section 3.2) facilitates the calculation of spectral templates (see Section 5.4) and thereafter the comparison of these templates with the individual spectra.
- The high number of spectra lying within a large redshift range (see Chapter 6) guarantees that representative spectral templates covering a broad wavelength range can be derived (see Section 5.4).
- The calculation of spectral templates (representing the spectral types) from the spectroscopic data allows to optimise the classification of the FORS Deep Field data in a self-consistent way.

Definition of a suitable spectral classification scheme

An important demand on a suitable spectral classification is that it has to work for low S/N spectra, that is, the scheme has to be sufficiently robust. Thus, a system which has several free parameters is not principally useful, since in case of low-quality spectra the risk of obtaining quite ambiguous results is high. Very different parameter combinations could lead to data fits of similar quality. Furthermore, in a strongly structured classification system the average number of objects per spectral type is small, so that the statistics can be insufficient to achieve representative templates. Moreover, high S/N templates cannot be expected, if the number of single spectra is small. Hence, an one-dimensional sequence consisting of five basic types was used. In this system the individual spectral types differ by the ratio of the UV flux to the flux in the optical. As initial templates for the allocation of the spectral types (iteration of zeroth order) semi-empirically SEDs applied to derive photometric redshifts (see Section 2.2) were used. Fig 5.5 shows *the* five SEDs which served as first basis for the definition of the spectral types. The classification essentially rests on the shape of the continuum. Line characteristics (strength and shape) did not played a

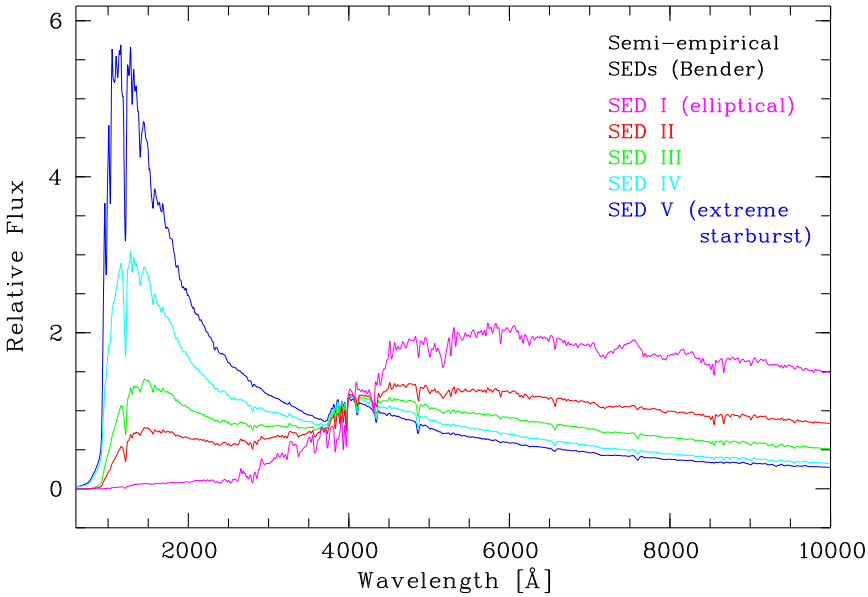

Figure 5.5: Semi-empirical spectral energy distributions (see Section 2.2) used for the initial classification of the FDF spectra. The 5 types (I – V) mainly differ in the ratio of the UV flux to the flux in the optical. SED I resembles spectra of elliptical and lenticular galaxies. SED II and SED III are rather typical of spiral galaxies. SED IV and SED V are representative of starburst galaxies.

greater role, since line profiles are distinctly more variable from galaxy to galaxy than the continuum shape. The use of line intensities as primary classification characteristic would make the spectral classes more 'diffuse'.

Astrophysically, the differences between the SEDs are mainly caused by the amount of the contribution of young hot stars (bright in the UV) to the total stellar population. Therefore, the classification scheme is primarily an indicator of the star formation activity in the galaxy (because of the short life time of hot stars). However, one has to be careful in interpreting the spectral types, since the type sequence is only one-dimensional, so that the impact of different properties on the template shape has to be taken into account. For instance, in the UV the amount of dust extinction (compare Section 4.7) can become very important for the shape of the continuum. Consequently, this effect can veil the true portion of young stars and the strength of the star formation activity. Hence, in ambiguous cases the spectral type was derived from the redder visible part of the spectrum in order to minimise the influence of dust extinction on the derivation of spectral types. The individual properties of the spectral types will be discussed in Chapter 6 on the basis of the final templates which will be presented in Section 5.4.

Spectra not covered by the classification system

In the end of this section I deal with objects which cannot be classified using the types described above. The objects concerned are extreme Lyα emission

galaxies, quasars and stars.

- **Extreme Lyα emission galaxies:** There are high-redshift galaxies which indicate a very strong Lyα emission (see Section 6.2 and 7.2). In principle, the continuum of these galaxies is crucial for the classification as in any other case. However, these galaxies are often very faint, so that the continuum shape can hardly be measured. Then, the identification and the redshift derivation mostly depends on the Lyα line. Since in such cases the use of the standard types (I – V) does not work, a further spectral type (VI) characterising Lyα bright galaxies (LABs) was introduced. Type VI should not be understood as an equivalent spectral type, since this type is defined by a profile of a spectral line and not by the shape of the continuum. Therefore, LABs were characterised as far as possible by two spectral types, type VI and one of the basic types.

- **Qusars:** Quasars (QSOs), or more generally galaxies dominated by an active galactic nucleus (AGN), may have spectra completely different from spectra of ordinary galaxies. The main energy source of quasars is the release of gravitational energy of matter falling into a massive black hole and not fusion processes in stars. Hence quasar spectra are often dominated by strong, broad emission lines (see Section 6.2) emerging in the so-called broad-line region (BLR) surrounding the black hole directly (e.g. Osterbrock 1989). Since quasar spectra are very variable, but rare, it is not practicable to construct quasar templates from the present data. For that reason, a systematic classification of quasar spectra was not carried out. For the redshift derivation of the conspicuous QSO spectra visual line measurements suffices (see Section 5.2), since broad, complex profiles do not allow a very accurate derivation anyway.

- **Stars:** In case of stars the construction of spectral templates is not necessary, since no redshifts have to be derived. The star spectra can be classified using the system of Morgan and Keenan (Morgan et al. 1976, Keenan & Mc Neil 1976) extended by very cool objects (Martín et al. 1999). For the identification and classification the star spectra can be compared with reference spectra from literature (e.g. Pickles 1985). The reliability of the identification of a star can be tested by comparison of the object's spatial intensity profile (see Section 1.4) with the point-spread function. Since star spectra are only a by-product of the spectroscopic survey the determination of accurate types was not attempted. Therefore, the classification was restricted to the determination of a rough spectral type like G, K, M or L.

5.4 Template spectra

In this section I discuss the construction of spectral templates using the FDF spectroscopic data. Spectral templates are very useful in order to derive high-quality redshifts and spectral types (see Section 5.5). Furthermore, templates form representative mean spectra of spectroscopic subsamples (see Section 7.1)

allowing the analysis of weak spectral features (because of the improved S/N by averaging). Therefore, such mean spectra may provide very valuable informations not accessible in case of using single spectra.

Before I describe the details of the template calculation I start with the discussion of some preparatory steps, in fact the determination of initial redshifts and spectral types, the masking of spectra in order to avoid contributions from strong defects and the shift of the spectra to the rest-frame.

Conditions for the calculation of spectral templates

For the purpose to derive redshifts and spectral types the templates have to be constructed for each spectral class separately using data of all redshift ranges. The optimisation of the results requires the alternating repetition of the derivation of redshifts and spectral types *and* the calculation of templates (self-consistent iterative approach). This procedure is necessary, since all analysis steps fall back on the same data. Thus, optimum spectral templates can be obtained after a few iterations only.

To start the procedure, independently derived initial redshifts and spectral types are needed. Suitable redshifts are derived by line centre measurements (see Section 5.2). A provisionally spectral classification is determined by the use of semi-empirical templates derived from data of the HDF-N (see Section 5.3). Consequently, the calculation of spectral templates can be carried out.

Masking of spectra

The optimal computation of mean spectra representative of a spectroscopic subsample requires the maximisation of the spectral information, that is the true signal-to-noise ratio. This can be realized by averaging wavelength regions which are mainly affected by statistical errors. The inclusion of wavelength ranges, which are obviously contaminated by systematic errors like residuals of strong night sky lines (see Fig. 4.13), can reduce the quality of the final spectra significantly. This is a serious problem, since in the rest-frame strong residuals may principally occur at every wavelength (because of the consideration of galaxies at various redshifts). Hence, affected wavelength ranges have to be expelled from the calculation of the mean spectrum.

The masking of the spectra can be carried out automatically using the signal-to-noise ratio as a decision criterion for the wavelength rejection. According to (4.6) the S/N is determined by the ratio $f(\lambda)/\Delta f(\lambda)$ where $f(\lambda)$ is the object flux and $\Delta f(\lambda)$ indicates the noise level. The measured object and error flux can significantly differ from the true value due to systematic errors (see Section 4.4 and 4.5). Therefore, it is necessary to minimise these effects in order to obtain reliable results.

In case of the object spectrum the flux was averaged over several 100 Å in order to cancel out small-scale deviations. In the near IR faint spectra are strongly affected by emission of OH bands (see Fig. 4.6). Hence, the object flux within these bands was estimated by the average values measured in adjacent ranges almost free of (strong) OH lines (→ atmospheric windows). Especially

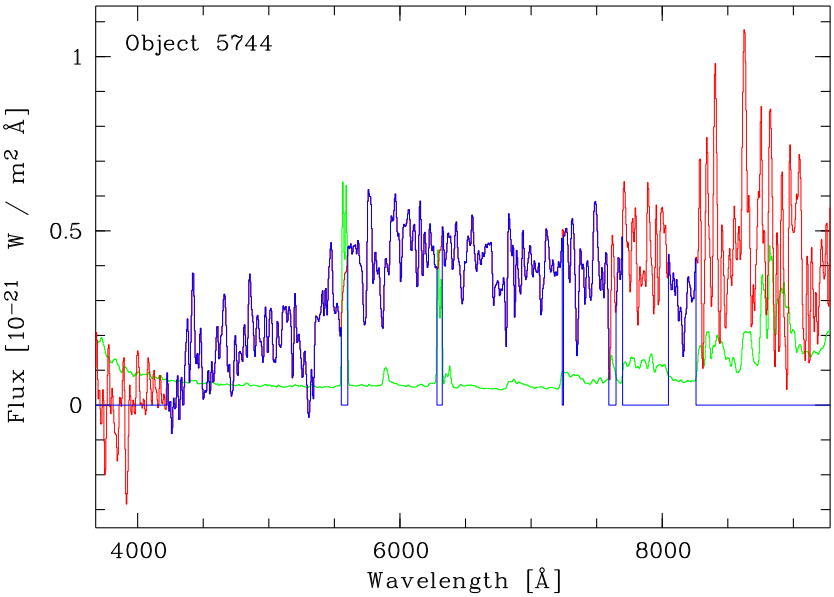

Figure 5.6: Example of the masking of spectra as preparation for the calculation of mean spectra. The accepted parts of the noisy spectrum of the faint high-redshift galaxy 5744 are shown in blue whereas the removed parts are shown in red. The shape of the noise function (green solid line; including the effects of sky line residuals) was decisive of the exclusion of wavelength ranges.

the window which roughly ranges from 8080 to 8255 Å was very important in this context. The averaging over large wavelength ranges has the disadvantage that potential emission lines showing a distinctly higher S/N than the continuum cannot be taken into account in an adequate way. In order to 'recover' such lines for the template construction the concerned wavelength ranges were considered if a certain strength of the emission lines could be expected by the spectral type (see Section 5.3). For instance, [O III]$\lambda\lambda$ 4959, 5007 were taken into account in the event of spectral type IV and V.

$\Delta f(\lambda)$ represents the error function (see Section 4.3 and 4.6) which indicates the level of the statistical noise. As this curve does not consider systematic errors like residuals of sky lines, the use of the error function is reduced within the critical wavelength regions. Hence, in each case the curve was multiplied by the average correction function for variable systematic errors shown in Fig. 4.13. Since the correction function could be calculated as average of a large part of the spectroscopic sample only, individual deviations could not be taken into account. But this does not seem to affect the masking significantly.

Fig. 5.6 shows the resulting masked spectrum of object 5744 (blue). As expected the rejected wavelength regions (red) are directly linked to ranges with strong sky lines, that is ranges with a high noise level (green). The masked spectra mostly indicates results of a similar quality as in the example. Therefore, the described approach is principally suitable to separate useful from defective data.

Shift to the rest-frame

A further preparatory step for the template calculation is the shift of the spectra from observer's frame to the rest-frame. According to (1.2) this is realized by dividing the wavelengths by the factor of $(z+1)$. This causes a corresponding increase of the flux level owing to flux conversation. The alteration of the wavelength scale requires to rebin the spectra. In order to loose no spectral information a bin size of 1 Å was selected (in contrast to 5 Å for unshifted spectra). This means particularly for low redshifts an amplification of the oversampling. Hence, the correction of the error functions for smoothing effects (see Section 4.3 and 4.6) was not necessary.

Calculation of templates

For the calculation of the templates spectra of different shape and wavelength coverage have to be added. This give rise to two big difficulties.

(1) The spectra have to be averaged in a way that the resulting line strengths will be representative of the respective subsample of galaxies of a certain spectral type.

(2) The shape of the template SEDs has to be derived in a reliable way, although the templates will cover a wavelength range distinctly larger than the usable wavelength domains of the single spectra.

First, I turn to the treatment of the line strength problem. The most robust way to measure a line strength represents the equivalent width (EW, see equation 7.2) which gives the integral of the line flux normalised on the continuum flux. This measure is principally independent of the instrumental set-up and does not need an accurate flux calibration. This suggests that a suitable averaging procedure should conserve the equivalent width. That is, the EW of the mean spectrum should equal the mean of the EW of the single spectra. This requires that the continuum of the spectra is normalised to one. Therefore, the spectra have to be divided in a continuum and a line part according to

$$f(\lambda) = f_{\mathrm{c}}(\lambda) f_{\mathrm{l}}(\lambda). \tag{5.1}$$

The continuum can roughly be determined by a large median filter of 100 Å width. The filter cancels out all small-scale fluctuations like spectral lines, so that the smoothed spectrum approximates the continuum. The fitting approach will show good results (deviations $< 5\,\%$) as long as the typical scale of the change of the continuum is larger than the width of the median filter. This condition is met in almost the whole wavelength range. Only at wavelengths smaller than 1400 Å suitable continuum fits are difficult to obtain, since there numerous strong lines (above all Lyα) 'destroy' the continuum (see Fig. 5.4). But at least for the wavelengths greater than Lyα (deviations mostly $< 20\,\%$) this does not mean a significant loss of accuracy, since the main task of the continuum fit is the derivation of the 'right' amplitude of the spectral fluctuations (spectral lines) in relation to the continuum. That is, for the averaging

only the relative continuum fit errors are important. In practice, the errors are even smaller, since usually spectra of similar shape are averaged. Therefore, the systematic errors of the continuum fit of different spectra are similar. Thus, the effective error should be given by the relative spectrum-to-spectrum variations of the apparent continuum shape. 'Red-wards' of Lyα the amount of this error should not be higher than a few percent which is small enough.

Now, continua and spectral fluctuations (lines) of the selected spectra can separately be averaged. And in the end, the product of both the mean spectra will result in the final templates according to

$$F(\lambda) = F_{\rm c}(\lambda) F_{\rm l}(\lambda). \tag{5.2}$$

The averaging of the normalised spectral fluctuations can be carry out calculating a simple mean

$$F_{\rm l}(\lambda) = \frac{1}{M(\lambda)} \sum_{i=1}^{n} f_{{\rm l},i}^{\rm m}(\lambda) \tag{5.3}$$

where

$$M(\lambda) = \sum_{i=1}^{n} m_i(\lambda) \tag{5.4}$$

is the sum of the mask functions $m_i(\lambda)$ (values either 0 or 1) of all n spectra and

$$f_{{\rm l},i}^{\rm m}(\lambda) = f_{{\rm l},i}(\lambda)\, m_i(\lambda) = \frac{f_i(\lambda)}{f_{{\rm c},i}(\lambda)}\, m_i(\lambda) \tag{5.5}$$

is the masked line spectrum in the rest-frame.

The averaging of the continua can be realized using the following recipe:

- First, the selected spectra are sorted by redshift in order to maximise the size of the overlapping wavelength range of consecutively added spectra.
- Next, the averaging procedure can be started with the lowest or highest redshift. Then, the averaging can be carried out step-by-step using

  $$F_{{\rm c},i}(\lambda) = F_{{\rm c},i-1}(\lambda) + \frac{f_{{\rm c},i}^{\rm m}(\lambda)}{c_i} \tag{5.6}$$

  with $F_{{\rm c},0}(\lambda) = 0$.

  $$f_{{\rm c},i}^{\rm m}(\lambda) = f_{{\rm c},i}(\lambda)\, m_i(\lambda) \tag{5.7}$$

  represents the masked continuum in the rest-frame. Moreover,

  $$c_i = \frac{\int_{F_{{\rm c},i-1}(\lambda)\neq 0} \frac{M_{i-1}(\lambda)\, f_{{\rm c},i}^{\rm m}}{F_{{\rm c},i-1}(\lambda)}\, {\rm d}\lambda}{\int_{F_{{\rm c},i-1}(\lambda)\neq 0} {\rm d}\lambda} \tag{5.8}$$

  where

  $$M_i(\lambda) = \sum_{j=0}^{i} m_j(\lambda), \qquad m_0(\lambda) = 0. \tag{5.9}$$

  c_i is the effective flux correction factor for the mutual adaption of the weights of $f_{{\rm c},i}^{\rm m}(\lambda)$ and $F_{{\rm c},i}(\lambda)$. In maximum the ratio of the weighting factors reaches $1/(i-1)$.

- Then, the average continuum can be calculated by

$$F_{\mathrm{c}}(\lambda) = \frac{1}{M(\lambda)} F_{\mathrm{c},n}(\lambda). \tag{5.10}$$

using (5.4). Correspondingly, the average errors result in

$$\Delta F_{\mathrm{c},i}(\lambda) = \sqrt{\left(\Delta F_{\mathrm{c},i-1}(\lambda)\right)^2 + \left(\frac{\Delta f^{\mathrm{m}}_{\mathrm{c},i}(\lambda)}{c_i}\right)^2} \tag{5.11}$$

assuming $\Delta c_i = 0$ and

$$\Delta F_{\mathrm{c}}(\lambda) = \frac{1}{M(\lambda)} \Delta F_{\mathrm{c},n}(\lambda). \tag{5.12}$$

The calculations should be performed in both redshift directions. Hence, a measure of the accuracy of this approach can be obtained by measuring the deviations between both results. In case of the spectral type templates (see below) the relative errors are smaller than 5 %, which shows the reliability of the approach.

- Thus, the final templates can be calculated by

$$F(\lambda) = \frac{1}{2}\left(F_{\mathrm{c},\uparrow}(\lambda) + F_{\mathrm{c},\downarrow}(\lambda)\right) F_{\mathrm{l}}(\lambda) \tag{5.13}$$

modifying (5.2).

Properties of the resulting templates

Fig. 5.7 shows the resulting templates for the individual spectral types defined in Section 5.3. The shape of the mean spectra clearly reflects the main classification criterion, namely the ratio of the UV and the optical flux. Since this criterion mainly indicates the star formation activity, the nebular emission line intensities of the templates increase (as the UV flux) from SED I (no emission) to SED V (numerous strong emission lines). Thus, the present templates show a reasonable development of the spectral properties from early-type to late-type galaxies and should be well suited to derive redshifts and spectral types. In this respect, the great wavelength extension of the SEDs is particularly noteworthy. For instance, SED V ranges from the Lyman limit to Hα and beyond. This is a lot in relation to the contributing wavelength range of single galaxy spectra to the mean spectrum which is frequently more narrow than 2000 Å. Fig. 5.8 shows $M(\lambda)$ (5.4), that is the wavelength dependent number of added spectra for the individual templates. The distributions indicate that the best statistics are achieved in the central wavelength ranges at around 4000 Å (low-redshift galaxies) and 1500 Å (high-redshift galaxies) of the templates (up to $\gtrapprox 30$ spectra in case of SED IV and V) whereas the marginal portions consists of a few spectra only. This means that the representativity of the SEDs is reduced in the wavelength regions beyond Hα and below Lyα. A positive property of the present templates is the nearly constant spectral resolution $\lambda/\Delta\lambda$ over

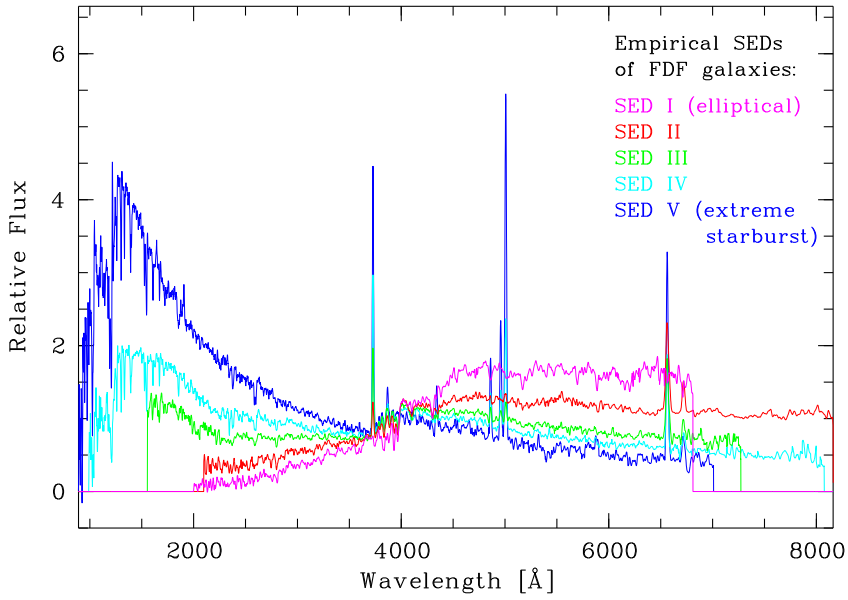

Figure 5.7: Empirical templates of the FDF spectroscopic sample. The five SEDs are marked by different colours (see legend inside the diagram). The templates were normalised in the wavelength range between 3500 and 4500 Å. The widths of unresolved lines decrease towards shorter wavelengths.

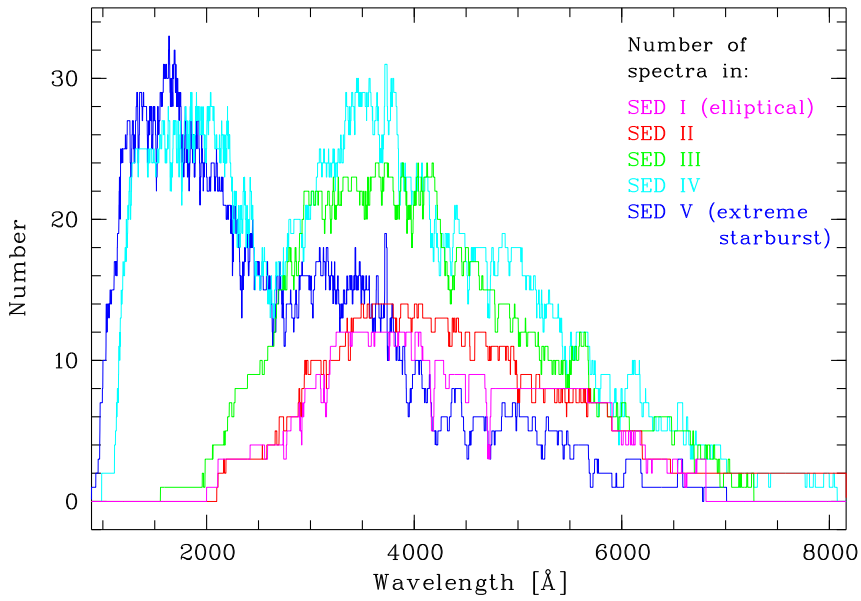

Figure 5.8: Wavelength dependent number of spectra which were used to the calculation of the templates shown in Fig. 5.4. The colour code is the same as in case of the representation of the SEDs.

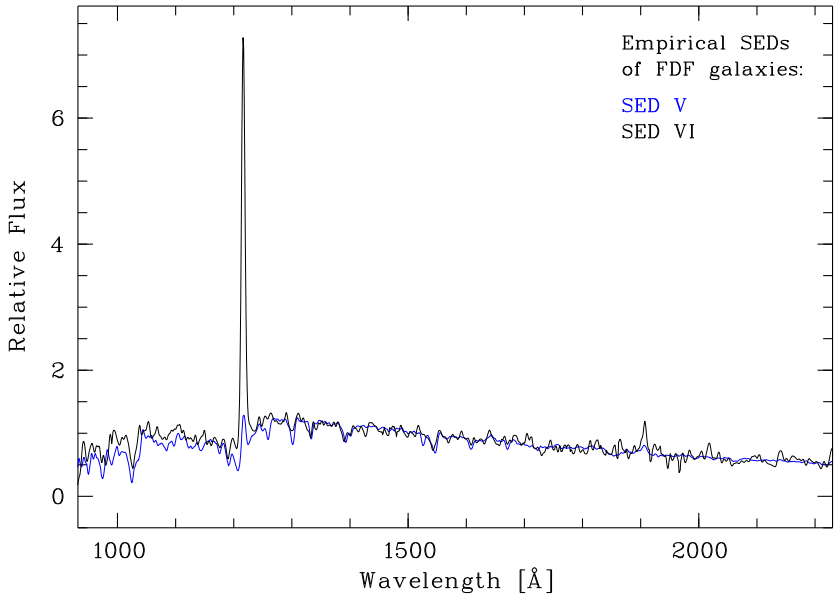

Figure 5.9: Comparison of the template for extreme Lyα emission galaxies (SED VI) with the template of the basic spectral type V (see Fig. 5.4). Both spectra show similar continua. The Lyα intensities are naturally very different.

the whole wavelength range. Thus, the template-based redshift derivation (see Section 5.5) can be carried out comparing spectra of similar resolution. This a big advantage of the self-consistent redshift determination approach.

In addition to the SEDs discussed above a supplementary template was constructed for the redshift derivation of strong Lyα emitting galaxies (see Section 5.3). Fig 5.9 shows SED VI in comparison with SED V. Both templates have obviously very similar continua. The differences are particularly caused by different line strengths and profiles. Above all, this naturally concerns Lyα. In context of the five-type classification system Lyα bright galaxies should belong to continuum class V with a high probability, whereas the use of the special template VI should clearly improve the redshift derivation of such objects.

In summary, the empirical templates consisting of FDF spectra form an excellent basis for the derivation of redshifts and spectral types. However, if one wants to investigate the properties of the templates in detail, one has to be aware of that the template spectra are composed of spectra of galaxies at different redshifts. Therefore, the templates may consist of galaxies showing very different properties. Thus, the templates cannot be mean spectra of the sample galaxies in the classical sense. Thus, one has to be careful with regard to comparing spectral features located in very different wavelength regions like lines in the UV and the optical. Nevertheless, I will come back to the discussion of the spectral templates in Section 7.1.

5.5 The cross-correlation method

As shown in Section 5.2 redshifts can be derived by line centre measurements. This is essentially a manual method, since a rough redshift has to be determined by visual line identification. Furthermore, the measurement of each line causes special problems, since effects like line blending, blue-shifted absorption components and other complicating features have to be taken into account. Thus, individual line measurements do not constitute an effective tool regarding the redshift analysis of large spectroscopic data samples. Particularly, for low S/N spectra the method is scarcely suited to derive reliable redshifts. The last section (5.4) has shown that excellent template spectra can be derived from the FDF spectroscopic data. This suggests to use these SEDs for a refined redshift derivation method comparing the templates with the spectra at unknown redshift. The great advantage of such an approach is that the entire spectral information can be exploited to derive the redshifts instead of the profiles of a couple of prominent lines alone. Moreover, the redshift analysis based on templates can be carried out automatically which allows the processing of large data samples in a reasonable time.

The whole procedure which was applied to the FDF spectroscopic data is described in the following. The algorithm is essentially based on the so-called 'cross-correlation function' $C(z)$ which represents a redshift dependent measure of the correspondence of object and template spectrum. Furthermore, the significance of the redshifts derived by $C(z)$ is estimated by a χ^2-like test. The significance test uses the whole spectral information of both spectra, whereas the cross-correlation method only exploits the spectral fluctuations which include the spectral lines. In summary, the procedure works as follows:

(1) Preparation of template and object spectra for redshift derivation by masking of residuals, subtraction of the continuum and transformation of the linear to a logarithmic wavelength scale

(2) Calculation of the cross-correlation function $C_{\rm fluct}(z)$ considering spectral fluctuations only

(3) Determination of the highest cross-correlation peaks (up to 10 and in minimum 5 with $z > 1$)

(4) Significance test for the redshift values found deriving a $\sigma_{\rm min}$ from the comparison of object and template spectrum

(5) Derivation of an empirical significance parameter S

(6) Taking the redshift with the highest S

Now, I describe the details.

Calculation of the cross-correlation function

The extent of correspondence of two spectra $f_1(\lambda)$ and $f_2(\lambda)$ can be derived by measuring the cross-correlation C which can simply be defined by

$$C = \int_0^\infty f_1(\lambda)\, f_2(\lambda)\, \mathrm{d}\lambda\,. \tag{5.14}$$

In order to use the cross-correlation method to the determination of redshifts, (5.14) has to be customised to this application. In principle, the most likely redshift can be derived by computing C from the template $T(\lambda)$ and the individual galaxy spectrum $G(\lambda)$ for every reasonable redshift of $G(\lambda)$. Then, the highest value of C will indicate the optimum redshift. The calculation of each point of the cross-correlation requires 'de-redshifting' of $G(\lambda)$ by the division of the factor $(z+1)$ according to (1.2). Thus, λ and z do not change in the same way. This is not advantageous for an efficient realization of the cross-correlation calculation. It will be much better, if a linear shift in z also implies a linear shift in the wavelength variable. For that reason, the variable λ should be substituted by

$$x = \ln \lambda\,, \tag{5.15}$$

that is the natural logarithm of the wavelength. Using (5.15) the cross-correlation function (compare Simkin 1974 and Tonry & Davis 1979) can be written in the suitable form

$$C(z) = a \int_{-\infty}^\infty T(x)\, G(x+z)\, \mathrm{d}x\,. \tag{5.16}$$

where a is a scaling factor which ensures the comparability of different $C(z)$.

A promising implementation of the cross-correlation approach requires the suppression of all disturbing effects which may hamper the identification of the true redshift. In any case, the continua from T and G have to be subtracted. This is necessary, since continua cause additive contributions to the cross-correlation function according to (5.16). Therefore, the use of complete spectra leads to a strong underground in $C(z)$ probably much stronger than the searched cross-correlation peak. Hence, $C(z)$ would mainly be determined by the continua and not by the extent of correspondence of spectral features in T and G. In practice, the continuum can roughly be derived using a median filter as described in Section 5.4. Then, the smoothed spectrum can be subtracted from the original one. This leaves over the small-scale spectral fluctuations indicating spectral lines and noise.

Properties of the cross-correlation function

An example of a cross-correlation function $C_{\mathrm{fluct}}(z)$ comparing T_{fluct} and G_{fluct} is shown in Fig. 5.10. Here, a late-type galaxy at low redshift (object 4686, Fig. 5.2) was correlated with SED IV (see Fig. 5.7). The strong emission lines ([O II], [O III] and Hα) have caused a prominent global maximum indicating the redshift 0.0943. However, there are further significant peaks mainly emerging by false matches of different emission lines. But in the present case this does

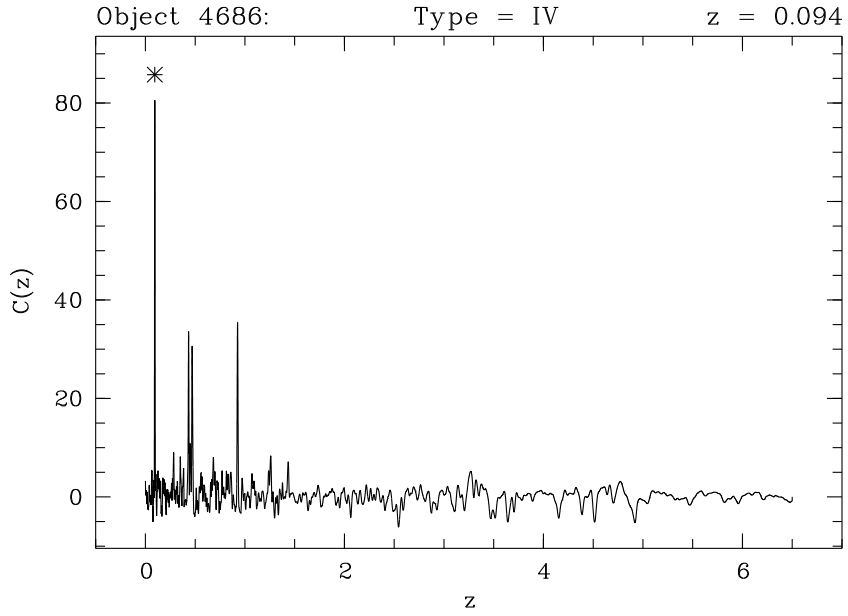

Figure 5.10: $C_{\mathrm{fluct}}(z)$ resulting from the cross-correlation of object spectrum 4686 (Fig. 5.2) and SED IV (see Fig. 5.7). The strong emission lines of object 4686 cause a maximum correlation peak at $z = 0.0943$ indicated by an asterisk.

not mean a problem for the redshift derivation. Nevertheless, at low signal-to-noise the identification of the 'right' peak may become a big problem. Especially residua of strong night sky lines (see Fig. 4.13) can lead to artificial peaks in the cross-correlation function. Thus, it is important to reduce such contaminations as far as possible. This is realized using the masking approach presented in Section 5.4. This means that wavelength regions which are strongly affected by residuals will be excluded from the further analysis. Hence, the number of peaks in the spectra and consequently the number of peaks in $C_{\mathrm{fluct}}(z)$ will be reduced. However, in case that an important emission line is located within a wavelength region affected by residuals (for instance within an OH band), it is advantageous to consider this range for the redshift derivation. Then, the influence of residuals on the cross-correlation function can be reduced by using a threshold-controlled median filter (see Section 4.4) which filters out the strongest peaks. This suggests to calculate redshifts twice. First, the redshift is derived avoiding affected wavelength ranges. And secondly, by means of filtered spectra the redshift is calculated without excluding larger wavelength ranges. Then, both results can be compared to achieve a higher significance and accuracy of z. Finally, in case that a redshift estimate is to be refined only, the restriction on narrow wavelength ranges can be useful, if the occurrence of a strong emission line can be expected (see Section 5.4).

Fig. 5.11 shows the cross-correlation function of a low S/N spectrum of a high-redshift galaxy (5744, see Fig. 5.6) and the template spectrum of type IV (Fig. 5.7). In contrast to the first example (Fig. 5.10), the highest peak (marked by a cross) does not represent the real redshift (indicated by an asterisk), al-

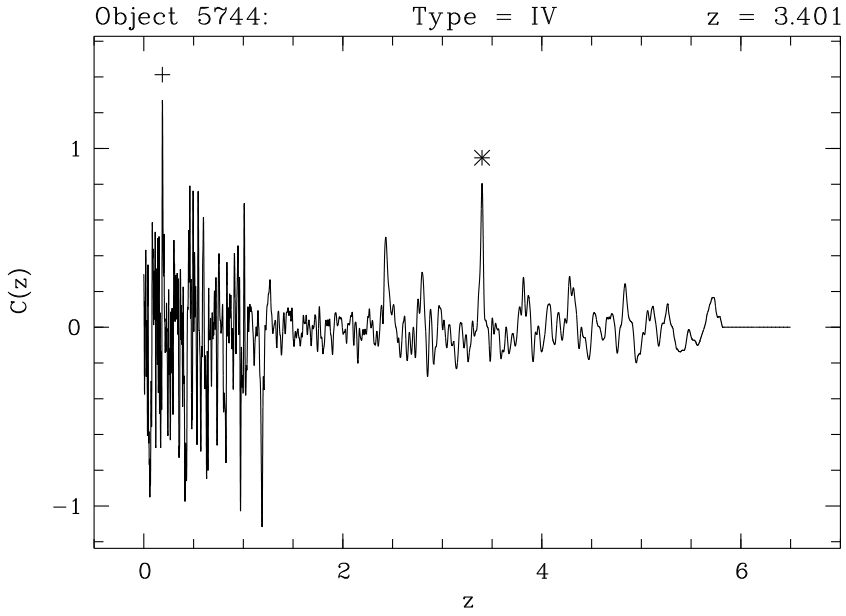

Figure 5.11: $C_{\mathrm{fluct}}(z)$ resulting from the cross-correlation of object spectrum 5744 (Fig. 5.10) and SED IV (see Fig. 5.7). The true correlation peak at $z = 3.401$ (asterisk) does not represent the global maximum (cross) due to the low S/N of the spectrum.

though the true redshift peak dominates the high-redshift domain. This can be explained by the possible strong positive correlation of a powerful emission line in the template and an 'emission-like' feature in the object spectrum easily caused by a strong noise peak or a moderate residual. In spectra of high-redshift galaxies showing rather weak absorption lines such an effect cannot be expected. Furthermore, the line profiles of UV lines (rest frame) can be vary a lot from galaxy to galaxy (see Section 5.2) which may further weaken the correlation. Thus, the maximum of $C_{\mathrm{fluct}}(z)$ may not indicate the true redshift, particularly in case of low S/N spectra dominated by absorption lines. Hence the cross-correlation method in its simple form is insufficient to derive reliable redshifts.

Significance test

For the cross-correlation in the previous form the information about the shape of the continuum was not used. Therefore, the redshift analysis procedure was extended by a complementary approach using the whole spectral information. This approach is based on the calculation of a normalised root mean square of the differences between the template and the object spectrum for a given redshift:

$$\sigma(x) = \frac{\left(\int_{G\neq 0,\, T\neq 0} \left(G(\lambda) - \frac{1}{x}\, T(\lambda)\right)^2 \mathrm{d}\lambda \int_{G\neq 0,\, T\neq 0} \mathrm{d}\lambda \right)^{1/2}}{\int_{G\neq 0,\, T\neq 0} G(\lambda)\, \mathrm{d}\lambda} \tag{5.17}$$

where the variable x is a scaling factor to the adaption of $T(\lambda)$ to $G(\lambda)$. The minimum of the function $\sigma(x)$ can be used as a further indicator for the extent of correspondence between the template and the object spectrum besides the height of the cross-correlation peak. In principle, the method can be applied as an independent opportunity to derive redshifts by dividing $G(\lambda_{\rm obs})$ by $(z+1)$ and calculating $\sigma_{\rm min}$. But this was not done, since the cross-correlation method constitutes the more accurate and faster way to derive redshifts.

In contrast, the σ calculation forms an excellent approach to check the reliability of the redshifts derived by the cross-correlation method due to the consideration of the continuum. Therefore, σ was calculated for a series of peaks of the cross-correlation function $C_{\rm fluct}(z)$. In practice, up to 10 redshifts were checked. Owing to the lower peak heights in the high-redshift range (due to the absence of strong emission lines in the spectra; see above) in minimum 5 of 10 peaks were taken from $z > 1$.

The σ values were not directly used to determine the 'best' redshift, instead a combined empirical significance parameter was used, which includes the peak height h of $C_{\rm fluct}(z)$ and the extent of the overlap region between object spectrum G and template spectrum T. The significance parameter S is defined as follows:

$$S = h^{\alpha}\left(\frac{1}{\sigma}\right)^{\beta}\left(\frac{N_{T\cap G}}{N_G}\right)^{\gamma} \tag{5.18}$$

where $N_{T\cap G}$ is the number of pixels where $T \neq 0$ *and* $G \neq 0$ and N_G is the number of pixels where $G \neq 0$. α, β and γ are weights which have to be determined empirically.

The form of (5.18) turned out to be the most effective one in identifying redshifts correctly. In fact, σ represents the dominant parameter which provides the most valuable information about the significance. However, the inclusion of the peak height h make sense, since especially in case of emission line galaxies with very weak continua (e.g. Lyα bright galaxies) indicating a pronounced h σ may reach unfavourably high values. The third parameter takes into account that the extent of the overlap region of object and template spectrum can vary a lot dependent on the redshift and the selected template (spectral type). This suggests that the correlation of the spectra in a small overlap region could accidentally become very high. This may turn the redshift derivation upside down. Therefore, the definition of S was preventively supplemented by the ratio described above. The empirical parameters α, β and γ were optimised by the analysis of a sample of galaxies with reliable redshifts (see Section 5.6). It has proved that $\alpha = 0.05$, $\beta = 1$ (fixed) and $\gamma = 2$ are suitable values. That is, S is mainly determined by the reciprocal σ. Only in case of strong correlation peaks or small overlap regions S will significantly be modified.

5.6 Final redshifts and spectral types

The cross-correlation method described in Section 5.5 represents a suitable tool to derive reliable and accurate redshifts. In order to obtain optimum results it is important to carry out the procedure several times using different templates

and versions of the input spectra. A suitable version of an object spectrum should be liberated from disturbing residuals and other systematic errors. On the other hand, one should avoid to remove prominent spectral features which are important for an accurate redshift derivation. As already mentioned in Section 5.5, just the masked spectra described in Section 5.4 and the defect-cleaned spectra explained in Section 4.4 are suitable for this job. Hence, the redshift derivation approach was carried out in minimum two times using both versions. This is a good opportunity to crosscheck the reliability of a cross-correlation peak.

Since the FDF galaxies show a variety of spectral shapes (see Section 6.2), different spectral templates have to be used to obtain high-quality redshifts. As described in Section 5.4, six suitable SEDs were constructed by the spectroscopic sample itself. Therefore, the cross-correlation approach was carried out for each template. Thus, the optimum redshift is given by the best matching template (minimum σ). As a 'by-product' of this procedure a classification of the spectrum is achieved. Hence, objects can be allocated to empirical spectral types defined by the set of templates used.

For each object the procedure was applied to the six templates and the two versions of input spectra. Furthermore, in each cross-correlation function up to 10 peaks were identified. Consequently, the number of derived redshifts is quite high. Nevertheless, for high S/N spectra a solely dominating redshift and spectral type combination which is indicated by a high significance S (5.18) can mainly be identified. Sometimes two similar redshifts, derived by different spectral types, yielded significance values of the same order. Hence, the interpolation between such redshift values can be useful to improve the accuracy. In this context, Fig. 5.17 in Section 5.7 demonstrates that calculated redshifts may differ from type to type. At low signal-to-noise ratios the identification of the true redshift can be quite difficult, since significance values S of different redshifts can be similar, so that an completely automatic identification of the redshift will not be possible. Thus, the redshift options with the highest S values have to be inspected by eye. Frequently, false detections can be recognised by residuals identified as emission lines or implausible continuum fits. Therefore, in part a reasonable redshift can be derived among detections showing a somewhat smaller S than the apparent maximum. However, in some cases it was impossible to obtain a tolerably stable redshift. These spectra were excluded from the further analysis. In total 86 % of the FDF spectra with a certain redshift were derived automatically. That is, the redshift with the highest significance parameter represents the true one. This value increases to 91 % if the redshift with the second best S is taken into account as well. Thus, the true redshift can frequently be obtained by checking a few redshift candidates only.

Significance S and redshift quality Q_z

Whether a redshift is certain or not depends on the evidence of prominent spectral features. Partly the identification of such structures should be possible even in case of a low S/N (strong emission lines, strong broad absorption), partly the S/N has to be rather high (typical absorption lines). One cannot assume that

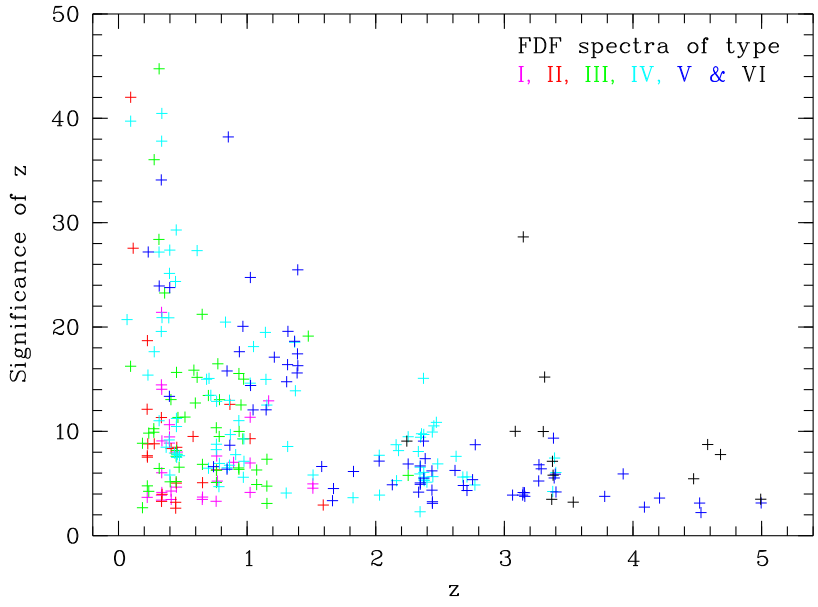

Figure 5.12: Redshift significance estimates according to (5.18) as a function of redshift. The symbol colours denote the spectral templates used for the redshift derivation (see colour assignment inside the diagram and Fig. 5.4). The diagram was restricted to spectra of $Q_z \geq 3$.

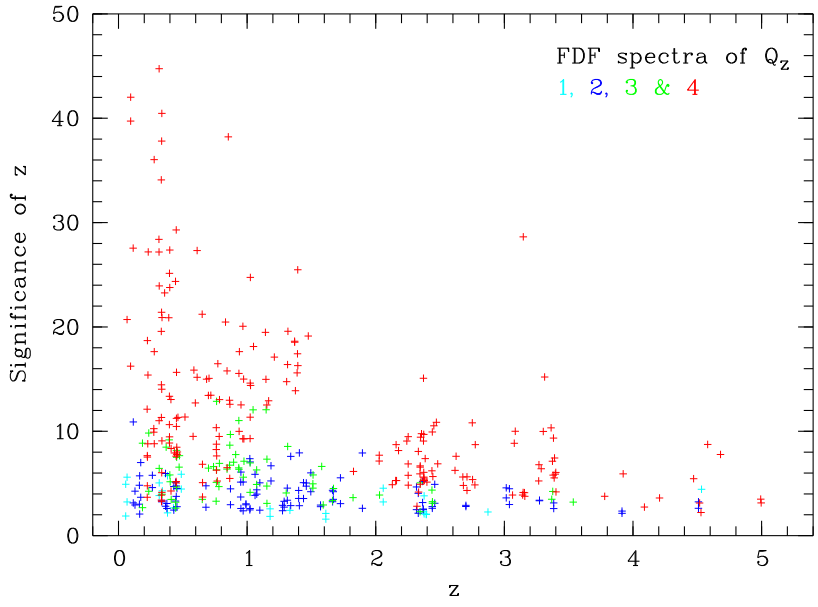

Figure 5.13: Redshift significance estimates according to (5.18) (represented as a function of the derived redshift) in comparison with the redshift quality Q_z. This classification parameter is indicated by coloured crosses (see colour assignment inside the diagram). Accordingly, certain redshifts ($Q_z = 4$) are represented by red symbols.

such details will be taken into account by the significance parameter in the right order of magnitude. Fig. 5.12 shows the S values in relation to the redshift and the spectral type (coloured symbols). Obviously the high-redshift galaxies with absorption line dominated spectra and a variety of line profiles show distinctly lower significance values than emission line galaxies at low redshift. Early-type galaxies (magenta) are absorption-line dominated as well and indicate values which resemble the ones of high-redshift galaxies.

Since the differences in S for different redshifts and spectral types cannot really reflect the true quality of the redshift derivation, it is advisable to introduce a further classification parameter Q_z (quality of redshift) which describes, e.g., whether a redshift is 'certain' or 'probable'. The five classes of Q_z were defined as follows:

$Q_z = 4$: Certain redshift: Spectral lines are clearly identifiable.

$Q_z = 3$: Preferred redshift but not certain: The identification of spectral lines is questionable. However, all other alternatives are significantly less favourable.

$Q_z = 2$: Different possibilities for the redshift: Two or three alternatives provide correspondences of similar quality.

$Q_z = 1$: Redshift very uncertain: No line identifications are possible. Even the rough shape of the continuum can be questionable.

$Q_z = 0$: No redshift derivation was carried out, because of a very low S/N ($\lesssim 1$).

Table 5.2 shows the results for the FDF spectroscopic sample (539 object spectra). For the great majority of the spectra certain redshifts could be derived (59 % of the spectra with $Q_z \geq 1$). Since the spectra with $Q_z = 3$ are useful at least to statistical analyses, about 300 object spectra with $Q_z \geq 3$ were mainly used for further investigations.

Fig. 5.13 shows a comparison of the significance parameter S and Q_z as a function of redshift. In principle, the probability to obtain a certain redshift scales with S. However, the diagram confirms that the corresponding threshold for a certain identification is linked to the properties of the spectra. It is evident that in case of high-redshift galaxies lower S values suffice as in case of low-redshift galaxies. The situation is particularly difficult in the redshift range between 1.5 and 2 where a reliable redshift could hardly be derived. This can be explained by the lack of prominent spectral features in observer's frame (see Fig. 5.14) in case of such redshifts. Thus, neither the striking emission lines of [O II] and [O III] important at low redshift nor the strong Lyα line (absorption as well as emission) important at high redshift are visible. In contrast, the strongest lines in the wavelength range between 2000 and 3700 Å are several Fe II lines and Mg II$\lambda\lambda$ 2796, 2803. These lines are not very strong. Furthermore, the strengths and line profiles (absorption or P Cygni) can differ significantly from galaxy to galaxy. Even the redshift derivation via templates is difficult, since there are no strong, reliable spectral features in the wavelength region concerned. Thus, very high signal-to-noise ratios are needed to obtain certain redshifts.

Table 5.2: Redshift quality Q_z for the spectroscopic sample of the FORS Deep Field. The table represents the absolute numbers $N(x = Q_z)$ of each class as well as the cumulative numbers $N(x \geq Q_z)$.

Q_z	Definition	$N(x = Q_z)$	$N(x \geq Q_z)$
0	S/N not sufficient	133	539
1	z very uncertain	56	406
2	different possibilities for z	52	350
3	preferred z but not certain	60	298
4	certain z	238	238

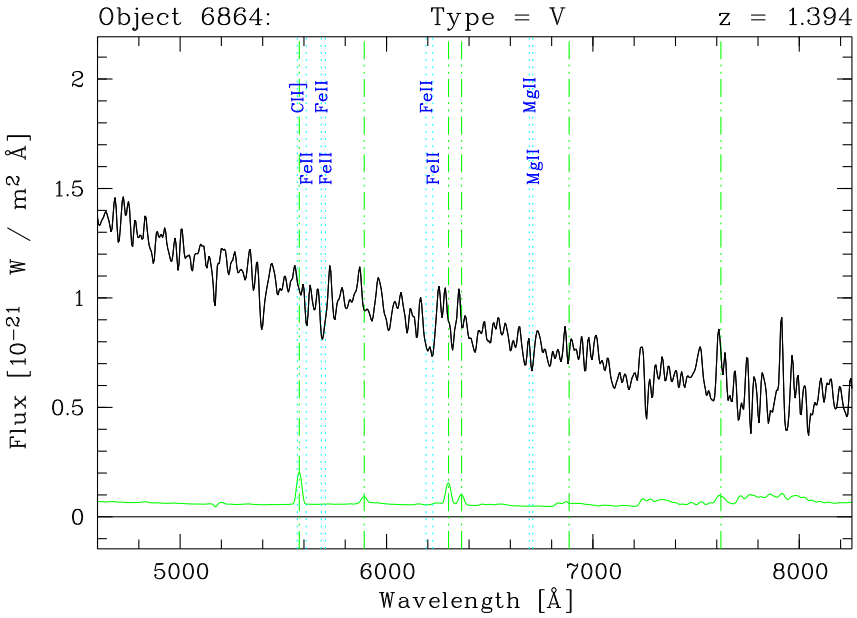

Figure 5.14: Critical wavelength range (2000 – 3700 Å in the rest-frame) of a galaxy spectrum at medium redshift. Object spectrum 6864 at $z = 1.394$ (derived by means of [O II] at 8920 Å!) hardly indicates significant spectral features in the optical wavelength range. The 'most prominent' lines are Mg II$\lambda\lambda$ 2796, 2803 and several Fe II lines. Representation details are described in Appendix D.

As already mentioned in the beginning of this chapter, the redshifts and spectral types were derived by an iterative procedure. The procedure is marked by a repeated and alternating calculation of redshifts, spectral types and redshifts. This has led to an improvement of the consistency of the set of spectral templates defining the spectral classes and, of course, the redshifts. Therefore, this method may harmonise the characteristic spectral parameters of the spectroscopic sample with regard to the reduction of systematic deviations.

5.7 Redshift accuracy

Now, I turn to the discussion of the errors concerning the redshift derivation. The significance of redshifts was already discussed in the previous section. Here, I focus the view on the accuracy of redshifts. I show that the measure HW99M representing the half width of the relevant cross-correlation peak at 99 % of the maximum is principally suitable to estimate the redshift uncertainties. Therefore, I compare this measure to values derived by different approaches. This comprises a comparison with an independent sample of medium resolution spectra, accuracy measurements using spectral line positions and the comparison of redshifts derived by the use of different templates.

General aspects to the redshift accuracy

First of all, the accuracy of the wavelength calibration represents a basic limitation of the precision of redshifts. An error $\Delta\lambda$ of 1 Å constitutes a reasonable value regarding the wavelength calibration (see Section 4.2). Using

$$\Delta z = \frac{\Delta\lambda}{\lambda_0} \tag{5.19}$$

(where λ_0 is the rest-frame wavelength; compare (1.2)) this converts in an Δz of 2×10^{-4} at 5000 Å in the rest-frame, that is the wavelength region of the [O III] lines. In contrast, a Lyα line located at this wavelength ($z \approx 3.1$) would show an error of about 8×10^{-4}. This suggests to use the relative redshift error

$$\frac{\Delta z}{(z+1)} = \frac{\Delta\lambda}{\lambda} = \frac{\Delta\lambda_0}{\lambda_0} \tag{5.20}$$

for the comparison of redshift uncertainties, particularly since the principal resolution $\frac{\lambda}{\Delta\lambda}$ of a spectrum is independent of the redshift.

HW99M as reference measure of the redshift accuracy

To derive redshift errors as universal and precise as possible it seems to be obvious to use the data gathered in the framework of the redshift derivation procedure itself. This means that the correlation function could be applied to measure redshift uncertainties. However, the width of the correlation peaks is mainly determined by the square sum of the similar widths of the (instrumental) profiles

$$\sigma_z^2 = \sigma_G^2 + \sigma_T^2 \tag{5.21}$$

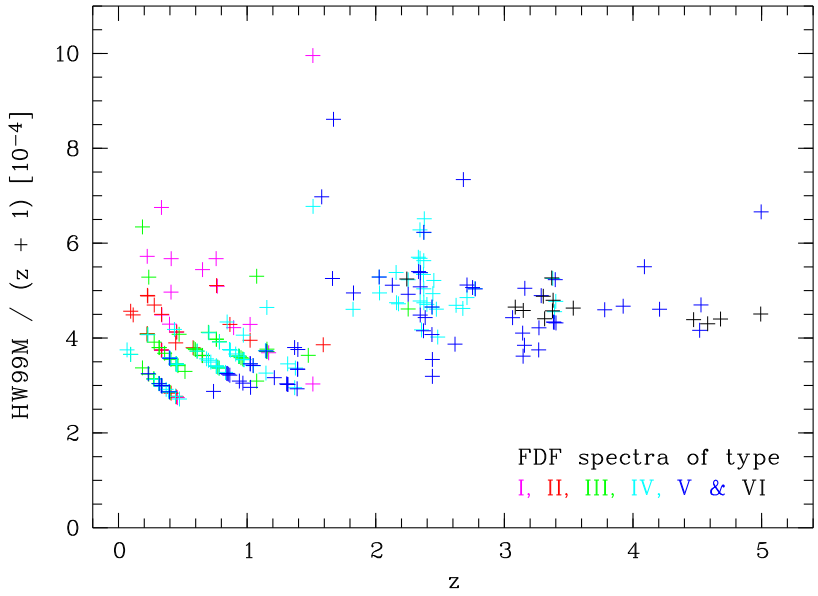

Figure 5.15: HW99M, that is half width of the cross-correlation peak at 99 % height of the maximum, as a function of redshift. The spectral templates used are marked by differently coloured crosses (see description inside the diagram). The values of HW99M are normalised on $(z+1)$ and multiplied by 10^4. For the diagram all FDF spectra with $Q_z \geq 3$ were taken into account.

(given in $\ln \lambda$) of the galaxy and the template spectrum. The resulting width is distinctly higher than the redshift uncertainties which are determined by the precision achievable by measuring peak centres. Nevertheless, a rough estimate of the redshift errors is possible, since one can imagine that a real peak of the correlation function is composed of numerous peaks differing in centre positions and intensities. If the single peaks have similar intensities, then this will lead to a flattening of the profile in the range around the maximum. This information can be used to derive the accuracy of redshifts. Therefore, the half width of the correlation peak at 99 % of the maximum height (HW99M) was measured. The resulting values of the calculation of this measure are represented in Fig. 5.15 and Table 5.3. The diagram clearly shows that the variations of HW99M mainly depend on $(z+1)$, since the quantity HW99M$/(z+1)$ does not indicate strong fluctuations. Nevertheless, a marked dependency of the values on the redshift and the spectral type can be found. At low redshifts a relation between the spectral type and HW99M seems to exist indicating that the redshifts of early-type galaxies have got higher uncertainties than late-type galaxies. This can be understood with regard to the line profiles dominating each class (see Section 5.2 and 5.3). Hence, the redshift derivation using absorption lines and blends (early-type spectra) should be more difficult than the use of strong emission lines (late-type spectra). A similar situation as for the early-type spectra is present for the UV spectra of high-redshift galaxies. The finding that the derivation of redshifts between 1.5 and 2 is particularly challenging (Section 5.6) is confirmed by the

Table 5.3: Comparison of redshift accuracies derived by different methods. The values are given for several subsamples ($Q_z \geq 3$) of the FDF spectroscopic sample. The nine groups differ in spectral type and redshift range. For the redshift interval ranging from 1.5 to 2 only one class was defined due to the small number of objects (8). The presented redshift uncertainty measures have the following meaning: HW99M = half width of the cross correlation peak at 99 % height of the maximum; $\sigma_{TF} = \sigma$ derived by comparison with higher resolution spectra of the Tully-Fisher project of the FDF (only measured in two extended groups comprising the types 2 & 3 and 4 & 5, respectively); $\sigma_{lines} = \sigma$ derived by the comparison with the results of individual line measurements; $\sigma_{z1-z2} = \sigma$ derived by the comparison of redshifts obtained by the use of different spectral templates (best and second best fitting templates). All errors are normalised by the factor $(z+1)$ and multiplied by 10^4.

Group	Type	z range	HW99M / $(z+1)$ $[10^{-4}]$	σ_{TF} / $(z+1)$ $[10^{-4}]$	σ_{lines} / $(z+1)$ $[10^{-4}]$	σ_{z1-z2} / $(z+1)$ $[10^{-4}]$
1	1	< 1.5	4.2		4.5	15.3
2	2	< 1.5	4.0	3.7	3.1	6.3
3	3	< 1.5	3.7	3.7	2.6	1.5
4	4	< 1.5	3.6	4.4	2.5	1.1
5	5	< 1.5	3.2	4.4	2.5	1.3
6	$1-5$	$1.5-2$	6.0		4.8	7.3
7	$3-4$	≥ 2	5.1		4.9	3.2
8	5	≥ 2	4.7		5.8	4.3
9	6	≥ 2	4.6		7.7	5.4

conspicuously high correlation peak widths of objects lying within this redshift range. Thus, HW99M indicates redshift and type dependent tendencies already outlined before. However, the introduction of the measure HW99M seems to be a little bit artificially. But the following discussion of alternative approaches will show that the values derived are not so bad, that is, HW99M indicates the right order of magnitude.

Comparison to the sample of medium resolution spectra

The best way to measure errors is to compare the results with values obtained with a completely different instrumental set-up (compare 3.2). Fortunately, there is another FDF spectroscopic programme investigating the Tully-Fisher relation of galaxies at $z < 1$ (see Ziegler et al. 2002). This project is also based on FORS observations but uses the higher resolution grisms 600 B and 600 R (see FORS Manual). Thus, the spectra of the Tully-Fisher project are suitable to check the redshift accuracy of the 150 I spectra. In total, there are 23 galaxies which were observed by both projects. The subsample is quite homogeneous, since a majority of the spectra (57 %) could be classified as type III. The redshifts range from 0.09 to 0.84 ($\langle z \rangle = 0.41$). According to Böhm (2001) the redshifts of the TF project were measured with an accuracy of about 2×10^{-4}. The differences between the corresponding redshift values can be converted into

a standard deviation representing the accuracy of the 150 I redshifts. The resulting relative value of the small subsample amounts to about 4×10^{-4} indicating the quality of the 150 I redshifts in comparison with the redshifts derived from higher resolution spectra. Remarkably, the value is of the same order as the corresponding average of the HW99M measurements.

Spectral line position uncertainties

The 'Tully-Fisher' sample is composed of galaxy spectra with similar characteristics, that is redshifts and spectral types. Therefore, this sample can only provide informations for a small fraction of the present spectroscopic sample. Thus, it is necessary to check the redshift uncertainties by further approaches using the whole sample. One opportunity forms the measurement of individual line position fluctuations (see Section 5.2) by comparing the measured line redshifts with the final redshifts mainly derived by using spectral templates. Table 5.1 shows the resulting uncertainties of lines covering the whole available wavelength range. The error of the redshift measurement can be estimated by calculating the root mean square $\sqrt{\langle \sigma_z^2 \rangle}$ of all lines important to the derivation of redshift. For instance, for a late-type galaxy at moderate redshift this means that the corresponding effective redshift error can be derived from the square sum of the individual uncertainties of the [O II], [O III] and Balmer lines (like Hβ). On the assumption, that the peak of the correlation function is essentially caused by the spectral features considered, the position uncertainties of the these lines will be the main error source of the total redshift error. Thus, the error estimate should provide realistic values.

Fig. 5.16 shows the derived $\sigma_z/(z+1)$ dependent on redshift and spectral type. Interestingly, the diagram looks very similar to the corresponding plot for the HW99M values, although the scatter is distinctly higher. In general, all dependencies discussed above can also be found in Fig. 5.16. Nevertheless, there are a few differences. For example, σ_z is lower than HW99M (see Table 5.3) in case of galaxies with several strong emission lines ($z < 1$, SEDs IV & V). In view of the 'Tully-Fisher' results the σ_z values are probably somewhat too small. Likely a high number of lines used pretends an apparent accuracy not achieved in reality. On the other hand, in case of galaxies essentially identified by their Lyα emission (see Section 6.2) the σ_z are conspicuously higher than the corresponding HW99M values. This can be explained by the problem that at low resolution the derivation of the centre of the Lyα line is quite difficult because of its complex structure. This type of error does not affect the cross-correlation function, since in this special case the correlation peak is mainly caused by a single line fit cancelling out any line shifts. In summary, $\sigma_z/(z+1)$ represents an useful estimate of the redshift errors for the majority of spectra.

Spectral type dependent redshift uncertainties

Finally, I deal with redshift deviations caused by the use of different spectral templates. This type of error is not covered by the correlation function, since $C(z)$ is the result of the comparison of *one* object spectrum with *one* template.

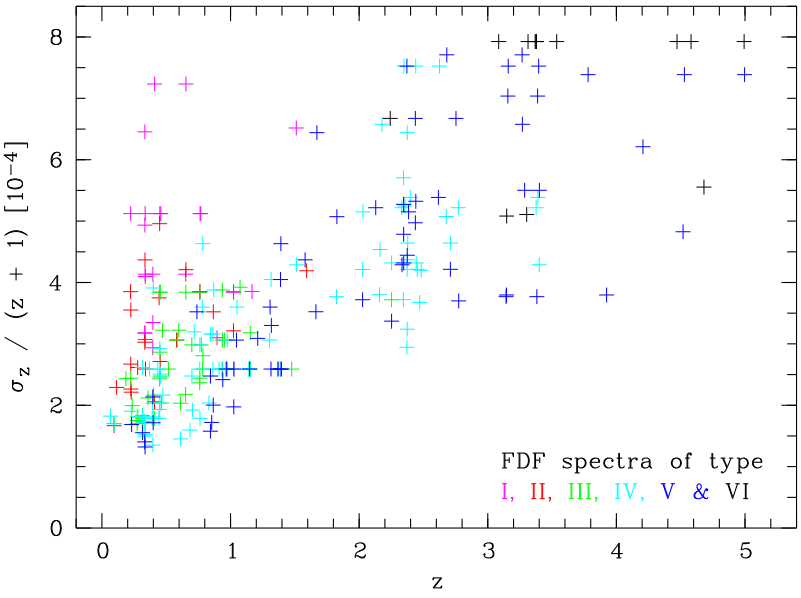

Figure 5.16: Redshift errors derived by line centre variations in relation to the central wavelengths belonging to the respective redshift. For the description of presentation details see Fig. 5.15.

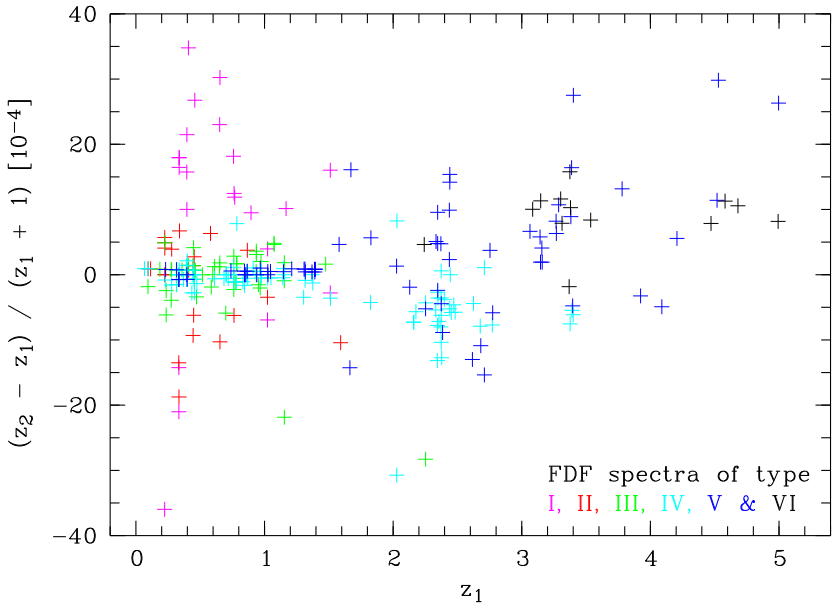

Figure 5.17: Redshift differences caused by the use of different templates. $(z_2 - z_1)/(z_1 + 1)$ is shown, that is the z difference of the second best and the best matching template (determining the spectral type) divided by the redshift factor. For the description of presentation details see Fig. 5.15.

Thus, deviations between two template SEDs should lead to redshift uncertainties not considered so far. As already stated in Section 5.2, in part the line profiles can be very different from spectrum to spectrum. This particularly concerns the UV lines which are important to high-redshift galaxies. If the average line profiles vary systematically with changing spectral type, the redshift derivation using different spectral templates will lead to various results. In this connection, Fig. 5.17 shows the deviations between the redshifts obtained using the best and the second best fitting template. It is obvious that at high redshifts the results for the spectral types IV and V indicate systematic differences in the order of a few 10^{-4} (relative). The corresponding shifts for individual galaxies should distinctly be smaller, since usually one template fits significantly better to the respective spectrum than all the others. In the rare case where a clear type allocation was not possible (order of a few %), the redshift estimate was improved by interpolating between the extreme values. Consequently, the main error source regarding the redshifts is not a systematic shift caused by a bad matching template, but the statistical scatter which is also visible in Fig. 5.17 (see Table 5.3 as well).

At low redshifts Fig. 5.17 indicates two extreme situations. First, in case of late-type galaxies systematic shifts cannot be proved. The scatter is also very low (Table 5.3). This confirms that redshifts can be determined very accurate, if strong nebular emission lines are present. The opposite situation is realized in case of the early-type galaxies, since there are strong deviations between the redshifts derived by SED I and II. The reasonable explanation is that the redshift calculation of type I is only based on absorption lines like Ca H and K whereas in case of type II already emission lines like [O II] and Hα can be used. Furthermore, the characteristics of the composition of stellar populations in early-type galaxies lead to a strong increase of the continuum in the range of the calcium lines (see Fig. 5.3). Moreover, the amount of this '4000 Å break' can be very different from type to type. Consequently the redshift derivation via Ca H and K should significantly depend on the shape of the continuum, that is the spectral type. Hence, the redshift uncertainties of early-type spectra are significantly higher than expected by the HW99M measurements, although the value in Table 5.3 seems to be somewhat too large.

A comparison of the redshift accuracies represented in Table 5.3 shows that the measure HW99M is generally suitable to derive reliable redshift errors. Only in case of errors which are caused by a not optimally matching template, the real errors can significantly be higher than calculated. Exceptions are Lyα emission galaxies or ellipticals (early-type galaxies), for instance. Nevertheless, HW99M is used in the spectroscopic catalogue (see Section 6.1) as indicator of the redshift uncertainties, since the calculation can be carried out for each object without greater problems.

Chapter 6

Observational results

In this chapter I outline the properties of the spectroscopic sample using the results of the derivation of redshifts and spectral types (Chapter 5). First, I present a catalogue with the object informations obtained by the previous analyses (Section 6.1). Then I describe the spectra of FDF spectroscopic sample in detail (Section 6.2). Finally, the sample is discussed as a whole. In particular, I describe the distribution of redshifts and spectral types (Section 6.3).

6.1 The catalogue

After the acquisition of the final spectra (Chapter 4) and the derivation of the basic parameters redshift and spectral type (Chapter 5), now a catalogue with all available informations of the sample objects can be created. Three categories of information can be defined:

(1) **Results of the photometry:**
Almost all sample objects were previously detected and photometrically measured in the images of the FORS Deep Field. The resulting photometric catalogue (Heidt et al. 2002) provides identification numbers, positions, fluxes in magnitudes (measured with flexible as well as fixed aperture) and more. These data are also relevant to the spectroscopic sample, particularly since the photometric redshifts (Section 2.2) were used for the spectroscopic sample selection. Furthermore, the photometry was applied to the absolute flux calibration of the spectra (see Section 4.4).
→ **catalogue parameters:** No., RA, DEC, B and I

(2) **Quality of the spectra:**
For the suitability of the spectra for further analysis it is important to know how reliable spectral features are. For that reason, the quality of the spectra was characterised by the signal-to-noise ratio and a parameter Q_s indicating the extent of spectral distortions by systematic errors (see Section 5.1). As a further parameter the effective slit losses f/f_0 of each object (Section 4.4) can provide information about the coverage of the observed targets by spectroscopy. In case of a low coverage of a highly

structured object (e.g. a spiral galaxy) one runs the risk to getting a non-representative spectrum.
→ **catalogue parameters:** $T_{\rm exp}$, f/f_0, S/N and $Q_{\rm s}$

(3) **Basic spectral parameters:**
Each spectrum can roughly be characterised by the redshift and the spectral energy distribution which can be described by the spectral type. In combination these two parameters give an assessment on the appearance of a spectrum, that is the occurrence, location, strength and shape of spectral features. Particularly the redshift (Chapter 5), which locates the positions of spectral lines and represents *the* cosmological distance measure, constitutes the indispensable basis of further spectroscopic investigations.
→ **catalogue parameters:** Type, z, dz, S and $Q_{\rm z}$

The fundamental catalogue of the spectroscopic sample of the FDF spectroscopic survey providing the informations stated above is represented in Appendix C. The table comprises data for the 350 object spectra with derived spectroscopic redshifts, since spectra with no redshift ($Q_{\rm z} \leq 1$, see Section 5.6) do not provide any valuable information for further analysis.

6.2 Basic properties of the spectra

In this section I describe some general properties of the object spectra obtained in this work. For this, I show representative spectra of different redshift ranges and spectral types. The complete sample of 233 spectra with certain redshift ($Q_{\rm z} = 4$) and no strong spectral distortions ($Q_{\rm s} \geq 2$) is shown in Appendix D.

Stars

I am starting with the 33 stars found in the FORS Deep Field. Fig 6.1 shows star spectra of different spectral type (see Section 5.3) ranging from G to L. The spectra demonstrate the transition from stars having their flux maximum in the optical (G, K) to stars showing almost no emission in the optical wavelength range (L). The predominating spectral lines are Ca H and K and the G band in case of type G. Regarding type K the Mg I band is the most prominent spectral feature. Type M is dominated by molecule bands like the TiO_2 bands. In case of L vanadium oxide bands are also important. The very cool late M and early L stars (of which 4 – 5 were discovered) may be brown dwarfs. However, the crucial point of this interpretation is the age of the objects, since brown dwarfs gradually cool down. As the region of the milky way which is covered by the FORS Deep Field (location close to the south galactic pole) is not suspected to be a region with a young stellar population one has to be cautious with this kind of interpretation. Since stars earlier than G and brighter than $18^{\rm m}$ were not observed (see Appendix C) one can assume that the observed stars (maybe with exception of the coolest ones) are located in the halo or at least in the thick disk (scale height $\sim 1\,$kpc) and belong to the population II.

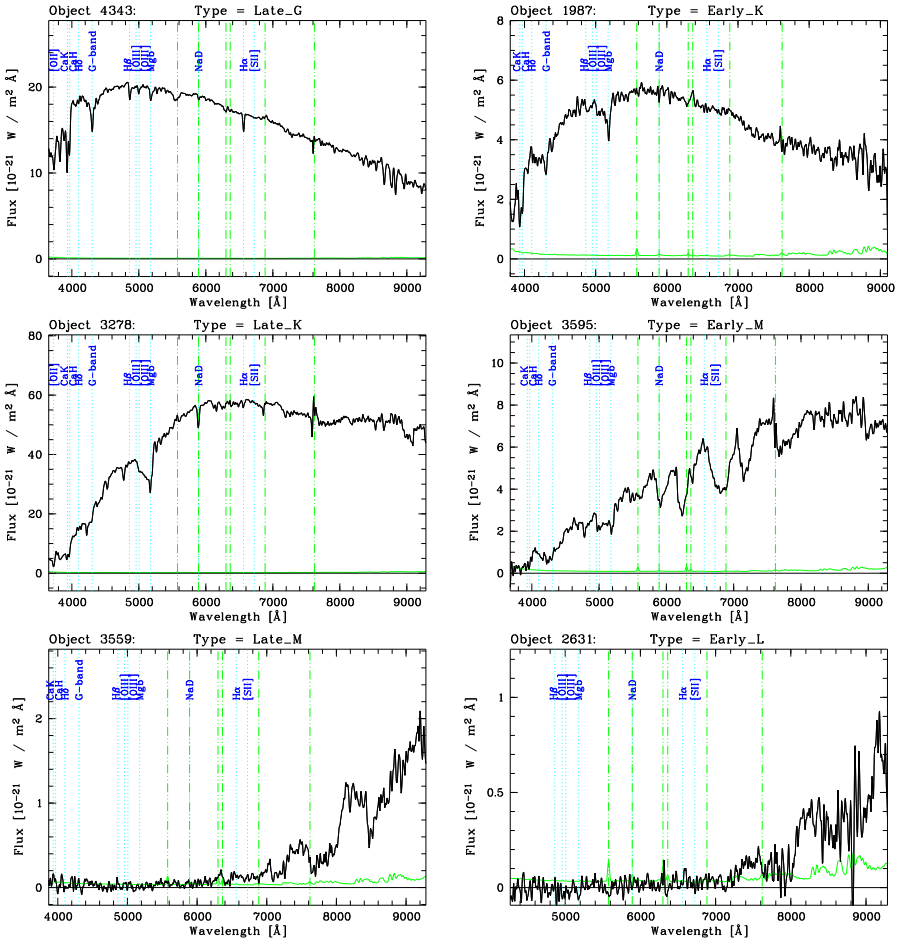

Figure 6.1: Star spectra of the FDF spectroscopic sample of distinct spectral types, in fact: late G (4343), early K (1987), late K (3278), early M (3595), late M (3559) and early L (2631). An explanation of the representation of the spectra is given in Appendix D.

Low-redshift galaxies

At low redshift ($z < 1$) a higher number of galaxies with spectral types ranging from early to late type are present (SEDs I – V, see Section 5.4). Fig. 6.2 shows some representative spectra.

According to the primary classification parameter, the spectra show an increase of the 'blue flux' in relation to the 'red flux' in case of the transition from type I to type V. Furthermore, an increase of the strength of nebular emission lines towards later types can be seen whereby the behaviour of the individual lines can be very different. In general, the different types show the following characteristics (compare Section 5.2):

Type I: No detectable emission lines, strong Ca II absorption (H and K), striking 4000 Å break

Type II: Significant emission lines of [O II] and Hα, Ca II absorption less pregnant

Type III: Strong emission of [O II] and Hα, weak emission of Hβ and [O III], weak 4000 Å break

Type IV: Comparable strength of [O II], Hβ, [O III] and Hα, inconspicuous absorption features

Type V: Dominating [O III] emission, high number of emission lines (e.g. Hδ)

In most cases this scheme is correct. However, since the classification was carried out via the continuum shape, objects of the same class may show a huge variety of line strengths. This may lead to the situation that the intensities and profiles of spectral lines indicate an spectral type differing from the continuum type.

A comparison of the different spectra represented in Fig. 6.2 shows that the most striking differences exist between the spectra of type I and II. The FDF spectroscopic sample lacks of objects filling the gap. This indicates that either transitional types are basically rare or that the evolutionary life time of the objects having such spectra is rather short.

Medium-redshift galaxies

At $z > 1$ the accessible wavelength range is characterised by the lack of prominent spectral features. This is demonstrated by Fig. 6.3 showing spectra of different types in the redshift range between 1.1 and 1.5.

Early-type galaxies (see object 2256) are marked by a strong decrease of the spectral flux towards shorter wavelengths. This makes it difficult to find such objects at high redshifts, particularly since at $z > 1.3$ the prominent 4000 Å break is located beyond the last accessible spectral window. Up to now, no type I galaxy beyond $z = 1.16$ (object 2256) could reliably be identified in the FDF.

Excluding the prominent [O II] emission redshifted to the near infrared, late-type spectra show a rather smooth monotonous increase towards shorter wavelengths. An exception forms the conspicuous 'dip' in the spectrum of object 4049 around 5500 Å (observer's frame). This structure is probably caused by

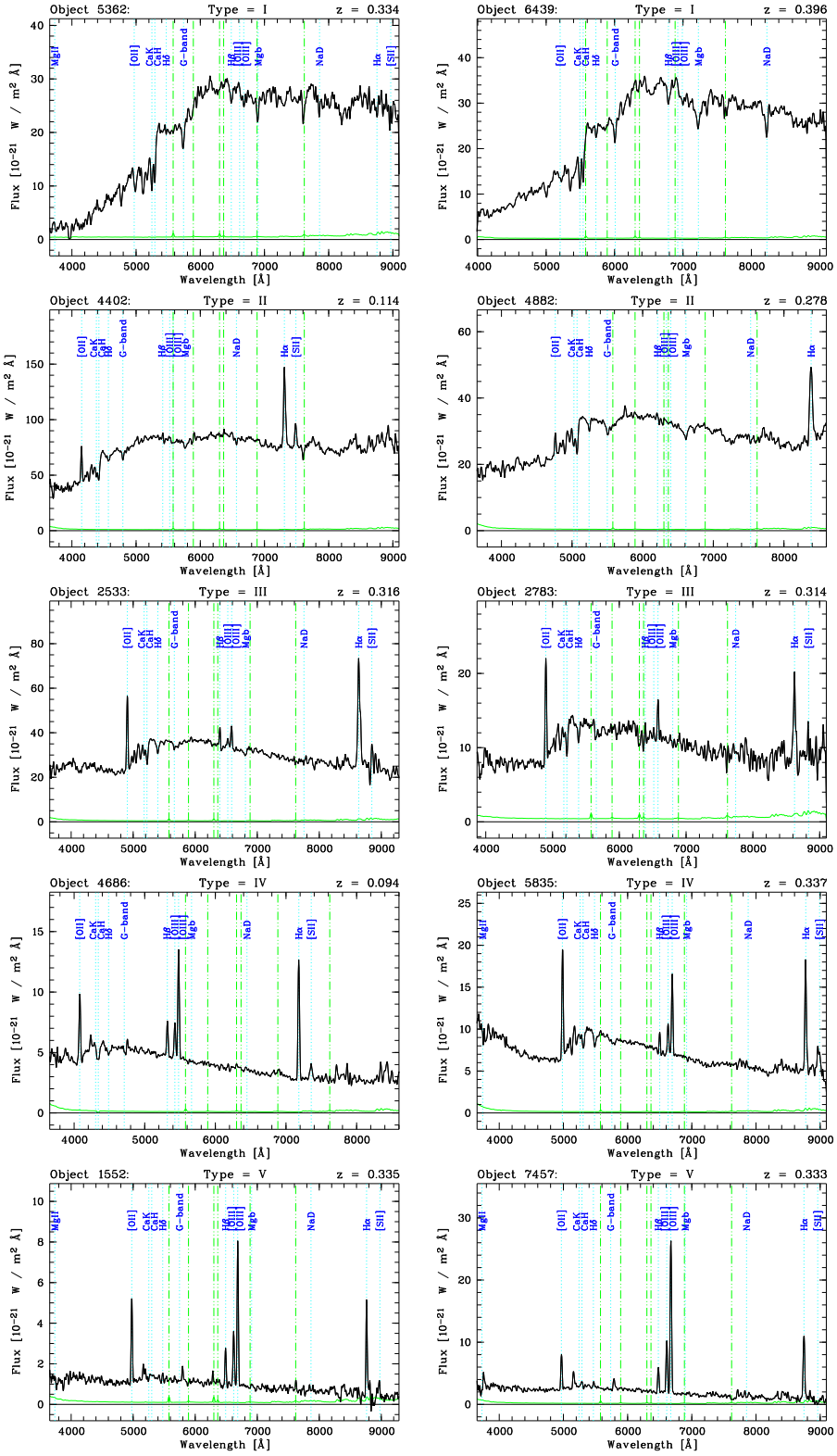

Figure 6.2: Galaxy spectra of the FDF spectroscopic sample of different spectral types (I – V) at low redshift ($z < 0.4$). Representation details are described in Appendix D.

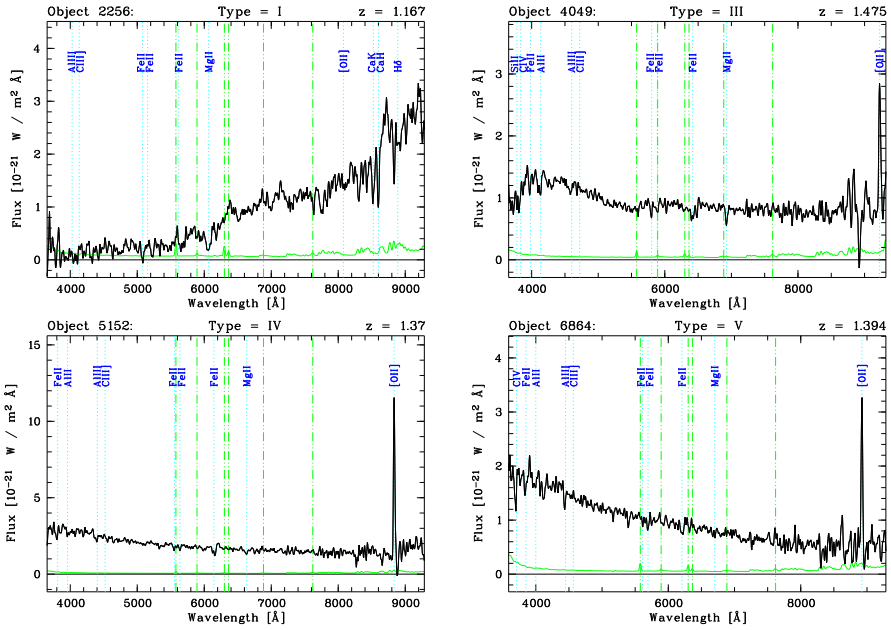

Figure 6.3: Galaxy spectra of the FDF spectroscopic sample of different spectral types (I – V) at medium redshift ($1.1 < z < 1.5$). Representation details are described in Appendix D.

the well-known broad dust absorption feature at 2200 Å (see Cardelli et al. 1989) which is thought to be caused by small carbon-rich particles. I will discuss this feature in Section 7.1 in more detail.

As already discussed in Section 5.6 the rest-frame wavelength range between 2000 and 3700 Å is poor in prominent spectral lines (Fe II and Mg II are the most important ones, see Fig. 6.3) which complicates the derivation of reliable redshifts in the range between 1.5 and 2 (see Fig. 5.13). Therefore, there is only one object (1922, see Fig. D.4) for which a certain redshift ($z = 1.827$) could be obtained, so far.

High-redshift galaxies

Most attention was paid to galaxies with $z \geq 2$. For 80 objects certain redshift could finally be obtained from spectra with exposure times frequently reaching 10 h (see Table C.1). Fig. 6.4 shows a selection of the types of spectra which could be found up to $z = 3.5$.

The most striking features in UV rest-frame spectra are the Lyα line (profile ranging from strong absorption to strong emission, see Section 7.2) complemented by the absorptions of the Lyα forest short-wards of 1216 Å (compare Section 1.3) and the spectral break of the Lyman limit at 912 Å. These features are so strong that their identification is possible even at very low S/N (see Fig. 5.13). Furthermore, the rest-frame UV red-wards from Lyα is also marked by numerous spectral lines. As an example, the spectrum of object 5903 has got a S/N up to almost 40 which allows the identification of dozens of spectral lines (see Fig. 5.4). As Fig. 6.4 indicates, a large majority of the lines shows

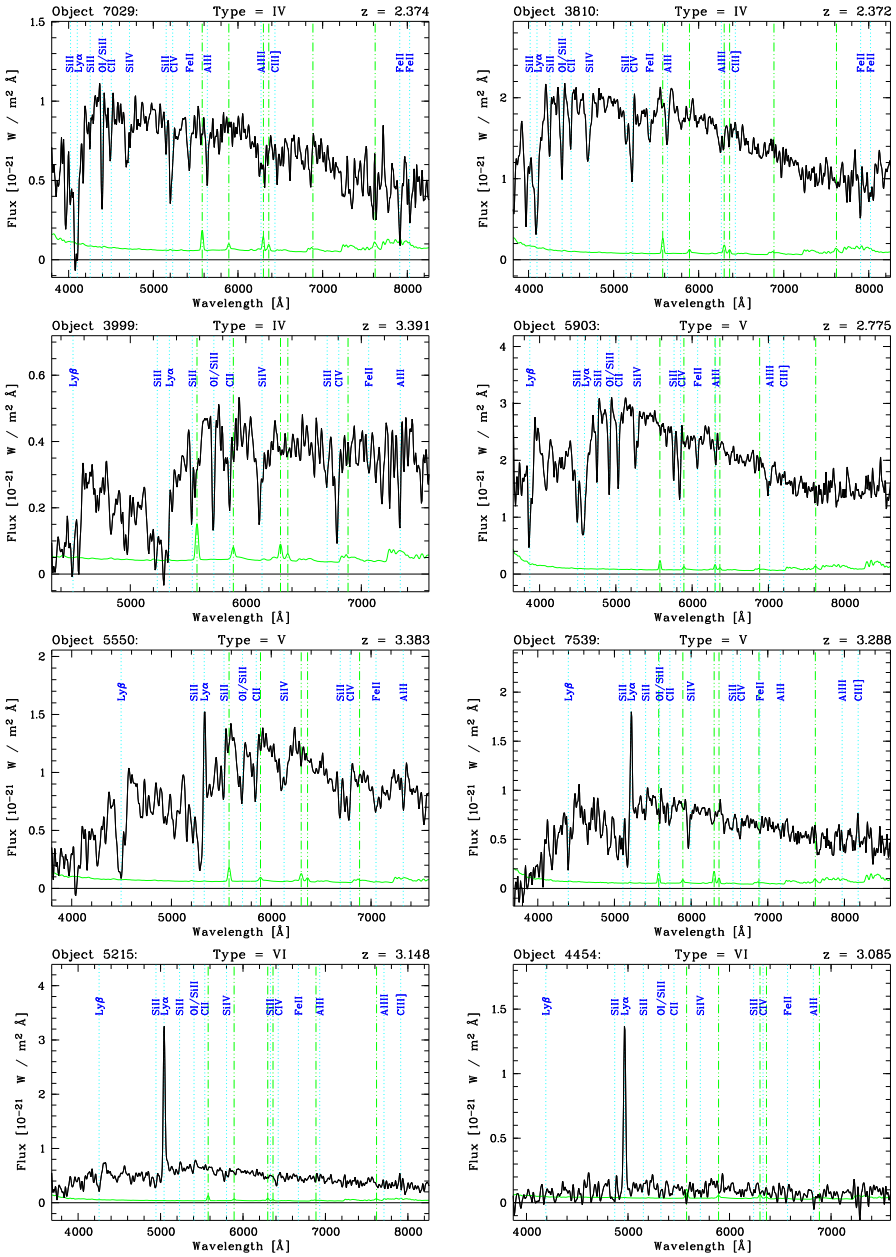

Figure 6.4: Galaxy spectra of the FDF spectroscopic sample of different spectral types (IV – VI) at high redshift ($2.3 < z < 3.4$). Representation details are described in Appendix D.

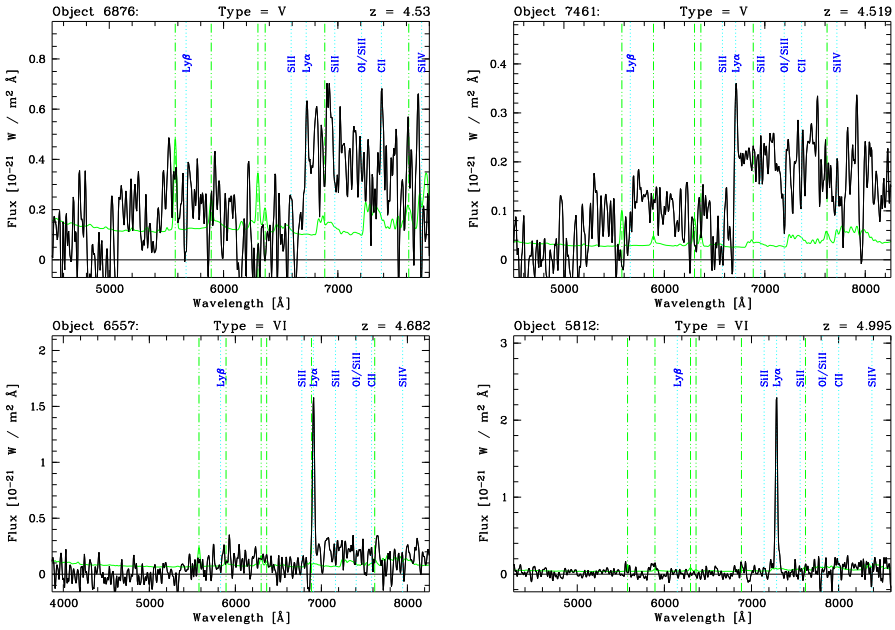

Figure 6.5: Galaxy spectra of the FDF spectroscopic sample of different spectral types (V – VI) at very high redshift ($4.5 < z < 5.0$). Representation details are described in Appendix D.

absorption profiles frequently caused by interstellar matter (e.g. Si II and C II, see Section 5.2). Except for Lyα significant emission components could hardly be identified. Only in a few cases emission components were detected as part of a P Cygni profile (e.g. C IV; see Section 7.3) or as pure emission lines (e.g. He IIλ 1641 and C III]).

As a basic property of the spectra obtained it turned out that the maximum of the spectral energy distribution is usually located close to Lyα ($\lambda_{\max} < 1500$ Å). This indicates the presence of a high amount of young stars which infers intense star formation. Therefore, a significant starburst activity has to be present in the observed Lyman-break galaxies (see Section 1.3).

Very-high-redshift galaxies

At very high redshifts ($z > 4.5$) galaxies showing Lyα in absorption as well as emission can be found (see Fig. 6.5). Nevertheless, Lyα emission galaxies (Section 5.3) are especially frequent in comparison with the situation at lower redshifts (see Section 7.2). Apparently this is not due to a problem with the redshift identification of faint absorption line spectra, since for all candidates with $I \lesssim 25^{\mathrm{m}}$ and $z \lesssim 5$ a certain redshift could be measured. Up to now, the objects with the highest discovered redshifts in the FDF so far are the galaxies 4522 (Fig. D.13) and 5812 (Fig. 6.5) with redshifts of 4.998 and 4.995, respectively.

At high redshifts the continuum below Lyα should be more reduced by absorption than at lower redshifts, since in these epochs the universe was significantly denser and probably less ionised (process of re-ionisation). In the FDF data,

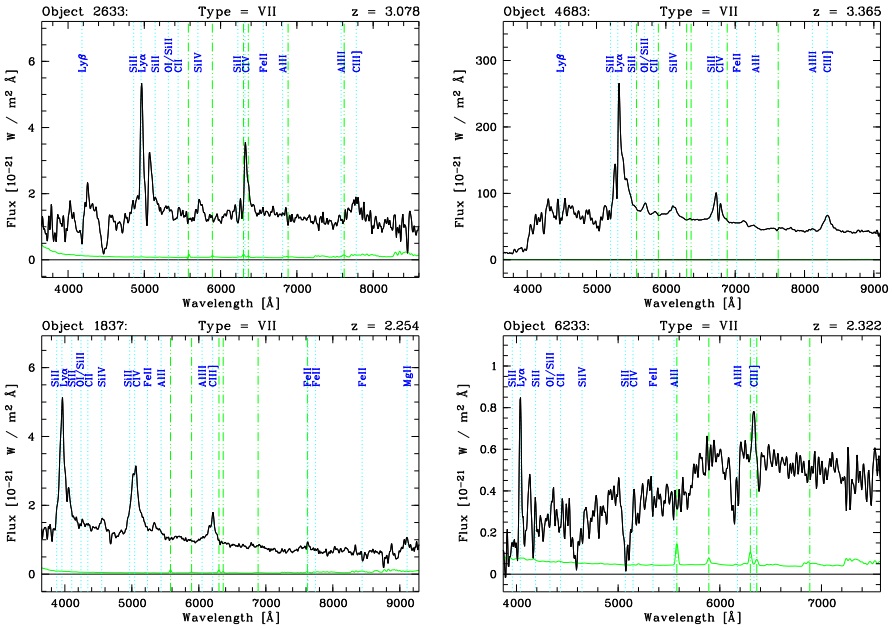

Figure 6.6: Quasar spectra of the FDF spectroscopic sample. 4683 represents the already known bright quasar Q 0130–260. 6233 is a rare BAL (broad absorption line quasar). Representation details are described in Appendix D.

this effect can easily be seen by comparing the wavelength regions concerned of the galaxies at $z > 4.5$ (Fig. 6.5) with the objects at $z < 3.5$ (Fig. 6.4).

Quasars

All in all, seven evident quasars (type VII, see Appendix C) were observed in the FDF, so far. However, further objects classified as type V or VI may also harbour an AGN, but their spectrum is dominated by the host galaxy.

The FDF quasars have very different spectra. The redshifts ranges from 0.865 to 3.365 (see Table C.1). A selection of four objects is shown in Fig 6.6. The spectra of the majority of the observed quasars are dominated by broad emission lines of Lyα, N V, Si IV, C IV, C III] and/or Mg II. These lines emerge from the broad-line region in the immediate vicinity of the black hole where gravitational energy is transformed into radiation and the gas rotation velocities reach several thousands of km/s. In present quasar spectra detectable absorption lines are essentially restricted to (weak) absorption components of the broad emission lines and the Lyman forest.

A great exception forms object 6233 (see Fig 6.6) which can be classified as one of the rare broad absorption line quasars (BAL, e.g. Menou et al. 2001). The spectrum is dominated by strong, broad, blue-shifted absorption troughs of Si IV, C IV and Al III indicating outflow movements of several 1000 km/s. On the other hand, Lyα, N V, and C III] indicate relatively narrow emission components. In contrast to the other quasars the continuum conspicuously decreases short-wards of 1750 Å. The spectrum can be explained by the assumption that the observer may directly look into a fast outflow which is preferentially located

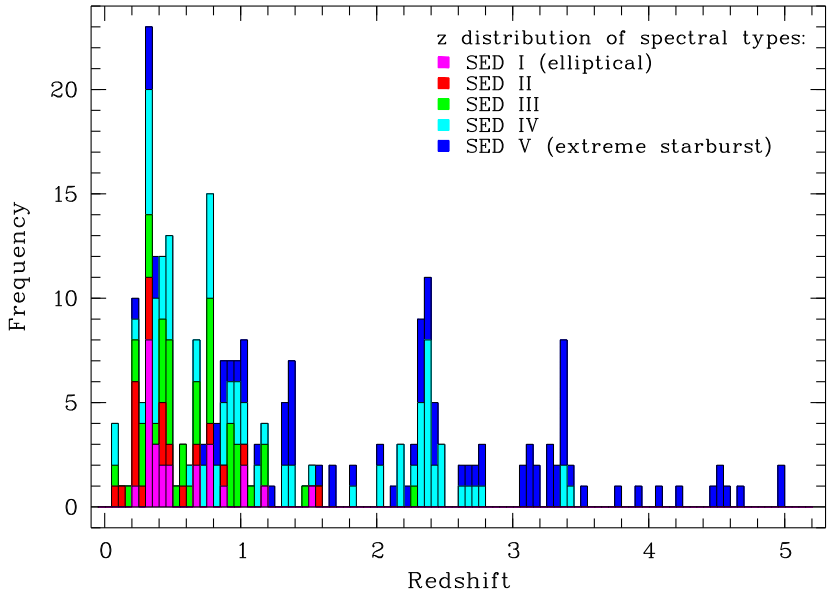

Figure 6.7: Distribution of redshifts and spectral types for the FDF objects with $Q_z \geq 3$ (no consideration of TF objects, see Section 5.7). The histogram bars are coloured according to the spectral type (see legend inside the diagram). The bin width of the bars amounts to 0.05.

in the plane of the accretion disk surrounding the central supermassive black hole (see Murray et al. 1995).

6.3 Distribution of redshifts and spectral types

Next, I discuss the FDF spectroscopic sample with regard to the distribution of redshifts and spectral types. Both distributions are shown in Fig. 6.7 and will be described in the following. In part, I consider the redshift distribution of the FDF spectroscopic sample of bright low-redshift galaxies ($\langle z \rangle = 0.51 \pm 0.23$) obtained by Ziegler et al. 2002. Objects which were exclusively observed in the framework of this so-called Tully-Fisher project are marked by TF.

Distribution of spectroscopic redshifts

Fig. 6.7 indicates a strongly peaked redshift distribution with local maxima around $z = 0.325$ (23, with TF objects 31 galaxies), $z = 0.775$ (15, with TF 19), $z = 2.375$ (11) and $z = 3.375$ (8). Adjacent bins to the maximum bins show increased object numbers which indicate that the observed crowding extends over more than one bin. For instance, the three adjacent bins comprising the redshift range between 2.30 and 2.45 contain 26 objects which represent about 30 % of the whole high-redshift sample ($z \geq 2$). On the other hand, the peak around $z = 0.325$ is mainly produced by a redshift interval ranging from 0.332 to 0.339 ($\langle z \rangle = 0.335 \pm 0.002$), which is smaller than the bin size, but includes 23 galaxies (inclusively the Tully-Fisher objects). Such a fine structure of the

redshift distribution is also present at high redshifts. For instance, the small redshift bin between 2.371 and 2.379 ($\langle z \rangle = 2.374 \pm 0.002$) includes 8 galaxies which represent about 73 % of the objects within the standard bin around $z = 2.375$ (see above). Besides the striking peaks, there are also indications of marked gaps in the redshift distribution. At low redshifts this particularly concerns the bin around $z = 0.525$ where the redshift distribution reaches a local minimum. At high redshifts a lack of galaxies seems to exist between 2.80 and 3.05 where no objects could be detected, so far.

Regarding the absolutely bright objects in the FDF the observed distribution seems to be representative of the real distribution, since the spectroscopic sample is relatively complete for the most luminous objects at each redshift (see Section 2.3). In contrast, the distribution of the intrinsically faint objects ($M_\mathrm{B} > -20^\mathrm{m}$; compare Section 7.3) is highly uncertain, especially in case of the high-redshift domain where such objects are not accessible by spectroscopic observations. Nevertheless, at least the most conspicuous peaks at 0.34, 2.4 and 3.4 seem to show real galaxy overdensities. This assessment is supported by the fact that the peaks are frequently very narrow (see above) which contradicts statistical fluctuations.

A further interesting question concerns the extent of clustering of the objects in the peaks of the redshift distribution. Since the first photometric observations of the FORS Deep Field a small cluster is known which is located in the southwestern corner of the field. In Fig. 1.1 the cluster is marked by the accumulation of bright, extended, yellow/orange coloured galaxies. Interestingly, a significant part of the objects included in the highest peak at $z \approx 0.335$ can be assigned to the cluster. The found cluster represents a great exception in case of the FDF (but this is just as well, since the FDF project was designed to investigate field galaxies and not galaxy clusters), since the galaxies belonging to the other existing redshift peaks essentially show no hint for spatial clustering. Nevertheless, a few pairs of galaxies were discovered. In one case, a dense group at $z \approx 2.347$ comprising four members was even identified (objects 5135, 5165, 5167 and 5190, see Table C.1). However, in general strong clustering is a minor issue in the FDF, at least in case of the absolutely brightest objects which are accessible to spectroscopy. Therefore, the detected peaks in the redshift distribution should mainly be caused by large-scale structure. In this case one should not expect a conspicuous change of the redshift distribution dependent on the position in the FDF, since the diameter of the field (angular extension $7'$) amounts to a few Mpc only.

Distribution of spectral types

In the end of this section, I discuss the redshift distribution of the spectral types (see Fig. 5.4). Graphically this is shown in Fig. 6.7 by coloured bars (see legend). Furthermore, simple statistics (number, median z, mean z) for the individual spectral types are presented in Table 6.1.

Fig. 6.7 indicates a striking difference of the apparent composition of spectral types between the low and high-redshift domain. At low redshift there is rather a balanced distribution of all spectral types whereas at high redshift

Table 6.1: Redshift distribution of the FDF spectroscopic sample for $Q_z \geq 3$. The table indicates for each spectral type the total number of objects N, the median redshift $\overline{z}$ and the mean redshift $\langle z \rangle$ with its standard deviation.

Type	N	$\overline{z}$	$\langle z \rangle$
early-type galaxy (SED I)	26	0.4	0.6 ± 0.3
medium-type galaxy (SED II)	21	0.3	0.5 ± 0.4
medium-type galaxy (SED III)	45	0.6	0.7 ± 0.4
late-type galaxy (SED IV)	86	1.0	1.3 ± 0.9
late-type galaxy (SED V)	80	2.4	2.4 ± 1.3
AGN-dominated galaxy	7	2.3	2.4 ± 0.8
galaxy	265	1.0	1.4 ± 1.2
star	33	–	–

only late-type galaxies (types IV and V) can be found. This means that especially the types I and II are concentrated at low redshifts (median values 0.4 and 0.3, see Table 6.1). Spectra indicating such types could only be found up to a redshift of 1.6. Furthermore, type I shows a strong concentration in the overdense redshift range at ≈ 0.335 where 8 of 26 early-type galaxies are located. This high frequency is related to the galaxy cluster described above. The change of the apparent composition of spectral types with redshift is particularly obvious regarding the frequency of type V (which includes type VI, see Section 5.4): At low redshifts this type plays a minor role (7 % of the observed objects at $z < 0.5$), but at high redshifts type V becomes the dominating class. At $2 \leq z < 3$ the extreme starburst galaxies contribute 40 % to all identified objects, at $3 \leq z < 4$ they present 88 % and at $z \geq 4$ type V is the only class derived, so far.

The observed distribution of spectral types is strongly affected by type- and redshift-dependent selection biases, so that the observed change of the frequency of spectral types with redshift does not inevitably mean a strong evolution of the galaxy population. In this context, important effects are:

- **Type-dependent relative UV brightness**
  At high redshift only the intrinsically brightest objects are accessible to spectroscopic investigations. The most serious problem in this respect is the strong difference of the absolute brightness of the different spectral types in the UV rest-frame in comparison with the optical (see Fig. 5.7). Hence, early-type galaxies are very faint in the UV which makes it quite difficult to detect such objects at high redshifts. On the other hand, extreme late-type galaxies (SED V) are very luminous in the UV which should significantly increase the detection probability. Thus, this effect complicates the comparison of the type distribution at low and at high redshifts.

- **Influence of the evolution of the real field extension**
  The real area of the FDF is a function of redshift, which causes that the total number of objects at high redshift will clearly exceed the number

at low redshift if evolutionary effects are excluded. This can lead to an apparently redshift-dependent frequency of spectral types if the detection probability is a function of redshift as discussed above. Hence, the number of SED V galaxies can increase towards higher redshifts due to a change of the real field area whereas the same effect for early-type galaxies could remain unnoticed because of their faintness in the UV rest-frame. However, for $\Omega_\Lambda = 0.7$, $\Omega_\mathrm{M} = 0.3$ and $H_0 = 67\,(\mathrm{km/s})/\mathrm{Mpc}$ (see Section 1.1, Carroll et al. 1992) the evolution of the field extension is rather modest and the area even decreases at $z > 1.6$, so that this effect should only play a role at low redshifts.

Both effects lead to an apparent evolution of the composition of spectral types. Thus, the influence of the evolution of the galaxy population on the the observed distribution can only be estimated by a quantitative study of all relevant effects which cannot be carried out in this work. However, at least the *change* of the composition of spectral types of the absolute brightest objects in the UV between $z = 2$ and 4 seems to be real, since in this range the discussed redshift-dependent effects are negligible.

Chapter 7

Scientific implications and opportunities of the data set

Until now, all analyses were carried out using the entire data set. In this way, the general appearance of the spectra could be investigated, the distribution of redshifts and the frequency of spectral types dependent on redshift. These analyses are suited to get a general overview on the basic properties of the spectroscopic sample. In order to study the physical properties of galaxies in detail, the analysis of rough classification parameters like redshift or spectral type is not sufficient. In this case, the full information of the present spectra has to be used. Such detailed spectroscopic studies go beyond the scope of this thesis which primarily represents a basic description of the FORS Deep Field spectroscopic survey. However, I will give an introduction to the analysis of the physical properties of high-redshift galaxies ($z \geq 2$), the class of objects which has consumed the bulk of observing time.

I begin this chapter with a comparison of mean spectra calculated from subsamples of high-redshift galaxies (Section 7.1). In Section 7.2 I turn to a discussion about the occurrence and strength of Lyα emission. Finally, I deal with an analysis of the equivalent width of C IV$\lambda\lambda$ 1548, 1551. Since this study was already published in Mehlert et al. (2002), I restrict the discussion on a brief summary of the essentials of this work.

7.1 Mean spectra of high-redshift galaxy subsamples

Mean spectra of spectroscopic subsamples selected by redshift and/or spectral type form an excellent tool in order to investigate typical properties of galaxy populations. The great advantage of this approach is that the averaging of extended samples leads to spectra with signal-to-noise ratios significantly higher than in case of the individual spectra. Hence, mean spectra principally allow to investigate weak spectral features which are normally not accessible to detailed analyses.

In this section I restrict the investigation of mean spectra to the comparison of the redshift ranges $2 < z < 3$ and $3 < z < 4$. The treatment of mean spectra representative to the given redshift ranges can be motivated by the apparent

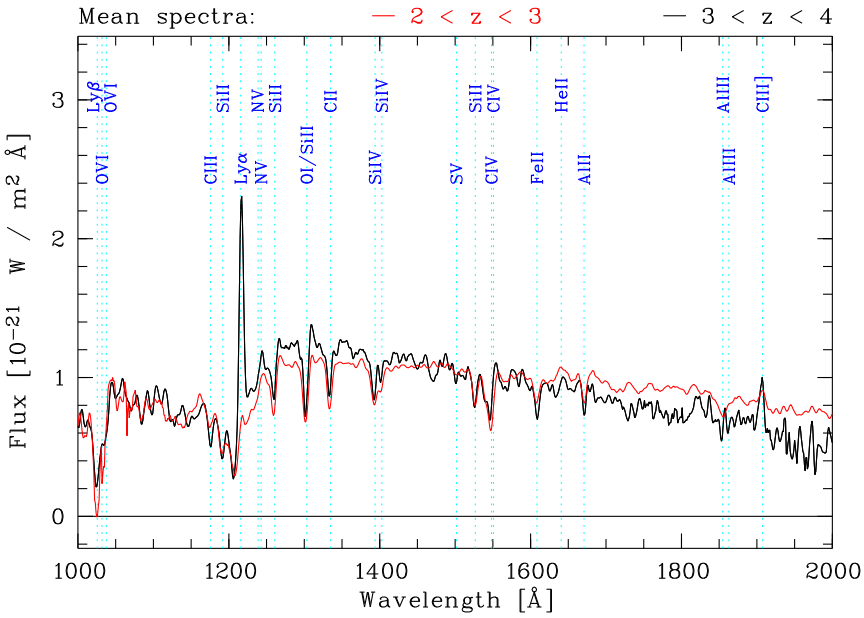

Figure 7.1: Comparison of mean spectra representative of the redshift domains ranging from $z = 2$ to 3 (red) and from $z = 3$ to 4 (black), respectively. Positions of prominent lines are indicated by cyan dotted lines and blue labels.

evolution of spectral types indicated in Fig. 6.7. In Section 6.3 it was stated that the fraction of type V increases from 40 % for $2 < z < 3$ to 88 % for $3 < z < 4$. This implies a possible change of the typical properties of the galaxy spectra. Best, this can be checked up by the calculation of corresponding mean spectra.

The basic approach to the calculation of mean spectra was already discussed in the framework of the construction of spectral templates for the redshift derivation via cross-correlation (see Section 5.4). The same procedure was adopted here.

Fig. 7.1 shows the final mean spectra of both redshift ranges. In order to minimise the noise of the average spectra only spectra with $S/N \geq 7$ were taken into account (see Section 5.1). The numbers of spectra which were included amount to 37 in case of $f_{2<z<3}(\lambda)$ ($\langle z \rangle = 2.39 \pm 0.19$) and 14 in case of $f_{3<z<4}(\lambda)$ ($\langle z \rangle = 3.35 \pm 0.19$). Fig. 7.2 shows the ratio $f_{3<z<4}(\lambda)/f_{2<z<3}(\lambda)$, which is also valuable for the comparison of the two spectra.

Both, Fig. 7.1 and 7.2 indicate striking differences between these two mean spectra. The most important ones are listed below:

Ly α emission: In $f_{3<z<4}(\lambda)$ Lyα shows a strong emission whereas in $f_{2<z<3}(\lambda)$ the emission component is almost absent (compare Section 7.2).

Ly α forest: The decrease of the flux ratio in Fig. 7.2 short-wards of Lyα by about (20 ± 5) % indicates an strengthening of the continuum absorption by the Lyα forest at higher redshifts.

C IV absorption: The strength of the C IV$\lambda\lambda$ 1548, 1551 absorption decreases towards higher redshifts (compare Section 7.3).

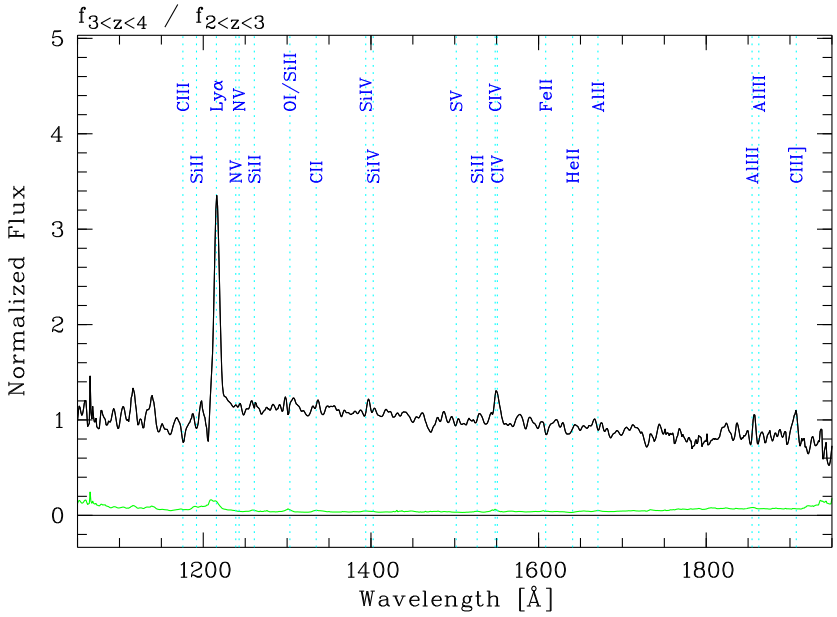

Figure 7.2: Ratio of the mean spectra $f_{3<z<4}(\lambda)$ and $f_{2<z<3}(\lambda)$ shown in Fig. 7.1. Positions of prominent lines are indicated by cyan dotted lines and blue labels. The green curve represents the noise level.

Continuum slope: $f_{3<z<4}(\lambda)$ indicates a pronounced increase of the continuum towards shorter wavelengths. In contrast, $f_{2<z<3}(\lambda)$ shows a rather flat spectrum.

The differences shown above imply a significant change of the observed galaxy population in the FDF between $\langle z \rangle = 2.4$ and 3.4. In order to get an idea which reasons could lead to the changes I will analyse some of the effects stated above in more detail. Since Lyα emission and C IV absorption will be treated in the following sections (7.2 and 7.3), I focus the discussion on the aspect of the continuum shape.

Continuum shape of high-redshift galaxy spectra

There are six causes which principally determine the slope of a galaxy (UV) spectrum. These are:

(1) **The star formation history:**
The evolution of the star formation rate determines the composition of the stellar population. Hence, a high active star formation (starburst) is the basis for the presence of high numbers of short-lived O and B stars necessary for a strong continuum in the UV.

(2) **Mass dependence of the star formation process:**
The course of the initial mass function (IMF) determines to what extent massive blue stars are created by the star formation process.

(3) **Chemical composition of stars:**
The UV continuum of massive stars is distinctly reduced by numerous absorption lines. Therefore, the decrease of the fraction of metals (elements heavier than helium) leads to an increase of the continuum.

(4) **Interstellar absorption:**
Numerous broad and optical thick interstellar absorption lines can cause a significant decrease of the UV continuum flux.

(5) **Dust extinction:**
Interstellar dust grains absorb and scatter continuum radiation which causes a reduction of the continuum flux especially in the UV. The effect gain in importance towards shorter wavelengths (see Cardelli et al. 1989). Strong dust extinction may lead to unusual red SEDs.

(6) **Active Galactic Nucleus:**
AGNs cause an additional non-stellar continuum increasing towards shorter wavelengths. It is assumed that this emission originates mainly in a hot accretion disk surrounding the central black hole.

In principle, all these effects could be responsible for the change of the mean spectra dependent on redshift. However, Heckman et al. (1998) have found a strong anti-correlation of the UV continuum slope β and the strengths of Si IV and C IV (mainly originating in stellar winds, compare Section 7.3) indicating that age effects of the stellar population are negligible as explanation of β regarding local starburst galaxies. In contrast, the relation implies a metallicity effect (portion of elements heavier than helium), since a lower metallicity will cause weaker wind lines as well as a lower dust extinction. Consequently, a higher β should mainly be caused by an increase of dust. This assumption is supported by the finding that the UV slope is related to the ratio of IR to UV flux. Meurer et al. (1999) could determine a similar relation for high-redshift galaxies using only the UV flux and β. Hence, the slope of the UV continuum in (high-redshift) galaxies should mainly be affected by dust extinction.

This hypothesis suggests that the increasing slope towards higher redshifts indicated by Fig. 7.2 will be caused by a decreasing dust extinction and hence a lower metallicity. This assumption has to be proved by a detailed analysis of the FDF spectroscopic data. Here, I concentrate on an estimate of the influence of dust by using the UV bump at 2200 Å (see Cardelli et al. 1989) which represents a prominent, broad dust absorption feature, probably caused by small carbon-rich particles. This feature should be a suitable indicator of the global dust extinction as long as the characteristic dust composition does not change a lot.

The best method to determine the change of the average UV bump with redshift would be to obtain the informations directly from the ratio $f_{3<z<4}(\lambda)/f_{2<z<3}(\lambda)$. But this is impracticable, since the UV bump can hardly be observed regarding galaxies at $z > 3$. Therefore, one has to apply a more indirect approach. Hence, the redshift distribution of spectral types shown in Fig. 6.7 suggests that the differences between $f_{2<z<3}(\lambda)$ and $f_{3<z<4}(\lambda)$ could be connected with the differences between type IV and V (Fig. 5.7), since the lower

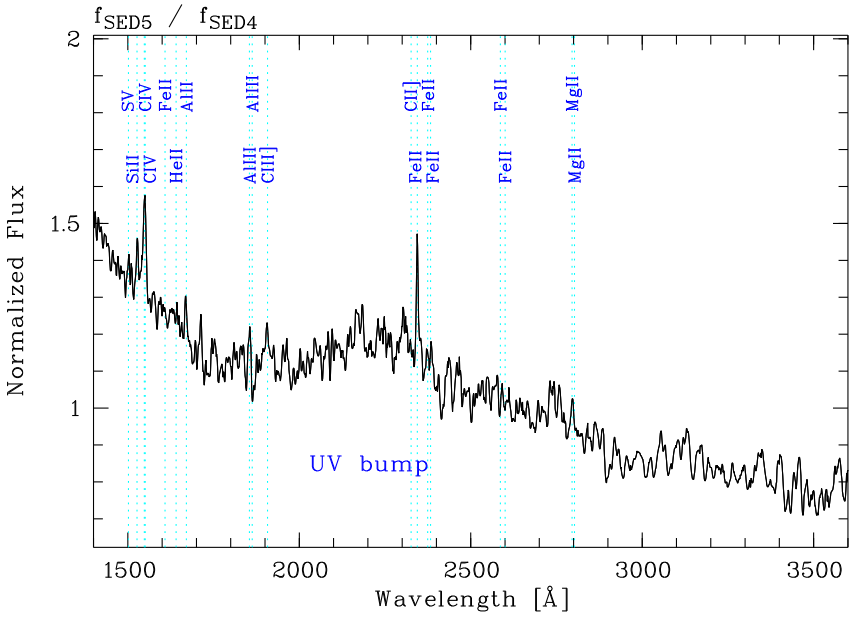

Figure 7.3: Ratio of SED V and SED IV (see Fig. 5.7). Positions of prominent lines are indicated by cyan dotted lines and blue labels. The range of the UV bump around 2200 Å is marked by a blue extra label.

redshift domain ($z < 3$) is dominated by SED IV spectra whereas the higher redshift range mainly shows SED V objects. Consequently, the ratio of the two SEDs ($f_{\mathrm{V}}(\lambda)/\ f_{\mathrm{IV}}(\lambda)$) was computed. Fig. 7.3 shows the resulting function in the wavelength range between 1400 and 3600 Å. In fact, the shape of the continuum indicates the presence of an excess flux in SED V or a depression in SED IV around 2200 Å. Since the UV bump of the interstellar extinction law results in a depression of galaxy spectra at this wavelength, the shape of the structure indicates that the UV bump is significantly stronger in type IV spectra than type V spectra. This is confirmed by a direct inspection of the templates (Fig. 5.7), since the UV bump could not be detected in SED V contrary to SED IV. This finding suggests that SED IV spectra are distinctly more affected by dust extinction as SED V spectra.

Now, the result of the comparison of SED IV and SED V can be transfered to the redshift selected samples which implies a decrease of the dust extinction between $\langle z \rangle = 2.4$ and 3.4. But this is still a very tentative result, since the knowledge about the origin of the UV bump is quite poor and dust destruction processes as caused by strong radiation sources like AGNs are not taken into account. A more quantitative treatment of this important issue has to be the subject of a future study. Nevertheless, a decrease of the UV bump intensity towards higher redshifts would agree with a corresponding increase of the continuum slope. Both effects could be caused by a decrease of the amount of dust which would mean a lower metallicity at higher redshifts. Thus, the metallicity seems to be a key parameter with regard to the interpretation of high-redshift data.

7.2 Occurrence and strength of Lyα emission

The Lyα line is the most important feature in optical high-redshift galaxy spectra. The line is generated by the transition between the inner L ($n = 2$) and K shell ($n = 1$) in (neutral) hydrogen (H I). The tremendous importance of the line has two reasons: (a) Lyα represents the transition with the highest probability in H I. (b) Hydrogen is by far the most frequent element in the universe.

Lyα essentially represents an interstellar resonance line. The origin of the emission feature basically depends on the existence of a hard radiation field ($\lambda < 912\,\text{Å}$, Lyman limit). This is mainly caused by either hot O and B stars located in star forming regions or an AGN providing a hot non-stellar thermal continuum. In detail, the hard radiation ionises the hydrogen of the interstellar medium to a high degree. Then, subsequent recombination processes of the H II are frequently realized by a series of successive transitions (cascade) ending up at the ground level. In this connection, the transition causing Lyα emission occurs especially frequently. In this way, a strong Lyα emission line can be created.

But this is not that what a remote observer usually sees in case of ordinary starburst galaxies. The problem is that the Lyα photons generated in the inner parts of the star forming regions have to manage to escape from the galaxy. The escape of Lyα is hampered by the presence of neutral hydrogen and of interstellar dust (see Charlot & Fall 1993). First of all, neutral hydrogen is necessary to produce Lyα in absorption. However, the 'hiding' of a Lyα photon by the excitation of a neutral hydrogen atom is only a temporary effect, since the excited state is not stable. Therefore, the Lyα will be re-emitted, but in any direction. Thus, the resonance absorption of Lyα photons effectively causes a scattering of the Lyα radiation. Multiple scattering can distinctly increase the path length which has to be covered by the photons in order to allow a successful escape from the galaxy. This enhances the probability that processes which ultimately destroy the Lyα photons will have an significant effect. In this respect, the absorption of UV photons by dust grains and the re-emission of the energy by IR photons plays a crucial role. Consequently, the combination of H I and dust may cause a complete destruction of the Lyα emission, so that a pure Lyα absorption feature is possible.

Dependent on the respective local conditions Lyα profiles of galaxy spectra could principally range from strong emission to pure absorption. In order to investigate the occurrence of the various profiles among the FDF high-redshift galaxies the spectra were classified by the strength of the Lyα emission in relation to the estimated intensity of the continuum without the line. As suitable measure (particularly for weak features) the emission equivalent width $W_{0,\mathrm{e}}$ was used. This quantity is defined by

$$W_{0,\mathrm{e}} = W_0 - W_{0,\mathrm{a}} = -\int_{\lambda_1}^{\lambda_2} \left(\frac{S_\mathrm{e}(\lambda)}{C(\lambda)}\right) \mathrm{d}\lambda \tag{7.1}$$

where $S(\lambda)$ represents the flux of the emission component and $C(\lambda)$ the approximated continuum flux. By convention emission lines have negative equivalent

Table 7.1: Distribution of Lyα types $T_{\mathrm{Ly}\alpha}$ (definition see text) classifying the FDF high-redshift galaxies with $Q_{\mathrm{z}} = 4$. The table indicates for each Lyα type the total number of objects N, the median redshift $\overline{z}$ and the mean redshift $\langle z \rangle$ with its standard deviation.

$T_{\mathrm{Ly}\alpha}$	N	$\overline{z}$	$\langle z \rangle$
0	30	2.4	2.6 ± 0.4
1	13	2.3	2.8 ± 0.8
2	20	3.2	3.2 ± 0.8
3	11	3.4	3.7 ± 0.9

widths. (7.1) is based on the definition of the universal equivalent width W_0 which is given by

$$W_0 = \int_{\lambda_1}^{\lambda_2} \left(1 - \frac{S(\lambda)}{C(\lambda)}\right) \mathrm{d}\lambda \tag{7.2}$$

with $S(\lambda)$ as the measured spectral flux (line + continuum).

The measurement of $W_{0,\mathrm{e}}$ is connected with high uncertainties caused by the complexity of the line. So, it is a challenging task to derive the shape of the continuum in the range of Lyα. This is mainly caused by the strong variation of the continuum in the wavelength region concerned, the large width of the feature and the Lyα forest on the blue side of the line. Furthermore, especially in case of absorption and emission components of a comparable strength the clean separation of both structures can be quite difficult. Finally, regarding low S/N the discrimination between weak Lyα emission and noise peaks may become impossible.

Therefore, the specification of accurate values was abandoned. In contrast, the galaxy spectra were divided in four classes using $W_{0,\mathrm{e}}$ as primary classification parameter. This is precise enough regarding the following discussion which shall give a first review on the Lyα characteristics of the FDF spectroscopic sample. The Lyα types ($T_{\mathrm{Ly}\alpha}$) were defined in the following manner:

$T_{\mathrm{Ly}\alpha} = 0$: No (evident) emission
$T_{\mathrm{Ly}\alpha} = 1$: Very weak or uncertain emission
$T_{\mathrm{Ly}\alpha} = 2$: Significant emission ($-W_{0,\mathrm{e}} > 2\,$Å)
$T_{\mathrm{Ly}\alpha} = 3$: Strong emission ($-W_{0,\mathrm{e}} > 20\,$Å, all SED VI galaxies)

The results of the Lyα classification of the FDF spectroscopic sample are shown in Fig. 7.4. The different Lyα types are indicated by coloured bars (see legend). The histogram shows a conspicuous change of the typical Lyα characteristics from $z = 2$ to 5. For instance, at redshifts $2 < z < 3$ significant Lyα emission is rather an exception, since only 19 % of the spectra shows significant emission components ($T_{\mathrm{Ly}\alpha} \geq 2$). Furthermore, only one of 11 Lyα bright galaxies (LABs, $T_{\mathrm{Ly}\alpha} = 3$) is located at $z < 3$. A completely different situation is given at higher redshifts. Here, the fraction of galaxies indicating significant emission increases to 63 % at redshifts $3 < z < 4$ and finally 78 % at $4 < z < 5$. Considering only the galaxies with strong Lyα emission the corresponding values amount to 25 % and 44 %. In Table 7.1 mean and median redshifts of the

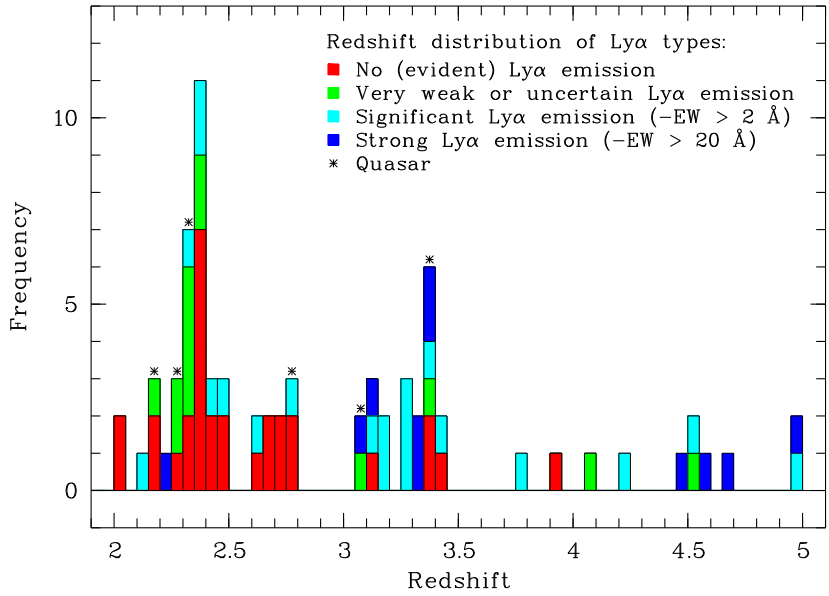

Figure 7.4: Redshift distribution of different Lyα types classifying the FDF high-redshift spectra with $Q_z = 4$ according to the strength of the Lyα emission. The individual classes are described by the legend inside the diagram. Furthermore, each type is allocated a colour indicating the corresponding galaxies in the histogram. The occurrence of quasars is marked by asterisks above the bars.

individual Lyα classes are represented. These values also demonstrate the striking increase of frequency and strength of Lyα emission towards higher redshifts.

Possible errors of the type distribution were already discussed in Section 6.3. Furthermore, the number of Lyα bright galaxies ($T_{\mathrm{Ly}\alpha} = 3$) probably exceeds the representative value, since it is easier to detect a galaxy with strong Lyα emission as without. Hence, three objects represented in Fig. 7.4 (2206 at $z = 4.473$, 4454 at $z = 3.085$ and 4691 at $z = 3.304$) were discovered serendipitously (secondary objects) because of their strong Lyα emission. Nevertheless, this selection effect scarcely depends on redshift. Only at $z > 4.6$ where Lyα runs into strong OH bands the identification of galaxies without strong Lyα emission could systematically be hampered. Hence, the central finding that the frequency and strength of Lyα emission tends to be higher at higher redshifts should not be affected by strong selection biases.

Origin of strong Lyα emission

In the second part of this section I treat the issue of the origin of strong Lyα emission. An answer to this question is the basis to the interpretation of Fig. 7.4. However, a detailed investigation of this topic is beyond the scope of this work, so that the following discussion can only show tendencies.

As already discussed above, Lyα emission is distinctly reduced by high amounts of neutral hydrogen and interstellar dust. Hence, there are essentially three scenarios which might lead to a significant conservation of the Lyα emission. These

are:

(1) **Low metallicity:**
This causes a distinct reduction of the dust production which enhances the probability that a Lyα photon is not destroyed by dust absorption and can escape from galaxy.

(2) **Special structure and dynamics of the interstellar medium:**
Escape of Lyα photons by gaps in the veiling screen of neutral hydrogen and dust in direction towards the observer (see Giavalisco et al. 1996). In case of strong outflows: As consequence of the Doppler effect the outflowing interstellar matter essentially absorbs at the blue side of the Lyα line, so that Lyα photons contributing to the red side of the profile (backscattered from the opposite inner 'wall' of the expanding gas) could escape (see Kunth et al. 1998).

(3) **External ionization by a quasar:**
Lyα photons as consequence of the ionisation of outer regions of a galaxy (or a hydrogen cloud) by a nearby quasar. Moreover, the resonant scattering of Lyα photons (from the quasar) could already lead to an emission profile.

In the following I discuss to what extent the three scenarios could be used to explain the observed strong Lyα emission lines.

To scenario (1): The UV spectroscopy of the starburst dwarf galaxy IZw 18 (Kunth et al. 1994) has shown that even in the case of a extremely low metallicity of $Z = 0.02\,Z_{\odot}$ a Lyα emission component can be completely absent. Thus, the resonance scattering of Lyα photons by neutral hydrogen (Charlot & Fall 1993) has to be so effective, that the appearance of an emission profile only caused by low metallicity seems to be very unlikely. Therefore, this scenario is not further discussed with regard to the present sample, particularly since significant metal lines could be found in almost all FDF galaxy spectra having a sufficient S/N (see Appendix D).

To scenario (2): According to Kunth et al. (1998) structure and especially dynamics of the interstellar medium are responsible for the origin of Lyα emission. With reference to this scenario the FDF object 4691 at $z = 3.304$ shows a remarkable spectrum (Fig. 7.5). The S/N is sufficiently high (~ 10 regarding the continuum) that various spectral lines can be identified besides the strong Lyα emission which amounts to about 100 Å in the rest-frame (see Fig. D.13). The most striking features are the strong P Cygni profiles of N V, C II, Si IV and C IV and the pronounced emission lines of He II and C III]. The various strong metal lines exclude a low metallicity (see above) in explanation of the powerful Lyα emission. However, the large separation between the emission and the blue-shifted absorption of the P Cygni profiles indicates outflow velocities higher than 1000 km/s. These large values and the very steep continuum point to a powerful energy source in the interior which could be strong enough to break up (by ionisation) the barrier of H I and dust preventing the escape of Lyα photons. At least the dynamical aspect concerning the strong blue-shift of

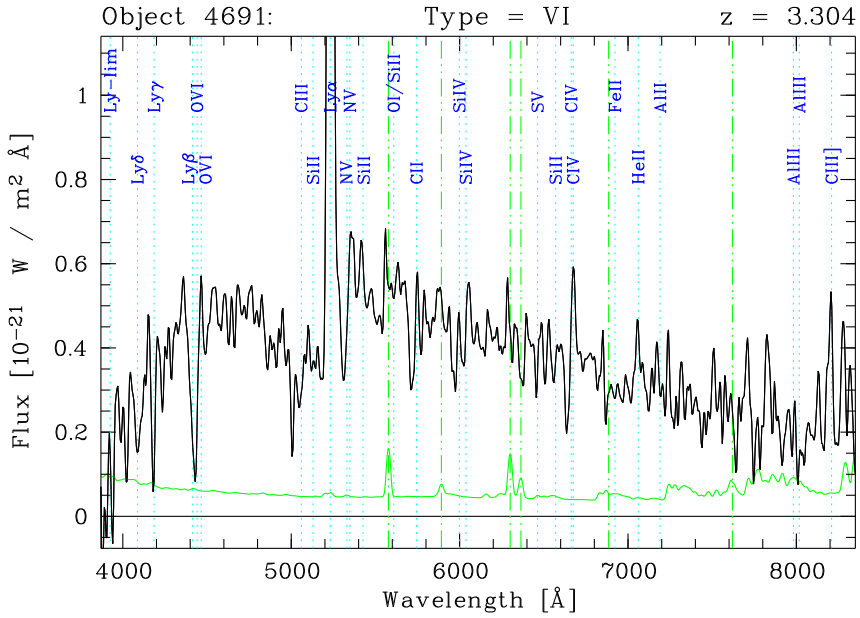

Figure 7.5: Spectrum of the strong Lyα emitter 4691 ($-W_0 \sim 100$ Å). It was renounced to represent the full Lyα profile (see Fig. D.13) in order to show the prominent P Cygni profiles of N V, C II, Si IV and C IV and the pronounced emissions of He II and C III] in an optimum way. Details to the representation can be found in Appendix D.

the absorption should lead to a significant increase of Lyα emission. The strong outflow velocities primarily suggest an AGN as central energy source, although then the continuum would be surprisingly faint. This interpretation would mean that the strong Lyα emission was not mainly caused by star formation. Nevertheless, before a detailed spectroscopic analysis will not be carried out it cannot be excluded that an extreme starburst event may be able to produce a spectrum as plotted in Fig. 7.5.

Regarding the high-redshift sample of the FDF 4691 represents an extreme example indicating various emission components and strong outflows. Usually the spectra are dominated by absorption lines (e.g. Fig. 7.1). Significant P Cygni profiles are rare. However, blue-shifted (interstellar) absorption lines seem to be a common feature in high-redshift galaxies. Hence, in Section 5.2 the centre positions of spectral lines were related to the position determined by the respective spectroscopic redshift (see Table 5.1). The given relative redshift deviations can be transformed in velocities by

$$v = c\,\frac{\Delta z}{z+1}\,, \qquad v \ll c \tag{7.3}$$

where c is the velocity of light. Then, the interstellar absorption lines indicate significant outflows typically amounting to 200 – 300 km/s with an uncertainty not higher than 100 km/s mainly caused by systematic redshift errors (see Section 5.7). This agrees well with results of Pettini et al. (2000) and Frye et al. (2002). Furthermore, measurements of the position of Lyα emission components indicate a significant red-shift also in the range of a few 100 km/s. This implies

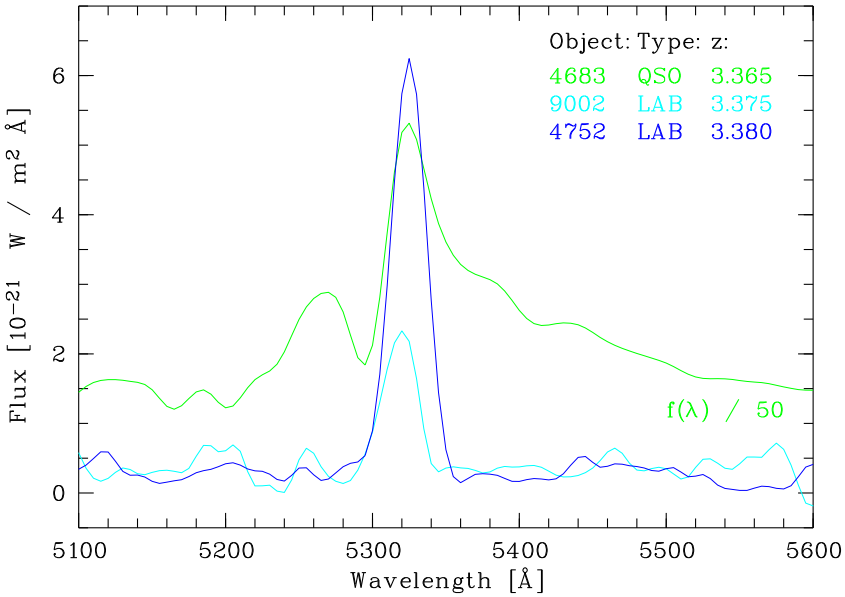

Figure 7.6: Lyα lines of the LABs 4752 (blue) and 9002 (cyan) and the QSO 4683 (green; Q 0130–260, see Section 1.4) in observer's frame. The bright spectrum of 4683 was divided by 50 in order to allow a direct comparison. For the measured redshifts of the objects see legend inside the plot.

that the origin of strong Lyα emission cannot usually be explained without the existence of large-scale outflows (see Kunth et al. 1998). However, the derivation of the average outflow velocities for the different Lyα classes has turned out that the typical velocities seem to be almost independent of the Lyα strength. Strong Lyα emitters like 4691 could form a probable exception, but this cannot be proved owing to the frequent weakness of the continua. Therefore, strong outflows cannot be the only criterion for the occurrence of Lyα emission, so that further aspects like the morphology or the internal energy source(s) have to be taken into account. Moreover, a suitable model should also explain the increase of occurrence and strength of Lyα emission with redshift as indicated in Fig. 7.4. Frye et al. (2002) suggest that such a trend can be the consequence of a genuine evolutionary effect towards younger stellar populations at higher redshift. However, such explanations remain speculative with regard to the FDF spectroscopic sample as long as no detailed analysis will have been carried out. Therefore, an extended discussion of this issue has to be postponed to a future study.

To scenario (3): As last aspect of the discussion, now I turn to the impact of close quasars on the occurrence of strong Lyα emission. In Fig. 7.4 the redshifts of evident quasars (type VII) are indicated by asterisks plotted above the bars. There are three coincidences of strong Lyα emitters and quasars, in fact 4454 with QSO 2633 at $z \sim 3.08$ and 4752 and 9002 with QSO 4683 (Q 0130–260, see Section 1.4) at $z \sim 3.37$. By way of illustration, in the latter case the observed Lyα profiles are plotted in Fig. 7.6. The flux of 4683 was divided by 50 because

of the extremely high luminosity in comparison with the LABs. The shown redshift discrepancies reaching up to 0.015 should not be overvaluated, since the redshift accuracies of the concerned objects are not very high (several 10^{-3}) and the redshift does not consider the peculiar velocities of the objects. However, Fig. 7.6 demonstrates a good correspondence of the Lyα profile maxima.

The observed LABs which are located in the vicinity of QSOs show the following properties:

- The projected distances of 4752 and 9002 to QSO 4683 amount to less than $5''$. According to Carroll et al. (1992) this transforms to 40 kpc and less when taking the cosmological parameters $\Omega_\Lambda = 0.7$, $\Omega_\mathrm{M} = 0.3$ and $H_0 = 67\,(\mathrm{km/s})/\mathrm{Mpc}$ (compare Section 1.1). Regarding 4454 the projected distance to the quasar 2633 results in $91''$ (≈ 730 kpc) which is distinctly higher than in the first case.

- The projected angular extensions of the Lyαemission in relation to the nearby quasar are about 25° for 4752, 20° for 9002 and 1° for 4454. The images of the LABs (see Heidt et al. 2002) indicate a rather cloudy and diffuse character, respectively.

- The LABs are characterised by very weak continua (e.g. $\sim 0.1 \times 10^{-21}$ W/m^{2}Å in case of 4454) which causes great problems to obtain an accurate photometry of these objects. On the other hand, the Lyα emission is quite strong, so that high rest-frame equivalent widths are achieved like (120 ± 20) Å in case of 4752.

The interpretation that the quasar forms the energy source of the Lyα emission of the LAB requires a high luminosity of the AGN, a minimum of Lyα destruction in the range between AGN and LAB, a small mutual distance and a significant coverage of an assumed sphere centred on the quasar. The strength of the Lyα emission can be estimated on the assumption that the quasar radiates isotropically, the projected distance is the real distance (upper threshold) and the LAB re-radiates the Lyα emission without significant losses. Regarding 4752 a diameter of 25° (as seen from the quasar) results in a coverage of $\approx 1.2\,\%$ whereas the ratio of the Lyα flux of LAB and QSO (see Fig. 7.6) results in $\approx 2\,\%$. Thus, the values are of the same order of magnitude, although the flux of the quasar seems to be too small. However, the uncertainties of the estimate are high because of the probable anisotropy of the quasar radiation, the uncertainties regarding the distance and size of the Lyα emitter and probable errors of the photometric fluxes. Hence, a final assessment of the situation is not yet possible. Nevertheless, 4752 and 9002 are sufficiently close to the quasar that, at least, a part of the emission can directly be caused by the QSO. Furthermore, the extremely faint continua and the diffuse appearance of the images are consistent with the scenario that the quasar affects very faint galaxies or even 'hydrogen clouds' in its neighbourhood. The relatively large distance between LAB 4454 and QSO 2633 seems to exclude scenario (3) as possible explanation of the observed Lyα emission.

7.3 Equivalent width measurements of C IV

In the final part of this chapter I discuss a detailed study of C IV equivalent widths measured by the high-redshift galaxies of the FDF spectroscopic sample. The analysis was already published in Mehlert et al. (2002). Thus, I only give a brief summary of the study in order to demonstrate the capacity of the present sample.

C IV equivalent widths

According to Walborn et al. (1995) high-excitation lines like C IV are produced mostly in stellar photospheres and winds and their strengths depend sensitively on the stellar metallicity. In fact, there is partly a non-negligible contamination by an interstellar absorption component, but normally the line profile is dominated by the stellar features (Heckman et al. 1998). Furthermore, investigations of synthetic starburst spectra of Leitherer et al. (2001) have shown that for ages $\geq 10\,\mathrm{Ma}$ the strength of C IV strongly depends on metallicity and is almost independent of the age of the starburst.

Therefore, the rest-frame equivalent widths W_0 of this feature were measured applying the approximation

$$W_0 = \Delta\lambda - \frac{1}{C(\lambda_0)} \int_{\lambda 1}^{\lambda 2} S(\lambda)\mathrm{d}\lambda \text{ with}$$
$$\lambda_1 = \lambda_0 - \frac{\Delta\lambda}{2};\ \lambda_2 = \lambda_0 + \frac{\Delta\lambda}{2} \tag{7.4}$$

(compare 7.2). $\lambda_0 = 1549.5\,\text{Å}$ and $\Delta\lambda = 30\,\text{Å}$ were used as parameters for C IV. The continuum flux at λ_0 was approximated by the mean flux within two well defined continuum windows (width of 75 Å each) enclosing the central line window (for further details see paper).

W_0 was measured for 51 galaxies with reliable spectroscopic redshifts $z > 1.35$ (i.e. galaxies where the C IV doublet was redshifted into the spectral range accessible by the observations). High-redshift galaxies showing strong Lyα emission (type VI, see Table C.1) and/or clear P Cygni profiles (e.g. 4691, see Fig. 7.5) were excluded from the sample in order to avoid the contamination of the C IV profile by an emission component. W_0 measurements were also done using IUE[1] low resolution spectra for a comparison sample of 36 starburst galaxies at $z \approx 0$ (see Heckman et al. 1998).

Fig. 7.7 shows the results of the measurements. The plot indicates that the high-redshift galaxies with $z < 2.5$ have about the same average C IV equivalent widths and about the same scatter around the average as the local starburst galaxies. However, for redshifts larger than about 2.5 the average C IV equivalent widths and their scatter clearly decrease with redshift. In order to estimate the statistical significance of the effect, averages and their mean errors of the W_0(C IV) values were calculated for selected redshift bins. From Fig. 7.8 it is

[1] **I**nternational **U**ltraviolet **E**xplorer

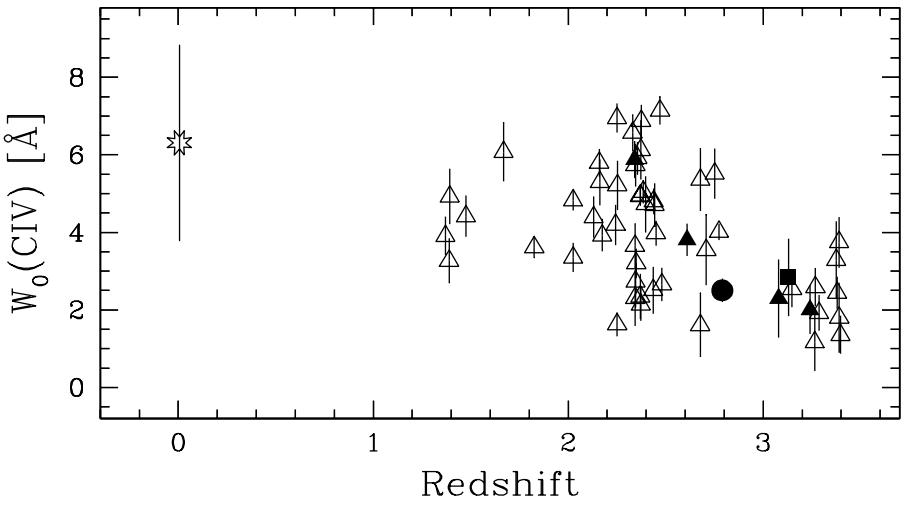

Figure 7.7: Measured C IV equivalent widths as a function of z. Open star at $z \approx 0$: Average and $1\,\sigma$ rms scatter for the 36 local starburst galaxies (Heckman et al. 1998). Open triangles – FDF galaxies. Filled triangles – Galaxies from cluster 1E0657-558 (see Mehlert et al. 2001). Filled circle and square – Galaxies in the HDF-S and AXAF Deep Field, respectively (see Cristiani et al. 2000).

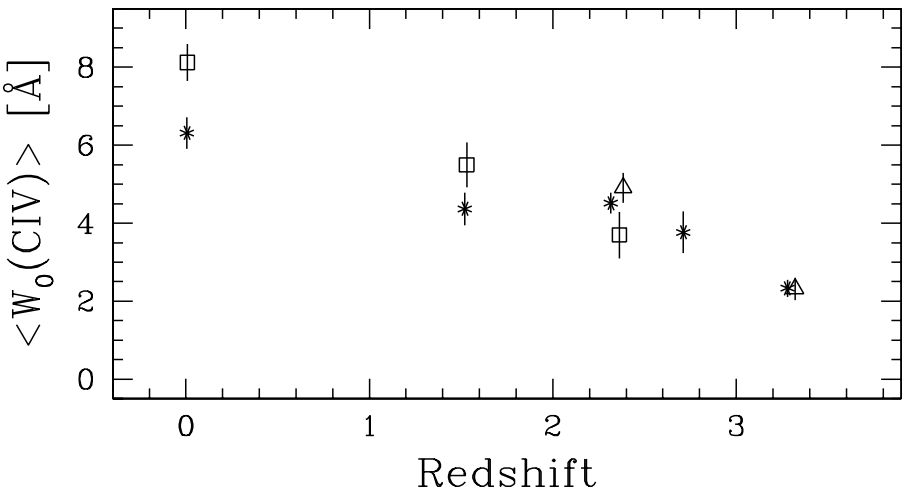

Figure 7.8: Averages of the measured C IV equivalent widths within selected z bins as a function of z. Asterisks – all galaxies shown in Fig. 7.7. Open triangles and squares – FDF galaxies with magnitude $M_B \leq -22^m.36$ and $-21^m.52 \leq M_B \leq -20^m.38$, respectively (see Fig. 7.9). The bars indicate the mean errors of the averages.

clear that for the three bins with $z < 2.5$ no statistically significant differences are present. However, the difference between the local sample and the high-redshift galaxies with $z > 3.0$ is highly significant ($> 9\,\sigma$).

Metallicities

Since differences of the C IV line strength cannot be easily explained by population differences in the starburst galaxies, the observed decrease of the C IV equivalent width values for $z > 2.5$ can at present only be interpreted as a metallicity effect. Hence, the decrease of W_0(C IV) with redshift is expected to contain information on the evolution of the metal content of starburst galaxies with cosmic age. In order to derive a more quantitative measure of this metallicity evolution the observed W_0(C IV) were calibrated in terms of the O/H ratios by using the oxygen abundances listed for 45 local starburst galaxies in Heckman et al. (1998). The metallicity derived obviously correlates with the measured W_0(C IV) values and the best linear least square fit to these data gives

$$\log Z/Z_\odot = 0.13(\pm 0.02) \times W_0(\mathrm{C\,IV}) - 1.10(\pm 0.12)\,.$$

Assuming that this correlation is also valid for the high-redshift starburst galaxies the observed C IV equivalent width values can be converted to metallicities. In this way the FDF galaxies with $z > 3$ ($\langle z \rangle = 3.24$) have an average metallicity of about $0.16\,Z_\odot$ and for $\langle z \rangle = 2.34$ a value of $0.42\,Z_\odot$. The corresponding local ($z \approx 0$) value would be $0.56\,Z_\odot$. In terms of cosmic time scales ($\Omega_\Lambda = 0.7, \Omega_\mathrm{M} = 0.3, H_0 = 67\,(\mathrm{km/s})/\mathrm{Mpc}$, compare Section 1.1) this would correspond to an increase of the mean metallicity in starburst galaxies by a factor of 2.5 within $\approx 1\,\mathrm{Ga}$ between cosmic ages of about 1.9 Ga and 2.9 Ga. For later epochs the data suggest only little further enrichment.

Luminosity effects

For local ($z \approx 0$) galaxies the metallicities are known to depend on the galaxies' blue and infrared luminosities, with luminous galaxies tending to have higher metallicities (see e.g. Kobulnicky & Zaritsky 1999 and Heckman et al. 1998). To test whether at high redshifts a metallicity-luminosity correlation does exist and may affect the apparent metallicity evolution, Fig. 7.9 shows the absolute rest-frame B magnitudes $\mathrm{M_B}$ of all high-redshift FDF galaxies as well as for the local starburst galaxies.

For the FDF galaxies $\mathrm{M_B}$ was computed applying the semi-empirical SEDs used to the derivation of the photometric redshifts (see Section 2.2 and Gabasch et al. 2002). In detail, for each galaxy the SED fitting best the photometric data was taken and scaled to the total I flux. Then this SED was transformed to $z = 0$ using the observed spectroscopic redshifts (see Appendix C). Finally, the absolute B magnitudes were derived assuming the cosmology parameters $H_0 = 67$, $\Omega_m = 0.3$, $\Omega_\Lambda = 0.7$. The values have been corrected for foreground Galactic extinction but not for any internal extinction in the starburst galaxies. For the local objects the $\mathrm{M_B}$ was taken from Heckman et al. (1998), but transformed to the cosmology used.

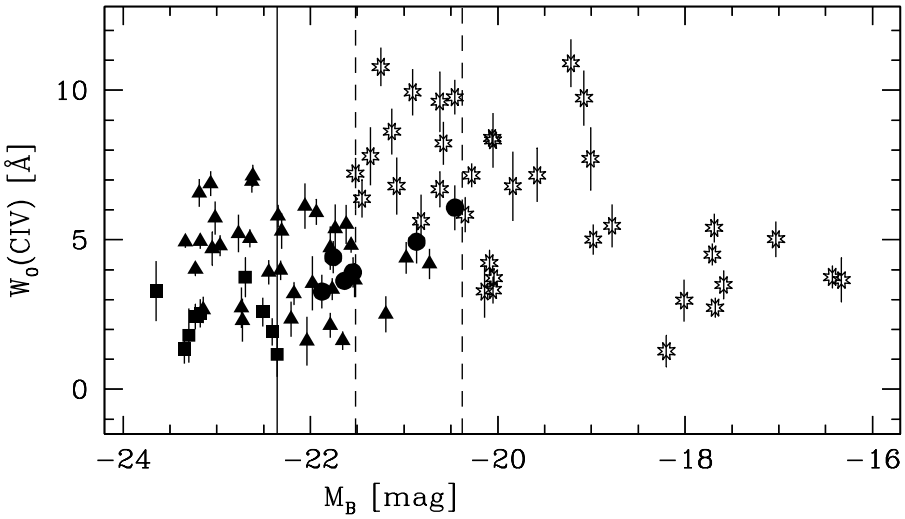

Figure 7.9: C IV equivalent widths of the local (open stars) and the high-redshift FDF (filled symbols) starburst galaxies versus the absolute B magnitude. For the latter ones we indicated objects within the different redshift bins. The solid vertical line indicates $M_B = -22\overset{m}{.}36$ and the dashed vertical lines indicate $M_B = -21\overset{m}{.}52$ and $M_B = -20\overset{m}{.}38$.

Fig. 7.9 demonstrates that the local starburst galaxies indeed show the expected correlation between W_0(C IV) (metallicity indicator) and the luminosity. Whether a metallicity-luminosity correlation does exist for the high-redshift galaxies cannot be determined, since there are no faint objects in the high-redshift sample. But it is evident that the high-redshift galaxies are on average overluminous for their metallicities as compared to local starburst galaxies. This agrees well with earlier results by Pettini et al. (2001) and Kobulnicky & Koo (2000) who find this trend for Lyman-break galaxies. Hence, if a metallicity-luminosity relation does exist at high redshifts, the present data suggest a clear offset to the local correlation, which seems to evolve with redshift. Moreover, it is obvious that for the high-redshift galaxies there is no correlation between the measured W_0(C IV) and the luminosity that may produce the observed metallicity evolution.

At high redshifts no faint objects are in the sample, while in the local universe bright starburst galaxies are not be found. Thus, one has to make sure that the observed metallicity evolution is not an artifact due to comparing different objects at different redshifts. Therefore, all galaxies which are brighter than the faintest one at $z \geq 3$ (which is $M_B = -22\overset{m}{.}36$, solid line in Fig. 7.9) were separately investigated. In the FDF sample only galaxies can be found which are brighter than this limit for $z \geq 2$. From their average values of the measured W_0(C IV) (open triangles in Fig. 7.8) and the mean error it is obvious that these subsample show the same trend with decreasing redshift as the total galaxy sample at $z \geq 2$. The same is true for all galaxies fainter than $M_B = -21\overset{m}{.}52$ (brightest local galaxy) and brighter than $M_B = -20\overset{m}{.}38$ (faintest galaxy with $z \geq 1$, open squares in Fig. 7.8). From this test one can conclude that the observed dependence of W_0(C IV) on redshift is not caused by luminosity effects.

Chapter 8

Conclusions

In the present thesis I presented the low-resolution spectroscopic survey of the FORS Deep Field project. The main objective of this work was to set up a spectroscopic data base of a quality suited to investigate important questions concerning the evolution of galaxies with cosmic age.

To achieve this aim the sample selection and the observation planning was mainly based upon three criteria:

- Statistically significant subsamples of galaxies for the different redshift domains ($\Delta z = 0.5 - 1$) for $z \leq 5$
- Large wavelength coverage of the spectra to facilitate the derivation of redshifts and spectral types and to allow comparative studies of galaxies over a wide redshift range
- High S/N spectra ($S/N > 10$), particularly in case of faint high-redshift galaxies, in order to enable detailed spectroscopic studies.

For the success of such an ambitious project it is fundamental to have a large high-quality observational data set. This could be achieved, since the FDF spectroscopic survey was carried out as part of the guaranteed time project for the two FORS instruments at the VLT (see Section 1.4). Hence, more than 56 h of multi-object spectroscopy with the low resolution grism 150 I could be achieved in the FDF (see Chapter 3). All in all 539 objects were observed.

The main part of the work was devoted to develop and carry out an accurate data reduction (Chapter 4) and to the derivation of fundamental parameters like redshift and spectral types (Chapter 5). This data reduction and a basic analysis form the basis of further studies. As result of the entire procedure, the FDF spectroscopic sample consists now of 539 one-dimensional, co-added, optical spectra. The spectra are flux-calibrated and Galactic extinction corrected. In the case of 298 objects ($Q_z \geq 3$) redshifts and rough spectral types have been derived by cross-correlating the spectra with empirical templates gained from the FDF spectroscopic sample itself (see Chapter 4).

The spectra obtained were subjected to a first analysis regarding the individual properties of the FDF objects as well as the general properties of the whole sample. In this context, especially the distribution of the basic parameters, such

as the redshift and the spectral type was investigated (Section 6.3). In order to demonstrate the research opportunities of the FDF spectroscopic sample I exemplary discussed conspicuous properties of the FDF high-redshift galaxies using mean spectra of subsamples and equivalent width measurements of individual lines as analysis tools (Chapter 7). In summary, the first analysis of the properties of FDF spectroscopic sample has led to the following (preliminary) results:

(1) The sample contains 33 stars covering the spectral types from G to L. The faintness of the stars mainly indicates a location in the Galactic halo or the thick disk and consequently the membership of the population II.

(2) The sample includes 7 evident quasars in the redshift range between 0.8 and 3.4. QSO 6233 represents the rare class of broad absorption line quasars (BAL) with strong blue-shifted absorption troughs of Si IV, C IV and Al III.

(3) The sample includes 265 galaxies ($Q_z \geq 3$) ranging from $z = 0.09$ to 5.00.

(4) The observed redshift distribution indicates a clustering of redshifts in the FDF at $z = 0.3$, 0.8, 2.4 and 3.4 as consequence of the cosmic large-scale structure. In the small redshift range between $z = 0.332$ and 0.339 the clustering is particularly pronounced (23 objects). In part this can be attributed to a small evolved galaxy cluster in the field.

(5) The redshift distribution of spectral types indicates an apparent evolution of the galaxy population dependent on cosmic age. At low redshifts ($z < 0.5$) the population is dominated by early-type and medium-type galaxies like ellipticals and spirals, whereas at high redshifts ($z > 2$) the observed objects are mainly (strong) starburst galaxies.

(6) The ratio of the redshift-selected mean spectra $f_{3<z<4}(\lambda)$ and $f_{2<z<3}(\lambda)$ indicates a 20 % decrease of the continuum short-wards of Lyα as consequence of the increase of the Lyα forest absorption with redshift.

(7) The average slope of the UV continuum increases with redshift. The portion of observed galaxies with steep spectra (SED V) increases from 40 % for $2 < z < 3$ to 88 % for $3 < z < 4$.

(8) SED IV shows an pronounced UV depression at 2200 Å. In contrast, this feature is almost absent in case of SED V. This implies a significant decrease of dust extinction between SED IV and SED V.

(9) Results (7) and (8) in combination tentatively suggest an decrease of dust extinction towards higher redshifts.

(10) The occurrence and the average strength of Lyα emission increase with redshift.

(11) There are Lyα emission galaxies ($-W_0 > 20$ Å) showing conspicuous metallic absorption features. In case of 4691, which shows strong P Cygni profiles of metal lines, the origin of Lyα could be powered by an AGN.

(12) Outflows of a few 100 km/s are a general feature of high-redshift galaxies. Red-shifted Lyα emission in relation to the interstellar absorption lines implies an important role of outflows for the escape of Lyα photons from the galaxy, although a significant relation of outflow velocity to Lyα equivalent width could not be proved.

(13) There are two strong Lyα emitters (4752 and 9002) whose Lyα emission is probably caused by a nearby quasar (Q 0130–260).

(14) A detailed study of the C IV equivalent width indicates a decrease of the metallicity with increasing redshift. This result does not seem to depend on luminosity effects.

The great variety of (preliminary) results shown above suggests that the FDF spectroscopic sample seems to be well suited as a basis for numerous applications concerning the evolution of galaxies. Hence, the main objective of this work to set up a representative spectroscopic data basis of a quality suitable to investigate the evolution of the physical properties of galaxies on cosmic age could be achieved.

Of course, the FDF spectroscopic survey has its limits. The size of the field ($7' \times 7'$), while larger than the HDFs, is still rather small, so that the number of bright high-redshift galaxies accessible to a detailed spectroscopy remains small. Furthermore, the distribution of object properties dependent on redshift is certainly affected by the characteristics of the large-scale structure in direction to the field. However, at least the comparison of the measured C IV equivalent widths with data from literature (see Mehlert et al. 2002) has shown that the FDF does not seem to be an untypical field.

A further restriction of the usability of the data set is the low resolution of the spectra. However, regarding the high-redshift domain the galaxies are often to faint to achieve suitable signal-to-noise ratios in case of a significantly higher resolution. Only in case of the investigation of the brightest high-redshift galaxies and Lyα emission lines high spectral resolution appears feasible.

In summary, the spectroscopic sample of the FORS Deep Field seems to be a representative deep probe of the universe which is mainly limited by the capacity of today's observing instruments.

Appendix A

Journal of observations

The low-resolution spectroscopic observations of the FORS Deep Field were carried out at the ESO-VLT (Paranal, Chile) using the two FORS instruments (see Chapter 3). A summary of the 102 multi-slit or long-slit spectroscopic observations is given by Table A.1. In all cases the low resolution grism 150 I (see Fig. 3.5) without order separation filter was used. In each case the slit width was $1''$.

The individual columns of Table A.1 contain the following information:

ID: Identity number of the exposure used as reference.

Type: Character of the observing run. C = commissioning run, B = backup programme, M = main programme.

Run: Internal run designation.

Mask: Internal mask set-up designation.

N: Number of exposure for this mask set-up.

UT x: Number of the VLT telescope. 1 = Antu, 2 = Kueyen, 3 = Melipal, 4 = Yepun.

FORS x: Number of the FORS instrument.

Mode: Spectroscopic mode. LSS = long-slit spectroscopy, MOS = multi-object spectroscopy (19 flexible slitlets), MXU = mask exchange unit (laser-cut mask).

Date: Date of the start of the observing night in the format year–month–day.

LMST: Local mean sidereal time at Paranal in hours at the start of the exposure.

T_{exp}: Exposure time in minutes.

AM: Effective airmass of the exposure calculated from equation 4.3.

Seeing: Average DIMM-seeing (seeing monitor) of the exposure in arcseconds. The DIMM-seeing can differ from the actual seeing at the telescope. The amount of the deviations depends on the climatic conditions. Especially at low wind velocities the actual seeing may be better by up to $0\overset{m}{.}3$ (or even more). This happened, e.g., during the nights starting at 2001-10-13 and 2001-10-14.

Observers: Observers of the run. In case of commissioning and service mode observations no individual observer is specified.

Table A.1: List of the spectroscopic observations of the FORS Deep Field carried out at the VLT with grism 150 I. The individual columns are explained in the text.

ID	Type	Run	Mask	N	UT x	FORS x	Mode	Date	LMST [h]	$T_{\rm exp}$ [min]	AM	Seeing [″]	Observers
001	C	F1c1	cl1	1	1	1	LSS	1998-09-23	02.7	15	1.09	0.58	I. Appenzeller et al.
002				2				1998-09-23	03.1	15	1.13	0.62	(FORS team)
003	C	F1c1	cm1	1	1	1	MOS	1998-09-28	03.9	30	1.32	1.40	I. Appenzeller et al. (FORS team)
004	C	F1c2	cm2	1	1	1	MOS	1998-12-13	04.5	30	1.54	0.92	I. Appenzeller et al.
005				2				1998-12-17	05.3	30	1.98	0.91	(FORS team)
006				3				1998-12-23	02.4	30	1.07	0.69	
007				4				1998-12-23	02.9	30	1.14	0.65	
008	B	aug99	bm0	1	1	1	MOS	1999-08-14	22.8	30	1.13	1.97	J. Heidt, K. Jäger
009				2				1999-08-15	00.1	35	1.01	0.96	
010				3				1999-08-16	20.9	30	1.68	1.30	
011				4				1999-08-16	21.4	30	1.45	1.24	
012	B	oct99	bm1	1	1	1	MOS	1999-10-06	23.8	30	1.03	1.34	W. Kollatschny,
013				2				1999-10-06	00.4	30	1.01	1.30	B. Ziegler
014				3				1999-10-06	04.7	30	1.60	2.21	
015				4				1999-10-06	05.2	22	1.86	2.49	
016	B	nov99	bm2	1	1	1	MOS	1999-11-03	00.4	30	1.01	1.20	U. Hopp
017				2				1999-11-03	03.3	30	1.20	1.15	
018				2				1999-11-03	03.8	30	1.31	1.14	
019				4				1999-11-03	04.4	30	1.48	1.01	

Table A.1: *continued*

ID	Type	Run	Mask	N	UT x	FORS x	Mode	Date	LMST [h]	$T_{\rm exp}$ [min]	AM	Seeing ["]	Observers
020	C	F2c1	bm2	5	2	2	MOS	1999-11-03	02.5	30	1.09	1.43	I. Appenzeller et al.
021				6				1999-11-13	00.6	09	1.02	0.56	(FORS team)
022				7				1999-11-13	02.7	30	1.11	0.91	
023	C	F2c1	bm3	1	2	2	MOS	1999-11-05	03.2	30	1.19	0.67	I. Appenzeller et al.
024				2				1999-11-05	04.1	30	1.39	0.61	(FORS team)
025	C	F2c2	bm4	1	2	2	MOS	2000-01-25	05.5	30	2.19	1.07	I. Appenzeller et al.
026				2				2000-01-26	04.7	30	1.61	0.59	(FORS team)
027				3				2000-02-01	04.8	30	1.68	0.99	
028				4				2000-02-03	05.0	30	1.76	0.91	
029	M	sep00	m01	1	2	2	MOS	2000-09-24	19.7	30	1.99	0.66	S. Noll
030				2				2000-09-24	20.9	30	1.66	0.93	
031				3				2000-09-24	21.7	30	1.37	0.58	
032				4				2000-09-24	22.2	30	1.24	0.66	
033	M	sep00	m02	1	2	2	MOS	2000-09-24	23.0	30	1.11	0.56	S. Noll
034				2				2000-09-24	23.5	30	1.05	0.47	
035				3				2000-09-24	00.1	25	1.02	0.57	
036				4				2000-09-24	00.5	25	1.00	0.63	
037	M	sep00	m03	1	2	2	MOS	2000-09-24	01.7	30	1.02	0.68	S. Noll
038				2				2000-09-24	02.2	30	1.06	0.63	
039				3				2000-09-24	02.8	30	1.12	0.88	
040				4				2000-09-24	03.3	30	1.20	0.95	

Table A.1: *continued*

ID	Type	Run	Mask	N	UT x	FORS x	Mode	Date	LMST [h]	$T_{\rm exp}$ [min]	AM	Seeing ["]	Observers
041	M	sep00	m04	1	2	2	MOS	2000-09-24	04.1	30	1.38	0.71	S. Noll
042				2				2000-09-24	04.6	30	1.57	0.77	
043				3				2000-09-25	19.8	30	2.00	0.77	
044				4				2000-09-25	20.9	30	1.66	0.62	
045	M	sep00	m05	1	2	2	MOS	2000-09-25	21.7	30	1.37	0.71	S. Noll
046				2				2000-09-25	22.2	30	1.23	0.65	
047				3				2000-09-25	22.7	30	1.14	0.57	
048				4				2000-09-25	23.3	30	1.07	0.64	
049	M	sep00	m06	1	2	2	MOS	2000-09-25	00.1	30	1.02	0.85	S. Noll
050				2				2000-09-25	00.6	20	1.00	0.91	
051				3				2000-09-25	01.7	30	1.02	0.48	
052				4				2000-09-25	02.2	30	1.05	0.53	
053	M	sep00	m07	1	2	2	MOS	2000-09-25	02.9	30	1.14	0.61	S. Noll
054				2				2000-09-25	03.5	30	1.23	0.56	
055				3				2000-09-25	04.0	30	1.36	0.44	
056				4				2000-09-25	04.6	30	1.55	0.65	
057	M	sep00	m08	1	2	2	MOS	2000-09-26	01.8	30	1.03	0.61	S. Noll
058				2				2000-09-26	02.4	30	1.07	0.62	
059	M	oct00	m08	3	2	2	MOS	2000-10-03	01.5	30	1.01	0.65	D. Mehlert
060				4				2000-10-03	02.0	30	1.04	0.69	

Table A.1: *continued*

ID	Type	Run	Mask	N	UT x	FORS x	Mode	Date	LMST [h]	$T_{\rm exp}$ [min]	AM	Seeing ["]	Observers
061	M	oct00	m09	1	2	2	MOS	2000-10-03	02.8	30	1.12	1.00	D. Mehlert
062				2				2000-10-03	03.4	30	1.21	0.94	
063				3				2000-10-03	03.9	30	1.34	0.76	
064				4				2000-10-03	04.5	30	1.51	0.83	
065	M	oct00	m10	1	2	2	MOS	2000-10-04	01.5	30	1.01	0.75	D. Mehlert
066				2				2000-10-04	02.1	30	1.05	0.83	
067				3				2000-10-04	02.6	30	1.10	1.05	
068				4				2000-10-05	01.6	30	1.02	0.94	
069	M	oct00	m11	1	2	2	MOS	2000-10-05	02.4	30	1.07	0.92	D. Mehlert
070				2				2000-10-05	02.9	30	1.13	0.79	
071	M	oct01	mva	1	3	1	MOS	2001-10-10	20.6	40	1.77	0.47	J. Heidt, S. Noll
072				2				2001-10-10	21.3	40	1.45	0.47	
073				3				2001-10-10	22.0	40	1.25	0.52	
074				4				2001-10-10	22.8	40	1.12	0.63	
075	M	oct01	mvb	1	3	1	MOS	2001-10-11	23.6	40	1.04	0.67	J. Heidt, S. Noll
076				2				2001-10-11	00.3	33	1.01	0.78	
077				3				2001-10-12	22.7	40	1.13	1.06	
078				4				2001-10-12	23.4	40	1.05	1.07	
079	M	oct01	mvc	1	3	1	MOS	2001-10-11	02.8	40	1.13	0.87	J. Heidt, S. Noll
080				2				2001-10-11	03.5	40	1.26	0.63	
081				3				2001-10-11	04.2	40	1.47	0.67	
082				4				2001-10-11	04.9	40	1.80	0.46	

Table A.1: *continued*

ID	Type	Run	Mask	N	UT x	FORS x	Mode	Date	LMST [h]	$T_{\rm exp}$ [min]	AM	Seeing ["]	Observers
083	M	oct01	mvd	1	3	1	MOS	2001-10-13	01.8	40	1.03	1.00	J. Heidt, S. Noll
084				2				2001-10-13	02.5	40	1.09	0.88	
085				3				2001-10-13	03.2	40	1.20	0.99	
086				4				2001-10-13	03.9	40	1.36	0.90	
087	M	oct01	mve	1	3	1	MOS	2001-10-12	01.7	40	1.02	1.02	J. Heidt, S. Noll
088				2				2001-10-12	02.4	40	1.08	1.16	
089				3				2001-10-13	21.0	40	1.59	0.87	
090				4				2001-10-13	21.7	40	1.34	0.91	
091	B	oct01	mvf	1	3	1	MOS	2001-10-13	05.0	40	1.85	0.77	J. Heidt, S. Noll
092	M	sm01	msa	1	4	2	MXU	2001-10-11	21.7	48	1.33	0.71	ESO staff
093				2				2001-10-11	22.5	48	1.16	0.57	(service mode)
094				3				2001-10-11	23.3	48	1.06	0.61	
095				4				2001-10-11	00.2	41	1.01	0.79	
096				5				2001-10-11	01.8	48	1.04	0.70	
097				6				2001-10-11	02.6	48	1.12	0.77	
098	M	sm01	msb	1	4	2	MXU	2001-12-18	02.3	48	1.07	0.77	ESO staff
099				2				2001-12-18	03.1	48	1.19	0.75	(service mode)
100				3				2001-12-18	04.0	48	1.40	0.80	
101				4				2001-12-19	02.3	48	1.08	0.70	
102				5				2001-12-19	03.2	48	1.21	0.73	

Appendix B

List of spectral lines used for the redshift derivation

In order to determine redshifts by visual line identifications and following line centreing (see Section 5.2) one needs numerous lines. Thus, the investigation of galaxies with redshifts between 0 and 5 requires the consideration of lines ranging from the Lyman limit at 912 Å to the Ca II triplet in the near infrared. Furthermore, in spectra of different type (see Section 5.3) strength and profile of individual lines can differ a lot. For that reason, one needs for each spectral type a specific set of suitable lines. This naturally causes a further increase of the necessary lines.

Table B.1 lists the spectral lines used. The individual columns are described in the following:

No.: Wavelength sorted numbering.

λ: Wavelength in Å. Vacuum wavelengths for $\lambda < 3000$ Å, else wavelengths in air. Partly the values are only estimates with an accuracy of the order of a few 10^{-1} Å, since frequently either the lines have multiplet character or they are blended with other lines (or both). Detailed line lists can be found in Moore (1945 and 1952), Saidel et al. (1961) or Reader et al. (1980).

Ion: Chemical element (letters) and ionisation state (Roman numbers; I = neutral, II = single ionised). Brackets mark forbidden transitions. Two or three entries are listed in case of inhomogeneous blends.

Label: Specific name of a spectral line or blend.

Profile: Predominant shape of spectral lines. In case of two or three entries the first one represents the most probable line profile considering the composition of the present sample (see Chapter 6). The abbreviations have the following meaning: A = absorption, E = emission, PC = P Cygni (central emission and blue shifted absorption) and L = line series limit. Tendentiously one can say that the earlier the spectral type of the galaxy is (less star formation) the more likely a line occur in absorption.

Remarks: Essentially the entries indicate line blending. In part weaker components of a blend are quoted by the name of the ion, in part blending lines, which are separately listed, are indicated by their ordinal number. In principle, almost all lines are blended, but only the quoted lines should have an significant impact on the determination of common line centres.

Table B.1: List of spectral lines used for the redshift determination. The individual columns are described in the text.

No.	λ [Å]	Ion	Label	Profile	Remarks
1	912.	H II $\rightarrow$ H I	Ly-lim	L	
2	949.7	H I	Lyδ	A	
3	972.5	H I	Lyγ	A	
4	1025.7	H I	Lyβ	A	+ 5, 6
5	1031.9	O VI		PC, A	+ 4, 6
6	1037.6	O VI		PC, A	+ 4, 5
7	1175.7	C III		A	
8	1191.9	Si II		A	
9	1215.7	H I	Lyα	A, PC, E	
10	1238.8	N V		PC, A	+ 11
11	1242.8	N V		PC, A	+ 10
12	1260.9	Si II		A	+ S II, Si II*
13	1303.3	O I, Si II		A	blend
14	1334.7	C II		A	+ C II*
15	1393.8	Si IV		A, PC	+ 16
16	1402.8	Si IV		A, PC	+ 15
17	1501.8	S V		A	
18	1526.7	Si II		A	
19	1548.2	C IV		A, PC	+ 20
20	1550.8	C IV		A, PC	+ 19
21	1608.5	Fe II		A	
22	1640.7	He II		E	
23	1670.8	Al II		A	
24	1854.7	Al III		A	+ 25
25	1862.8	Al III		A	+ 24
26	1907.5	C III]		E	doublet
27	2326.0	C II]		E	
28	2344.2	Fe II		A	
29	2374.5	Fe II		A	+ 30
30	2382.8	Fe II		A	+ 29
31	2586.5	Fe II		A	
32	2600.2	Fe II		A	
33	2795.5	Mg II		PC, A	+ 34
34	2802.7	Mg II		PC, A	+ 33

Table B.1: *continued*

No.	λ [Å]	Ion	Label	Profile	Remarks
35	3646.	H II $\rightarrow$ H I	H-lim	L	
36	3727.5	[O II]		E	doublet
37	3868.8	[Ne III]		E	
38	3933.7	Ca II	K	A	
39	3968.5	Ca II	H	A	+ H I (Hϵ), [Ne III]
40	4101.7	H I	Hδ	A	
41	4226.7	Ca I		A	
42	4304.	CH, Fe I, Ca I	G-band	A	blend
43	4340.5	H I	Hγ	A, E	
44	4861.3	H I	Hβ	E, A	
45	4958.9	[O III]		E	
46	5006.9	[O III]		E	
47	5175.	Mg I	Mgb	A	triplet
48	5199.2	[N I]		E	
49	5268.6	Fe I, Ca I	E-band	A	blend (+ MgH)
50	5875.7	He I	D_3	E	
51	5890.0	Na I	D_2	A, (E)	+ 52
52	5895.9	Na I	D_1	A, (E)	+ 51
53	6300.3	[O I]		E	
54	6496.9	Ba II		A	
55	6548.1	[N II]		E	+ 56
56	6562.8	H I	Hα	E, A	+ 55, 57
57	6583.4	[N II]		E	+ 56
58	6716.4	[S II]		E	+ 59
59	6730.8	[S II]		E	+ 58
60	8498.0	Ca II		A, (E)	
61	8542.1	Ca II		A, (E)	
62	8662.1	Ca II		A, (E)	

Appendix C

Catalogue of the spectroscopic sample

This appendix provides a listing of the basic data characterising the FDF spectroscopic sample. The representation is limited to the 350 objects with a redshift quality $Q_z \geq 2$. The individual columns of the catalogue have the following content:

No.: Identity number of the object according to Heidt et al. 2002. There are a few objects which are not listed in the photometric catalogue. These objects are indicated by numbers above 9000.

RA: Right ascension of the object in hours, minutes and seconds.

DEC: Declination of the object in degrees, arcminutes and arcseconds.

B: Total apparent B magnitude in mag (Vega system, see Heidt et al. 2002). The fluxes were measured using adjustable elliptical apertures. Non-detections in B are marked by the value 99.0.

I: Total apparent I magnitude in mag (as above).

$T_{\rm exp}$**:** Total exposure time of the co-added spectra in minutes.

f/f_0**:** Ratio between the flux which passed through the slit and the actual object flux in % (see Section 4.5). The amount of the slit losses depends on the seeing conditions and the object size. Large flux losses (low f/f_0) usually correspond to large object extensions.

S/N: Signal-to-noise ratio measured in the filter band given in parentheses (B, g, R or I). In each case the band where the highest S/N is achieved was selected (see Section 5.1). The S/N as a function of wavelength was calculated by dividing the object spectrum by its error function (see Section 4.3).

Q_s**:** Quality of the spectrum (see Section 5.1). The scale ranges from $Q_s = 1$ (spectrum highly distorted) to $Q_s = 3$ (spectrum essentially free of systematic errors).

Type: Spectral type of the object. An classification system comprising eight different types was used. Type = I – V correspond with the spectral galaxy types defined in Section 5.3. The respective spectral templates are shown in Fig. 5.7. Type = VI indicates Lyα emission line galaxies defined by the template shown in Fig. 5.9. Since these galaxies can also be assigned a continuum type (≤ 5), type VI is generally given in combination with a basic galaxy type. Type = VII indicates AGN dominated objects (quasars or Seyferts, see Section 6.2) for which the spectral templates I – VI could not be applied. Finally, Type = VIII refers to stars (see Section 6.2 as well).

z: Redshift of the object. For the derivation see Chapter 5.

dz: Error of the redshift derivation. The values were estimated by the measure HW99M (see Section 5.7).

S: Significance of the redshift. For the interpretation of the values see Section 5.6.

Q_z: Quality of the redshift (see Section 5.6). $Q_z = 4$ indicates objects with certain redshift. In case of several possible identifications ($Q_z = 2$) two redshift alternatives are specified in the table.

Remarks: Further informations to the objects. In case of stars a rough spectral type is indicated (MK classification, see Section 5.3). Quasars and strong Lyα emission galaxies are indicated by the entries QSO and LAB (Lyα bright). The acronym BAL refers to a broad absorption line quasar (object 6233, see Section 6.2). TF indicates galaxies whose redshift and spectral type were derived by means of the spectroscopic data of the FDF Tully-Fisher project (see Section 5.7).

Table C.1: Catalogue of the FDF spectroscopic sample. The list is restricted on the 350 objects with redshift qualities $Q_z \geq 2$. Descriptions to the individual columns are given in the text.

No.	RA 01:...	DEC −25:...	B [mag]	I [mag]	T_{exp} [min]	f/f_0 [%]	S/N (Band)	Q_s	Type	z	dz	S	Q_z	Remarks
400	05:48.6	44:53	23.2	21.4	180	41	21.0 (R)	3	IV	0.4488	0.0005	29.3	4	
734	05:50.0	44:35	24.0	22.6	300	31	7.8 (g)	3	III	1.4951	0.0011	4.2	2	
									III	1.2424	0.0012	5.3		
745	05:50.1	48:03	22.6	20.3	60	33	23.6 (R)	2	III	0.6986	0.0007	13.4	4	
794	05:50.3	43:23	25.4	23.8	60	74	2.6 (R)	3	IV	0.9111	0.0007	7.5	3	
809	05:50.3	44:48	22.7	21.4	502	59	68.4 (g)	3	VII	0.8650	0.0007		4	QSO
870	05:50.5	44:36	21.5	19.6	40	27	31.0 (g)	3	III	0.2772	0.0005	36.0	4	
889	05:50.6	47:52	24.7	21.5	120	46	12.3 (R)	3	I	0.3340	0.0009	3.7	4	
944	05:50.9	43:49	25.2	23.8	240	47	4.4 (R)	3	IV	0.9756	0.0007	7.1	3	
960	05:50.9	45:37	25.7	24.0	240	61	6.3 (g)	2	V	3.1598	0.0017	3.2	4	
970	05:51.0	45:37	27.2	25.0	400	58	3.5 (g)	3	V	3.1574	0.0017	3.1	4	
1063	05:51.3	44:44	24.4	21.7	240	48	18.2 (I)	3	II	0.8660	0.0008	12.6	4	
1064	05:51.4	45:40	24.0	23.3	240	51	13.4 (g)	3	V	0.8536	0.0006	38.2	4	
1078	05:51.4	47:51	22.9	19.6	232	31	57.6 (R)	3	I	0.3361	0.0005	14.0	4	
1114	05:51.5	48:05	23.5	20.1	60	47	46.9 (R)	3	I	0.3347	0.0004	21.4	4	
1165	05:51.7	48:08	99.0	23.3	210	29	2.7 (g)	3	IV	2.3174	0.0024	2.5	2	
									IV	0.3319	0.0005	3.7		
1208	05:51.9	48:04	25.1	23.7	651	66	13.8 (g)	3	IV	2.1779	0.0015	8.2	4	
1221	05:51.9	47:46	26.2	23.3	240	45	5.6 (R)	3	I	0.3362	0.0006	3.3	2	
									I	0.2551	0.0004	2.9		
1224	05:51.9	44:25	23.6	22.3	112	41	7.4 (g)	3	V	0.3987	0.0005	23.8	4	

Table C.1: *continued*

No.	RA 01:...	DEC −25:...	B [mag]	I [mag]	$T_{\rm exp}$ [min]	f/f_0 [%]	S/N (Band)	$Q_{\rm s}$	Type	z	dz	S	$Q_{\rm z}$	Remarks
1265	05:52.1	47:47	22.5	19.1	120	8	19.1 (R)	2	I	0.3360	0.0005	6.0	4	
1327	05:52.4	47:23	21.2	19.1	120	7	22.5 (g)	2	IV	0.3158	0.0004	8.8	4	
1331	05:52.4	47:29	26.8	23.9	491	58	5.6 (R)	3	V	3.3847	0.0017	2.6	2	
									II	0.3336	0.0004	3.1		
1337	05:52.4	48:33	25.9	23.6	330	66	7.6 (g)	2	V	3.4025	0.0019	4.2	4	
1395	05:52.7	45:15	25.9	24.0	393	41	3.0 (g)	3	IV	0.8631	0.0007	6.8	3	
1413	05:52.7	44:04	24.4	22.5	290	59	17.8 (R)	3	VIII	0.0000			4	K/G
1416	05:52.7	46:01	23.9	22.3	60	52	10.1 (g)	3	IV	0.3910	0.0004	20.9	4	
1422	05:52.7	45:13	23.8	22.1	40	56	6.9 (g)	3	IV	0.8629	0.0007	12.9	4	
1450	05:52.8	44:59	24.4	22.8	160	59	8.3 (g)	3	III	0.1727	0.0005	7.0	2	
									III	1.6626	0.0018	3.7		
1452	05:52.9	44:07	24.6	23.1	450	47	17.4 (g)	2	IV	0.2778	0.0004	17.6	4	
1472	05:52.9	44:27	23.3	21.7	40	34	11.5 (R)	2	IV	0.3987	0.0005	24.4	4	
1473	05:52.9	45:19	23.9	23.3	480	53	16.6 (g)	3	V	1.5801	0.0018	6.6	3	
1496	05:53.0	48:04	24.1	22.9	120	54	10.8 (g)	3	IV	1.3756	0.0008	13.9	4	
1502	05:53.1	45:23	99.0	23.6	360	35	5.4 (R)	3	V	3.2739	0.0022	3.3	2	
									IV	2.6940	0.0026	3.4		
1507	05:53.1	43:19	24.7	22.8	110	20	2.8 (R)	3	IV	0.4521	0.0005	5.7	3	
1530	05:53.1	47:44	24.8	23.1	240	55	9.4 (g)	3	IV	0.8319	0.0006	20.5	4	
1536	05:53.2	43:22	26.6	23.6	350	56	6.0 (R)	3	I	0.4488	0.0006	3.6	2	
									II	0.5734	0.0007	4.8		
1552	05:53.2	47:44	24.3	23.1	240	46	12.6 (g)	3	V	0.3352	0.0004	58.1	4	

Table C.1: *continued*

No.	RA 01:...	DEC −25:...	B [mag]	I [mag]	$T_{\rm exp}$ [min]	f/f_0 [%]	S/N (Band)	$Q_{\rm s}$	Type	z	dz	S	$Q_{\rm z}$	Remarks
1555	05:53.3	45:21	26.0	23.9	393	58	7.6 (R)	3	V	3.2681	0.0016	5.2	4	
1569	05:53.3	47:47	24.5	22.6	160	53	9.8 (R)	3	III	0.4625	0.0005	10.8	4	
1578	05:53.3	44:16	25.9	24.3	670	53	6.6 (g)	3	IV	2.7103	0.0018	5.6	4	
1595	05:53.4	44:17	26.5	24.9	663	44	5.1 (g)	2	V	2.7103	0.0024	3.3	4	
1600	05:53.4	43:00	25.1	23.4	120	56	8.2 (g)	3	III	0.1864	0.0004	7.2	3	
1616	05:53.4	47:44	25.6	24.7	120	66	1.3 (g)	3	V/VI	2.3312	0.0016	4.1	2	
									V	2.2546	0.0017	1.9		
1627	05:53.5	44:00	25.4	23.8	120	31	2.5 (R)	3	III	0.4302	0.0004	3.1	2	
									V	3.2749	0.0027	2.4		
1676	05:53.7	45:19	24.6	22.3	100	39	7.3 (R)	3	II	0.2240	0.0005	7.7	4	
1691	05:53.7	45:29	25.1	23.9	400	67	10.0 (g)	2	IV	2.3444	0.0021	5.9	4	
1694	05:53.7	47:27	25.4	23.6	281	71	11.1 (g)	3	IV	0.3327	0.0004	17.8	4	
1696	05:53.7	46:05	26.6	23.4	240	43	3.9 (R)	2	III	0.6799	0.0006	4.3	2	
									II	0.2148	0.0005	2.7		
1699	05:53.8	47:36	22.7	21.1	120	37	32.5 (g)	3	V	0.2313	0.0005	24.1	4	
1709	05:53.8	47:41	24.8	24.3	280	71	8.4 (g)	3	V	1.6717	0.0023	4.5	3	
1710	05:53.8	46:38	24.0	22.7	90	51	7.7 (g)	3	V	0.9674	0.0006	20.1	4	
1713	05:53.8	45:30	26.1	25.2	400	46	2.7 (g)	3	IV	2.3456	0.0019	2.3	3	
1744	05:53.9	46:06	25.5	24.1	450	68	10.0 (g)	3	IV	2.3742	0.0019	6.1	4	
1789	05:54.1	46:32	23.7	21.4	112	25	5.8 (g)	3	III	0.9667	0.0007	8.9	4	
1813	05:54.1	43:22	24.7	20.7	120	65	44.3 (I)	3	VIII	0.0000			4	M
1823	05:54.2	43:30	23.8	22.3	120	54	14.0 (g)	2	IV	1.0496	0.0007	18.1	4	

Table C.1: *continued*

No.	RA 01:...	DEC −25:...	B [mag]	I [mag]	$T_{\rm exp}$ [min]	f/f_0 [%]	S/N (Band)	$Q_{\rm s}$	Type	z	dz	S	$Q_{\rm z}$	Remarks
1837	05:54.2	46:41	23.9	22.9	360	93	38.5 (g)	3	VII	2.2540	0.0030		4	QSO
1922	05:54.6	47:00	23.9	23.4	280	74	21.7 (g)	3	V	1.8271	0.0014	6.2	4	QSO?
1928	05:54.6	46:30	23.8	22.3	40	50	4.8 (g)	3	IV	0.7175	0.0006	13.5	4	
1932	05:54.6	46:12	25.1	24.8	160	34	2.9 (g)	2	V	2.3702	0.0016	2.6	2	
									V	1.9145	0.0014	2.2		
1954	05:54.7	43:17	26.5	24.6	110	89	2.2 (g)	3	IV	0.7627	0.0006	8.3	3	
1976	05:54.8	45:57	25.1	23.4	160	67	5.0 (R)	2	III	1.4008	0.0007	3.8	2	
									III	1.2215	0.0010	3.3		
1987	05:54.8	43:27	23.1	21.2	180	71	42.2 (g)	3	VIII	0.0000			4	K
1991	05:54.8	46:16	25.1	24.3	400	57	6.4 (g)	3	V	2.3339	0.0018	4.2	4	
2003	05:54.9	43:25	26.3	23.2	490	59	9.9 (R)	3	II	0.4491	0.0004	5.0	4	
2033	05:55.0	48:19	25.0	24.1	561	51	11.1 (g)	3	V	2.7537	0.0021	4.3	4	
2048	05:55.1	46:20	25.4	24.2	400	59	7.2 (g)	3	V	2.7018	0.0017	2.9	2	
									V	2.6765	0.0024	2.7		
2073	05:55.2	43:20	25.2	24.8	160	62	3.7 (g)	3	V	1.5711	0.0018	2.9	2	
									V	2.2316	0.0015	2.7		
2127	05:55.4	45:49	99.0	25.1	553	68	2.0 (R)	3	IV	3.9159	0.0018	1.2	2	
									IV	3.7741	0.0020	1.8		
2194	05:55.6	47:24	99.0	25.7	281	60	1.4 (I)	2	V/VI	4.5103	0.0022	3.2	2	
									IV	0.7972	0.0007	2.2		
2195	05:55.6	47:54	25.0	22.2	180	60	13.3 (R)	2	I	0.3340	0.0006	3.4	4	
2206	05:55.6	43:28	99.0	26.0	540	64	2.0 (R)	3	V/VI	4.4728	0.0024	5.5	4	LAB
2228	05:55.7	43:11	23.6	19.9	153	6	6.9 (R)	2	I	0.4505	0.0006	4.7	3	

Table C.1: *continued*

No.	RA 01:...	DEC −25:...	B [mag]	I [mag]	$T_{\rm exp}$ [min]	f/f_0 [%]	S/N (Band)	$Q_{\rm s}$	Type	z	dz	S	$Q_{\rm z}$	Remarks
2229	05:55.7	47:22	22.0	20.8	60	74	64.2 (g)	3	VII	2.1560	0.0030		4	QSO
2236	05:55.7	48:45	24.2	22.5	150	49	11.9 (R)	2	VIII	0.0000			4	K
2244	05:55.8	44:39	25.6	24.1	120	61	4.6 (g)	2	V	0.3167	0.0004	23.9	4	
2246	05:55.8	44:32	23.0	20.8	380	31	30.7 (R)	3	III	0.6507	0.0006	21.2	4	
2252	05:55.8	44:27	23.5	19.0	110	7	20.4 (I)	3	VIII	0.0000			4	M
2256	05:55.8	43:02	26.6	22.3	430	47	12.2 (I)	3	I	1.1670	0.0008	12.9	4	
2262	05:55.8	45:03	25.5	24.0	153	47	2.2 (g)	2	IV	0.9520	0.0008	5.6	2	
									III	1.3528	0.0018	2.6		
2265	05:55.9	43:26	99.0	22.3	160	14	3.7 (g)	3	IV	0.7603	0.0006	6.5	4	
2267	05:55.9	45:08	99.0	21.2	60	27	9.7 (R)	3	VIII	0.0000			4	K
2274	05:55.9	44:34	24.3	23.3	590	55	18.3 (g)	3	V	2.2529	0.0013	5.9	4	
2282	05:55.9	44:28	24.0	22.0	120	58	2.9 (g)	2	IV	0.4505	0.0005	7.8	4	
2289	05:56.0	44:38	26.3	25.1	390	25	1.7 (g)	2	V/VI	3.0399	0.0020	4.5	2	
									IV	0.3177	0.0005	2.8		
2295	05:56.0	43:12	24.0	22.5	153	36	9.0 (g)	3	IV	1.8240	0.0016	3.4	3	
2333	05:56.1	43:29	26.0	24.0	180	45	3.1 (R)	2	III	0.7612	0.0006	4.6	3	
2334	05:56.1	44:40	24.0	23.0	390	57	20.0 (g)	3	V	1.3916	0.0008	17.4	4	+ object at z = 0.1991
2340	05:56.2	43:27	25.8	22.9	240	67	10.8 (R)	3	II	0.5799	0.0006	9.5	4	
2341	05:56.2	43:36	23.9	21.2	250	49	24.1 (R)	3	III	0.7603	0.0007	10.3	4	
2368	05:56.3	48:21	26.8	24.1	441	72	5.4 (R)	2	II	0.4446	0.0004	2.3	3	
2384	05:56.3	47:37	26.0	23.8	681	66	9.8 (g)	3	V/VI	3.3143	0.0019	15.2	4	LAB

Table C.1: *continued*

No.	RA 01:...	DEC −25:...	B [mag]	I [mag]	$T_{\rm exp}$ [min]	f/f_0 [%]	S/N (Band)	$Q_{\rm s}$	Type	z	dz	S	$Q_{\rm z}$	Remarks
2412	05:56.4	46:26	24.4	21.9	40	51	5.9 (R)	3	III	0.6528	0.0006	6.8	4	
2418	05:56.4	45:12	24.4	23.1	500	37	11.8 (g)	3	IV	2.3319	0.0019	8.1	4	
2444	05:56.6	45:16	25.5	24.3	110	60	3.1 (g)	2	V	1.0613	0.0007	5.9	2	
									V	0.9552	0.0006	3.9		
2495	05:56.7	43:44	24.6	23.3	720	51	18.0 (g)	3	IV	2.4528	0.0018	10.5	4	
2498	05:56.8	45:11	25.6	23.4	120	45	3.2 (R)	2	IV	0.8694	0.0007	9.7	3	
2533	05:56.9	44:51	21.1	19.1	110	24	65.9 (R)	3	III	0.3159	0.0005	44.7	4	
2535	05:56.9	47:28	25.0	22.8	120	53	6.0 (R)	2	I	0.1284	0.0004	3.3	2	
									II	0.2401	0.0005	1.9		
2552	05:57.0	44:54	26.1	99.0	110	32	2.2 (g)	2	IV	0.2631	0.0005	4.0	2	
									V/VI	2.8729	0.0019	5.8		
2572	05:57.0	48:04	23.4	21.4	30	61	21.8 (g)	1	III	0.4483	0.0005	2.5	4	TF
2580	05:57.1	48:09	23.9	20.7	30	24	9.7 (R)	3	I	0.3369	0.0006	4.1	4	
2586	05:57.1	43:13	23.6	22.0	180	62	21.2 (g)	3	VIII	0.0000			4	G
2631	05:57.3	45:00	99.0	24.4	440	61	3.2 (I)	3	VIII	0.0000			4	early L
2633	05:57.3	44:57	24.5	22.8	382	55	22.0 (g)	3	VII	3.0780	0.0030		4	QSO
2636	05:57.3	44:02	24.8	23.4	480	36	8.7 (g)	3	III	2.2531	0.0018	3.0	4	
2642	05:57.3	46:11	23.8	21.9	412	66	28.6 (R)	3	VIII	0.0000			4	K/G
2661	05:57.4	44:26	24.5	22.3	40	46	5.4 (R)	3	III	0.2743	0.0004	8.4	4	
2704	05:57.5	44:04	26.0	24.9	120	59	3.1 (g)	3	V	1.0233	0.0007	7.1	2	
									IV	1.8575	0.0018	2.6		
2783	05:57.8	45:27	22.3	20.4	30	48	25.1 (g)	3	III	0.3141	0.0004	28.4	4	

Table C.1: *continued*

No.	RA 01:...	DEC −25:...	B [mag]	I [mag]	$T_{\rm exp}$ [min]	f/f_0 [%]	S/N (Band)	$Q_{\rm s}$	Type	z	dz	S	$Q_{\rm z}$	Remarks
2822	05:58.0	45:46	23.2	21.3	180	31	14.2 (R)	2	III	0.5862	0.0006	14.4	4	
2847	05:58.1	44:31	23.4	21.4	40	38	10.7 (g)	3	III	0.2745	0.0004	10.3	4	
2957	05:58.4	45:43	23.3	21.9	60	74	25.7 (g)	3	VIII	0.0000			4	G
3003	05:58.6	46:20	25.7	22.8	60	83	8.6 (R)	3	VIII	0.0000			4	K
3005	05:58.6	48:14	24.7	23.5	690	55	14.7 (g)	3	IV	2.2530	0.0017	9.5	4	
3022	05:58.7	43:48	24.1	21.5	125	42	10.7 (R)	3	III	0.4480	0.0005	7.6	4	
3071	05:58.8	45:09	19.5	17.6	120	41	288.9 (R)	3	II	0.0949	0.0005	42.0	4	
3121	05:59.0	46:09	24.9	22.1	40	32	3.3 (R)	3	II	0.3763	0.0005	2.7	2	
									I	0.2473	0.0004	2.4		
3122	05:59.0	46:21	23.5	21.6	110	18	7.5 (R)	2	III	0.5976	0.0006	12.7	4	
3123	05:59.0	46:27	23.0	21.2	232	52	45.3 (g)	3	VIII	0.0000			4	K/G
3124	05:59.1	45:14	22.6	20.2	60	26	17.0 (R)	3	III	0.7852	0.0007	13.0	4	
3129	05:59.1	45:31	23.8	21.3	180	77	35.5 (R)	3	VIII	0.0000			4	K
3163	05:59.2	45:38	24.8	23.4	770	52	17.0 (g)	2	IV	2.4407	0.0016	9.9	4	
3173	05:59.2	46:26	26.1	23.9	860	61	10.6 (R)	3	V	3.2702	0.0018	6.8	4	
3230	05:59.4	44:08	23.9	22.0	60	35	5.5 (R)	3	III	1.1538	0.0008	7.3	3	
3232	05:59.4	45:18	24.9	23.9	160	27	2.8 (g)	2	V	2.3651	0.0019	2.6	2	
									IV	0.0975	0.0004	4.2		
3267	05:59.5	46:29	25.9	24.3	570	66	6.2 (R)	3	IV	0.3962	0.0005	17.7	4	
3268	05:59.5	48:25	24.4	23.0	120	66	2.1 (g)	2	IV	0.7805	0.0006	4.3	3	
3278	05:59.6	44:38	21.4	18.6	245	44	226.9 (R)	3	VIII	0.0000			4	K
3295	05:59.6	44:36	99.0	19.9	125	18	27.5 (R)	3	II	0.6535	0.0006	5.1	4	

Table C.1: *continued*

No.	RA 01:...	DEC −25:...	B [mag]	I [mag]	$T_{\rm exp}$ [min]	f/f_0 [%]	S/N (Band)	$Q_{\rm s}$	Type	z	dz	S	$Q_{\rm z}$	Remarks
3300	05:59.6	46:30	24.9	23.9	851	48	13.4 (g)	3	V	2.3751	0.0015	4.6	4	
3312	05:59.7	47:44	26.2	24.0	511	57	8.9 (R)	3	V	3.3886	0.0019	5.5	4	
3321	05:59.7	44:43	99.0	21.9	160	19	3.4 (R)	2	I	0.6514	0.0006	3.5	3	
3339	05:59.7	43:54	24.9	22.9	120	48	4.9 (R)	3	II	1.3125	0.0009	4.6	2	
									III	1.0530	0.0017	2.8		
3341	05:59.7	46:19	25.5	24.3	120	61	4.0 (g)	3	V	1.0464	0.0007	12.1	3	
3374	05:59.9	45:11	24.3	23.3	473	62	19.3 (g)	3	V	2.3855	0.0015	7.4	4	
3389	05:59.9	44:40	99.0	23.5	690	36	2.5 (R)	3	V/VI	4.5821	0.0024	8.7	4	LAB
3414	06:00.0	45:40	25.0	23.5	240	72	7.8 (g)	3	IV	0.9748	0.0007	9.3	4	
3461	06:00.2	44:54	25.5	23.5	240	42	6.5 (R)	3	III	0.3163	0.0006	4.9	3	
3476	06:00.2	44:56	23.6	23.0	240	59	16.2 (g)	3	V	1.4380	0.0012	3.6	2	
									V	1.5243	0.0014	2.9		
3559	06:00.5	43:42	99.0	23.2	410	75	10.7 (I)	3	VIII	0.0000			4	late M
3592	06:00.6	46:24	99.0	21.8	40	29	3.2 (I)	3	I	0.7588	0.0010	3.3	3	
3595	06:00.6	45:35	24.4	20.5	120	63	51.2 (I)	3	VIII	0.0000			4	M
3644	06:00.8	43:39	25.0	24.1	280	55	6.2 (g)	2	V	1.1475	0.0008	12.1	3	
3688	06:00.9	47:05	25.3	24.1	470	66	11.9 (g)	3	IV	2.3750	0.0016	5.3	4	
3717	06:01.0	46:20	25.9	22.1	120	40	7.6 (I)	3	I	1.0235	0.0007	11.4	4	
3725	06:01.0	45:36	23.7	21.3	160	27	14.1 (R)	2	II	0.3350	0.0006	3.3	4	
3781	06:01.2	46:22	24.5	23.0	120	46	6.4 (g)	3	V	1.0267	0.0006	14.4	4	
3806	06:01.3	49:05	24.1	21.5	245	24	6.3 (R)	2	IV	0.4348	0.0006	7.9	4	
3810	06:01.3	45:28	24.1	22.7	592	55	21.1 (g)	3	IV	2.3717	0.0018	15.1	4	

Table C.1: *continued*

No.	RA 01:...	DEC −25:...	B [mag]	I [mag]	$T_{\rm exp}$ [min]	f/f_0 [%]	S/N (Band)	$Q_{\rm s}$	Type	z	dz	S	$Q_{\rm z}$	Remarks
3813	06:01.3	49:01	99.0	20.3	245	26	37.5 (R)	3	II	0.3335	0.0005	11.3	4	
3874	06:01.5	45:46	24.6	23.3	540	45	13.5 (g)	3	IV	2.4828	0.0014	6.9	4	
3875	06:01.5	47:34	25.0	24.5	281	83	11.3 (g)	3	V/VI	2.2426	0.0017	9.1	4	
3892	06:01.6	48:21	24.4	22.4	160	53	2.5 (B)	2	IV	0.3942	0.0005	6.5	3	
3909	06:01.7	46:46	24.0	20.8	40	48	17.0 (R)	3	I	0.3377	0.0004	9.1	4	
3921	06:01.7	43:06	99.0	17.4	30	13	80.4 (R)	3	II	0.2247	0.0006	18.7	4	
3958	06:01.8	44:29	24.6	23.9	280	58	11.3 (g)	3	V	2.1297	0.0016	4.9	4	
3995	06:02.0	48:31	23.2	22.1	320	55	36.8 (g)	3	IV	0.0666	0.0004	20.7	4	
3999	06:02.0	47:54	26.9	24.0	651	65	7.5 (R)	3	IV	3.3914	0.0020	7.4	4	
4006	06:02.0	44:29	25.0	23.5	120	37	2.6 (R)	3	IV	1.0985	0.0007	5.1	2	
									IV	2.5045	0.0015	2.4		
4049	06:02.1	47:17	24.3	23.0	671	64	21.9 (g)	3	III	1.4753	0.0009	19.1	4	
4068	06:02.2	43:35	25.4	22.9	120	75	6.3 (R)	3	III	0.7828	0.0006	9.5	4	
4088	06:02.3	47:03	24.1	22.9	60	68	8.7 (g)	3	V	0.8440	0.0006	15.8	4	
4092	06:02.3	43:30	24.2	23.7	280	54	12.3 (g)	3	V	1.3942	0.0009	16.3	4	
4115	06:02.4	47:25	22.5	21.5	125	58	24.0 (g)	3	V	1.3174	0.0007	19.6	4	
4162	06:02.5	44:34	26.2	23.9	120	46	2.1 (R)	3	III	0.9346	0.0007	5.8	3	
4259	06:02.9	44:00	25.2	23.9	281	32	5.3 (g)	2	IV	0.3707	0.0004	6.9	3	
4271	06:02.9	48:16	23.7	21.6	125	39	10.5 (R)	3	III	0.4078	0.0005	13.0	4	
4285	06:03.0	44:56	23.2	19.7	30	49	32.9 (R)	3	I	0.3967	0.0005	9.5	4	
4293	06:03.0	45:35	23.6	22.3	292	40	15.4 (g)	3	III	0.0942	0.0004	16.2	4	

Table C.1: *continued*

No.	RA 01:...	DEC −25:...	B [mag]	I [mag]	$T_{\rm exp}$ [min]	f/f_0 [%]	S/N (Band)	$Q_{\rm s}$	Type	z	dz	S	$Q_{\rm z}$	Remarks
4310	06:03.0	43:57	25.8	23.6	441	60	10.6 (g)	3	IV	1.6647	0.0017	4.3	2	
									IV	1.9907	0.0018	3.2		
4324	06:03.1	43:58	24.2	23.3	160	32	6.0 (g)	3	V	1.6701	0.0014	4.2	2	
									V	1.2394	0.0010	3.5		
4343	06:03.2	46:56	21.4	20.0	281	76	263.2 (g)	3	VIII	0.0000			4	G
4378	06:03.3	46:22	26.5	24.0	681	40	4.3 (g)	2	IV	2.4404	0.0019	2.8	2	
									IV	2.5454	0.0017	2.6		
4402	06:03.4	46:33	20.2	18.0	30	28	79.9 (g)	3	II	0.1139	0.0005	27.6	4	
4409	06:03.4	46:20	23.5	21.4	401	48	40.2 (R)	3	IV	0.6111	0.0006	27.3	4	
4430	06:03.5	46:08	25.5	24.2	120	75	3.6 (R)	2	IV	0.4738	0.0005	7.6	3	
4431	06:03.5	46:51	24.7	21.2	90	46	4.2 (R)	3	II	0.8706	0.0007	4.5	2	
									II	0.7034	0.0008	3.0		
4442	06:03.5	46:53	24.8	22.8	210	61	9.7 (g)	3	III	0.9728	0.0007	15.0	4	
4444	06:03.6	46:36	99.0	22.9	401	19	6.2 (g)	2	II	0.1645	0.0004	5.7	2	
									III	1.2397	0.0010	1.7		
4454	06:03.6	45:29	27.4	25.6	736	70	3.8 (g)	3	V/VI	3.0854	0.0019	10.0	4	LAB
4457	06:03.6	46:24	24.9	23.1	240	39	6.3 (g)	3	III	1.2875	0.0012	3.3	2	
									III	1.2297	0.0010	2.3		
4461	06:03.6	47:19	27.4	23.2	160	53	4.7 (I)	3	I	1.5112	0.0025	4.6	3	
4465	06:03.6	46:20	23.6	20.9	120	39	22.0 (R)	3	III	0.6110	0.0006	15.2	4	
4479	06:03.7	44:54	24.3	23.2	160	47	6.5 (g)	3	IV	1.3042	0.0041	3.6	3	
4480	06:03.7	45:26	99.0	22.4	681	22	6.6 (I)	3	I	1.0231	0.0007	7.0	3	

Table C.1: *continued*

No.	RA 01:...	DEC −25:...	B [mag]	I [mag]	$T_{\rm exp}$ [min]	f/f_0 [%]	S/N (Band)	$Q_{\rm s}$	Type	z	dz	S	$Q_{\rm z}$	Remarks
4520	06:03.8	46:18	25.1	99.0	120	49	3.2 (R)	3	III	0.3658	0.0005	3.8	2	
									IV	3.0520	0.0021	2.8		
4522	06:03.8	45:42	99.0	25.4	841	63	2.5 (I)	2	V	4.9980	0.0035	1.2	4	
4573	06:04.0	46:55	25.5	23.9	281	32	4.2 (R)	3	IV	0.6993	0.0006	6.3	3	
4617	06:04.2	48:29	25.2	23.7	270	44	3.4 (R)	3	III	1.1854	0.0008	6.6	2	
									III	1.1069	0.0007	4.7		
4654	06:04.3	47:19	22.2	20.1	30	6	3.9 (R)	3	IV	0.3989	0.0005	5.8	3	
4657	06:04.3	43:20	21.8	19.3	120	2	8.8 (g)	1	III	0.2244	0.0005	3.2	4	TF
4662	06:04.3	43:12	25.4	24.0	240	37	3.4 (g)	2	V	0.7386	0.0005	6.6	3	
4667	06:04.3	47:14	22.6	20.7	30	16	7.4 (R)	3	IV	0.4542	0.0005	7.3	4	
4682	06:04.4	46:15	99.0	23.6	510	46	6.3 (g)	2	V	3.1428	0.0017	3.9	4	
4683	06:04.4	46:51	20.2	18.6	155	61	283.5 (g)	3	VII	3.3650	0.0050		4	QSO
4684	06:04.4	48:00	25.7	23.6	30	81	2.7 (g)	3	IV	0.7843	0.0007	5.3	3	
4685	06:04.4	43:11	25.0	23.5	240	50	9.3 (g)	3	IV	2.6254	0.0017	7.6	4	
4686	06:04.4	45:54	22.7	21.8	442	55	43.1 (g)	3	IV	0.0943	0.0004	39.7	4	
4691	06:04.4	48:34	25.8	24.3	550	67	12.8 (g)	3	V/VI	3.3036	0.0021	10.0	4	LAB
4729	06:04.6	47:36	22.3	21.1	120	56	33.7 (g)	3	VIII	0.0000			4	G
4745	06:04.6	44:03	25.2	23.8	434	69	11.2 (g)	3	V	2.6173	0.0014	6.3	4	
4752	06:04.6	46:54	26.5	99.0	473	28	3.8 (g)	2	V/VI	3.3802	0.0021	5.8	4	LAB; near4683
4771	06:04.7	44:04	25.0	24.5	153	55	5.3 (g)	2	IV	1.8968	0.0017	2.6	2	
									V	1.3952	0.0008	7.9		

Table C.1: *continued*

No.	RA 01:...	DEC −25:...	B [mag]	I [mag]	$T_{\rm exp}$ [min]	f/f_0 [%]	S/N (Band)	$Q_{\rm s}$	Type	z	dz	S	$Q_{\rm z}$	Remarks
4795	06:04.8	47:14	24.4	23.3	570	54	15.9 (g)	3	IV	2.1593	0.0017	8.7	4	
4871	06:05.1	46:04	24.9	23.4	490	57	15.3 (g)	3	IV	2.4724	0.0016	10.9	4	
4882	06:05.1	48:38	21.3	19.0	120	31	74.1 (R)	3	II	0.2777	0.0006	8.8	4	
4910	06:05.2	46:04	25.5	24.3	120	41	2.1 (g)	3	V	0.8437	0.0006	6.4	3	
4954	06:05.4	46:20	25.8	23.8	160	38	2.1 (R)	3	IV	0.9703	0.0008	5.5	3	
4993	06:05.5	45:56	26.5	21.8	245	50	11.3 (I)	3	I	0.7632	0.0006	7.6	4	
4996	06:05.5	46:28	24.4	23.3	281	56	17.1 (g)	3	IV	2.0278	0.0016	7.7	4	
5006	06:05.5	48:42	24.3	21.7	125	31	9.5 (R)	3	II	0.2226	0.0005	12.1	4	
5011	06:05.5	48:49	24.8	20.9	125	12	5.7 (I)	3	I	0.6535	0.0008	3.6	4	
5020	06:05.6	43:28	23.1	21.1	125	45	19.7 (R)	3	III	0.4512	0.0005	15.7	4	
5022	06:05.6	46:15	23.6	22.0	40	56	8.7 (g)	3	IV	0.3383	0.0004	20.9	4	
5023	06:05.6	46:27	25.6	24.6	281	49	5.6 (g)	3	IV	2.0298	0.0015	3.9	3	
5027	06:05.6	44:21	25.8	21.5	120	40	9.2 (I)	3	II	0.7623	0.0009	6.3	3	
5058	06:05.7	46:26	24.1	23.3	686	57	19.3 (g)	3	V	2.0270	0.0016	7.1	4	
5072	06:05.8	45:19	23.5	22.4	401	44	27.4 (g)	3	V	1.3888	0.0007	15.6	4	
5090	06:05.8	46:42	99.0	23.4	530	60	7.8 (I)	3	VIII	0.0000			4	late M
5111	06:05.9	47:45	24.5	23.0	120	64	4.1 (g)	3	IV	0.9692	0.0008	3.9	2	
									III	1.2861	0.0094	1.8		
5134	06:06.0	47:50	22.7	19.1	120	7	7.6 (R)	3	VIII	0.0000			4	K
5135	06:06.0	44:44	99.0	23.6	761	34	8.5 (g)	3	IV	2.3462	0.0016	6.6	4	
5150	06:06.0	45:17	19.2	18.0	120	59	27.9 (g)	3	VIII	0.0000			4	G
5152	06:06.0	45:40	23.5	22.7	341	64	34.3 (g)	3	IV	1.3699	0.0007	18.5	4	

Table C.1: *continued*

No.	RA 01:...	DEC −25:...	B [mag]	I [mag]	$T_{\rm exp}$ [min]	f/f_0 [%]	S/N (Band)	$Q_{\rm s}$	Type	z	dz	S	$Q_{\rm z}$	Remarks
5154	06:06.0	42:55	23.2	20.4	125	59	41.7 (R)	3	VIII	0.0000			4	K
5165	06:06.1	44:43	24.2	23.3	561	20	10.3 (g)	3	V	2.3464	0.0015	6.7	4	
5167	06:06.1	44:42	25.0	23.9	320	51	7.3 (g)	3	V	2.3471	0.0018	5.1	3	
5182	06:06.1	45:34	24.2	23.5	441	53	16.1 (g)	3	V	1.3691	0.0009	18.6	4	
5190	06:06.1	44:43	25.4	24.4	561	55	8.6 (g)	3	V	2.3467	0.0017	4.9	4	
5207	06:06.2	45:53	21.9	19.4	112	52	76.4 (R)	3	VIII	0.0000			4	K
5215	06:06.2	45:04	25.5	23.0	804	60	16.2 (g)	3	V/VI	3.1480	0.0019	28.6	4	LAB
5227	06:06.3	43:52	24.9	23.9	320	51	7.8 (g)	3	IV	2.3986	0.0016	5.1	4	
5236	06:06.3	45:42	23.5	21.9	60	34	10.2 (g)	3	IV	1.1531	0.0010	12.5	4	
5246	06:06.4	46:27	99.0	24.0	811	70	8.1 (R)	3	V	3.9249	0.0019	4.2	4	
5269	06:06.5	43:12	25.1	22.6	120	56	6.0 (R)	3	III	0.4548	0.0006	3.9	2	
									II	0.4041	0.0003	2.8		
5282	06:06.5	45:03	24.8	20.6	160	4	2.8 (I)	3	II	0.9911	0.0014	3.0	2	
									II	0.9056	0.0008	2.3		
5289	06:06.5	45:05	99.0	21.6	153	16	4.0 (g)	2	IV	1.0210	0.0007	7.4	2	
									IV	1.2242	0.0014	2.5		
5362	06:06.8	47:34	22.6	19.2	30	41	48.6 (R)	3	I	0.3336	0.0004	14.5	4	
5428	06:07.1	46:30	25.4	24.2	373	67	8.5 (g)	3	IV	2.4596	0.0024	4.9	2	
									IV	2.5068	0.0236	3.1		
5448	06:07.1	47:31	23.7	21.5	40	31	4.2 (R)	3	III	0.7615	0.0007	5.7	4	
5458	06:07.2	46:44	24.1	23.1	400	49	12.5 (g)	3	IV	1.5131	0.0017	5.8	3	
5504	06:07.3	46:59	99.0	23.6	400	52	5.3 (R)	2	IV	3.3772	0.0023	4.2	3	

Table C.1: *continued*

No.	RA 01:...	DEC −25:...	B [mag]	I [mag]	$T_{\rm exp}$ [min]	f/f_0 [%]	S/N (Band)	$Q_{\rm s}$	Type	z	dz	S	$Q_{\rm z}$	Remarks
5510	06:07.3	47:30	99.0	24.2	400	46	2.4 (R)	3	V	4.0899	0.0025	2.7	4	
5549	06:07.5	46:40	23.6	21.9	240	45	18.8 (g)	2	IV	0.3149	0.0004	27.2	4	
5550	06:07.5	47:00	25.5	23.1	750	54	14.5 (R)	2	V	3.3829	0.0019	9.3	4	
5568	06:07.6	47:07	24.1	21.6	245	30	9.6 (R)	3	II	0.3388	0.0004	4.0	3	
5585	06:07.7	45:51	99.0	21.0	190	20	9.6 (R)	3	III	1.0741	0.0011	6.3	3	
5602	06:07.7	47:06	26.0	24.9	400	55	3.8 (g)	3	III	1.4597	0.0010	5.0	2	
									IV	1.0840	0.0009	4.7		
5667	06:07.9	46:37	99.0	23.0	120	62	5.8 (g)	3	IV	1.0241	0.0007	14.6	4	
5719	06:08.1	45:37	25.7	23.9	281	73	6.4 (g)	2	IV	0.7613	0.0006	8.5	4	
5744	06:08.2	45:34	27.3	24.1	594	53	7.6 (R)	3	IV	3.3411	0.0021	6.1	4	
5756	06:08.3	46:27	23.9	22.5	120	30	5.7 (g)	2	III	0.1623	0.0009	3.5	2	
									V	2.8404	0.0017	2.9		
5764	06:08.3	44:21	25.1	23.0	441	71	13.4 (g)	3	III	0.9361	0.0007	15.5	4	
5788	06:08.4	43:36	99.0	21.5	180	35	9.6 (B)	2	III	0.9525	0.0007	9.7	4	
5812	06:08.5	44:17	99.0	25.6	601	66	1.1 (I)	3	V/VI	4.9947	0.0027	3.5	4	LAB
5835	06:08.6	44:09	22.5	20.9	245	52	50.4 (g)	3	IV	0.3371	0.0004	40.5	4	
5874	06:08.7	45:49	25.3	23.7	60	55	3.8 (g)	2	III	0.2352	0.0004	7.6	3	
5899	06:08.8	42:57	23.8	21.0	120	49	20.9 (R)	2	II	0.4528	0.0006	8.5	4	
5903	06:08.8	44:54	23.9	22.3	592	52	31.2 (g)	2	V	2.7748	0.0017	7.9	4	
5908	06:08.8	48:07	19.7	16.5	270	0	4.3 (R)	2	I	0.2232	0.0007	3.7	4	
5953	06:09.0	46:45	25.8	23.1	153	57	5.8 (g)	3	II	1.5918	0.0010	2.9	3	
5979	06:09.1	45:45	24.0	22.1	60	74	12.2 (R)	3	III	0.7722	0.0007	16.3	4	

Table C.1: *continued*

No.	RA 01:...	DEC −25:...	B [mag]	I [mag]	$T_{\rm exp}$ [min]	f/f_0 [%]	S/N (Band)	$Q_{\rm s}$	Type	z	dz	S	$Q_{\rm z}$	Remarks
5982	06:09.1	46:10	23.0	20.6	40	39	13.1 (R)	3	III	0.4712	0.0006	6.6	3	
5987	06:09.1	48:13	99.0	22.2	280	39	11.2 (R)	3	II	0.4090	0.0004	8.4	4	
5989	06:09.1	44:48	25.6	22.2	120	59	9.7 (I)	3	II	1.0233	0.0008	9.3	4	
6007	06:09.2	43:26	25.2	24.1	281	54	6.5 (g)	3	VII	2.7515	0.0030		4	QSO
6024	06:09.2	48:14	22.7	22.0	560	34	29.0 (g)	3	V	2.3719	0.0014	9.1	4	lensed?
6063	06:09.4	48:07	24.5	22.6	270	46	11.3 (R)	3	V	3.3969	0.0019	4.8	4	lensed?
6069	06:09.4	44:45	25.3	24.2	320	69	7.5 (g)	3	V	2.6820	0.0022	4.3	4	
6100	06:09.5	42:45	23.9	22.1	60	37	6.5 (R)	3	IV	0.6849	0.0006	15.0	4	
6101	06:09.5	45:50	23.7	22.4	60	56	9.7 (g)	3	IV	1.1422	0.0008	19.5	4	
6145	06:09.7	48:16	26.3	24.1	240	20	1.7 (R)	3	V	3.0155	0.0017	1.5	2	
									IV	0.3094	0.0005	3.4		
6155	06:09.7	47:19	99.0	23.2	240	42	10.8 (g)	2	V	1.3392	0.0007	7.6	2	
									V	1.6192	0.0012	2.9		
6233	06:10.0	43:42	26.0	23.9	561	56	10.2 (R)	3	VII	2.3215	0.0030		4	QSO (BAL)
6269	06:10.1	44:25	99.0	22.6	281	37	7.6 (g)	2	III	0.9363	0.0007	6.4	3	
6275	06:10.1	42:28	23.3	19.7	30	31	24.0 (R)	3	I	0.3960	0.0005	10.6	4	
6287	06:10.1	44:24	25.9	24.1	281	54	8.2 (g)	3	IV	2.6778	0.0017	5.6	4	
6307	06:10.2	44:28	23.5	19.7	110	45	5.2 (R)	3	I	0.4094	0.0008	3.5	3	
6331	06:10.3	47:53	24.1	22.9	125	58	7.2 (g)	2	IV	0.1152	0.0005	10.9	2	
									IV	2.1381	0.0016	3.1		
6344	06:10.4	43:33	23.9	23.2	160	37	8.6 (g)	3	V	1.6640	0.0011	2.5	3	
6351	06:10.4	48:26	23.1	21.5	310	56	34.4 (g)	3	IV	0.3356	0.0004	37.8	4	

Table C.1: *continued*

No.	RA 01:...	DEC −25:...	B [mag]	I [mag]	$T_{\rm exp}$ [min]	f/f_0 [%]	S/N (Band)	$Q_{\rm s}$	Type	z	dz	S	$Q_{\rm z}$	Remarks
6358	06:10.4	44:31	99.0	22.7	110	41	7.0 (g)	3	IV	1.3153	0.0008	8.5	3	
6372	06:10.5	48:29	24.5	23.4	490	51	16.0 (g)	3	IV	2.3493	0.0018	9.4	4	
6384	06:10.5	45:13	23.8	22.9	110	57	14.7 (g)	3	V	1.3143	0.0007	16.4	4	
6394	06:10.5	48:32	24.5	22.7	110	38	9.6 (g)	3	IV	0.2287	0.0005	15.4	4	
6406	06:10.6	44:41	23.0	20.8	110	13	6.3 (R)	2	IV	0.8445	0.0007	5.9	4	TF
6407	06:10.6	45:32	25.0	23.6	320	54	9.9 (g)	3	IV	2.1624	0.0015	5.3	4	
6432	06:10.7	46:09	24.9	22.9	120	67	6.7 (R)	3	III	1.1530	0.0008	4.8	3	
6439	06:10.7	42:44	22.4	18.9	90	44	91.3 (R)	3	I	0.3962	0.0006	8.9	4	
6447	06:10.7	45:07	26.4	22.0	352	66	15.8 (I)	3	VIII	0.0000			4	M
6529	06:11.0	48:26	22.5	20.4	40	31	13.6 (R)	3	III	0.5169	0.0005	11.4	4	
6547	06:11.1	46:49	24.0	23.3	120	65	13.6 (g)	3	V	1.2116	0.0007	17.1	4	
6557	06:11.1	47:33	99.0	24.9	313	57	1.6 (R)	3	V/VI	4.6818	0.0025	7.8	4	LAB
6691	06:11.5	46:14	26.5	24.2	240	71	5.5 (R)	3	V	3.1467	0.0015	4.1	4	
6768	06:11.8	43:58	26.1	21.7	120	30	8.4 (I)	3	I	0.8952	0.0008	7.0	3	
6779	06:11.9	42:53	25.2	23.4	120	56	4.5 (g)	2	IV	0.9358	0.0007	11.0	3	
6810	06:12.0	48:09	22.2	20.7	160	17	22.2 (g)	3	VIII	0.0000			4	G
6850	06:12.2	44:55	24.6	23.5	60	30	2.1 (g)	3	IV IV	1.0752 0.9983	0.0007 0.0007	4.4 3.4	2	
6864	06:12.2	43:56	24.1	23.4	400	62	19.7 (g)	3	V	1.3938	0.0008	25.5	4	
6870	06:12.2	48:28	24.8	21.5	40	39	7.9 (R)	3	I	0.4083	0.0007	4.3	4	
6876	06:12.2	46:10	99.0	24.1	473	39	1.7 (R)	3	V	4.5300	0.0024	1.0	4	
6895	06:12.3	45:55	25.9	24.4	120	70	2.8 (g)	3	V	0.8653	0.0006	8.7	3	

Table C.1: *continued*

No.	RA 01:...	DEC −25:...	B [mag]	I [mag]	$T_{\rm exp}$ [min]	f/f_0 [%]	S/N (Band)	$Q_{\rm s}$	Type	z	dz	S	$Q_{\rm z}$	Remarks
6921	06:12.3	46:35	24.0	21.9	40	46	6.5 (R)	3	III	0.4542	0.0005	7.8	4	
6934	06:12.4	44:57	99.0	22.9	390	30	10.3 (g)	3	IV	2.4452	0.0017	5.7	4	
6947	06:12.4	48:15	25.3	23.8	640	65	13.0 (g)	3	IV	2.3565	0.0014	9.8	4	
6960	06:12.4	44:56	25.3	99.0	360	23	4.4 (g)	2	V	2.4415	0.0013	2.7	3	near 6934
6962	06:12.4	44:24	99.0	24.6	601	74	2.9 (R)	3	V	4.2076	0.0026	2.3	4	
7029	06:12.7	45:58	24.8	23.6	420	56	13.1 (g)	3	IV	2.3744	0.0017	9.7	4	
7078	06:12.8	46:01	25.0	24.0	110	51	5.5 (g)	2	IV	2.3782	0.0022	5.3	4	
7079	06:12.8	44:48	23.7	22.2	180	39	12.5 (R)	3	IV	0.4431	0.0005	24.2	4	
7084	06:12.8	44:38	24.4	22.2	292	41	11.5 (R)	2	II	0.2246	0.0005	7.5	4	
7099	06:12.9	44:53	23.6	22.5	245	42	7.3 (R)	3	IV	1.1461	0.0008	14.1	4	
7116	06:13.0	43:26	24.2	20.5	30	62	21.2 (R)	3	I	0.4578	0.0004	8.0	4	
7120	06:13.0	45:31	23.2	22.6	120	58	8.8 (R)	2	V	1.3072	0.0007	14.8	4	
7149	06:13.1	43:27	26.2	99.0	601	83	4.4 (g)	3	IV	0.4430	0.0004	4.7	2	
									IV	2.1994	0.0017	3.3		
7164	06:13.1	43:44	25.9	24.2	611	63	8.3 (g)	3	V	3.0646	0.0018	3.9	4	
7186	06:13.2	42:41	23.1	21.1	60	21	8.0 (R)	3	III	0.4509	0.0005	7.1	3	
7252	06:13.4	47:11	27.1	24.0	393	80	8.2 (R)	3	VIII	0.0000			3	K?
7253	06:13.4	43:52	99.0	22.6	210	49	9.0 (I)	3	VIII	0.0000			4	late M
7254	06:13.4	45:25	25.4	22.4	472	69	19.1 (R)	3	VIII	0.0000			4	K
7275	06:13.5	47:22	25.2	24.1	350	48	5.4 (g)	3	V	2.4381	0.0015	3.7	3	
7304	06:13.6	43:54	24.0	21.8	210	68	23.9 (R)	3	VIII	0.0000			4	K
7307	06:13.6	47:25	25.0	24.1	350	68	9.8 (g)	3	V	2.4378	0.0014	6.2	4	

Table C.1: *continued*

No.	RA 01:...	DEC −25:...	B [mag]	I [mag]	$T_{\rm exp}$ [min]	f/f_0 [%]	S/N (Band)	$Q_{\rm s}$	Type	z	dz	S	$Q_{\rm z}$	Remarks
7342	06:13.7	46:13	99.0	23.8	440	39	7.2 (g)	2	IV	2.3747	0.0021	5.6	4	
7345	06:13.7	46:24	24.1	23.1	240	67	17.0 (g)	3	V	1.0251	0.0007	24.7	4	
7373	06:13.8	48:43	23.3	19.5	30	48	38.4 (I)	3	VIII	0.0000			4	M
7441	06:14.1	45:15	21.0	19.1	125	53	126.5 (R)	3	VIII	0.0000			4	G/K
7457	06:14.2	46:42	23.6	22.4	262	46	16.6 (g)	3	V	0.3328	0.0004	34.1	4	
7461	06:14.2	48:09	99.0	24.8	1060	72	3.9 (R)	3	V	4.5193	0.0022	3.1	4	
7473	06:14.2	46:59	24.1	23.2	110	37	6.4 (g)	3	IV	1.7261	0.0019	2.8	2	
									IV	1.1408	0.0007	5.5		
7492	06:14.3	48:24	26.6	22.4	40	24	2.4 (I)	2	VIII	0.0000			3	M/L?
7504	06:14.3	44:04	24.6	22.6	120	52	6.4 (R)	3	III	0.9378	0.0007	10.0	4	
7526	06:14.4	46:05	99.0	19.5	30	39	38.3 (R)	3	III	0.3587	0.0005	23.3	4	
7539	06:14.4	47:08	25.5	23.5	490	59	12.1 (g)	3	V	3.2878	0.0019	5.2	4	
7547	06:14.5	43:24	99.0	24.8	961	74	2.5 (I)	2	I	1.2755	0.0010	2.9	2	
									I	1.4850	0.0022	2.4		
7624	06:14.7	46:40	99.0	21.4	120	32	6.8 (I)	3	II	0.9500	0.0010	5.1	2	
									II	1.0204	0.0011	3.7		
7683	06:14.9	47:30	27.4	24.2	313	64	4.1 (R)	3	V	3.7812	0.0020	3.4	4	
7827	06:15.6	44:25	24.0	23.3	120	64	8.0 (g)	3	V	0.3959	0.0004	13.4	4	
8167	06:16.7	47:48	25.2	20.8	112	33	14.5 (I)	3	VIII	0.0000			4	M
8236	06:17.0	45:38	23.4	22.3	270	47	19.3 (g)	3	V	0.9397	0.0006	17.6	4	
8333	06:17.4	48:31	25.5	21.8	112	31	9.7 (R)	1	III	0.4017	0.0004	3.0	3	
8360	06:17.5	46:14	23.6	22.0	150	38	10.0 (g)	3	IV	0.7037	0.0007	15.1	4	

Table C.1: *continued*

No.	RA 01:...	DEC −25:...	B [mag]	I [mag]	$T_{\rm exp}$ [min]	f/f_0 [%]	S/N (Band)	$Q_{\rm s}$	Type	z	dz	S	$Q_{\rm z}$	Remarks
8643	06:18.8	44:40	99.0	17.8	30	31	71.3 (I)	2	II	0.2276	0.0006	8.8	4	
9002	06:04.3	46:55	99.0	99.0	521	61	2.2 (g)	3	V/VI	3.3747	0.0020	7.1	4	LAB; near4683
9003	06:04.2	46:48	99.0	99.0	160	32	1.1 (B)	3	V/VI	3.3694	0.0023	3.5	3	LAB?; near4683
9006	05:55.3	44:58	99.0	99.0	153	52	0.3 (R)	3	V/VI	3.5366	0.0021	3.2	3	LAB?
9009	06:04.4	51:12	99.0	99.0	30	59	6.9 (I)	3	I	0.7680	0.0009	5.2	4	out of FDF
9010	06:09.3	48:15	99.0	99.0	560	61	7.9 (R)	3	IV	0.4505	0.0005	11.2	4	near 6024
9011	06:08.8	44:55	26.7	24.9	273	52	9.0 (g)	3	IV	2.7716	0.0019	4.9	4	near 5903
9014	06:07.7	45:51	24.3	22.7	40	52	4.1 (g)	3	III	1.4060	0.0009	7.5	2	near 5585
									III	1.4977	0.0017	2.9		

Appendix D

Atlas of the observed spectra

In this appendix, plots of 233 spectra of the FDF spectroscopic survey are shown. The selection comprises the objects with certain spectroscopic redshift ($Q_z = 4$) and no strong spectral distortions ($Q_s > 1$).

In the spectra strong residuals are filtered out by the application of a threshold-controlled median filter (see Section 4.4). At the positions of strong residuals the spectra are less trustworthy than they appear in the cleaned plots. Therefore, the positions of the most prominent night sky lines in the optical ([O I]λ 5577, Na D and [O I]$\lambda\lambda$ 6300, 6364) are marked by green dash-dotted lines. The strong OH bands in the infrared are recognisable by the increased error function (green solid line). The error function is a measure of the statistical noise level and can be used to the estimate of the signal-to-noise ratio (see Section 4.3). Besides the positions of strong telluric emission lines, the locations of the atmospheric absorption bands A and B (green dash-dotted lines at 6885 and 7620 Å) are also indicated. These bands were removed as described in Section 4.7.

To facilitate the identification of spectral features the positions of various expected prominent lines are marked by cyan dotted lines and blue labels. Further information on each object is given at the top of each diagram. There, one finds the identification number, the spectral type and the redshift of the spectrum displayed (see Appendix C).

A similar selection of spectra as shown in this atlas will be published in electronic form in the context of a forthcoming paper (see Noll et al. 2003).

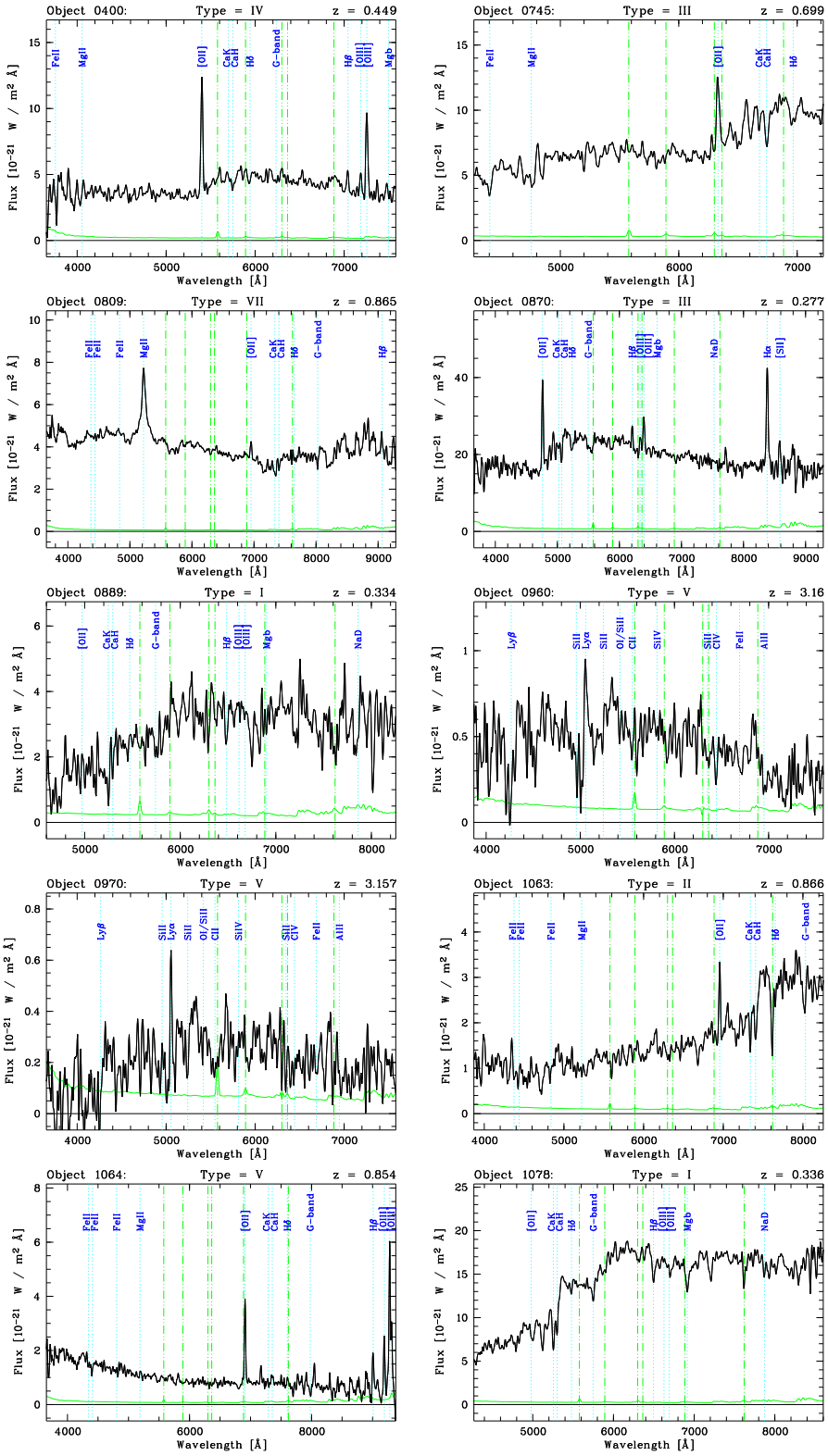

Figure D.1: Spectra of the objects 0400, 0745, 0809, 0870, 0889, 0960, 0970, 1063, 1064 and 1078.

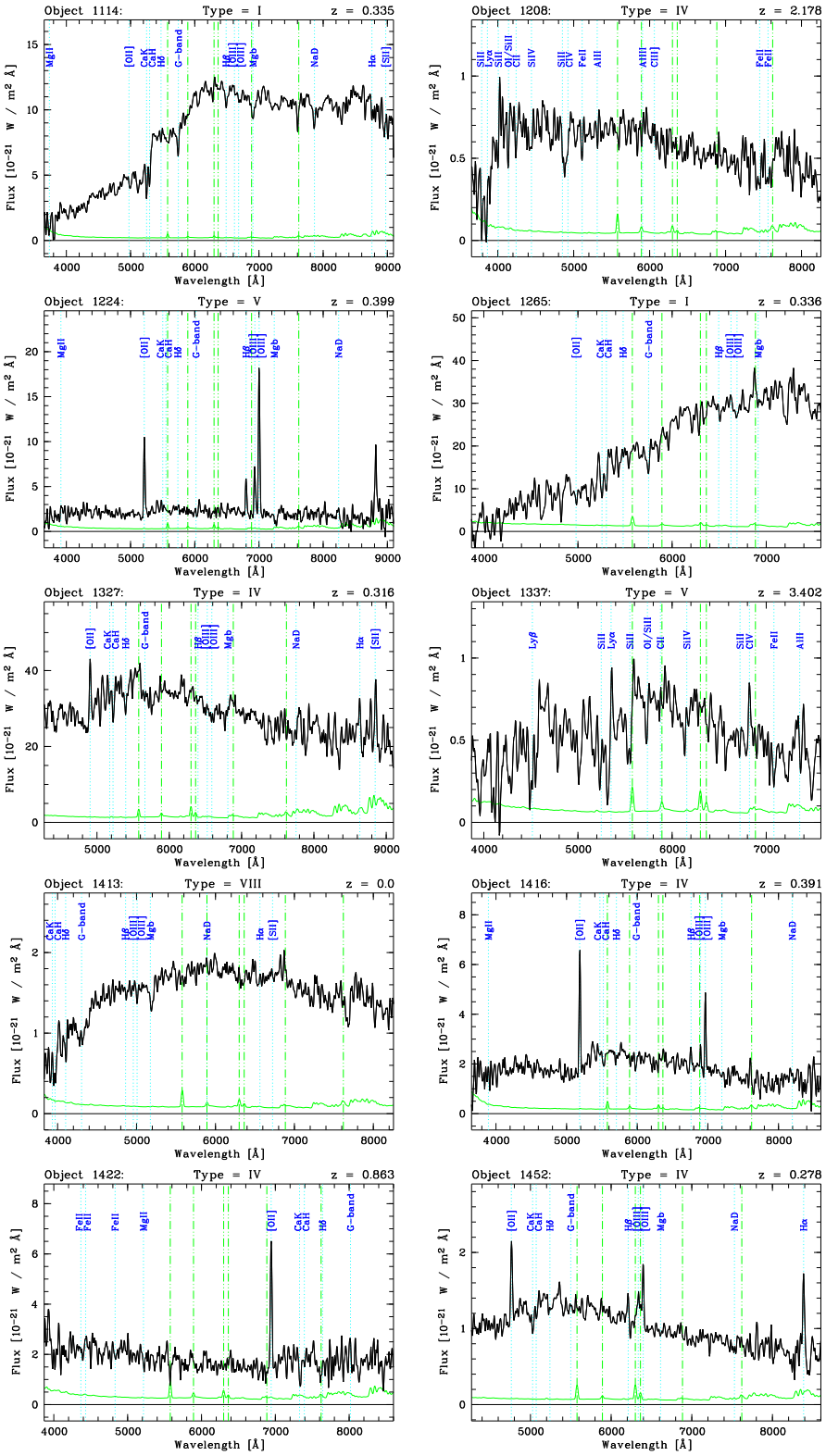

Figure D.2: Spectra of the objects 1114, 1208, 1224, 1265, 1327, 1337, 1413, 1416, 1422 and 1452.

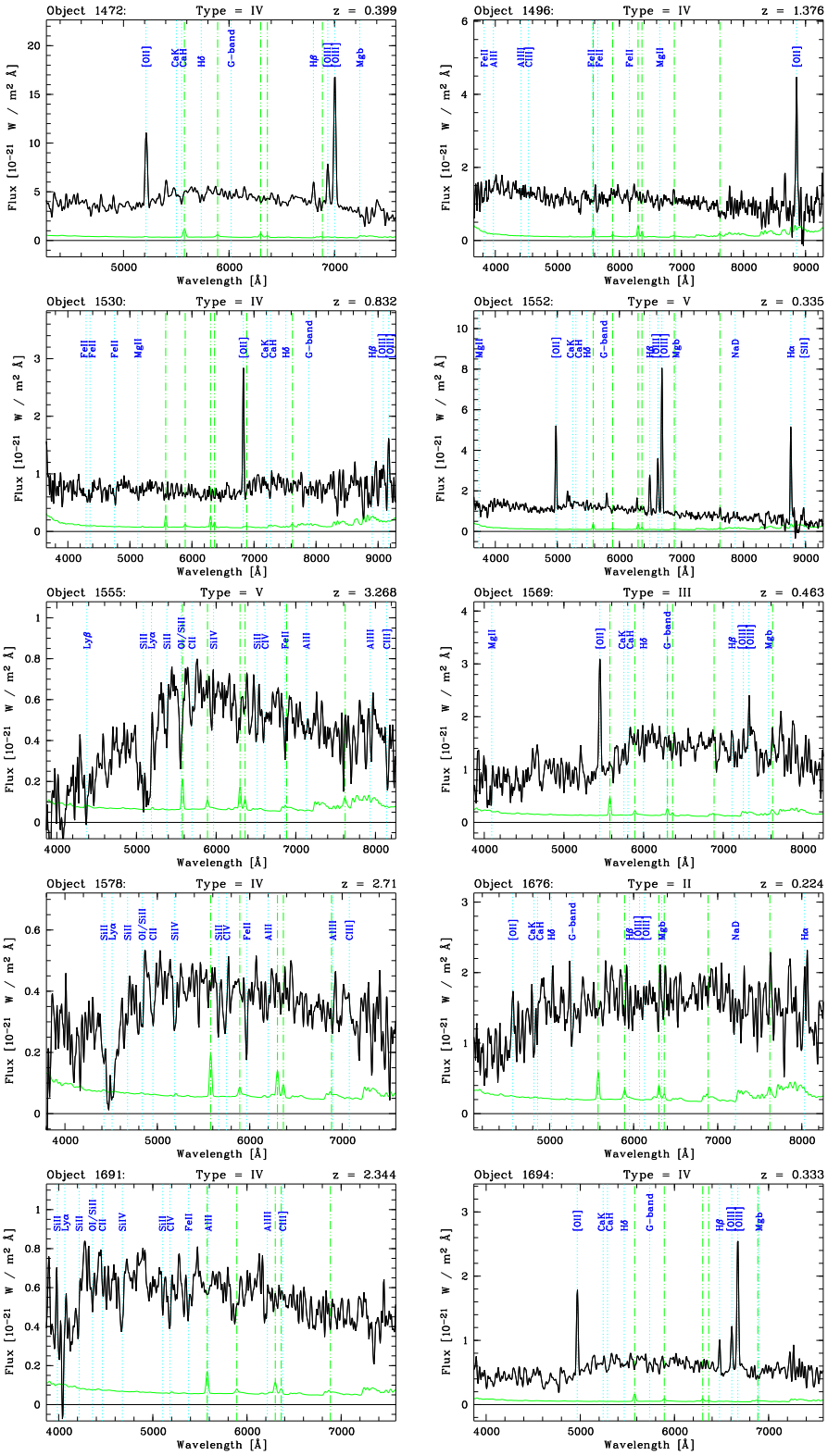

Figure D.3: Spectra of the objects 1472, 1496, 1530, 1552, 1555, 1569, 1578, 1676, 1691 and 1694.

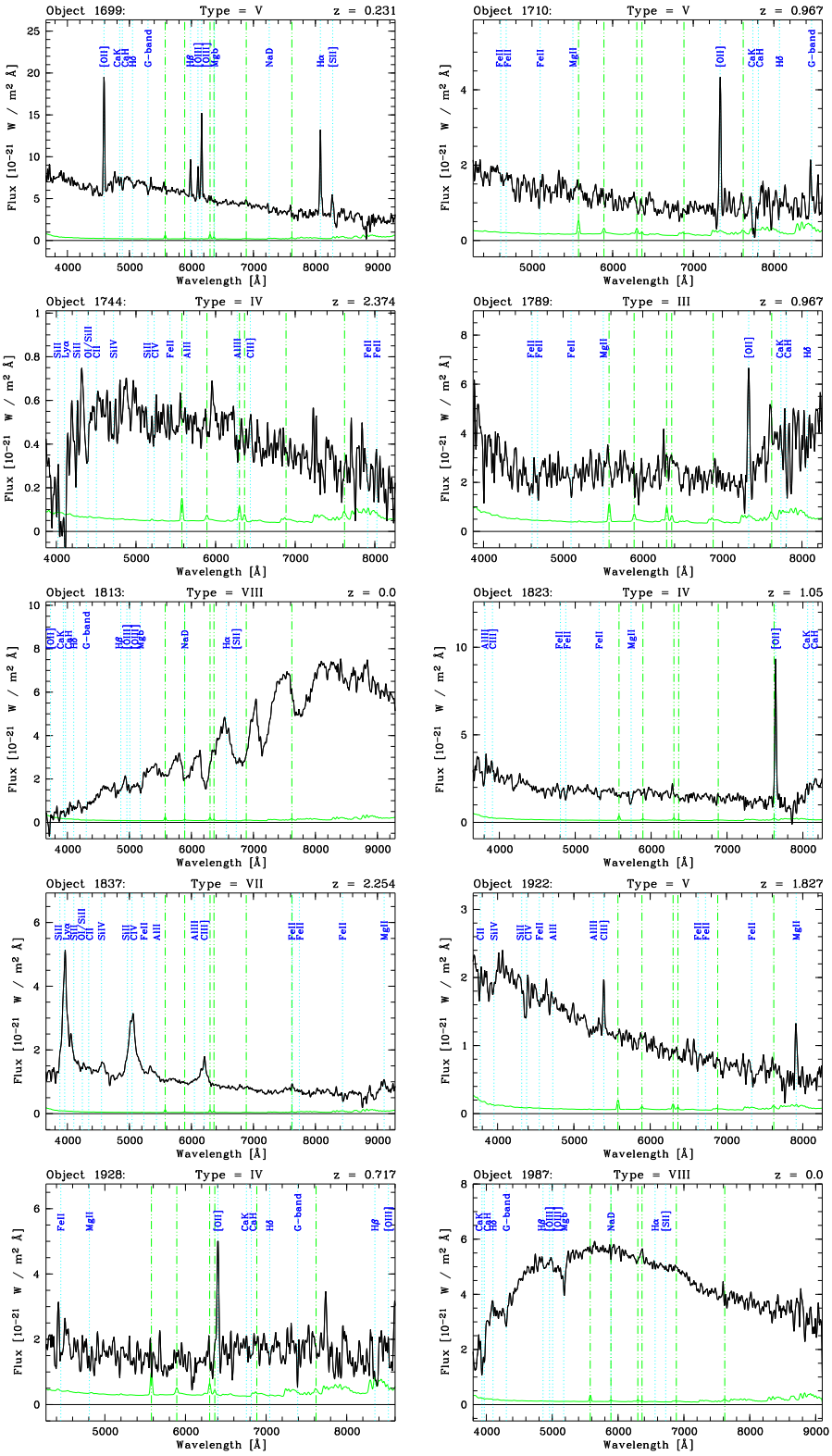

Figure D.4: Spectra of the objects 1699, 1710, 1744, 1789, 1813, 1823, 1837, 1922, 1928 and 1987.

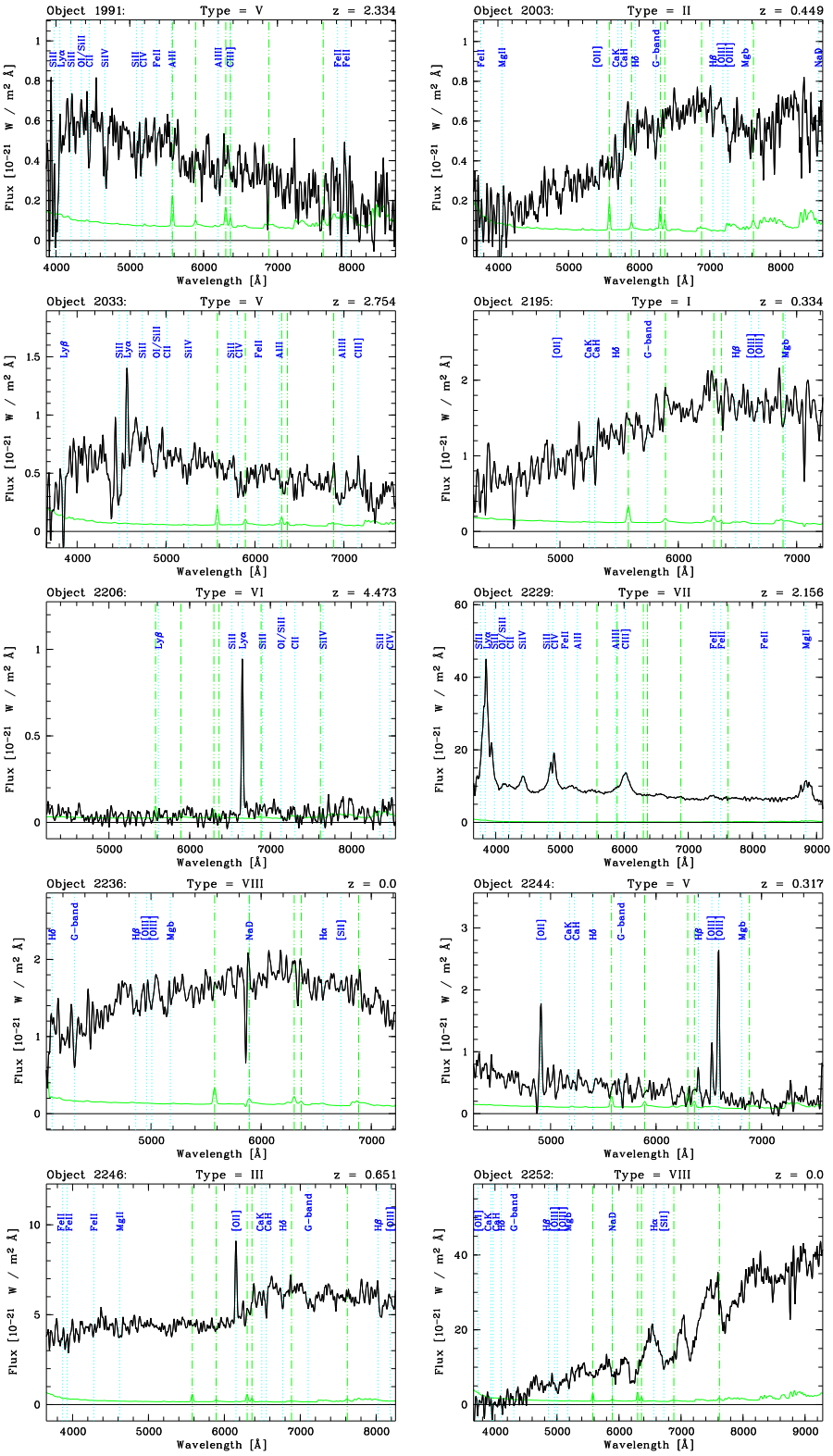

Figure D.5: Spectra of the objects 1991, 2003, 2033, 2195, 2206, 2229, 2236, 2244, 2246 and 2252.

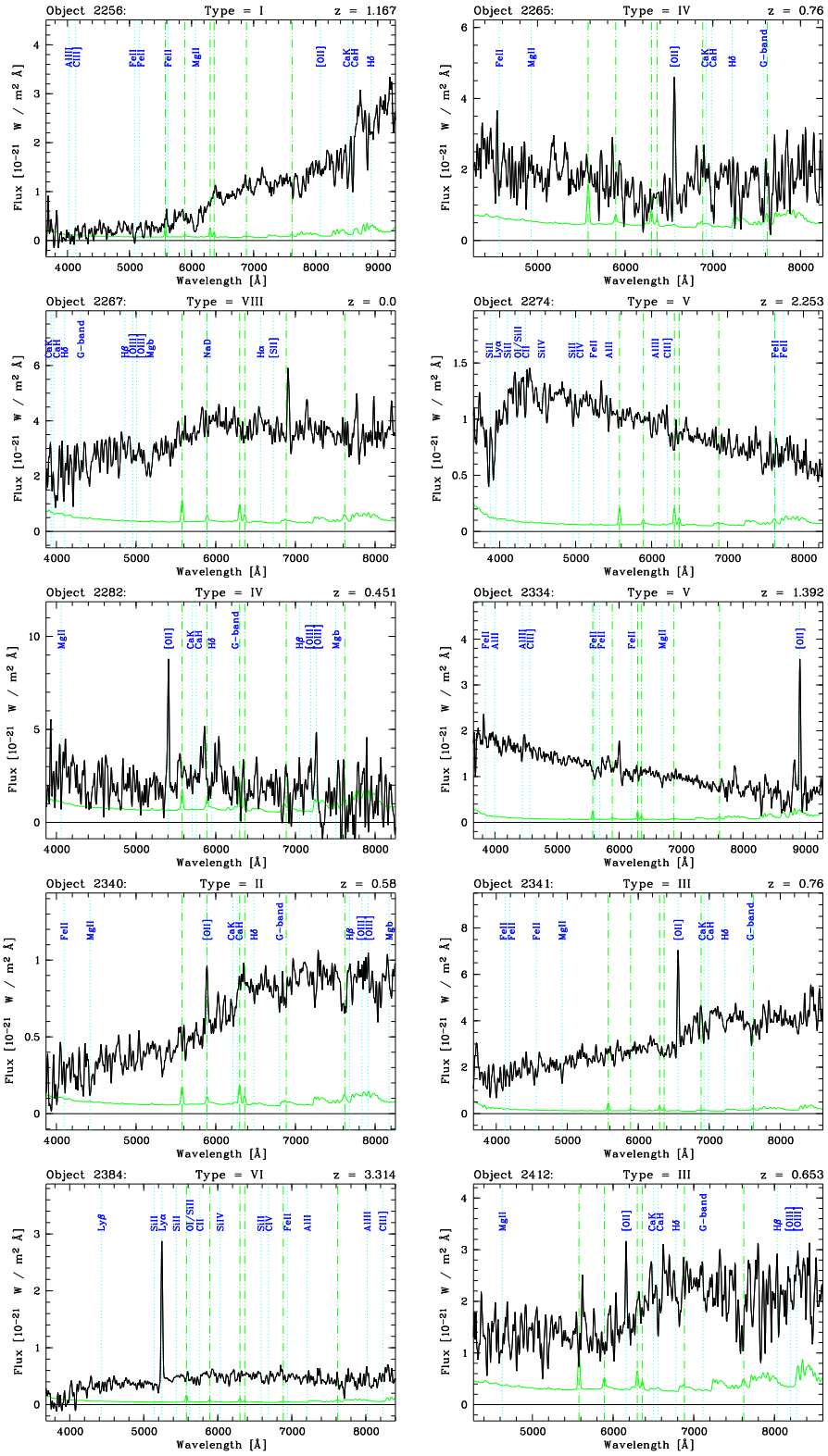

Figure D.6: Spectra of the objects 2256, 2265, 2267, 2274, 2282, 2334, 2340, 2341, 2384 and 2412.

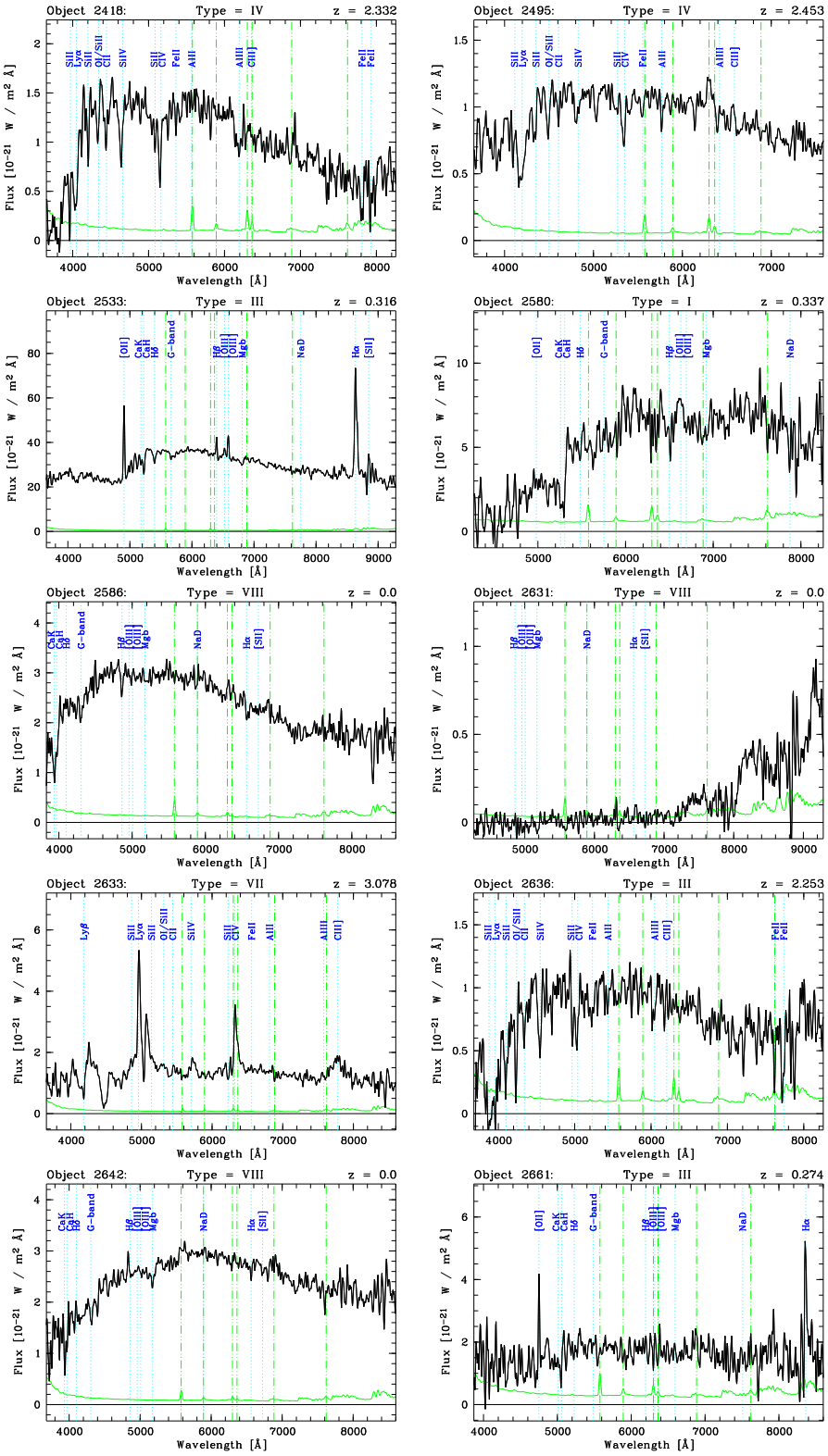

Figure D.7: Spectra of the objects 2418, 2495, 2533, 2580, 2586, 2631, 2633, 2636, 2642 and 2661.

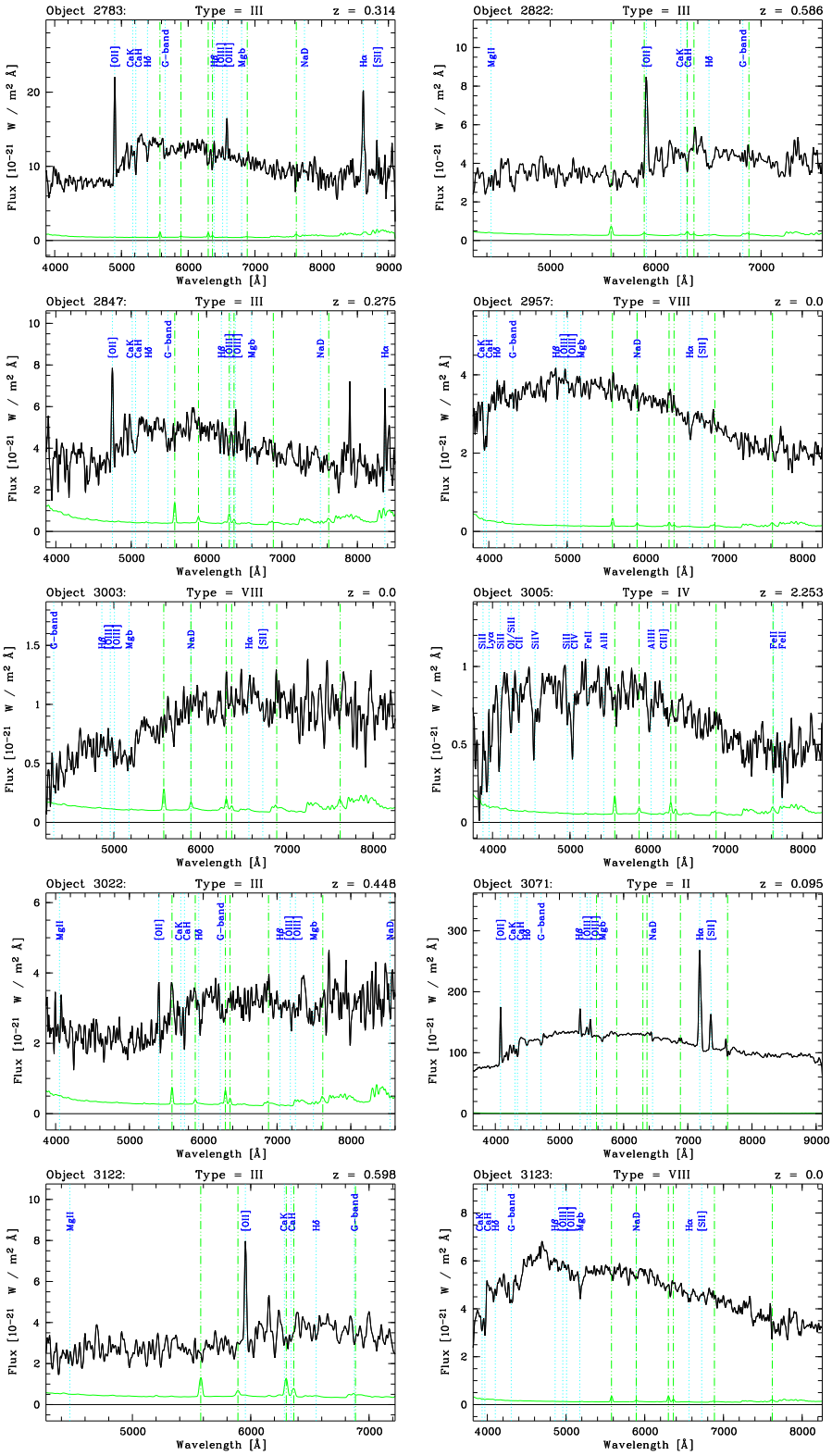

Figure D.8: Spectra of the objects 2783, 2822, 2847, 2957, 3003, 3005, 3022, 3071, 3122 and 3123.

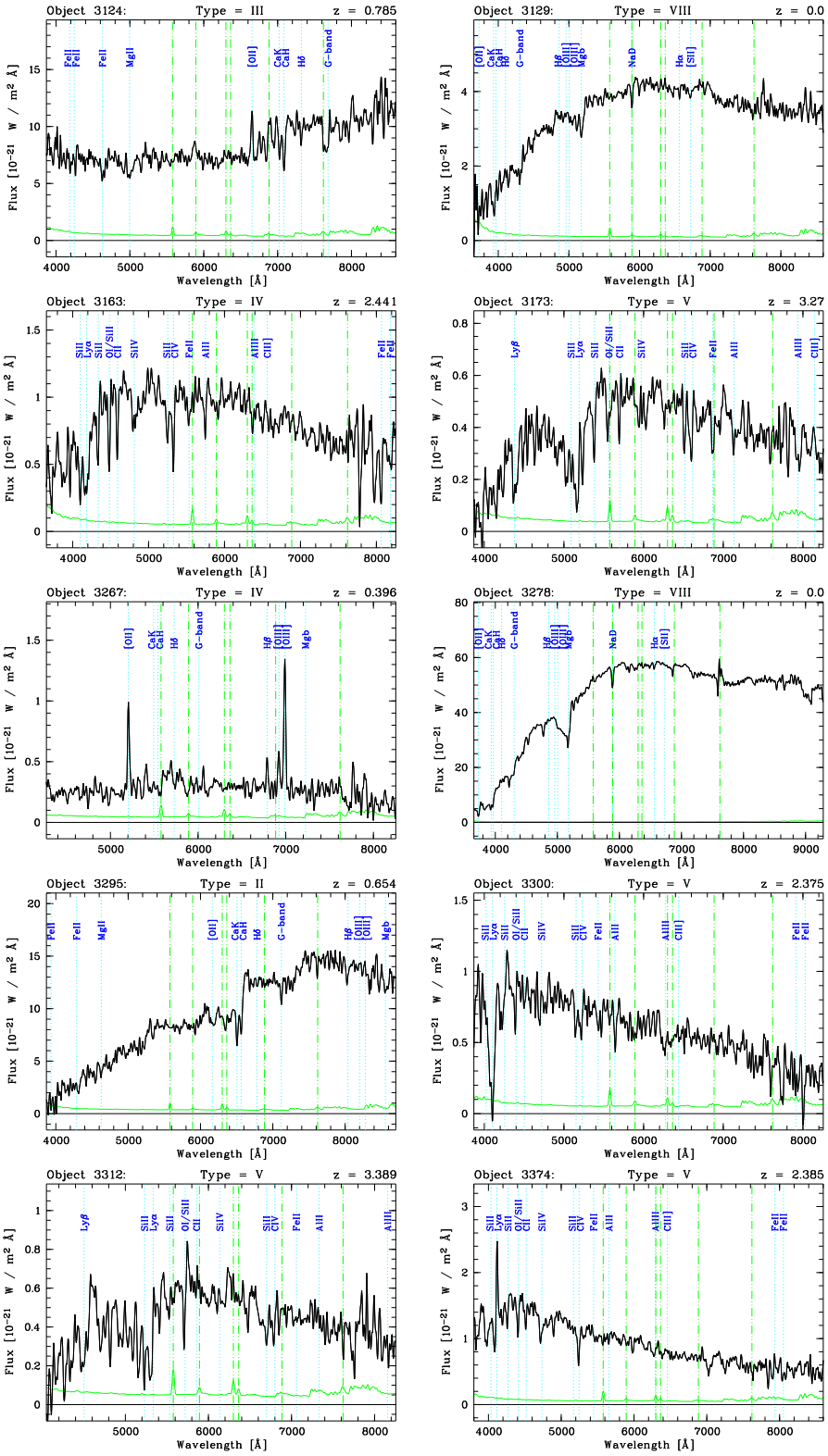

Figure D.9: Spectra of the objects 3124, 3129, 3163, 3173, 3267, 3278, 3295, 3300, 3312 and 3374.

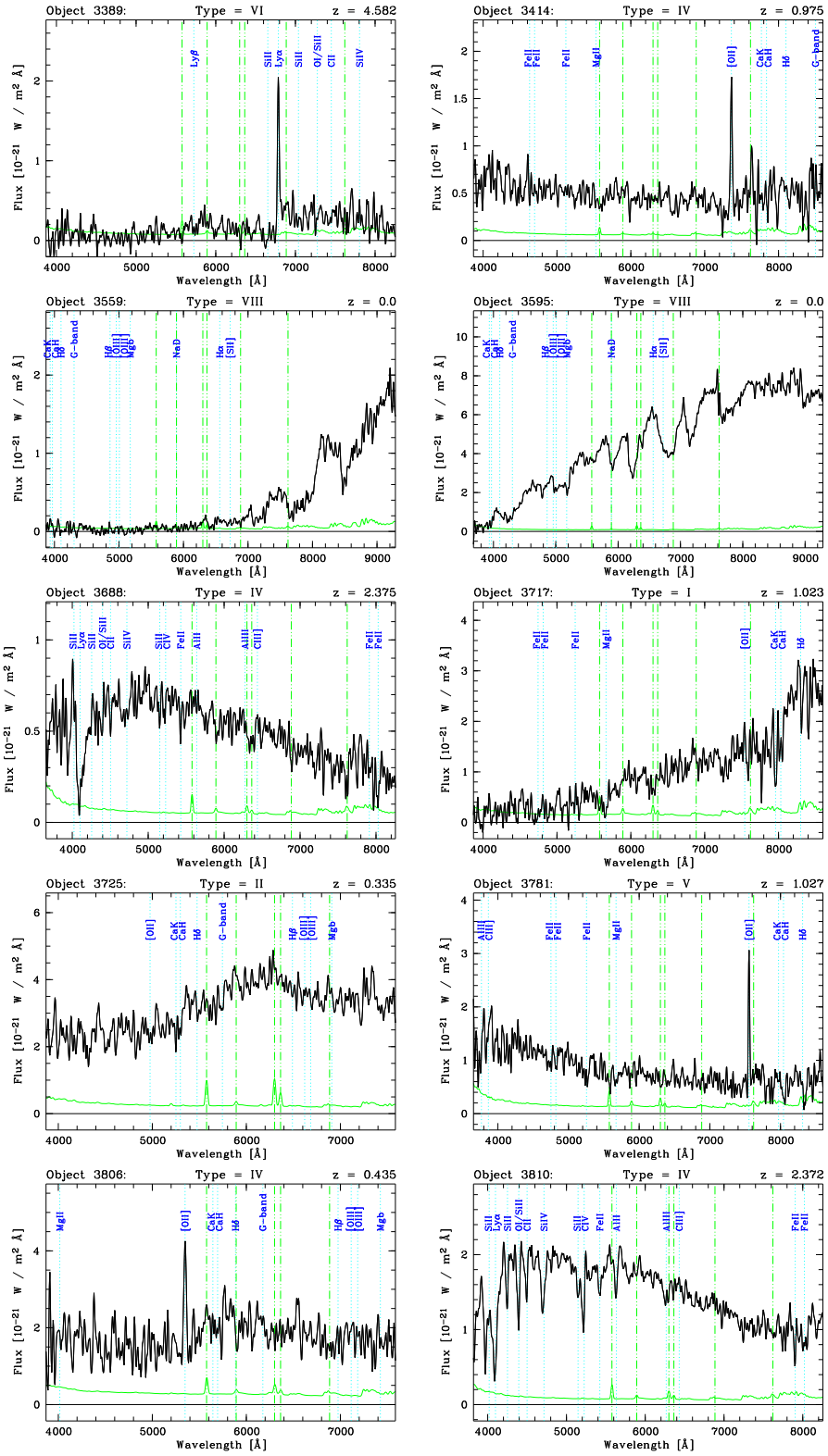

Figure D.10: Spectra of the objects 3389, 3414, 3559, 3595, 3688, 3717, 3725, 3781, 3806 and 3810.

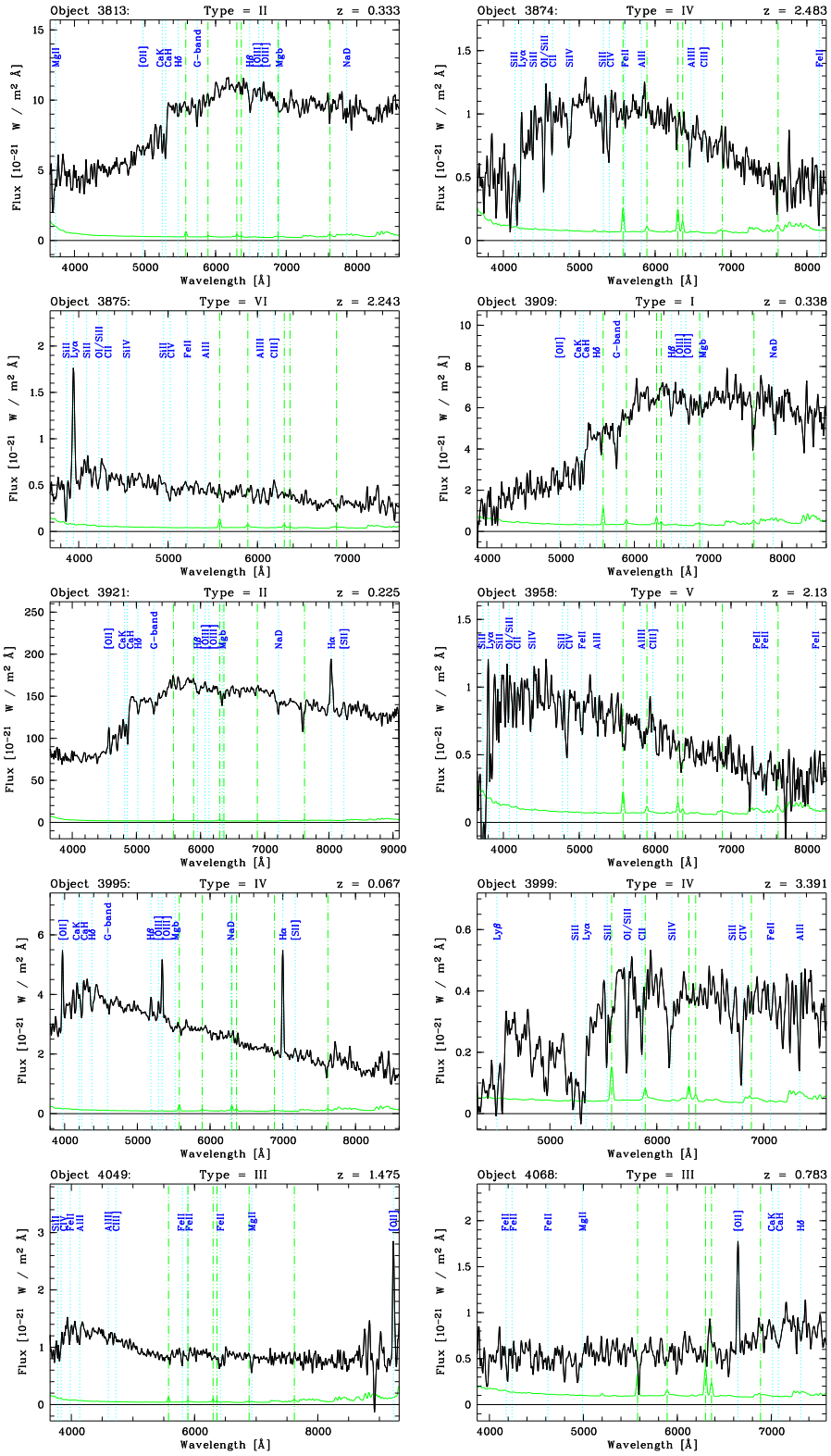

Figure D.11: Spectra of the objects 3813, 3874, 3875, 3909, 3921, 3958, 3995, 3999, 4049 and 4068.

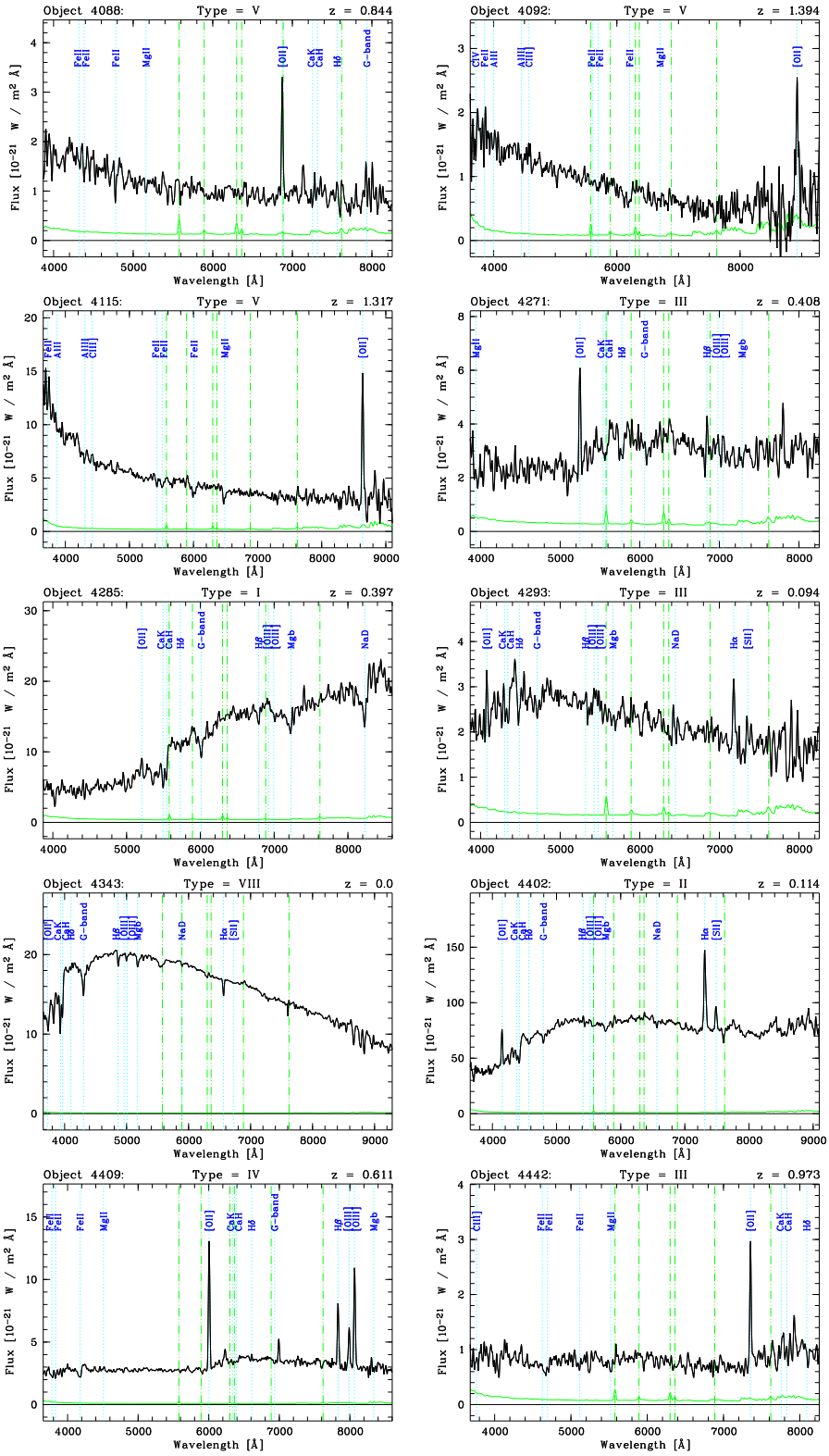

Figure D.12: Spectra of the objects 4088, 4092, 4115, 4271, 4285, 4293, 4343, 4402, 4409 and 4442.

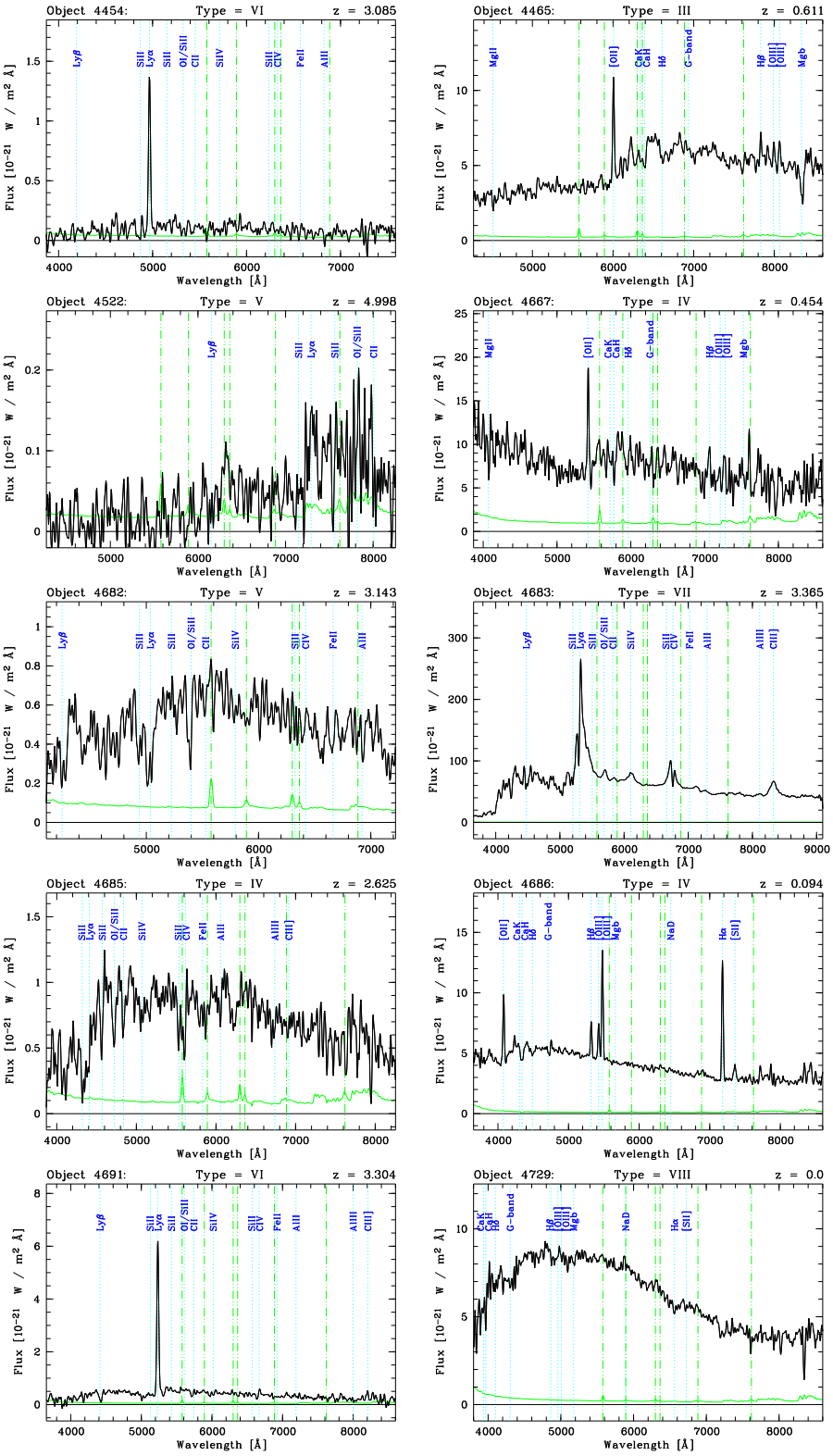

Figure D.13: Spectra of the objects 4454, 4465, 4522, 4667, 4682, 4683, 4685, 4686, 4691 and 4729.

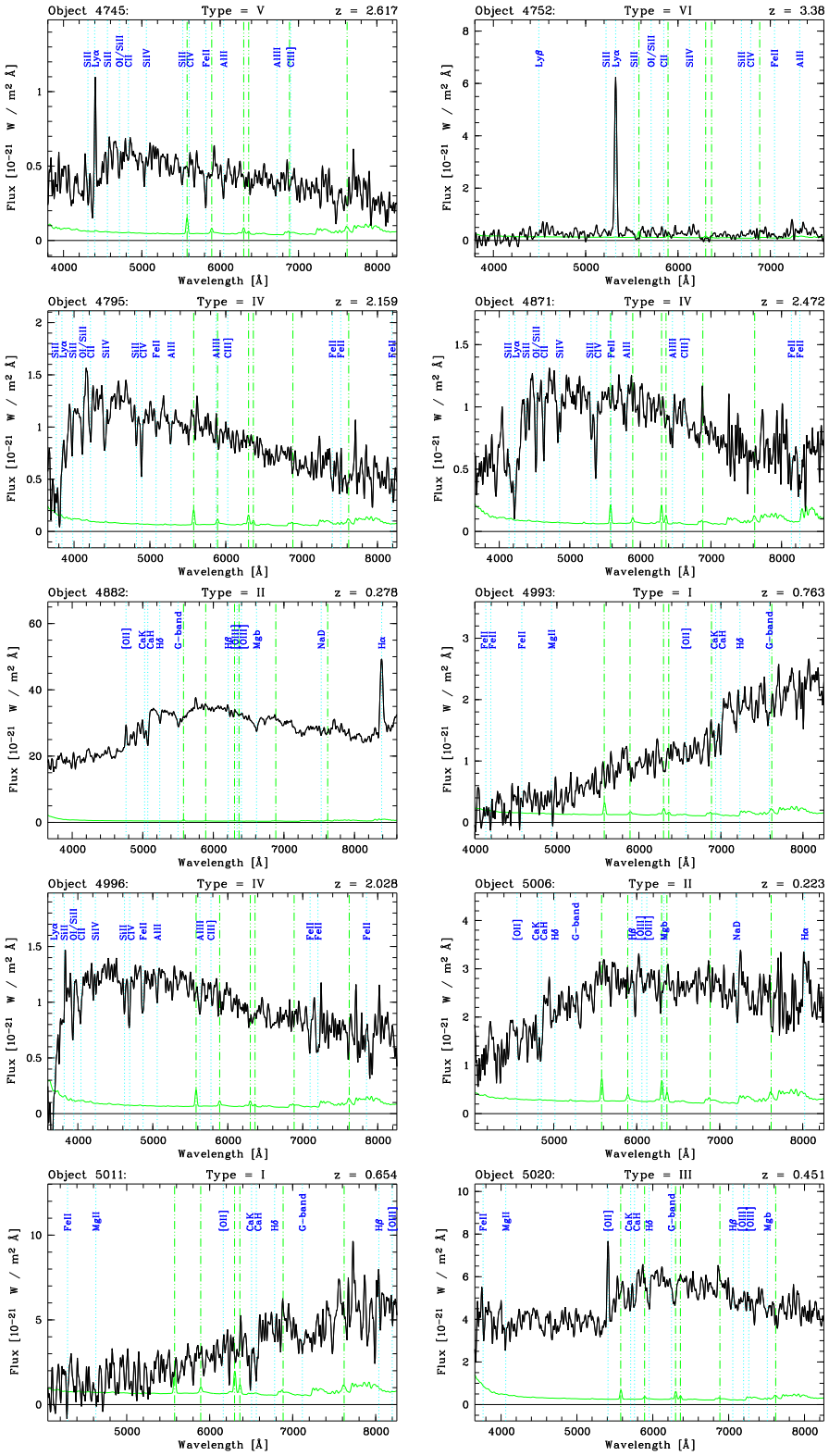

Figure D.14: Spectra of the objects 4745, 4752, 4795, 4871, 4882, 4993, 4996, 5006, 5011 and 5020.

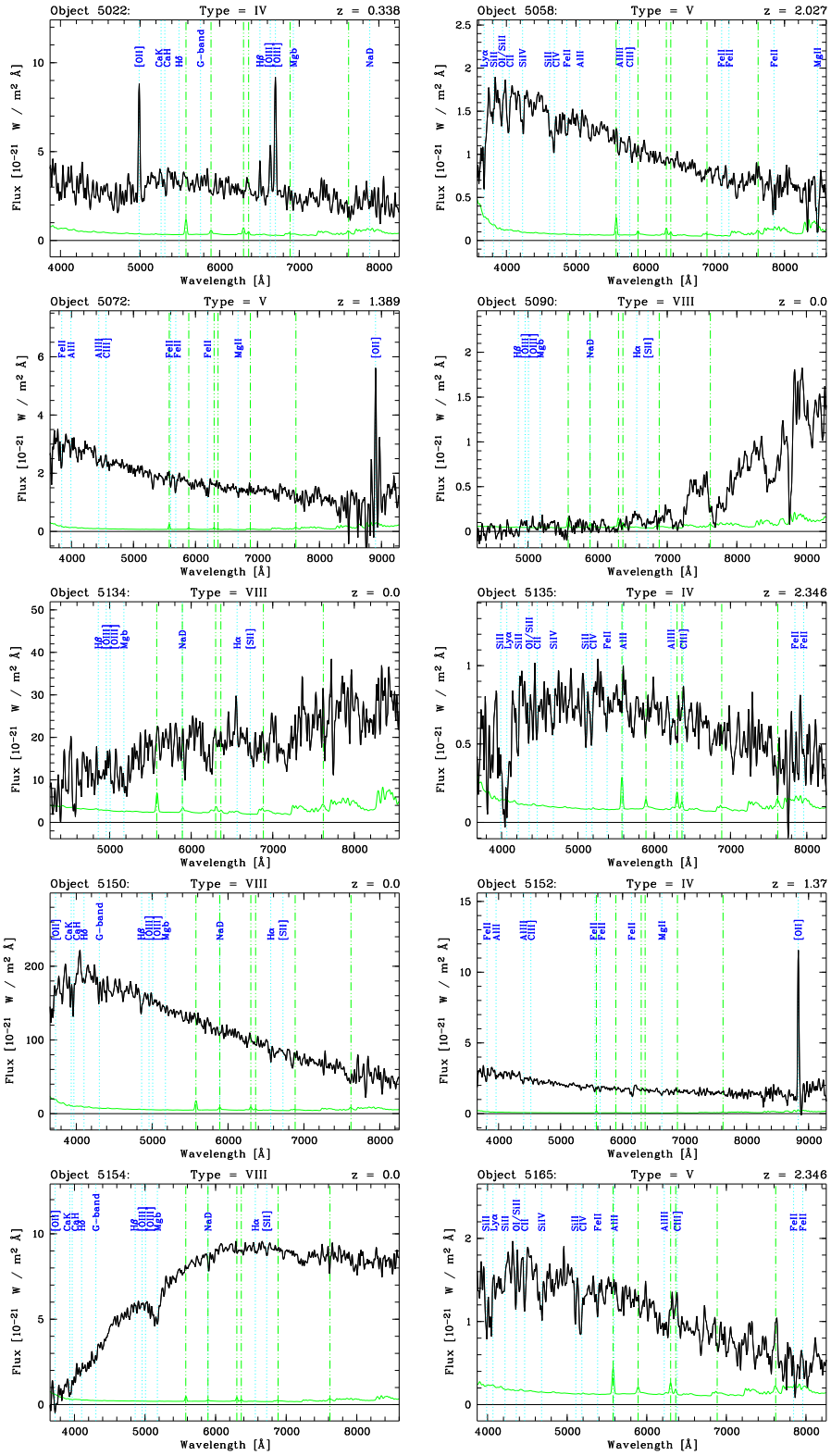

Figure D.15: Spectra of the objects 5022, 5058, 5072, 5090, 5134, 5135, 5150, 5152, 5154 and 5165.

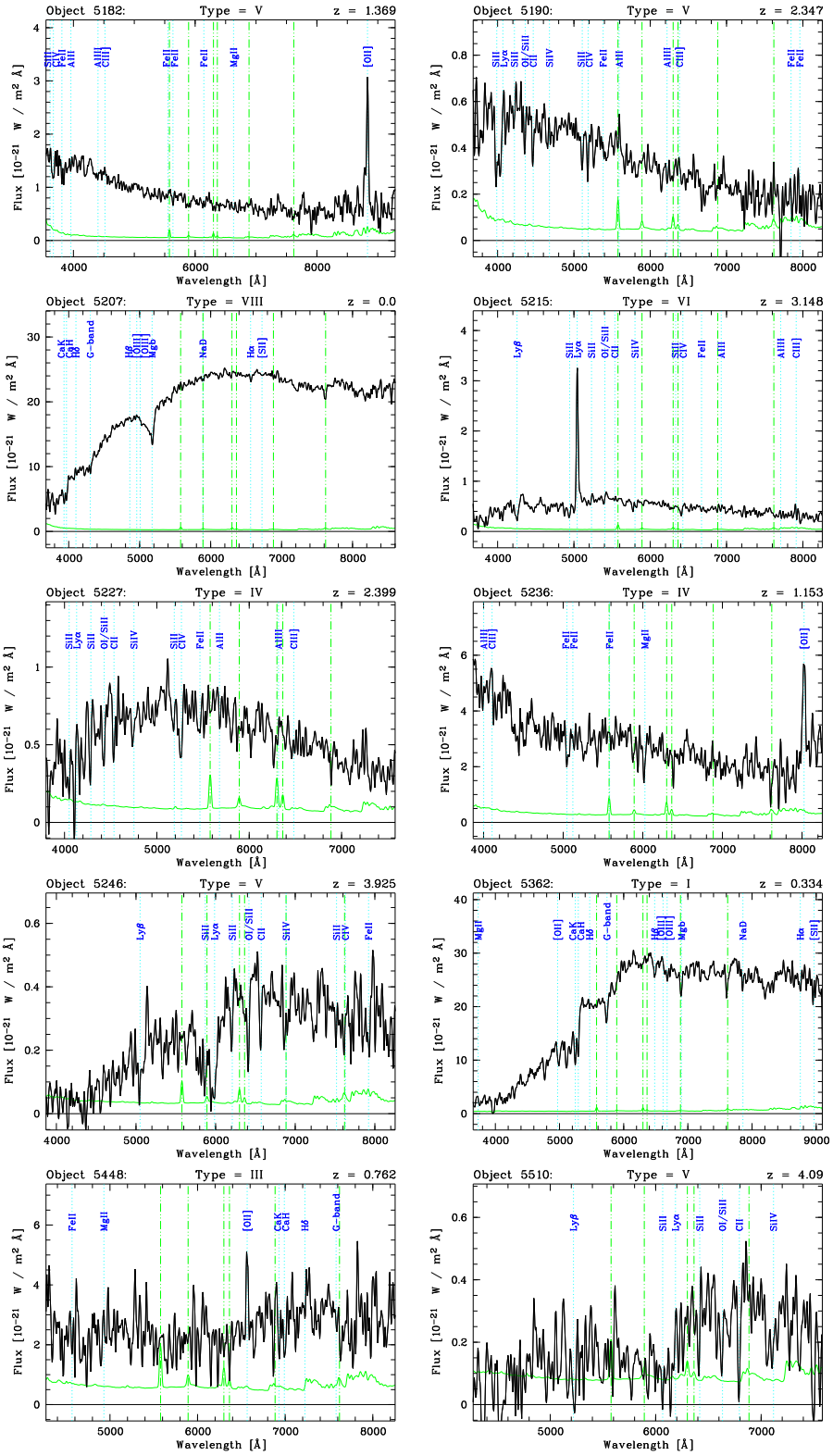

Figure D.16: Spectra of the objects 5182, 5190, 5207, 5215, 5227, 5236, 5246, 5362, 5448 and 5510.

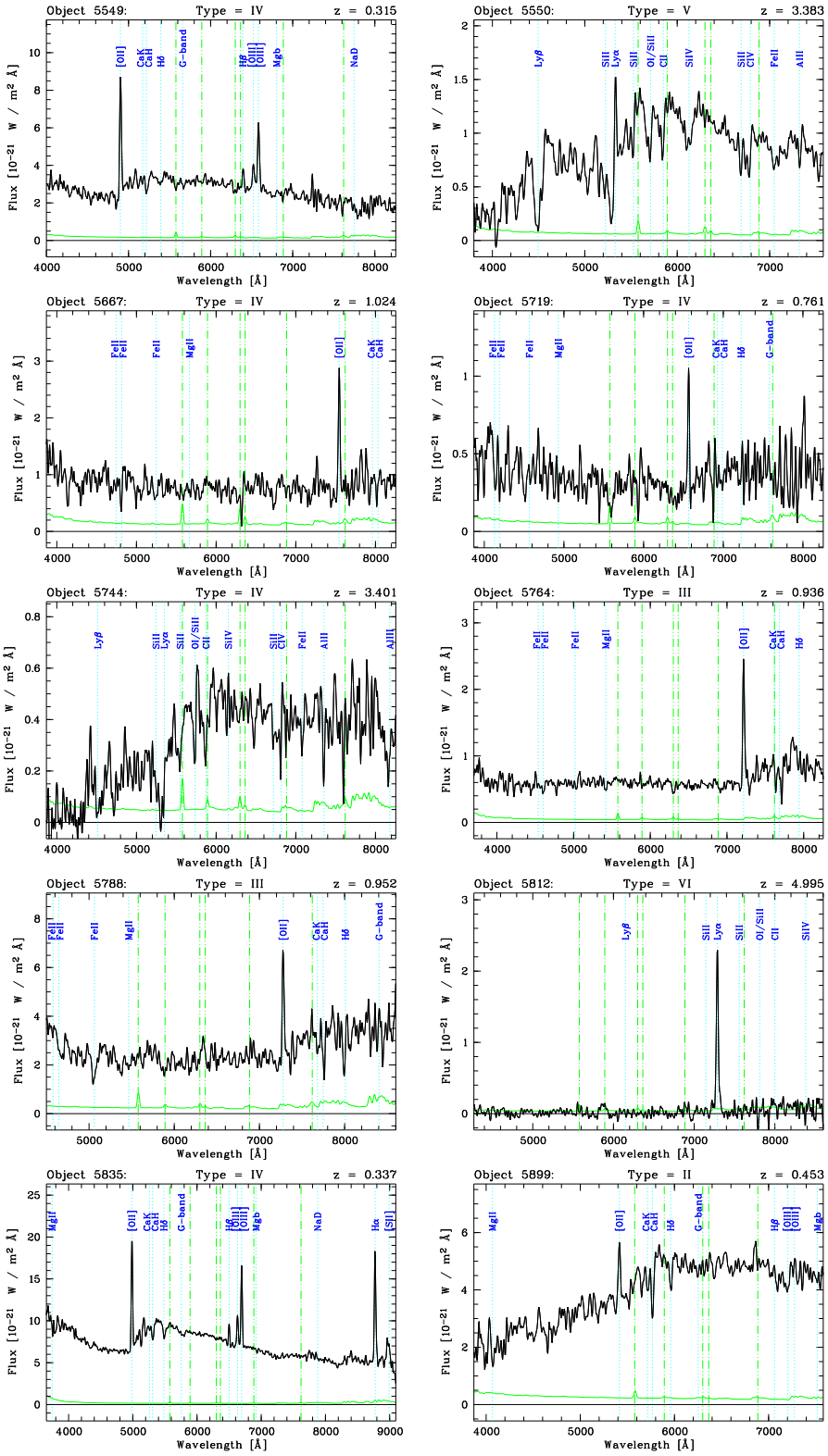

Figure D.17: Spectra of the objects 5549, 5550, 5667, 5719, 5744, 5764, 5788, 5812, 5835 and 5899.

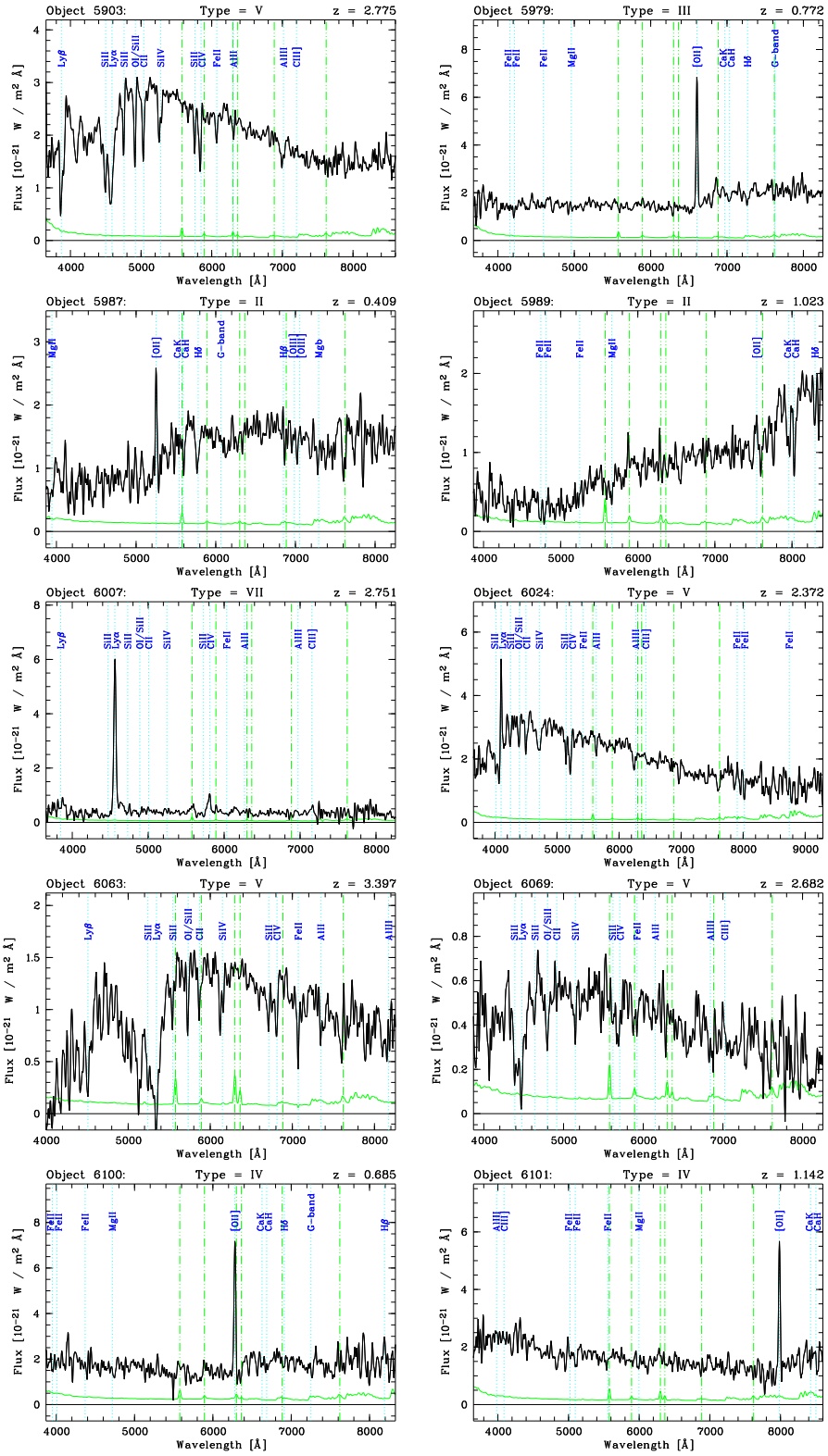

Figure D.18: Spectra of the objects 5903, 5979, 5987, 5989, 6007, 6024, 6063, 6069, 6100 and 6101.

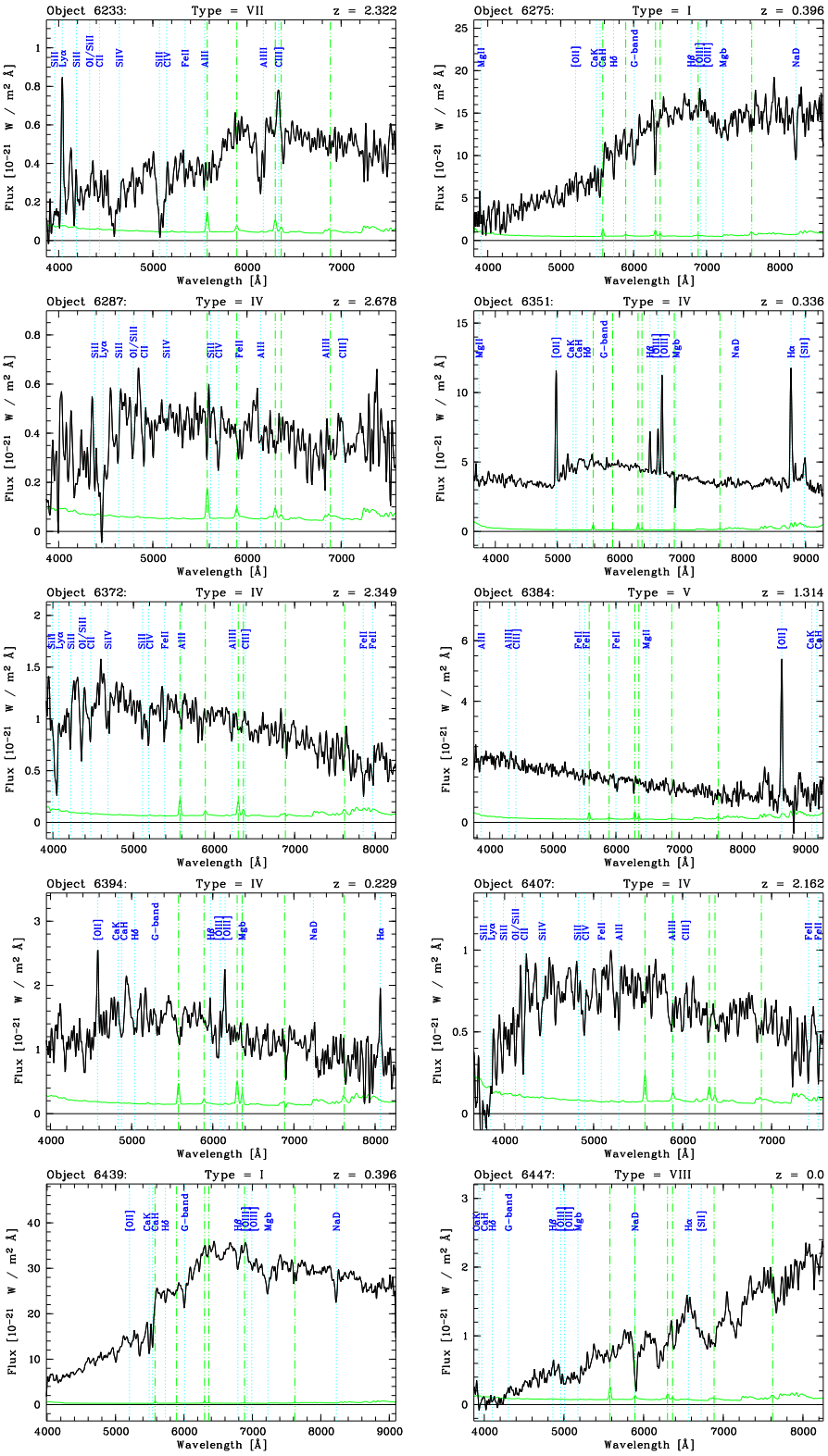

Figure D.19: Spectra of the objects 6233, 6275, 6287, 6351, 6372, 6384, 6394, 6407, 6439 and 6447.

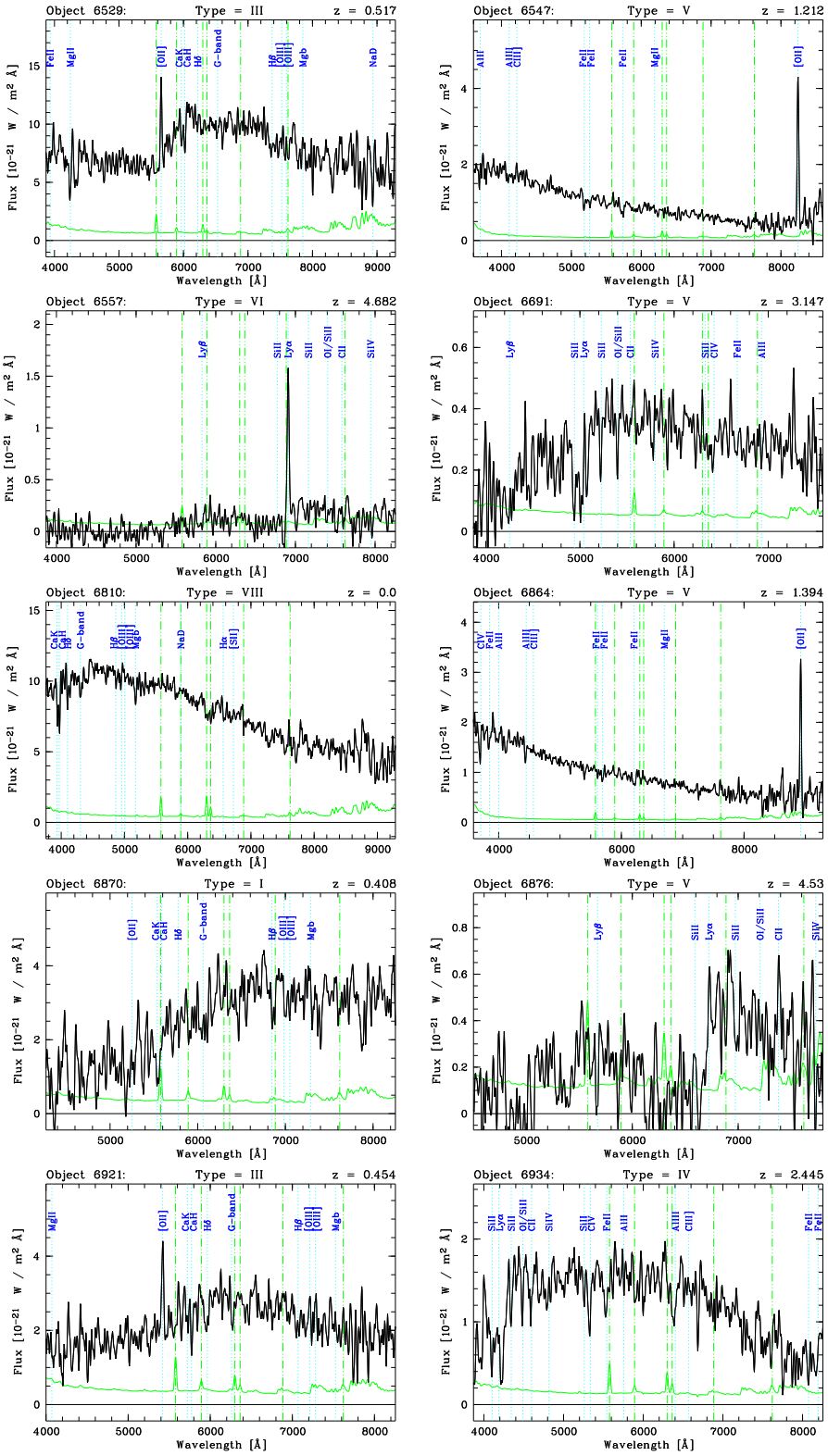

Figure D.20: Spectra of the objects 6529, 6547, 6557, 6691, 6810, 6864, 6870, 6876, 6921 and 6934.

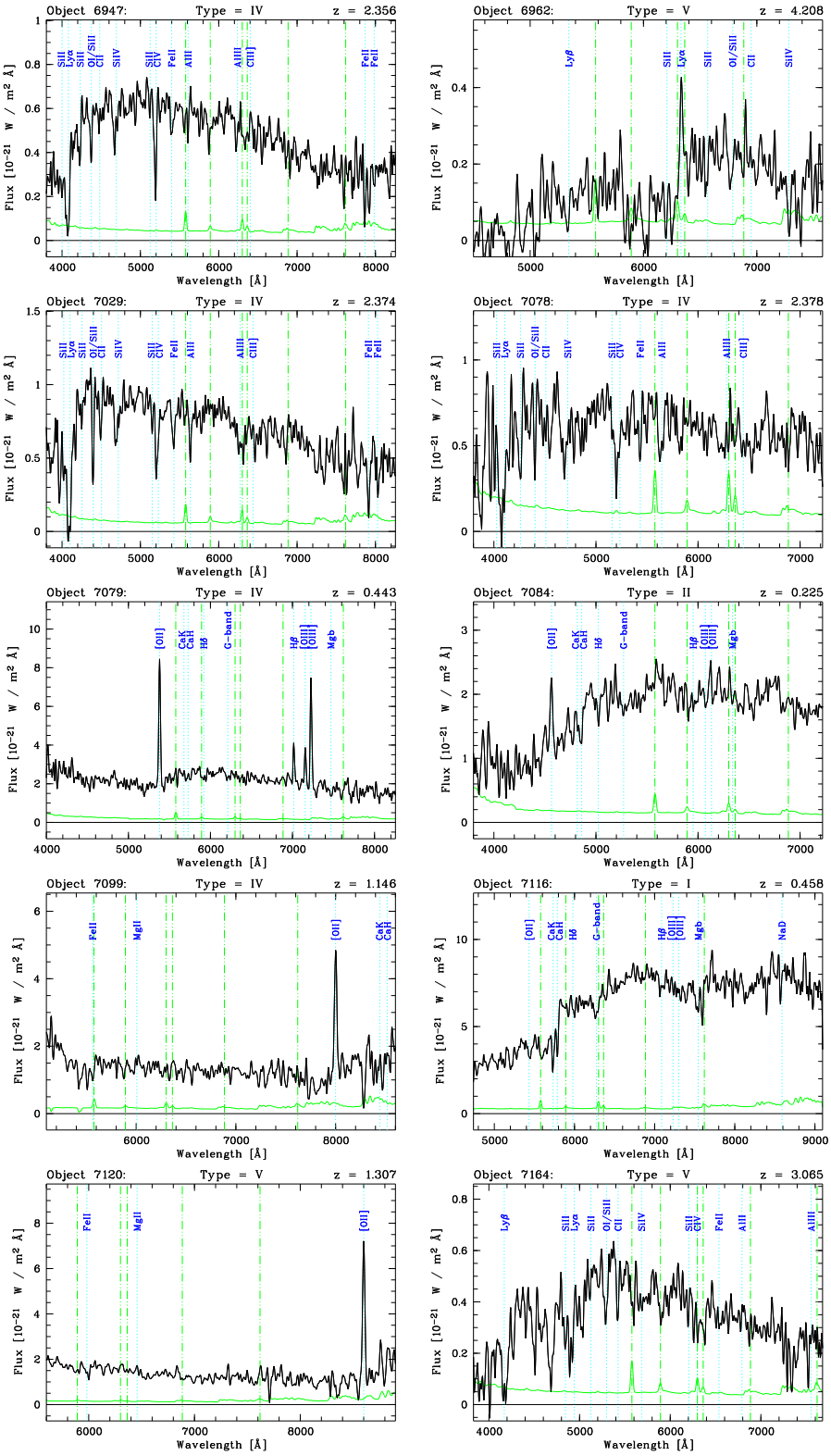

Figure D.21: Spectra of the objects 6947, 6962, 7029, 7078, 7079, 7084, 7099, 7116, 7120 and 7164.

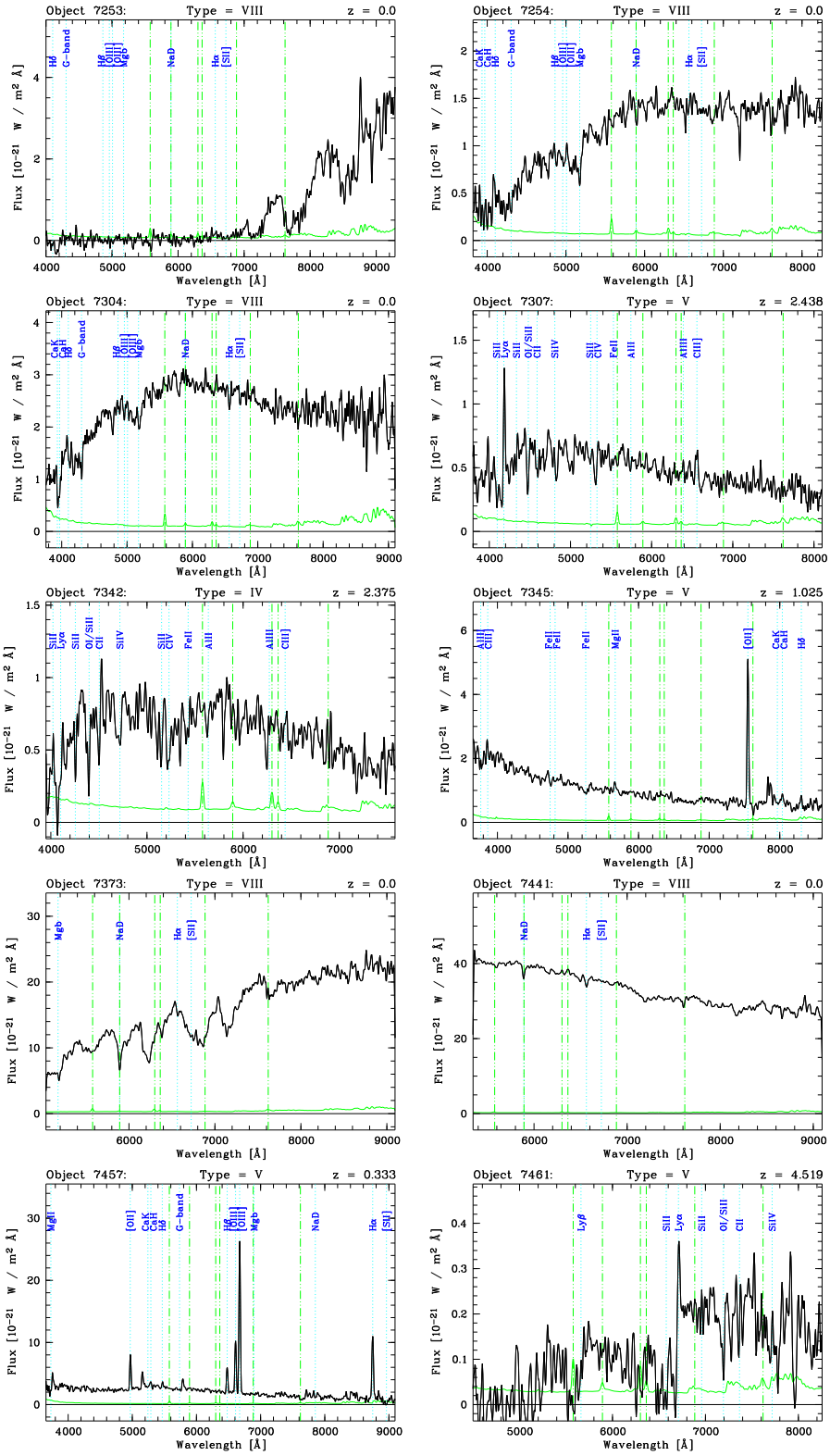

Figure D.22: Spectra of the objects 7253, 7254, 7304, 7307, 7342, 7345, 7373, 7441, 7457 and 7461.

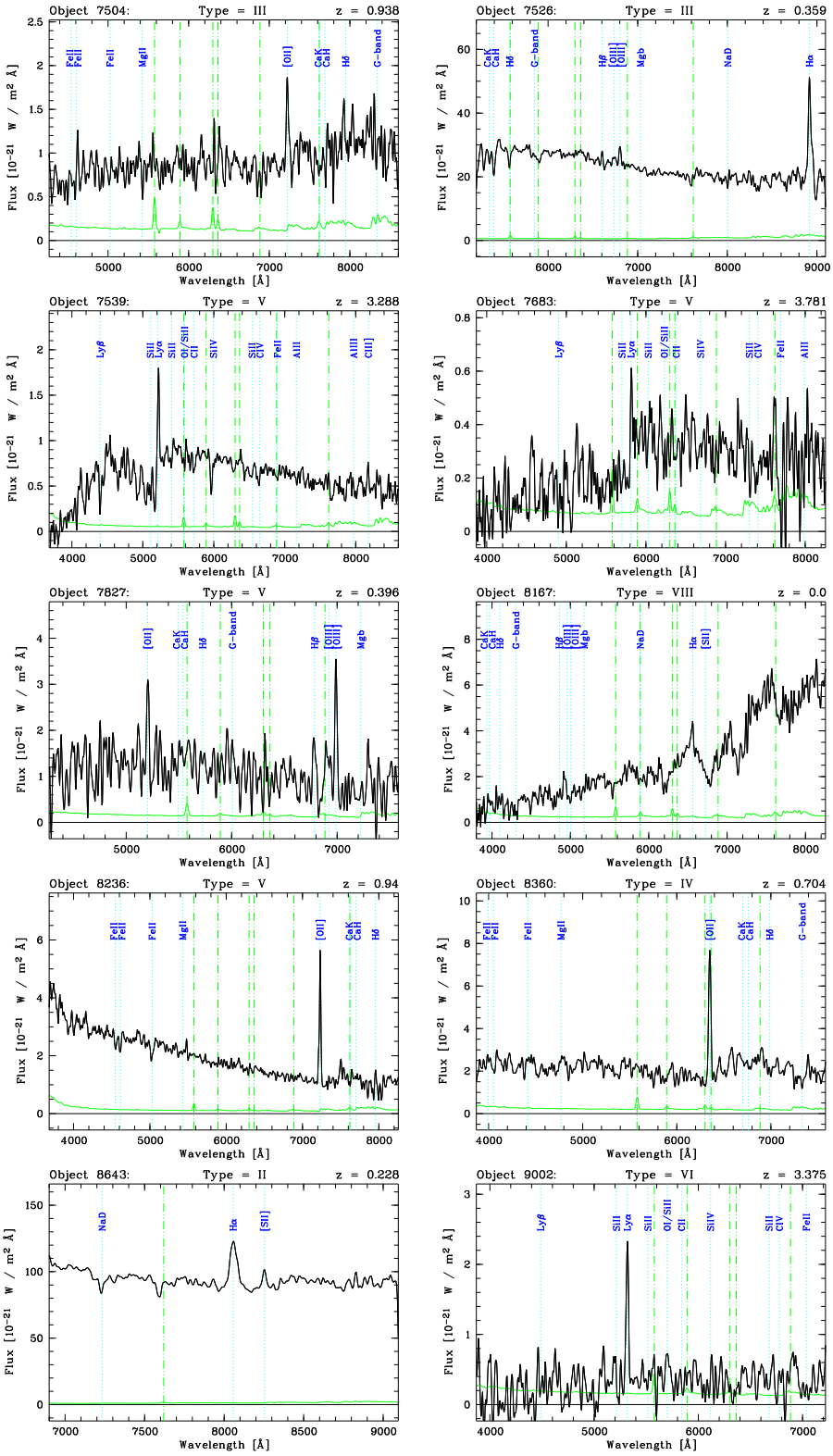

Figure D.23: Spectra of the objects 7504, 7526, 7539, 7683, 7827, 8167, 8236, 8360, 8643 and 9002.

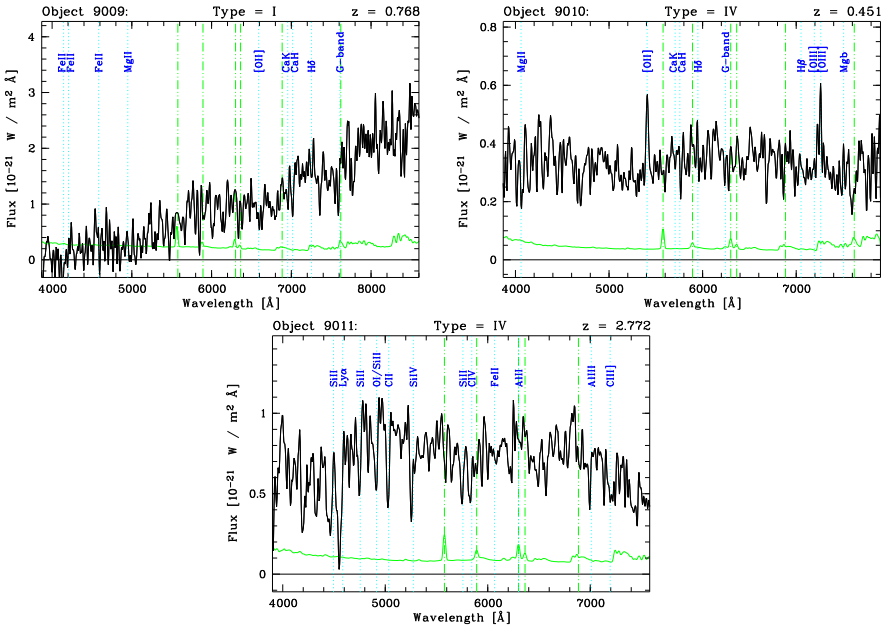

Figure D.24: Spectra of the objects 9009, 9010 and 9011.

Bibliography

Appenzeller, I., Rupprecht, G., 1992, The Messenger 67, 18

Appenzeller, I., Bender, R., Böhm, A., Drory, N., Fricke, K., et al., 2000, The Messenger 100, 44

Avila, G., Rupprecht, G., Beckers, J., 1997. in: Ardeberg, A., ed., SPIE 2871, 1222

Bender, R., Appenzeller, I., Böhm, A., Drory, N., Fricke, K.J., et al., 2001. in: Cristiani, S., Renzini, A., Williams, R.E., eds., *Deep Fields*, Springer, 96

Bennett, C.L., Banday, A.J., Gorski, K.M., Hinshaw, G., Jackson, P., et al., 1996, ApJ 464, 1

Böhm, A., 2001, private communication

Brandt, W.N., Alexander, D.M., Hornschemeier, A.E., Garmire, G.P., Schneider, D.P., et al., 2001, AJ 122, 2810

Cardelli, J.A., Clayton, G.C., Mathis, J.S., 1989, ApJ 345, 245

Carroll, M., Press, W.H., Turner, E.L., 1992, ARA&A 30, 499

Charlot, S., Fall, M.S., 1993, ApJ 415, 580

Colless, O., Bridle, S.L., Percival, W.J., Peacock, J.A., Efstathiou, G., et al., 2001, MNRAS 328, 1039

Cristiani, S., Appenzeller, I., Arnouts, S., Nonino, M., Aragón-Salamanca, A., et al., 2000, A&A 359, 489

de Bernardis, P., Ade, P.A.R., Bock, J.J., Bond, J.R., Borrill, J., et al., 2000, Nature 404, 955

Durrer, R., Novosyadlyj, B., 2001, MNRAS 324, 560

Efstathiou, G., Moody, S., Peacock, J.A., Percival, W.J., Baugh, C., et al., 2002, MNRAS 330, 29

Fan, X., Narayanan, V., Lupton, R.H., Strauss, M.A., Knapp, G.R., et al., 2001, AJ 122, 2833

Ferguson, H.C., Dickinson, M., Williams, R., 2000, ARA&A 38, 667

Freedman, W.L., Madore, B.F., Gibson, B.K., Ferrarese, L., Kelson, D.D., et al., 2001, ApJ 553, 47

Frye, B., Broadhurst, T., Benítez, N., 2002, ApJ 568, 558

Gabasch, A., et al., 2002, in preparation

Ghosh, S.N., 2002, *The Neutral Upper Atmosphere*, Dordrecht, Kluwer Academic Publishers

Giacconi, R., Zirm, A., Wang, J., Rosato, P., Nonino, M., et al., 2002, ApJS 139, 369

Giavalisco, M., Koratkar, A., Calzetti, D., 1996, ApJ 466, 831

Hamuy, M., Walker, A.R., Suntzeff, N.B., Gigoux, P., Heathcote, S.R., et al., 1992, PASP 104, 533

Hamuy, M., Suntzeff, N.B., Heathcote, S.R., Walker, A.R., Gigoux, P., et al., 1994, PASP 106, 566

Heckman, T.M., Robert, C., Leitherer, C., Garnett, D.R., van der Rydt, F., 1998, ApJ 503, 646

Heidt, J., Appenzeller, I., Gabasch, A., Jäger, K., Seitz, S., et al., 2002, A&A, in press

Horne, K., 1986, PASP 98, 609

Hu, E.M., Cowie, L.L., Mc Mahon, R.G., Capak, P., Iwamuro, F., et al., 2002, ApJ 568, L75

Kennicutt, R.C. Jr., 1992, ApJS 79, 255

Kennicutt, R.C. Jr., 1998, ARA&A 36, 189

Kinney, A.L., Bohlin, R.C., Calzetti, D., Panagia, N., Wyse, R.F.G., 1993, ApJS 86, 5

Kinney, A.L., Calzetti, D., Bohlin, R.C., Mc Quade, K., Storchi-Bergmann, T., et al., 1996, ApJ 467, 38

Kobulnicky, H.A., Zaritsky, D., 1999, ApJ 511, 188

Kobulnicky, H.A., Koo, D.C., 2000, ApJ 545, 712

Kunth, D., Lequeux, J., Sargent, W.L.W., Viallefond, F., 1994, A&A 282, 709

Kunth, D., Mas-Hesse, J.M., Terlevich, E., Terlevich, R., Lequeux, J., et al., 1998, A&A 334, 11

Legrand, F., Kunth, D., Mas-Hesse, J.M., Lequeux, J., 1997, A&A 326, 929

Leitherer, C., Leão, J.R.S., Heckman, T.M., Lennon, D.J., Pettini, M., et al. 2001, ApJ 550, 724

Lowenthal, J.D., Koo, D.C., Guzman, R., Gallego, J., Phillips, A.C., et al., 1997, ApJ 481, 673

Kajisawa, M., Yamada, T., 2001, PASJ 53, 833

Martín, E.L., Basri, G., Zapatero-Osorio, M.R., Rebolo, R., López, R.J. García, 1998, ApJ 507, L 41

Martín, E.L., Delfosse, X., Basri, G., Goldman, B., Forveille, T., et al., 1999, AJ 118, 2466

Maraston, C., 1998, MNRAS 300, 872

Mehlert, D., Seitz, S., Saglia, R.P., Appenzeller, I., Bender, R., et al., 2001, A&A 379, 96

Mehlert, D., Noll, S., Appenzeller, I., Saglia, R.P., Bender, R., et al., 2002, A&A 393, 809

Meisenheimer, K., Beckwith, S., Fockenbrock, R., Fried, J., Hippelein, H., et al., 1997. in: Bergeron, J., ed., *The Early Universe with the VLT*, Berlin, Springer, 165

Menou, K., Vanden Berk, D.E., Željko, I., Kim, R.S.J., Knapp, G.R., et al., 2001, ApJ 561, 645

Metcalfe, N., Shanks, T., Campos, A., Mc Cracken, H.J., Fong, R., 2001, MNRAS 323, 795

Meurer, G.R., Heckman, T.M., Calzetti, D., 1999, ApJ 521, 64

Moore, C.E., ed., 1945, *A Multipet Table of Astrophysical Interest, Part I – Table of Multiplets*, Contrib. Princeton Univ. Obs. No. 20, Princeton, Princeton University Observatory

Moore, C.E., ed., 1952, *An Ulraviolet Multiplet Table*, Circular of the National Bureau of Standards 488 Section 2, Washington, United States Department of Commerce

Murray, N., Chiang, J., Grossmann, S.A., Voit, G.M., 1995, ApJ 451, 498

Naab, T., Burkert, A., Hernquist, L., 1999, ApJ 523, 133

Noll, S., Mehlert. D., Appenzeller, I., et al., 2003, in preparation

Oke, J.B., 1990, AJ 99, 1621

Osterbrock, D.E., 1989, *Astrophysics of Gaseous Nebulae and Active Galactic Nuclei*, Sausalito (CA), University Science Books

Pettini, M., Rix, S.A., Steidel, C.C., Adelberger, K.L., Hunt, M.P., et al., 2002, ApJ 569, 742

Pettini, M., Shapley, A.E., Steidel, C.C., Cuby, J., Dickinson, M., et al., 2001, ApJ 554, 981

Pettini, M., Steidel, C.C., Adelberger, K.L., Dickinson, M., Giavalisco, M., 2000, ApJ 528, 96

Pickles, A.J., 1985, ApJS 59, 33

Raimann, D., Storchi-Bergmann, T., Bica, E., Melnick, J., Schmitt, H., 2000, MNRAS 316, 559

Reader, J., Corliss, C.H., Wiese, W.L., Martin, G.A., 1980, *Wavelengths and Transition Probabilities for Atoms and Atomic Ions*, Washington, National Bureau of Standards

Riess, A.G., Filippenko, A.V., Challis, P., Clocchiatti, A., Diercks, A., et al., 1998, AJ 116, 1009

Saidel, A.K., Prokofiev, V.K., Raiski, S.M., eds., 1961, *Tables of Spectrum Lines*, London, Pergamon Press

Sarazin, M., Navarrete, J., 1999, The Messenger 97, 8

Sarazin, M., 2000, The Messenger 99, 13

Schlegel, D.J., Finkbeiner, D.P., Davis, M., 1998, ApJ 500, 525

Simkin, S.M., 1974, A&A 31, 129

Spinrad, H., Stern, D., Bunker, A., Dey, A., Lanzetta, K., et al., 1998, AJ 116, 2617

Steidel, C.C., Giavalisco, M., Pettini, M., Dickinson, M., Adelberger, K.L., 1996a, AJ 462, L 17

Steidel, C.C., Giavalisco, M., Dickinson, M., Adelberger, K.L., 1996b, AJ 112, 352

Steidel, C.C., Pettini, M., Adelberger, K.L., 2001, ApJ 546, 665

Stetson, P., 1988, Dominion Astrophysical Observatory Preprint

Szeifert, T., Apenzeller, I., Fürtig, W., Seifert, W., Stahl, O., et al., 1998. in: D'Orico, S., ed., SPIE 3335, 20

Tonry, J., Davis, M., 1979, AJ 84, 1511

Tüg, H., 1977, The Messenger 11, 7

Tyson, J.A., 1988, AJ 96, 1

Walborn, N.R., Lennon, D.J., Haser, S.M., Kudritzki, R., Voels, S.A., 1995, PASP 107, 104

Warren, S.J., Hewett, P.C., Osmer, P.S., 1991, ApJS 76, 23

Weymann, R.J., Stern, D., Bunker, A., Spinrad, H., Chaffee, F.H., 1998, ApJ 505, 95

Williams, R.E., Blacker, B., Dickinson, M., Dixon, W.V., Ferguson, H.C., et al., 1996, AJ 112, 1335

Williams, R.E., Baum, S., Bergeron, L.E., Bernstein, N., Blacker B.S., et al., 2000, AJ 120, 2735

Ziegler, B.L., Böhm, A., Fricke, K.J., Jäger, K., Nicklas, H., et al., 2002, ApJ 564, 69

Acronyms

A&A	Astronomy and Astrophysics
A&AS	Astronomy and Astrophysics Supplement Series
AJ	Astronomical Journal
ApJ	Astrophysical Journal
ApJS	Astrophysical Journal Supplement Series
ARA&A	Annual Review of Astronomy and Astrophysics
ed./eds.	Editor(s)
MNRAS	Monthly Notices of the Royal Astronomical Society
PASJ	Publications of the Astronomical Society of Japan
PASP	Publications of the Astronomical Society of the Pacific

Danksagung

Diese Arbeit konnte nur durch die Unterstützung zahlreicher Leute entstehen. Ich bin diesen Menschen zu größtem Dank verpflichtet.

Für die finanzielle Unterstützung dieser Arbeit und die Bereitstellung des Arbeitsplatzes danke ich dem Land Baden-Württemberg als Träger der Landessternwarte sowie der Deutschen Forschungsgemeinschaft (Sonderforschungsbereich 439). Weiterhin bin ich der ESO zu Dank verpflichtet für die Ermöglichung meiner beiden Aufenthalte am VLT.

Ganz besonders bedanke ich mich bei meinem Doktorvater **Immo Appenzeller**, der diese Arbeit überhaupt erst ermöglicht hat. Er hat durch das große Interesse an meiner Arbeit, die Zeit, die er sich trotz seiner Vielbeschäftigung immer wieder genommen hat, den Freiraum den er mir gegeben hat und die gute Arbeitsatmosphäre, die er vermittelt, sehr viel dazu beigetragen, dass die vergangenen Jahre für mich zu einer schönen und lehrreichen Zeit geworden sind.

Klaus Meisenheimer danke ich dafür, dass er freundlicherweise die Zweitgutachtertätigkeit übernommen hat.

Dörte Mehlert sei Dank für die ausgezeichnete Zusammenarbeit und das gute Arbeitsklima. Hervorzuheben ist, mit welchem Fleiß sie sich durch mein höchst unvollkommenes Englisch hindurchgearbeitet hat.

Christian Tapken danke ich ebenfalls für eine ausgezeichnete Zusammenarbeit. Der gegenseitige Austausch über die Erfahrungen bei der Datenreduktion war sicher für uns Beide von großer Bedeutung.

Jochen Heidt danke ich für die gute Zusammenarbeit und seinen Einsatz für das Projekt. Außerdem danke ich ihm für seinen Anteil am gemeisamen angenehmen und interessanten Beobachtungsaufenhalt am VLT im November 2001.

Allen Mitarbeitern der Landessternwarte danke ich für dieses freundliche und familiäre Klima, welches die Sternwarte zu einem sehr angenehmen Arbeitsplatz macht.

Stella Seitz gebührt mein Dank für ihre Bemühungen die Photometrie für das spektroskopische Sample zu optimieren.

Otmar Stahl und **Monika Darr** danke ich dafür, dass sie Computerprobleme zu Nebensächlichkeiten werden ließen. Besonders **Otmar Stahl** war selbst am Wochenende oder an Feiertagen immer sofort bereit zu helfen.

Mareike Ziegler danke ich für ihr aufopferungsvolles Korrekturlesen.

Meinen Eltern danke ich dafür, dass sie mir die Freiheit gegeben haben, den Weg zu gehen, der mich schließlich zu dieser Doktorarbeit geführt hat.

Bei **meiner Freundin Irina** habe ich mich im besonderen Maße zu bedanken, da sie in den Monaten des Zusammenschreibens mir viel Verständnis entgegengebracht und mich aktiv unterstützt hat, obwohl sie es selbst auch nicht immer leicht hatte.